This is to certify that the

dissertation entitled

Femtosecond Gas-Phase Molecular Dynamics: Pump-Probe and Four-Wave Mixing Experiments

presented by

Emily J.S. Brown

has been accepted towards fulfillment
of the requirements for

Ph.D. degree in **Chemistry**

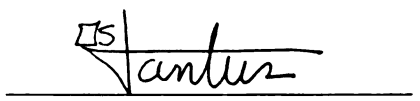

Major professor

Date 8-2-01

FEMTOSECO
PUMP-PROBE

FEMTOSECOND GAS-PHASE MOLECULAR DYNAMICS: PUMP-PROBE AND FOUR-WAVE MIXING EXPERIMENTS

By

Emily J. S. Brown

A DISSERTATION

Submitted to
Michigan State University
in partial fulfillment of the requirements
for the degree of

DOCTOR OF PHILOSOPHY

Department of Chemistry

2001

EMTOSECOND G
AND F

Time-resolved

rational constants of

ergy in chemical reacti

he well-known expressi

directional signal de

erpendicular component

Some unidirectional de

ge and demonstrated

rbon vapor. Fits to the

urate results. In addit

easurements are observe

ree orders of magnit

ds to apply to the loss o

unimolecular processes

easurements show an un

ection of a weaker p

ABSTRACT

FEMTOSECOND GAS-PHASE REACTION DYNAMICS: PUMP-PROBE AND FOUR-WAVE MIXING EXPERIMENTS

By

Emily J. S. Brown

Time-resolved rotational anisotropy measurements can be used to obtain rotational constants of molecules or information about the alignment and rotational energy in chemical reactions. For some of the most common experimental configurations, the well-known expression for obtaining the rotational anisotropy is not applicable; unidirectional signal detection measurements can overestimate the parallel or perpendicular components of the signal. New formulations that take into account different unidirectional detection schemes and the *f* number of the collection optics are given and demonstrated with femtosecond time-resolved anisotropy measurements on iodine vapor. Fits to the calculated anisotropy are shown to provide quantitatively accurate results. In addition, nonlinear saturation effects in ultrafast rotational anisotropy measurements are observed as a function of increased pump laser intensity (ranging over three orders of magnitude). These effects range from a mild reduction in overall anisotropy to the loss of anisotropy at time zero and the appearance of additional photochemical processes. At the highest intensities, the rotational anisotropy measurements show an unusual initial dip followed by a rise near time zero that is due to excitation of a weaker perpendicular state. Experimental results on molecular iodine,

chen as a model sys-

ermens rotational pop-

ar a nonlinear rotator

nsitements with sat-

Time-resolved tra-

FWM processes are ex-

ging from single at-

ferm species Ar and X

ar linear triatomic CS

mences that can be a

ar vibrational and rota-

nsitements on larger p

ara rotational dephasing

ngate and simulate the

herent excitation allow

ences, i.e. populations

ectronic states. These ca

pulation transfer betwe

herwave mixing. The in

e pulse sequence that c

equence timing causes a

ar state to coherent vi

chosen as a model system, fit with the conventional anisotropy formalism result in erroneous rotational populations. Incorporating the observation of the perpendicular state into a nonlinear rotational anisotropy model yields accurate rotational populations from measurements with saturated transitions.

Time-resolved transient grating techniques (TG) arising from four-wave mixing (FWM) processes are explored for the study of molecular dynamics in gas-phase systems ranging from single atoms to large polyatomic molecules with nonresonant pulses. Atomic species Ar and Xe show a peak only at zero time delay. For diatomic O_2 and N_2 and linear triatomic CS_2 molecules, the TG signals exhibit ground state rotational recurrences that can be analyzed to obtain accurate rotational constants. Both ground state vibrational and rotational dynamics are observed in the heavier triatomic HgI_2. TG measurements on larger polyatomic molecules (CH_2Cl_2, CH_2Br_2, benzene, and toluene) show rotational dephasing. A theoretical formalism is developed and used successfully to interpret and simulate the experimental transients. Four-wave mixing experiments with resonant excitation allow us to select between measurements that monitor wave packet dynamics, *i.e.* populations in the ground or excited states, or coherences between the two electronic states. These cases are explored with the $X \rightarrow B$ transition in I_2. Control of the population transfer between the ground and excited states is reported using three-pulse four-wave mixing. The inherent vibrational dynamics of the system are utilized in timing the pulse sequence that controls the excitation process. A slight alteration in the pulse sequence timing causes a change in the observed signal from coherent vibration in the ground state to coherent vibration in the excited state.

For Robert and Andrew,

Many people have

individuals who have

First, I would like

Department. Specifically

graduate office, and comm

MSU. I would like to pers

Knight and Tom Atkinso

members.

I would also like t

further assistance both p

Maria Gilchrest, Irene G

Sarah, Kathy Wakowicz,

expertise in the lab and cl

Marios Dantus, thank you

Xavier. Thank you for yo

State Michigan and I comp

I would also like t

further support, love, and

My parents and my husban

like every day!

ACKNOWLEDGMENTS

Many people have helped me along this journey– it is a difficult task to name all the individuals who have played a role during this portion of my life.

First, I would like to acknowledge all the support staff in the Chemistry Department. Specifically, the people in the machine shop, glass shop, business office, graduate office, and computer technology office were invaluable during my years at MSU. I would like to personally thank Lisa Dillingham for helping to keep all the details straight and Tom Atkinson and Paul Reed for their assistance with troublesome computers.

I would also like to recognize the past and present members of the research group for their assistance both professionally and personally. Specifically, Holly Bevsek, Martha Gilchrest, Irene Grimberg, Peter Gross, Vadim Lozovoy, Una Marvet, Igor Pastirk, Kathy Walowicz, Mark Waner, and Qingguo Zhang – thank you for your expertise in the lab (and classroom) and your advice out of the lab! To my advisor, Marcos Dantus, thank you for the opportunities to learn and grow as a scientist and teacher. Thank you for your understanding and patience as family matters took me away from Michigan and I completed this degree "long-distance".

I would also like to thank my friends (especially those I made at MSU) and family for their support, love, and encouragement (gentle nudges) over these years, especially my parents and my husband Robert. Lastly, to my son Andrew, thank you for making me smile every day!

TABLE OF CONTENTS

Table I. Semiclassica
detection (paralle
collection. Correct
made by using the

Table II. Rotational te
(3.3) (A) without th
parameter at differe
percentage ind cat
temperature .....

Table III. Rotational te
Equation (3.4) wh
reactive path para
the calculated temp

Table IV. Rotational te
Equation (3.11) wh
A_{AB} parameter (wh
that the calculated

LIST OF TABLES

LIST OF FIGURES

dotted line represe
arrive before t=0e

Figure 2.3. Experimer
unidirectional X-a
oriented along the
beam can be rotat
perpendicular to t

Figure 2.4. Beam arra
80 and 81) E_a and
delays, these fiel
E_c Bragg scatters
two other fields is
system. In our exp

Figure 3.1. Relevant p
be excited to the B
transition) with 622
induce a transition
probe beams) and
pump-probe beams
detected.....

Figure 3.2. (a) Simulat
distribution quickly
distribution (B_f) to a
as viewed from the
$n(f)$ at longer time d
develops. The dra
plane so that the s
is labeled with the d

Figure 3.3. (a) I_c and I
for I_2 with 622/311(
Because different v
by the two excitatio
(a). For the same re
two data sets result

Figure 3.4. URA measu
values calculated fr

shown as the sca
shown as the sc
distribution of 29
parameter. .....

Figure 3.5 Rotationa
Experimental data
fits are shown wi
saturation parame
measurements are
12K respectively

Figure 3.6 Rotationa
These URA meas
simple saturation
time zero and yie

Figure 3.7. Parallel an
different pump lase
significant increase
perpendicular tran
This increase is du
high laser intensit

Figure 3.8. Semiclass
perpendicular tran
include only the f-
with weak laser in
A-X excitation pat
preferential probin
arrangement leads
the dip that is obs
line was calculate
line assumed a la

Figure 3.9. Rotationa
The fits for these U
and reactive state
this model. The ro
intensities shown a

Figure 3.10. Rotation
fit the experimen
T_{RT} = 294 ± 3K is
one standard de
saturation is not
regime temperat
above the actua
the B–X transitio
B–X transition ar
the fitted tempera
high intensity reg

Figure 3.11. Depende
parameters or the
trend with similar

Figure 4.1. PS-I show
time delay betwee
fields E_b and E_c. P
τ is a variable time
delay between fie

Figure 4.2. Double-sid
processes observe
cases the signal. e
Based on the expe
E_b are overlapped
respect to these be
indicates the two b
the population is fo
grating and cause
scatters from this g
obtained. (b) Here
$\rho^{(2)}_{gg}$ into $\rho^{(2)}_{ee}$ or
excited state dynam
between fields E_a a
only observed only
diagrams E_c arrives
ground and excited
evolve for a time τ.
E_c which forms the

Figure 4.8. TG trans
(lower). The exp
calculated us ng
the time-zero co
rotational dephas
CH_2Cl_2 than in C

Figure 4.9. TG trans
experimental data
simulations from
benzene is strong
intensities of the
equal. The rotat
expected from the

Figure 4.10. Top: TG
experimental data
followed by a larg
simulated using E
curve with the circ
signal for CS_2 mu
inhomogeneous c
diffusional dephas
curve used by Ne
References 54 and

Figure 4.11. Bottom: T
seen at both negat
central wavelength
transition. Left inse
There is one main
209.9 ± 0.3 cm^{-1}. R
times. The frequen
and 312.0 ± 0.2 cm
combination freque
because of the sum
frequency (105 cm
rotational frequency

Figure 4.12. Semiclass
negative time delay
transforms. The sim
presented in Figure

Figure 4.13. Experim
τ_{ac} = 460 fs corre
the excited state
The power FFT o
0.2 cm^{-1} corresp
iodine. It reflects
state. The slow
dephasing.....

Figure 4.14. Experim
ps are shown). T
excited state of
power FFT of the
cm^{-1} correspond
iodine. It depicts
ground state. The
small contribution
around 1.5 ps is

Figure 4.15. Close-up
and Figure 4.14.
contribution at 10
the vibrational freq
the data show a p
frequency of the e
likely a second ha
region at low frequ
correspond to the
state (τ_{ac} = 614 fs,
in the frequency is
these two states. T
state dynamics bas

Figure 4.16. Experime
ps are shown). Not
The power FFT of
corresponding to vi
cm^{-1} is most probab

Figure 4.17. Experimen
ps are shown). The
106 cm^{-1} and 208 c

the amount of g
(see Figure 4.1

Understanding

al alignment condi

rations and torsion

emistry. For instanc

an be used to learn

hemical bonds.

In the late 18

1. INTRODUCTION

1.1. MOLECULAR DYNAMICS

Understanding chemical reactions — bond breakage and formation, orientation and alignment conditions, time of reaction, mechanism, transition state, and vibrations, rotations, and torsion before and after the reaction — is one of the fundamental areas of chemistry. For instance, the partition of energy among the products in a chemical reaction can be used to learn about the forces involved during the formation and breakage of chemical bonds.

In the late 1800's, Arrhenius introduced his kinetic equation

$$k(T) = Ae^{-E_a/kT} \tag{1.1}$$

---

[i] Reproduced in part with permission from E. J. Brown, I. Pastirk, and M. Dantus, J. Phys. Chem. A **103**, 2912 (1999). Copyright 1999 American Chemical Society.

[ii] Reproduced in part with permission from E. J. Brown, I. Pastirk, and M. Dantus, J. Phys. Chem. A, in press. Unpublished work copyright 2001 American Chemical Society.

[iii] Reproduced in part with permission from E. J. Brown, Q. Zhang, and M. Dantus, J. Chem. Phys. **110**, 5772 (1999). Copyright 1999 American Institute of Physics.

[iv] Reproduced in part with permission from E. J. Brown, I. Pastirk, B. I. Grimberg, V. V. Lozovoy, and M. Dantus, J. Chem. Phys. **111**, 3779 (1999). Copyright 1999 American Institute of Physics.

[v] I. Pastirk, E. J. Brown, B. I. Grimberg, V. V. Lozovoy, and M. Dantus, Faraday Discuss. **113**, 401 (1999) - Reproduced in part by permission of The Royal Society of Chemistry.

where $\delta(T)$ is the term
energy (the minimum
to go forward. It is
ollisions that lead to
ften replaced by the
probability of reactio
usually less than 1 or
greater attraction for e
n ensemble and react
ermal distribution of

In the early 19
f potential energy surf
ime to proceed from
eaction rates, transi
ctivation energies and
olecules would col
rrangement and the ori
formation also aided
dvanced this area of
losit into a molecul
ckings and the shap
pectroscopy using co
een progressed from

where $k(T)$ is the temperature-dependent rate constant of the reaction, E_a is the activation energy (the minimum energy required to reach the transition state and allow the reaction to go forward), k is the Boltzmann constant, and T is the temperature. The frequency of collisions that lead to a reaction are included in the pre-exponential factor A; this was later replaced by the expression z^*P, where z is the number of collisions and P is the probability of reaction (also called a steric or orientational factor). The probability is usually less than 1 unless the reaction includes a catalyst or ionized species that have a greater attraction for each other. This equation advanced our understanding of kinetics of an ensemble and reactions in bulk matter, but it provided statistical information about a thermal distribution of molecules rather than information about individual molecules.

In the early 1900's, London and Eyring and Polanyi worked on the development of potential energy surfaces (PES) that would provide a path for molecules to follow in order to proceed from reactants to products. These PES eventually led to the calculation of reaction rates, translational and vibrational motion of molecules on these surfaces, and activation energies and transition states. With the development of the molecular beam, molecules would collide only once with a given energy in a particular angular arrangement and the orientational dependence of the reaction could be studied. Rotational information also aided in determining the lifetime of the intermediate species. Lasers advanced this area of research even more by providing discrete amounts of energy to deposit into a molecule and polarization to study orientational effects. Energy level spacings and the shape of the PES could be determined with frequency-resolved spectroscopy using continuous wave and nanosecond lasers. As the time duration of lasers progressed from nanosecond to picosecond to femtosecond, the shorter pulse

provided a method fo

the pulse temporal w

developed by Zewail

transition state[2]; in

a dissociation reactio

transition state, time

the reaction, and

framework for the s

including the concert

X_2Y_2 compounds ((

photodissociation react

1.1.1. Wave Packet

With resonant e

electronic state (V_2). T

state (V_1). By the Unc

direction will have a la

Thus, the frequency s

Thus, a number of quan

pulse which produces a

Gaussian, $\varepsilon_0 \exp\left[-t^2 / \alpha\right]$

$\alpha = 2\ln 2$, τ is the full w

provided a method for studying molecular dynamics that were on the same time scale as the pulse temporal width. Femtosecond transition state spectroscopy (FTS) is a technique developed by Zewail and co-workers at Caltech to investigate the dynamics of the transition state[1,2]; in 1987 they made the first real-time observation of a transition state in a dissociation reaction.[3] This technique can be utilized to gain information about the transition state, time of reaction, vibrational and rotational dynamics of species involved in the reaction, and potential energy surfaces.[1,4-6] This work has laid the conceptual framework for the studies conducted by our group at Michigan State University, including the concerted molecular photoelimination reactions of CH_2I_2 and the related CX_2Y_2 compounds ($CX_2Y_2 \rightarrow CX_2 + Y_2$) (bound-to-free transitions)[7-12] as well as the photoassociation reaction to form Hg_2 (free-to-bound transition).[13-15]

1.1.1. Wave Packet Motion

With resonant excitation, a photon is absorbed by a molecular system in a ground electronic state (V_0). This absorption causes a vertical transition to an excited electronic state (V_1). By the Uncertainty Principle, we know that a pulse that has a short temporal duration will have a large spectral bandwidth; for most molecular systems and ultrafast pulses, the frequency spread of the pulse is wider than the vibrational energy spacing. Thus, a number of quantum states are populated on V_1 by the absorption of a short laser pulse which produces a coherent superposition of states. The laser pulse is assumed to be Gaussian, $\varepsilon_0 \exp\left[-t^2/\alpha\tau^2\right]\cos(\omega t)$, where ε_0 is the amplitude of the field, α is equal to $2\pi^2/\ln(2)$, τ is the full width at half maximum (FWHM) of the temporal duration, and ω is

the central frequency

states φ_n in V, with ω

Only one $a_n \neq 0$, the

nstationary state re

by using first-order pe

$$a_n = C \quad \varphi_n \quad \omega$$

where C is a constan

Spin moment. ω

the state φ_n, and $\hbar$ i

where $\omega_n = \left| E_n - E_i \right.$

Notice that as

the central frequency of the pulse. The resulting wave function is a sum of all the possible states φ_n in V_1 with amplitudes a_n,

$$\Psi = \sum_n a_n \varphi_n \,. \tag{1.2}$$

If only one $a_n \neq 0$, then $\Psi = a_n\varphi_n$ and is a stationary state. If more than one $a_n \neq 0$, then a nonstationary state results that can evolve in time. These amplitudes, a_n, can be calculated by using first-order perturbation theory,[16]

$$a_n = C\left\langle \varphi_n \middle| \varphi_0^{(0)} \right\rangle \int_{-\infty}^{\infty} \exp\left[-i(E_n - E_0)t/\hbar\right]\cos(\omega t)\exp\left[-t^2/\alpha\tau^2\right]dt \tag{1.3}$$

where C is a constant that includes the amplitude of the electric field and the transition dipole moment, $\varphi_0^{(0)}$ is the ground state wave function, E_n is the energy that corresponds to the state φ_n, and $\hbar$ is Planck constant divided by 2π. Integrating this equation yields

$$a_n = C\left\langle \varphi_n \middle| \varphi_0^{(0)} \right\rangle \exp\left[-(\omega_n - \omega)^2 \alpha\tau^2/4\right] \tag{1.4}$$

where $\omega_n = \left(E_n - E_0'\right)/\hbar$ and E_0' is the energy corresponding to the ground state.

Notice that as the temporal duration increases ($\tau \rightarrow \infty$) in Equation (1.4),

$$a_n = C\left\langle \varphi_n \middle| \varphi_0^{(0)} \right\rangle \delta(\omega_n - \omega)\,. \tag{1.5}$$

The delta function in

will be only a sing

ependence or evolut

ery short pulses ($\tau \to$

hich correspond to τ

at $x / = 0$. the wave

The wave packet can

ation

The general solution to

Therefore, the wave pack

The delta function in this equation ensures that only one $a_n \neq 0$ when $\omega = \omega_n$. Thus, there will be only a single eigenstate φ_n (stationary state) and no possibility for time dependence or evolution with long pulses. Examining Equation (1.4) again for the case of very short pulses ($\tau \rightarrow 0$),

$$a_n = C\left\langle \varphi_n \middle| \varphi_0^{(0)} \right\rangle \tag{1.6}$$

which correspond to the Franck-Condon factors. Therefore, the wave packet on V_1 is

$$\Psi = C\sum_n \left\langle \varphi_n \middle| \varphi_0^{(0)} \right\rangle \varphi_n \tag{1.7}$$

and at $t = 0$, the wave packet on V_1 is a reproduction of the ground state wave function. This wave packet can now evolve in time according to the time-dependent Schrödinger equation

$$i\hbar \frac{\partial \psi(t)}{\partial t} = \hat{H}\psi(t). \tag{1.8}$$

The general solution to this differential equation is

$$\psi_n(t) = \varphi_n \exp\left[-iE_n t/\hbar\right]; \tag{1.9}$$

therefore, the wave packet on V_1 is

We can imagine th
potential energy curv
rave. Classical and
ackets are available
references 17-22 an
ngth from the excite
ackets on the excited
ckets a coherent w
mpulsive stimulated
re discussed.

11.2 Time-Resolve

High-resolution
he molecular dynamic
mperatures, large po
he spectroscopic analy
pectra by taking the
me-resolved data yie
ples. Although freque
eems more intuitive to

$$\Psi(t) = \sum_n a_n \exp[-iE_n t/\hbar]\varphi_n \,. \qquad (1.10)$$

We can imagine this wave packet as a classical particle oscillating on the excited potential energy curve showing the periodic nature of the molecular vibrations on this curve. Classical and semiclassical descriptions of the temporal evolution of this wave packet are available and can be applied to ultrafast spectroscopy, for example see References 17-22 and a review in Reference 23. The laser induced fluorescence (LIF) signal from the excited V_2 state corresponds to the dynamics (time evolution of the wave packet) on the excited V_1 state. In the case of non-resonant excitation with ultrashort laser pulses, a coherent wave packet is produced in the ground electronic state due to impulsive stimulated scattering[24] and similar wave packet dynamics can be calculated and discussed.

1.1.2. Time-Resolved Spectroscopy

High-resolution frequency-resolved spectroscopy can provide information about the molecular dynamics of the system. However, under certain conditions such as high temperatures, large polyatomic molecules, and mixtures, spectral congestion complicates the spectroscopic analysis. Molecular dynamics can be obtained from frequency-resolved spectra by taking the Fourier transform of the data; similarly, the Fourier transform of time-resolved data yields the frequency information about the molecular system (*vide infra*). Although frequency-resolved spectroscopy can be used to obtain the dynamics, it seems more intuitive to consider these dynamics in the time-resolved domain where the

dynamics can be ob

other advantages

processes, including

ational reaction

frequency-resolved

ow spectral intensit

esolved experiments.

ther species and resu

n gas-phase samples

ser pulse; therefor

haracteristics of the

mp) can be manipul

The past de

nvestigation using

dynamics in the g

Various probing tec

higher-order nonli

molecular dynamics

four-wave mixing

rotational and

experiments cond

dynamics can be observed directly ("snapshots") by the femtosecond pulses. There are other advantages of ultrafast time-resolved spectroscopy. The ease of nonlinear processes, including multiphoton excitation due to high peak intensities allows for additional reaction pathways that may not be seen otherwise. In time-integrated (frequency-resolved) experiments, the short lifetimes of intermediate species lead to very low spectral intensities for these species compared to the reactants and products. In time-resolved experiments, the selection of the detection wavelength can discriminate against other species and results in an increased signal-to-noise ratio for the intermediate species. In gas-phase samples, collisions occur on a time scale much greater than the ultrafast laser pulse; therefore, collisions do not affect these measurements. In addition, the characteristics of the ultrafast laser pulse (such as phase, frequency components, and chirp) can be manipulated (or "tailored") to control chemical reactions (*vide infra*).

The past decade has witnessed rapid growth of real-time molecular dynamics investigation using ultrashort laser pulses.[1,4-6] Most ultrafast experiments on molecular dynamics in the gas phase have been carried out using the pump-probe technique. Various probing techniques have been exploited in this endeavor. More recently, third- or higher-order nonlinear techniques have been employed increasingly for studying molecular dynamics in the gas-phase environment; one of these nonlinear techniques is four-wave mixing (FWM). The focus of this research is to examine the extraction of rotational and vibrational information from pump-probe and four-wave mixing experiments conducted with femtosecond pulses.

Pump-probe

nitored by a

employed for over a

solution of the me

of control over the

nterferometer.[25,26] A

were used with micro

[5,9,30]

Pump-probe sp

of molecular dynamic

non-reactive systems w

where bond dissociat

concentrate on the an

the parent and daugh

show the time evolut

reactive systems, one l

well as the emergence

or the determination of

well established for t

spectroscopy.[36,37] The

1.2. PUMP-PROBE TECHNIQUE

Pump-probe techniques, in which a process is initiated by a burst of light and is monitored by a subsequent burst of light aimed at the sample some time later, have been employed for over a hundred years. The advantage of this technique is that the time resolution of the measurement depends only on the duration of the pulse and the degree of control over the time delay, which can achieved by the use of a Mach-Zehnder interferometer.[25,26] Around the middle of the twentieth century, pump-probe techniques were used with microsecond pulses[27,28] and today can be used with pulses as short as 5 or 6 fs.[29,30]

Pump-probe spectroscopy using ultrafast lasers has advanced our understanding of molecular dynamics and chemical reactions in real time. Studies have been done on non-reactive systems where vibrational motion is observed as well as on reactive systems where bond dissociation and formation take place.[1,4,5,31] In the following studies we concentrate on the angular motion of gas-phase molecules which reflects the rotations of the parent and daughter species. Polarized lasers are used in these measurements to follow the time evolution of the rotational alignment of the isolated molecules.[32-35] For reactive systems, one learns about the rotational impulse during the chemical reaction as well as the emergence of the final rotational population,[21,33] which in some cases can aid in the determination of a reaction mechanism.[8,9,15] Rotational anisotropy techniques are well established for the study of molecular structure as in rotational coherence spectroscopy.[36,37] The measurements are relatively simple and can yield quantitative

information on the

or the overall rotati

In our pump-

molecule from its

wave packet is create

dynamics of a system

multiphoton excitati

electronic or vibrati

rise I_{probe}) then ca

energy than the fir

vals into fragment

the process, vari

mission, laser indu

Stokes Raman s

photoionization or p

the excited molecul

dynamics. In Figure

information on the molecular structure of the molecule studied in addition to information on the overall rotational population.

In our pump-probe studies, a linearly polarized femtosecond pulse (λ_{pump}) excites a molecule from its (bound) ground electronic (V_0) state to an excited state (V_1) where a wave packet is created (see Figure 1.1a). In these experiments, a pump laser initiates the dynamics of a system typically through a one-photon excitation process. In a few studies multiphoton excitation by the pump laser has been utilized to access higher-lying electronic or vibrational states.[7,8,38-40] After a variable time delay, a second femtosecond pulse (λ_{probe}) then causes a transition to another excited state (V_2) either higher or lower in energy than the first excited state (V_1). If this excitation process causes the molecule to break into fragments, the process is called photodissociation (reactive system). For the probe process, various techniques have been used; examples include absorption, emission, laser induced fluorescence (LIF), fluorescence up-conversion, coherent anti-Stokes Raman scattering (CARS), and multiphoton excitation followed by photoionization or photoelectron detection.[1,4,5,23,41] We have generally measured LIF of the excited molecule or one of its fragments, from either V_1 or V_2, to monitor the dynamics. In Figure 1.1a, LIF is detected from the second excited state.

Figure 1.1. Obtainin
The pump pulse is
packet propagates
probe pulse excites
which is detected. T
states in the case s
fluorescence as a f
for a full vibrational
effects were neglec

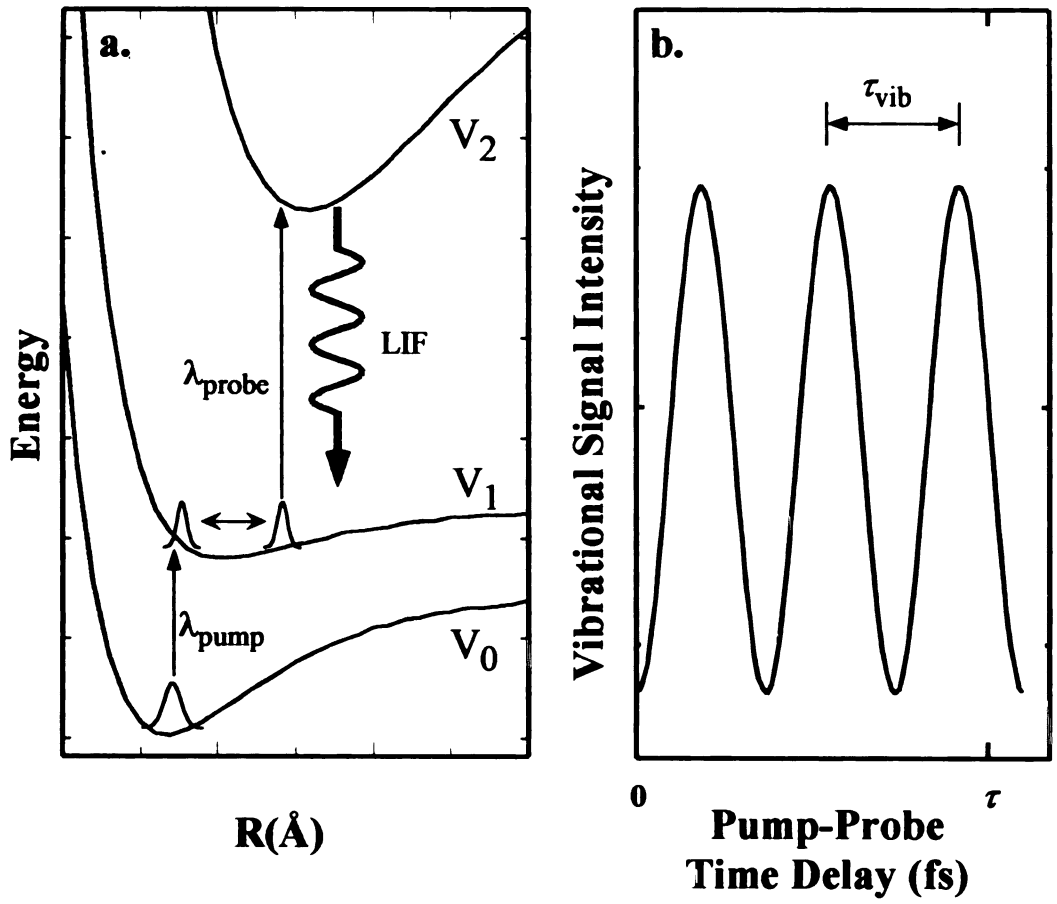

Figure 1.1. Obtaining vibrational information from the pump-probe technique. (a) The pump pulse is resonant with the transition between V_0 and V_1. The wave packet propagates on the V_1 excited state. At the Franck-Condon region, the probe pulse excites the molecules to the V_2 state where they emit fluorescence which is detected. The ground (V_0) and excited states (V_1 and V_2) are all bound states in the case shown here. (b) The changes in the laser-induced fluorescence as a function of the pump-probe time delay show the time it takes for a full vibrational oscillation of the molecules in the V_1 excited state. Rotational effects were neglected here.

As the wave p

ages and the ability

mount of LIF that

figure 1.1a, when t

overlap is minimized

ming point, the Fr

gnal. Thus, the vibr

ump-probe time del

scillations of the w

1.1b, from these osc

$\omega_e = 2\pi\, c_{(e)}$).

As the molecu

se to induce a tra

ecules on V_1 with the

well aligned with th

ases, the overlap of

decreases, resulting in

scillations will be a s

nsients. Thus, as the

fraction of the pump

ddition, the separatio

iscussed in Chapter 3.

As the wave packet on V_1 propagates, the Franck-Condon factor of the transition varies and the ability of the probe pulse to cause an excitation to V_2 changes. Thus the amount of LIF that can be detected oscillates with the pump-probe time delay. Thus in Figure 1.1a, when the wave packet is at the inner turning point, the Franck-Condon overlap is minimized resulting in a decrease in the LIF signal. Conversely at the outer turning point, the Franck-Condon overlap is maximized resulting in an increase in the signal. Thus, the vibration dynamics of the V_1 surface are measured as a function of the pump-probe time delay and are equal to the summation of cosines.[42] The vibrational oscillations of the wave packet on the V_1 potential energy curve are shown in Figure 1.1b; from these oscillations, we can determine the excited state vibrational frequency ($\omega_{vib} = 2\pi/\tau_{vib}$).

As the molecule vibrates, it also rotates in space. Thus, the ability of the probe pulse to induce a transition is also affected by the relative alignment of the excited species on V_1 with the polarization of the laser. When the dipole moment of the molecule is well aligned with the probe laser polarization, the LIF signal is high. As the molecule rotates, the overlap of the polarization of the probe and transition dipole of the molecule decreases, resulting in a decrease in the LIF signal. So, underneath the fast vibrational oscillations will be a slower undulation corresponding to rotations in the experimental transients. Thus, as the fragment rotates, rotational anisotropy effects can be observed as a function of the pump-probe time delay and will be discussed in detail in Chapter 3. In addition, the separation of the rotational and vibrational dynamics in the data will be discussed in Chapter 3. The formalisms for quantitative analysis of these measurements,

r the extraction of

ave investigated re

nd intense pump las

Techniques s

pioneered by Heritage

workers for their

olved third-order

ulses.[24,56-66] only

femtosecond dynamic

ne-resolved CARS

olecules.[67] Zewail

ving real-time re

DFWM pump pul

ise with the depl

apor using time-r

he incident pulses

he vibrational an

lectronic states.

esolved transien

n-linear optical

i.e. the extraction of vibrational and rotational populations, are well known[21,42,43] and we have investigated recently how these formulae may change for unidirectional detection and intense pump lasers.[44,45]

1.3. FOUR-WAVE MIXING TECHNIQUE

Techniques similar to coherent transient birefringence in vapor samples, pioneered by Heritage *et al.* in the picosecond regime,[46] were recognized by Fayer and coworkers for their potential for probing gas-phase dynamics.[47-49] Although time-resolved third-order nonlinear optical techniques have long been used in condensed phases,[24,50-66] only recently have these novel probes been applied to the study of femtosecond dynamics in the gas phase.[67-70] Hayden and Chandler used femtosecond time-resolved CARS to study coherent rotational dephasing of large gas-phase molecules.[67] Zewail and coworkers used degenerate four-wave mixing (DFWM) for probing real-time reaction dynamics.[68] They demonstrated three types of arrangements: DFWM, pump pulse followed by DFWM probing, and pump pulse followed by a control pulse with the depletion dynamics probed by DFWM. Schmitt *et al.* have studied iodine vapor using time-resolved CARS and DFWM.[69-72] By varying the time delay of one of the incident pulses while maintaining the other two incident pulses fixed, they showed that vibrational and rotational dynamics can be observed for both the ground and excited electronic states. Here, the different types of dynamics that can be observed by time-resolved transient-grating (TG) techniques, involving four-wave mixing (FWM) nonlinear optical processes, are examined. The name "transient grating" is used here to

ghlight the fact that
he time ordering of
ring. One of the g
uantitative analysis
ating experiments a

One of the m
ixing techniques is
ses.[4,73,74] Consider
teracting with a me
rms of pulse enve
is is not to be cons
atial modulation o
nterference (see Figu
ectric field intensitie
ransient grating of po
ved easily by the
ation of the gratin
ng as the coherence
hoton echo experime
herence dephasing ti

highlight the fact that most of the information obtained in these experiments derives from the time ordering of various ultrashort pulses and not from high-resolution frequency tuning. One of the goals of this work is to gain an increased level of understanding of the quantitative analysis of ultrafast molecular dynamics measured by gas-phase transient grating experiments arising from four-wave mixing nonlinear processes.

One of the most physically intuitive explanations of time-resolved four-wave mixing techniques is based on the formation of transient gratings by the incident lasers.[47,73,74] Consider three incident light pulses with electric fields $E_a(t)$, $E_b(t)$ and $E_c(t)$ interacting with a medium. From here on we will assume that the three fields are identical in terms of pulse envelope and frequency components, *i.e.*, they are degenerate; however, this is not to be considered as a necessary condition. At the crossing of two beams, the spatial modulation of their electric fields varies due to constructive and destructive interference (see Figure 1.2a). The molecules in the interaction region experience varying electric field intensities according to their position, and this leads to the formation of a transient grating of polarized molecules in space. The transient grating formation can be probed easily by the detection of Bragg scattering of a third laser beam.[47,73,74] The formation of the grating does not require that the two crossing beams coincide in time as long as the coherence is maintained in the sample.[75] This property has been exploited in photon echo experiments where the time delay between the lasers is used to probe the coherence dephasing time.[76-81]

gure 1.2 Transient
rmation of the trans
ecs (b) The transie
racted in the k_S =
eam in this case is
d) This is the pu
ating signal (TG) s
ec coming before t
gnal (RTG) shown

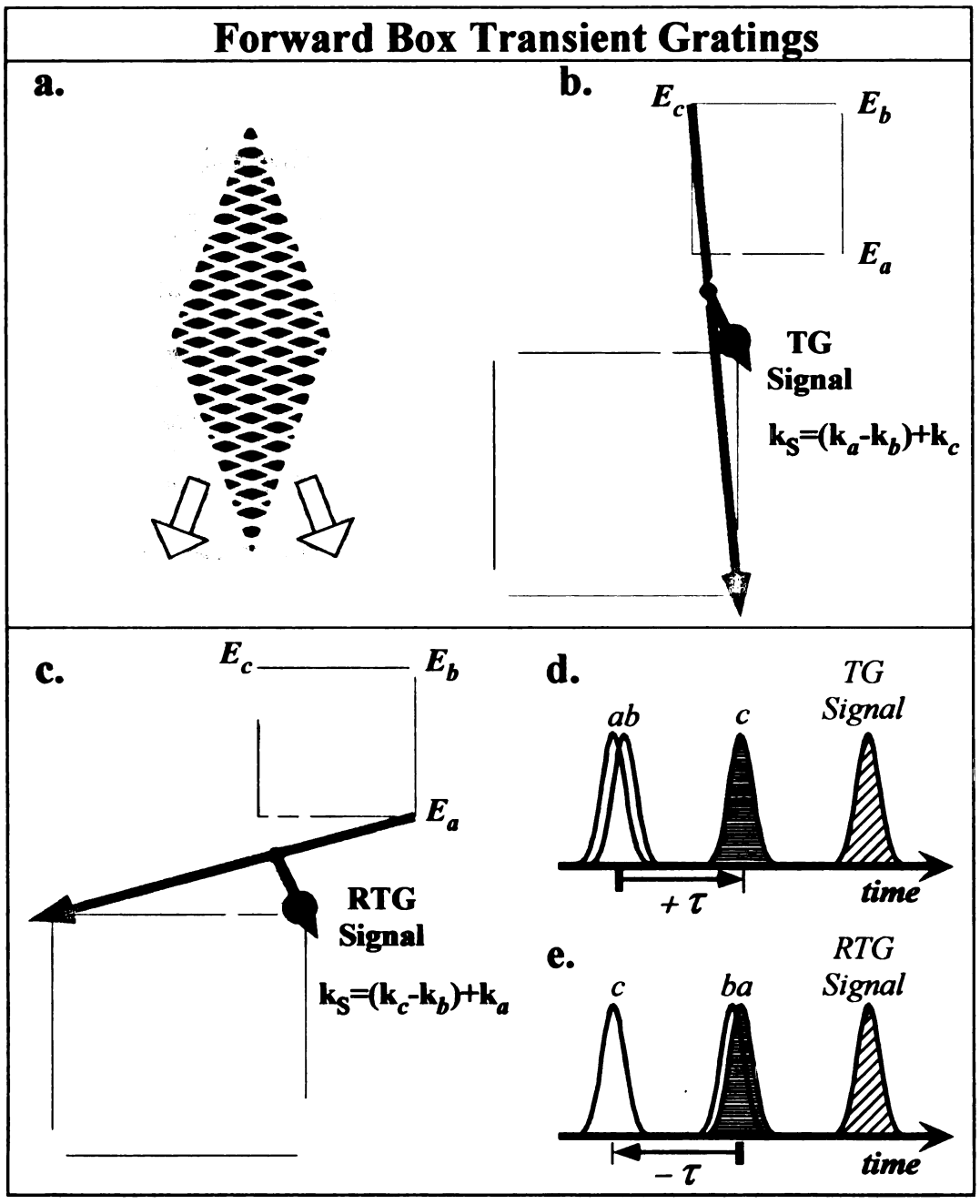

Figure 1.2 Transient gratings formed in the forward-box configuration. (a) The formation of the transient grating is due to interference by two interacting electric fields. (b) The transient grating formed by fields E_a and E_b cause E_c to be diffracted in the $k_s = k_a - k_b + k_c$ direction; this is the signal beam. (c) The signal beam in this case is formed by field E_a diffracting off the grating formed by E_c and E_b. (d) This is the pulse sequence that leads to the generation of the transient grating signal (TG) shown in (b). The pulse sequence here, with the scanned field coming before the fixed fields, corresponds to the reverse transient-grating signal (RTG) shown in (c). Fields E_a and E_b are coincident in time here.

Experimenta

FWM signal. For o

Figure 1.2 because

the incident fields.[8]

mmer of the forward

$k_s - k_1$. Note that

irections. In our

experimental scan E_s

precede E_2, it is called

Based on the

gratings being formed

forming a grating in t

In this case (TG s

shown in Figure 1.2d.

forming a grating in t

Using this latter conf

ngure[8] here, fields E_1

1.2. The third gratin

takes place in the dire

$k_s - k_2$. The medi

cited molecules th

ause the decay and

experimentally expl

Experimentally, there are various configurations that can be used to observe the FWM signal. For our studies, we have chosen the forward box arrangement as shown in Figure 1.2 because it provides the best temporal resolution and phase matching between the incident fields.[82,83] For all cases, the FWM signal that is detected at the upper right corner of the forward box, as shown in Figure 1.2, is defined by the wave vector $\mathbf{k}_S = \mathbf{k}_a - \mathbf{k}_b + \mathbf{k}_c$. Note that other FWM signals are possible and they are observable in other directions. In our studies we restricted our measurements such that within an experimental scan E_a and E_b are fixed in time and E_c is scanned. When fields E_a and E_b precede E_c, it is called positive time; negative time refers to field E_c preceding E_b and E_a.

Based on the relative timing of the three fields, one can envision three types of gratings being formed.[73,74,84] The first one, shown in Figure 1.2b, involves E_a and E_b forming a grating in the horizontal plane from which E_c scatters for positive delay times, τ. In this case (TG signal), fields E_a and E_b are overlapped in time and arrive before E_c as shown in Figure 1.2d. The second arrangement, shown in Figure 1.2c, involves E_c and E_b forming a grating in the vertical plane with subsequent scattering of E_a. More information about this latter configuration, known as a reverse transient grating (RTG), will be given later;[85] here, fields E_a and E_b are coincident in time but arrive after E_c as shown in Figure 1.2e. The third grating is formed by E_a and E_c in a diagonal plane, but scattering of E_b takes place in the direction $\mathbf{k}_s = \mathbf{k}_a - \mathbf{k}_c + \mathbf{k}_b$ which does not coincide spatially with $\mathbf{k}_s = \mathbf{k}_a - \mathbf{k}_b + \mathbf{k}_c$. The medium that constitutes the gratings discussed so far is composed of the sample molecules that in the gas phase move freely. Therefore, molecular dynamics cause the decay and reformation of the transient grating. Our group has theoretically and experimentally explored the ground and excited states vibrational and rotational

populations and the

for-wave mixing

demonstrations of

ynamics of various

1

In the past de

nonstration of La

viewed recently

"Pump-Dump", "Mod

The probability

o-level system is ex

where μ is the trans

xpression implies tha

d one with $E(t)^*$, to

xcitation process, as n

e type of population

neral excitation proc

populations and the coherence dynamics from gas-phase samples by these time-resolved four-wave mixing techniques.[86,87] The theoretical considerations and experimental demonstrations of the quantitative extraction of rotational and vibrational molecular dynamics of various molecular systems from these experiments are shown in Chapter 4.

1.4. CONTROL OF MOLECULAR DYNAMICS

In the past decade, we have witnessed tremendous progress in the experimental demonstration of laser control of chemical reactions. This area of research has been reviewed recently[88,89] and includes wide-ranging techniques such as "Coherent Control", "Pump-Dump", "Mode-Selective Control", "Quantum Control", and "Optimal Control".

The probability of excitation from the ground, $|g\rangle$, to the excited state, $|e\rangle$, in a two-level system is expressed quantum mechanically as

$$\left|\langle e|\boldsymbol{\mu}\cdot\mathbf{E}(t)|g\rangle\right|^2 = \langle e|\boldsymbol{\mu}\cdot\mathbf{E}(t)|g\rangle\langle g|\boldsymbol{\mu}\cdot\mathbf{E}(t)^*|e\rangle, \tag{1.11}$$

where $\boldsymbol{\mu}$ is the transition dipole moment and $\mathbf{E}(t)$ is the applied electric field. This expression implies that two interactions with the electric field are required, one with $\mathbf{E}(t)$ and one with $\mathbf{E}(t)^*$, to transfer part of the population from one state to the other. The excitation process, as measured in all linear spectroscopy methods, is a good example of this type of population transfer. Although both interactions are with the same field for a general excitation process, the two interactions do not imply that it is a two-photon

process. Population

he rates of absorp

excitation process w

ontrol over each c

chieved. Control o

nvolved in the trans

me or in phase.

It has long be

between two states s

ectric fields by a co

hase-locked laser pu

e phase-locked las

olecular iodine coul

ere combined out-o

ntrol of chemical re

an interact with the s

pulation transfer fro

pproach to controllin

ped laser pulses.

Three-pulse fou

ombines the interactio

ected time sequence

process. Population inversion is not usually achieved because of the competition between the rates of absorption and stimulated emission. The possibilities for influencing the excitation process with a simple laser pulse are minimal. However, if one had individual control over each of the electric fields involved in the excitation, full control could be achieved. Control of the population transfer can be achieved if the two electric fields involved in the transition probability in Equation (1.11) are different and are correlated in time or in phase.

It has long been recognized that in order to optimize the transfer of population between two states sophisticated electric fields are required.[88,90-92] One can create such electric fields by a combination of phase and amplitude masks,[93-95] or one can combine phase-locked laser pulses to achieve the desired field. Scherer *et al.*[96] showed that when two phase-locked laser pulses were combined in-phase, the excited state dynamics of molecular iodine could be observed as fluorescence enhancement; however, when they were combined out-of-phase, the signal is observed as fluorescence depletion. Coherent control of chemical reactions depends on the relative phase of two different laser pulses that interact with the sample. The relative phase of the pulses can be used to control the population transfer from the ground state to two different excited states.[97-99] A different approach to controlling population transfer[100] and enhancing reaction yields[11,101] uses chirped laser pulses.

Three-pulse four-wave mixing (FWM) is a nonlinear spectroscopic method that combines the interaction of three laser pulses in a phase-matched geometry with a well-defined time sequence of the pulses. The principles of transient gratings apply here as

well the differences

rasition that is re-

ot overlapped in t

olarization resulti

oherent beam corr

milar to the pump-

ariable time delay. I

egree of control ov

echnique allows ind

ed to gain control

ates. This technique

ase-matching geom

ld probes the syste

ne-unity or near-zer

oherence) matrix ele

he group has explore

uantum mechanical p

emonstrations of this

Chapter 4.

well; the differences are that the molecular system being studied must have an electronic transition that is resonant with the frequency of the laser pulses and fields E_a and E_b are not overlapped in time. The signal from these measurements arises from a third-order polarization resulting from the interaction of the three electric fields and is itself a coherent beam corresponding to a fourth electromagnetic wave. Three-pulse FWM is similar to the pump-probe technique in that a preparation step is followed, after some variable time delay, by a probing step.[102] However, three-pulse FWM allows for a greater degree of control over the preparation and probing processes. Thus, the three-pulse FWM technique allows individual manipulation of the electric fields $\mathbf{E}(t)$ and $\mathbf{E}(t)^*$ and can be used to gain control over the transfer of population between the ground and the excited states. This technique allows one to combine three non-phase-locked electric fields in a phase-matching geometry. The first two fields cause the population transfer and the third field probes the system. The specific timing between the pulses can be used to achieve near-unity or near-zero values of diagonal (population) and off-diagonal (ro-vibrational coherence) matrix elements of the molecules that interacted with the two electric fields. Our group has explored this technique as an ideal tool to learn about and manipulate the quantum mechanical processes involved in laser control of chemical reactions.[81,103-109] Demonstrations of this control involving two of the possible pulse sequences are shown in Chapter 4.

A number

studying chemical re

systems used by th

producing 13 fs pu

CPM producing 50

were conducted using

2.1.1. Oscillator

The laser syst

ooled dye laser (

4 prisms (P), and

ethafluoroborate (R6

ed is further diluted

5 nm line of a con

laser is used to pump

cited singlet state. T

ser emits broad-band

vibrational levels in

2. EXPERIMENTAL

2.1. LASER SETUP

A number of different types of femtosecond laser systems are available for studying chemical reactions. At Michigan State University, there are two different laser systems used by the Dantus research group – a titanium-sapphire laser (Ti-sapphire) producing 13 fs pulses centered at 805 nm and a colliding pulse mode-locked laser (CPM) producing 50 fs pulses centered at 622 nm. All of the experiments described here were conducted using the CPM laser system; it is described in some detail below.

2.1.1. Oscillator

The laser system used for these experiments is a home-built colliding pulse mode-locked dye laser[110-112] (CPM), which is a ring cavity consisting of 7 mirrors (M and SM), 4 prisms (P), and 2 dye jets (J). (See Figure 2.1.) A gain laser dye, rhodamine tetrafluoroborate (R6G), is dissolved in ethylene glycol (stock solution is 1.0 g /100 ml and is further diluted by a factor of 10) and flows through one of the dye jets (J_G). The 514 nm line of a continuous wave Coherent Argon ion laser (typically 4-6 W across all lines) is used to pump the R6G dye optically to an excited vibrational level in the first excited singlet state. This wave packet then decays to the bottom of the excited state and then emits broad-band fluorescence centered around 590 nm due to numerous transitions to vibrational levels in the ground state.

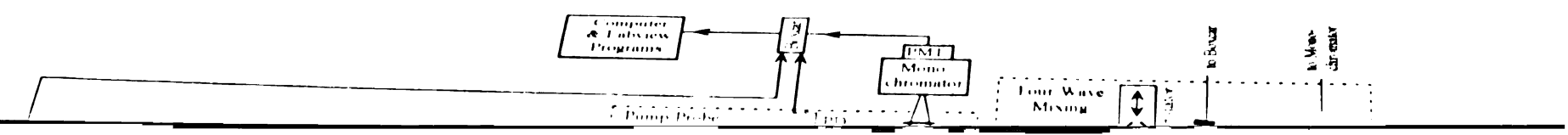
Computer
& Labview
Programs
PMT
Mono
Chromator
Four Wave
Mixing
Pump Probe

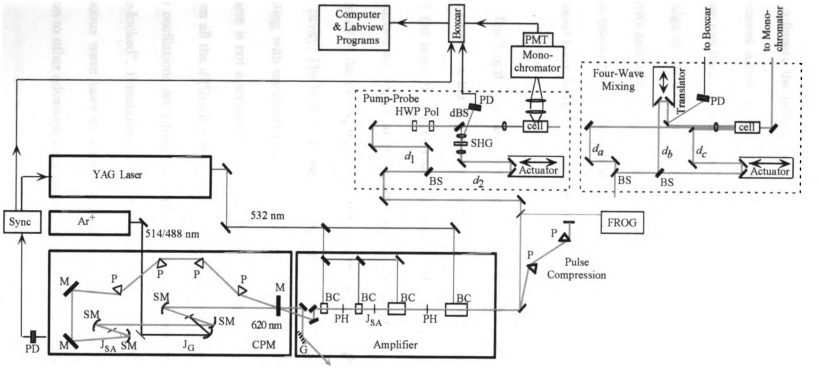

Figure 2.1. Diagram of the colliding pulse mode-locked femtosecond laser system used in these experiments. The femtosecond pulses are generated in the CPM, then amplified and compressed to produce 60 fs, unchirped pulses (average energy is about 300 μJ). The experimental setup shown here (dotted boxed area) is for the pump-probe technique with two beam arms (d_1 and d_2, 622 nm and 311 nm) and fluorescence detected perpendicularly by the monochromator. For the four-wave mixing technique (separate dotted boxed area), two beam splitters are used to create three arms (one fixed (d_a), two variable - manual (d_b) and automated (d_c)) and the signal beam is directed into the monochromator.

The three m

SM) collimate the

rrangement allows

his we can think

ight edge of the C

he cavity and light

sed to monitor the

ontinuous wave las

The length o

e that cavity. In th

ustain the laser: th

bservations are de

ustainable in the c

of the cavity. The l

scillating with un

or there is not a s

between all the di

f the oscillations

"mode-locked". Be

ontinuous wave l

ddition to other a

The three mirrors (M) form a ring for the cavity while two of the spherical mirrors (SM) collimate the fluorescence generated by the R6G gain dye. Notice that this cavity arrangement allows light to travel in both clockwise and counter-clockwise directions; thus, we can think of two "arms" or oppositely propagating beams. Note that mirror at the right edge of the CPM cavity is only partially reflective; some light is allowed to escape the cavity and light from one arm enters the amplifier and light from the other arm can be used to monitor the pulse characteristics. With this laser cavity and gain dye, we obtain a continuous wave laser with wavelengths in the range of 580-630 nm.

The length of a laser cavity defines the specific frequencies of light that can exist in that cavity. In the ring cavity, constructive interference of the radiation is required to sustain the laser; the phase must be reproduced after each pass around the ring. These observations are described by the equation $\nu_q = qc/L$ where ν_q are the frequencies of light sustainable in the cavity, q is an integer, c is the speed of light, and L is the entire length of the cavity. The light in the laser cavity consists of a number of different frequencies all oscillating with unrelated phases (multimode). In this case, the laser is continuous wave and there is not a series of laser pulses. In order to produce pulses, the phase relationship between all the different frequencies must be constant in time. When the initial phases of all the oscillations are equal, we obtain Fourier transform-limited pulses and the laser is "mode-locked". Equations (as well as figures) describing this change from a multimode continuous wave laser to a mode-locked pulsed laser can be found in Reference 41 in addition to other advanced laser books and ultrafast laser articles.

In order to

by R6G, we intro

23 (DODCI) disso

ified by a factor

nsity-dependent

sorbed and no li

of light, e g a spik

sorbence transitio

This signal passes th

ble saturable absorb

ble saturable absor

rocess of gain-satu

ble saturable absor

ified by the gai

ot affected by th

sequence of the

ain femtosecond

ot change as it pr

because the durat

certainty princip

ly further due to th

Recall that

face at two points

In order to obtain femtosecond pulses from the continuous wave laser (generated by R6G), we introduce a saturable absorber dye, 3,3'-diethyloxadicarbocyanine iodide 2,3 (DODCI) dissolved in ethylene glycol (stock solution is 0.50 g /100 ml and is further diluted by a factor of 10) in the other dye jet (J_{SA}). The saturable absorber dye has an intensity-dependent absorbance. When the light intensity is low, all the radiation is absorbed and no light passes through the saturable absorber. If there is a higher intensity of light, *e.g.* a spike due to a noise fluctuation in the laser, the spike saturates the absorbance transition and allows partial passage of light through the saturable absorber. This signal passes through the gain dye and is amplified and then easily passes through the saturable absorber on the next trip around the cavity. This pattern through the gain and saturable absorber dyes repeats until the gain dye is saturated. As this alternating process of gain-saturable absorber occurs, the leading edge of the pulse is absorbed by the saturable absorber (because of the low intensity) while the trailing edge is not amplified by the gain dye (because of saturation). Note that the maximum of the pulse is not affected by the saturable absorber while it is increased by the gain dye. The consequence of these properties is that the time duration of the pulse narrows and we obtain femtosecond pulses. The final shape of the pulse is obtained when the pulse does not change as it propagates through the cavity. This steady state condition is obtained because the duration of the pulse in time is inversely related to the spectral width (uncertainty principle) and a point is reached where the time duration cannot decrease any farther due to the spectral width limit.

Recall that we have two counter-propagating pulses; they must collide in time and space at two points in the cavity. If they collide at the saturable absorber dye, there will

he less loss of the

individually; thus, c

collide at the gain

through the gain; t

recovery time for t

e the two jets sho

The clockwise prop

urable absorber d

ise characteristics

pectrum (it last pas

ye is added to the

ives from about 5

m. This change

pectrum off the dif

bsorber dye pairs to

ong with their corre

The four pris

e pulses which

Spoil and mirror

Currently with respe

known as group vel

locities in a particu

ther wavelengths ar

be less loss of the intensity of the pulse than if they pass through the saturable absorber individually; thus, colliding at the saturable absorber jet is the optimal situation. If they collide at the gain dye, each pulse will be amplified less than if they separately passed through the gain; therefore, this is the worst situation. So to allow for the maximum recovery time for the gain dye while having the pulses collide at the saturable absorber jet, the two jets should be placed at a distance apart equal to ¼ of the length of the cavity. The clockwise propagating pulse is used in the experiment because it last passed the saturable absorber dye; the counter-clockwise propagating pulse is used to monitor the pulse characteristics in the CPM by diffracting off a grating (G) and displaying the spectrum (it last passed the gain dye and is broader in time). When the saturable absorber dye is added to the ring cavity, the central wavelength of the radiation from the gain dye moves from about 590 nm to 622 nm with an increase in the bandwidth from 0.2 nm to 10 nm. This change in the laser can be observed while adding DODCI by observing the spectrum off the diffraction grating. Note that there are other possible gain dye-saturable absorber dye pairs to generate femtosecond pulses; others can be found in Reference 41 along with their corresponding wavelength range.

The four prisms (P) in the cavity are used to compensate for temporal broadening of the pulses which is introduced by transparent media in the ring cavity, *e.g.* ethylene glycol and mirror coatings. The indices of refraction of different materials vary differently with respect to frequency (wavelength). The consequence of this behavior is known as group velocity dispersion (GVD); different wavelengths travel at different velocities in a particular medium. This phenomenon is also referred to as chirp. The "bluer" wavelengths are slowed down by these transparent media more than the "redder"

wavelengths are, re

GVD can be found

13. Various prism

introducing "negativ

ravel a shorter path

ne wavelengths to

re arranged to com

nsistors which ca

roadest spectrum).

From the unc

se must be broad in

ses. For Gaussian

ximum (FWHM) v

as lists the values th

Gaussian pulses, the

rresponds to a widt

The output fr

verage power of 20

roduced at about 10

periments, we need

ne *infra*). The C

wavelengths are, resulting in a temporal broadening of the pulse. Equations that define GVD can be found in advanced optics or laser books, for example References 41 and 113. Various prism arrangements can correct for this "positive" GVD (or chirp) by introducing "negative" GVD where the wavelengths towards the blue end of the spectrum travel a shorter pathlength than the ones toward the red end of the spectrum allowing the blue wavelengths to "catch-up" to the red ones. Here in the CPM cavity, the four prisms are arranged to correct for the GVD introduced in the cavity with two of the prisms on translators which can be adjusted to produce the shortest pulses (those which have the broadest spectrum).

From the uncertainty principle ($\Delta t \Delta \omega \geq ½$), we know that pulses that are short in time must be broad in frequency. The value of this inequality depends on the shape of the pulses. For Gaussian shaped pulses, $\Delta t \Delta \nu \geq 0.441$ where Δt and $\Delta \nu$ are full-width at half-maximum (FWHM) values for time and frequency (cm^{-1}), respectively.[41] Reference 41 also lists the values that make this inequality true for non-Gaussian pulses. For 50-60 fs Gaussian pulses, the frequency bandwidth is approximately 245-300 cm^{-1}, which corresponds to a width of 10-12 nm (FWHM) for pulses at 622 nm.

The output from the CPM is centered at 622 nm and is usually 50-60 fs with an average power of 20 mW which translates to about 200 pJ per pulse. The pulses are produced at about 100 MHz in our ring cavity with length 3.3 m. In order to conduct experiments, we need larger pulse energies and must amplify the pulses from the CPM (*vide infra*). The CPM oscillator is fairly stable and requires only minor mirror

adjustments on a d

environmental condi

21.2 Amplifier

For a more

research group at M

and Una Marvet wh

consists of four

transversely pumped

typically 10.5 W or

synchronized with th

PM in Figure 2.1)

synchronization ensu

random noise fluctua

his cell and rhodam

mission from the ex

addition to the stimu

mission. The sponta

thus it can cause ten

preferentially over th

of spontaneous emiss

modes, PH) and ten

the path of the bea

adjustments on a daily basis. Dye changes are needed every 4-8 weeks depending on the environmental conditions in the laboratory and the amount of time the laser was used.

2.1.2. Amplifier

For a more complete description of the specific amplifier used by the Dantus research group at Michigan State University, see the doctoral theses by Marcos Dantus and Una Marvet who built our amplifier.[114,115] The four-stage dye amplifier[116] (Figure 2.1) consists of four Bethune cells[117] (BC) which contain circulating gain dyes which are transversely pumped by the frequency-doubled 532 nm output of a 30 Hz Nd:YAG laser (typically 10.5 W or about 300 mJ average energy per pulse). The Nd:YAG laser is synchronized with the CPM by detecting femtosecond pulses with a photodiode (PD near CPM in Figure 2.1) and using this electronic signal to trigger the Nd:YAG. This synchronization ensures that the femtosecond pulses are being amplified rather than random noise fluctuations. The gain is achieved using kiton red dissolved in water in the first cell and rhodamine 640 dissolved in water in the other three cells; the stimulated emission from the excitation process of these dyes is what amplifies the CPM beam. In addition to the stimulated emission of these gain dyes, we also obtain spontaneous emission. The spontaneous emission is incoherent and on the nanosecond time scale; thus, it can cause temporal and spectral distortion of the output when it is amplified preferentially over the femtosecond pulses from the CPM. Reduction of the amplification of spontaneous emission (ASE) is achieved through both spatial filtering (using diamond pinholes, PH) and temporal filtering (using malachite green as a saturable absorber, J_{SA}) in the path of the beam in the amplifier. Notice that the pulses have now traveled through

an appreciable am

introducing negati

2.1) recompresses

temporal width FW

and have zero chirp

2.1.3. Pulse Cha

The tempor

an be measured b

ommercial system

ave been recomp

esolution, the set

plit into two arms.

ntensity autocorre

istribution with re

equency (vertical)

rrive at the same t

requencies in the p

and c). The dotted

egatively chirped P

requencies); the lin

requencies delayed

an appreciable amount of water and glass in the amplifier and are broadened by GVD. By introducing negative GVD, a double-pass prism pair after the amplifier (shown in Figure 2.1) recompresses the pulses and removes the GVD. The resulting amplified 60 fs (temporal width FWHM) pulses have an energy of 0.35 mJ per pulse at a rate of 30 Hz and have zero chirp.

2.1.3. Pulse Characteristics

The temporal width and the spectral profile across the time duration of the pulse can be measured by a frequency resolved optical gating (FROG) setup.[118,119] We use a commercial system, Clark-MXR FRG-1, for our measurements to confirm that the pulses have been recompressed correctly without any remaining chirp. Without the frequency resolution, the setup would yield an autocorrelation of the pulses. The entering beam is split into two arms, one of which gates the other in time. Following this time resolution (intensity autocorrelation), the beam then passes to a grating where the frequency distribution with respect to time is recorded. A FROG trace of the pulse shows the frequency (vertical) and time (horizontal) profile as seen in Figure 2.2. If all frequencies arrive at the same time, the chirp is zero (*i. e.* unchirped, see Figure 2.2b). When the frequencies in the pulse change with respect to time, the chirp is nonzero (see Figure 2.2a and c). The dotted line in Figure 2.2a represents the trace that would be obtained for a negatively chirped pulse (higher (blue end) frequencies arriving before lower (red end) frequencies); the line in Figure 2.2c represents a positively chirped pulse trace (higher frequencies delayed compared to lower frequencies). By using the FROG trace, we can

frequency

adjust the position of one of the prisms in the pulse compression to yield pulses with the chirp needed for our experiments. For all experiments described here, the pulses were unchirped. Experiments in our group using chirped pulses (with both pump-probe and four-wave mixing techniques) have been published elsewhere.[11,105,106]

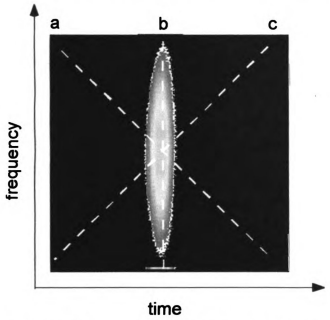

Figure 2.2. Example of a FROG trace with time increasing from left to right and frequency increasing from bottom to top. (a) The dotted line represents a negatively chirped pulse where blue wavelengths (high frequencies) precede red wavelengths (low frequencies). (b) Experimental FROG trace of an unchirped pulse where all the wavelengths arrive at the same time. (c) The dotted line represents a positively chirped pulse where red wavelengths arrive before blue wavelengths.

Following

are used to creat

nethods used he

specific temporal

and experiment

reparation specifi

2.2.1. Pump-Pro

In the pump-

pumps) the system

pled with another

de-excite the system

LF from one of the

2.2.1.1.

A beam spli

splitter into two arm

g one having a fixed

2.2. EXPERIMENTAL TECHNIQUES

Following the generation of the amplified femtosecond pulses, a number of optics are used to create the laser beam arrangement needed for each type of experiment; for the methods used here, either two or three femtosecond pulses must be used in their own specific temporal and spatial arrangement. The description of the laser beam setup for each experimental technique is described in detail below. In addition, the sample preparation specific to the experimental technique used is listed below.

2.2.1. Pump-Probe Technique

In the pump-probe experiments, two femtosecond pulses are required. One excites (pumps) the system to an excited state and then at some later time, t, the excited state is probed with another pulse. This probing may excite the system to another excited state or de-excite the system. In order to monitor the reaction, often laser-induced fluorescence (LIF) from one of the excited states is measured.

2.2.1.1. Time Delay

A beam splitter (BS) was used to divide the femtosecond beam from the amplifier into two arms. These two beams followed separate paths with distances d_1 and d_2, one having a fixed pathlength and the other having an adjustable pathlength. The time

/between the

Mach-Zehnde

collinearly rec

= λ_0, the puls

separated in

"Negative" tim

before the pum

the pump arriv

the pulses are o

ariator was pl

oved 0.2 µm

into a temporal

controlled with

r any time res

Sweeping the p

luorescence, co

fraction of this t

0 scans.

2.2.1.2.

Variable w

econd harmonic

t between these pulses must be well defined and controlled and was done so here with a Mach-Zehnder interferometer (shown in Figure 2.1). These two beams were then collinearly recombined before the sample cell using a dichroic beam splitter (dBS). If $d_1 = d_2$, the pulses arrive at the sample at the same time. If $d_1 \neq d_2$, then the pulses are separated in time and this time delay can be calculated using the speed of light. "Negative" time delay refers to the arrangement when $d_1 > d_2$ and the probe pulse arrives before the pump pulse. "Positive" time delay refers to the arrangement when $d_2 > d_1$ and the pump arrives before the probe pulse. "Time zero" refers to the case when $d_1 = d_2$ and the pulses are overlapped in time. To change the length of path d_2, a computer-controlled actuator was placed in the path. A mirror is mounted on this actuator; this mirror can be moved 0.2 μm accurately resulting in a distance resolution of 0.4 μm which translates into a temporal resolution of 1.3 fs. Obviously, the actuator can make larger steps (controlled with a LabVIEW™ program, see Appendices) such that the data can be taken at any time resolution between pump and probe pulses that is larger than 1.3 fs. Sweeping the pump-probe time delay results in a time transient that shows how the fluorescence, collected perpendicular to the propagation of the beams, varies as a function of this time delay. Typical transients have 100 time delays and are averages of 10 scans.

2.2.1.2. Excitation Wavelengths

Variable wavelengths can be obtained by frequency doubling the 622 nm with a second harmonic generation crystal (SHG) to 311 nm or by creating a frequency

ontinuum from

0.1 mm KDP cr

ight for our e

experiments req

wavelength was

fequency contin

pecifics of the ex

2.2.1.3.

The polari

the Z-axis in F

e parallel or pe

respectively) by

tained with the

hen the laser p

nsients were e

olarization of the

continuum from the 622 nm beam and filtering it to give the desired wavelength. Here a 0.1 mm KDP crystal was placed in the variable arm (pathlength = d_2) to produce 311 nm light for our experiments that require 311 nm as the probe. In addition, a few experiments required the wavelength of the pump to be 550 nm rather than 622 nm. This wavelength was obtained by focusing the 622 nm beam on a piece of quartz, creating a frequency continuum, and using the appropriate filter to pass 550 nm light. More specifics of the excitation of the iodine sample are described in Chapter 3.

2.2.1.3. Polarization

The polarization of the 311 nm probe pulse was fixed perpendicular to the laser table (Z-axis in Figure 2.3) while that of the 622 nm (550 nm) pump pulse was rotated to be parallel or perpendicular relative to the probe pulse (Z- or X-axis in Figure 2.3 respectively) by a zeroth-order half-wavelength plate (HWP). Parallel transients are obtained with the laser polarization vectors parallel; perpendicular transients are obtained when the laser polarization vectors are perpendicular. The parallel and perpendicular transients were examined to make sure that the time zero did not change when the polarization of the pump beam was rotated.

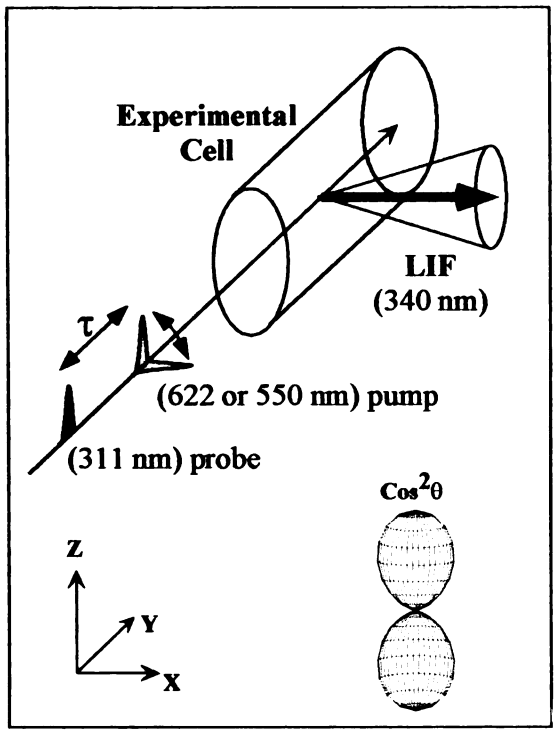

Figure 2.3. Experimental setup for rotational anisotropy measurements with unidirectional (X-axis) detection. The polarization of the probe beam remains oriented along the Z-axis while the orientation of the polarization of the pump beam can be rotated along either the X- (⊥) or Z-axis (||). LIF is collected perpendicular to the propagation of the laser beams.

Polarization measurements were performed with well-polarized beams. We measured polarization ratios (vertical:horizontal) after recombination of pump and probe lasers by the dichroic beam splitter. The pump laser polarization ratio was enhanced with a calcite polarizer (Pol) placed after the half-wavelength plate. The polarization ratio of the probe laser, at 311 nm, was measured to be higher than 10^2:1. With this setup, the polarization ratio of the pump beam was higher than we could experimentally determine ~10^4:1. Polarization ratios were also measured after the experimental cell to ascertain that no polarization scrambling occurred in the cell windows.

2.2.1.4.

Saturati
of pump and pr
the role of laser
used to attenuat
pulse was increa
minimize nonline

2.2.1.5.

A quartz
less than 10^{-6} T
room temperature

2.2.2. Four-Wa

In four-v
configuration. T
grating as a si
about the sampl
the beams that f

2.2.1.4. Intensity

Saturation of spectroscopic transitions and detectors was prevented by attenuation of pump and probe beams to energies below 1 μJ per pulse. For experiments investigating the role of laser intensity on the molecular dynamics, various neutral density filters were used to attenuate the pump laser intensity. In some cases, the pulsewidth of the laser pulse was increased from 50 fs to 120 fs in order to reduced the peak intensity and minimize nonlinear effects.

2.2.1.5. Sample

A quartz cell containing iodine was prepared on a vacuum line and degassed to less than 10^{-6} Torr before being permanently sealed. Experiments were conducted at room temperature (21 ± 3°C) where the vapor pressure of iodine is 0.25 Torr.

2.2.2. Four-Wave Mixing/Transient Grating Technique

In four-wave mixing experiments, three fields must cross in a specific geometric configuration. Two fields create a transient grating while the third one diffracts off the grating as a signal beam. This signal beam contains molecular dynamics information about the sample; the signal intensity depends on the time delay between the arrival of the beams that form the grating and the arrival of the beam that is diffracted.

2.2.2.1.

The laser

beams of comp

ombined at the

see Figure 2.4).

with 1 inch side

tripe spacing of

In order to

of the beam arra

before the focus

thickness, was p

ified beams. One

the PWM signal

nd space, a matr

These were the

ining processes

emporal overlap f

2.2.2.1. Beam Arrangement

The laser from the amplifier was attenuated by a factor of two and split into three beams of comparable intensity ~ 50 μJ using two beam splitters. The three beams were combined at the sample in the forward box geometry[82,83] by a 0.5 m focal length lens (see Figure 2.4). At the lens focus, the three beams occupied the three corners of a square with 1 inch sides. Each pair of beams were crossed at an angle of 2.6° resulting in a fringe spacing of 14 μm. The beam size at the interaction region was 40-50 μm.

In order to optimize the initial alignment of the four-wave mixing setup, templates of the beam arrangement were made and used to ascertain that all beams were parallel before the focusing lens. A second harmonic generation crystal, KDP of 0.1 mm thickness, was placed at the focus to optimize the spatial and temporal overlap of the fixed beams. Once the third beam was overlapped in space, it was scanned in time until the FWM signal beam appeared. When all three incident pulses were overlapped in time and space, a matrix of equally spaced red and UV beams could be seen after the crystal. These were the result of all combinations of second-, third-, and higher-order wave mixing processes occurring at the crystal. After further optimization of spatial and temporal overlap for the FWM signal, the crystal was removed from the beam path.

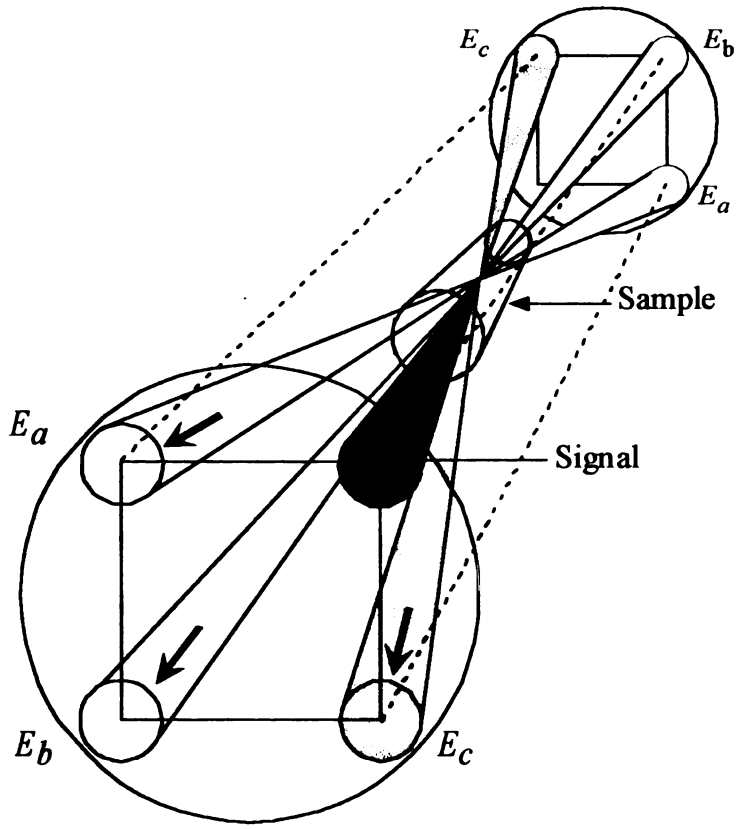

Figure 2.4. Beam arrangement in the forward box configuration (see References 82 and 83). E_a and E_b are overlapped and fixed in time. For positive time delays, these fields set up a transient grating in the horizontal plane off which E_c Bragg scatters to give the FWM signal. The time delay between E_c and the two other fields is varied to obtain the time-dependent dynamics of the system. In our experiments, all beams were horizontally polarized.

2.2.2.2. Time Delay

One of the fields (E_c) had a variable pathlength (d_c) and could be delayed by a computer-controlled actuator. There was a manual translator in the pathlength of field E_b (d_b) while field E_a had a fixed pathlength (d_a). (See Figure 2.1.) Therefore within a particular experimental scan, these fields E_a and E_b were fixed in time - either overlapped

$(d_2 = d_1)$ or

two fields. T

experiment.

defined as t

separated in

in time $(d_2$ =

time delays,

after the oth

experiments

when these t

2.2.2

The

wave vector

is possible t

focused he

on. The sig

sweeping th

affect the te

different time

scattered ligh

($d_a = d_b$) or separated ($d_a \neq d_b$) - while field E_c was scanned in time with respect to these two fields. The temporal relationship between fields E_a and E_b will be specified in each experiment. When E_a and E_b are overlapped in time, time zero for these transients is defined as the point at which all three fields are coincident in time. When E_a and E_b are separated in time, time zero is defined as the point when fields E_c and E_b are overlapped in time ($d_c = d_b$) for the specific pulse sequences used here (*vide infra*). For "negative" time delays, E_c arrives before the other two fields. For "positive" time delays, E_c arrives after the other two fields. See Figure 1.2 for positive and negative time delays for the experiments when E_a and E_b are coincident in time. Diagrams of the pulse sequences when these two fields are separated in time will be shown in Chapter 4.

2.2.2.3. Signal

The signal beam is generated at the fourth corner of the square defined by the wave vector $\mathbf{k}_s = \mathbf{k}_a - \mathbf{k}_b + \mathbf{k}_c$ with a wavelength equal to the incident beam wavelength. It is possible to collect the signal beam at other wavelengths;[103,105] however, in all cases discussed here, the data were collected at the central wavelength of the laser pulse, 622 nm. The signal beam was collimated and sent to the monochromator (see below). Sweeping the time delay between the variable and the fixed fields yields transients that reflect the temporal evolution of the dynamics. Typical transients contain data from 150 different time delays and are averages of 10 scans. Care was exercised to minimize scattered light and to ensure that the collected signal was background free.

2.2.2.4

All exp

liquid samples

conducted at r

°C and mercury

Followi

he fluorescenc

ollimated by le

irected with a

ransmitted to a

omputer. The

omputer progr

ith Brown (s

ctain time tra

Sapphire system

e time delay, t

was monitored

Assy-probe. 62

density varied

2.2.2.4. Sample

All experiments were performed on 30 to 760 Torr of gases or neat vapors (when liquid samples were used) contained in static quartz cells. The experiments were conducted at room temperature for the majority of these samples except for iodine (140 °C) and mercury iodide (280 °C).

2.3. SIGNAL COLLECTION

Following the experimental setup, the beams were focused on the sample cell and the fluorescence (pump-probe) or signal beam (four-wave mixing) was collected and collimated by lenses. The signal is directed to a 0.27 m monochromator (SPEX 270 M), detected with a photomultiplier tube (PMT), averaged in a boxcar integrator, and then transmitted to a Stanford Research 245 computer interface board for collection by the computer. The monochromator and interface board were controlled with LabVIEW™ computer programs. Two different LabVIEW™ computer programs were written by Emily Brown (see Appendices) to obtain either wavelength spectra of the samples or to obtain time transients. (Kathryn Walowicz has modified these programs for the Ti-Sapphire system to incorporate the CCD detector in the programs.) At each wavelength or time delay, the signal was collected for 10 laser shots. In all cases, the beam intensity was monitored by a reflective scatter from an optic directed to a photodiode (311 nm for pump-probe, 622 nm for four-wave mixing). Data points obtained when the laser pulse intensity varied more than one standard deviation from the mean were discarded. Both

the number of

number of in

wavelength sp

sample being m

the number of time delays (wavelengths) measured for a transient (spectrum) and the number of individual transients (spectra) summed to obtain the final time transient (wavelength spectrum) varied depending on the experimental technique and on the sample being measured (*vide supra*).

3. RO

EX

The

pulses are

in time by

and probe

in Chapter

The

molecules

Given the

laser-induce

to realize

discussed in

these well-

rotational p

fitting, Mo

3. ROTATIONAL ANISOTROPY MEASUREMENTS ON IODINE: EXAMINING UNIDIRECTIONAL DETECTION AND LASER INTENSITY

3.1. INTRODUCTION

The pump-probe technique has been described in Chapter 1. Two femtosecond pulses are used to excite and then probe the molecular sample; these pulses are separated in time by a variable delay. Rotational anisotropy measurements require the use of pump and probe pulses that are polarized parallel and perpendicular to each other as explained in Chapter 2.

Theories for time-resolved rotational anisotropy measurements of isolated molecules have been developed using both quantum and classical mechanics.[21,33,120-122] Given the multiple techniques available for ultrafast dynamics measurements such as laser-induced fluorescence, multiphoton ionization and four-wave mixing, it is important to realize that the rotational anisotropy theory applies differently in each case. As discussed in recent papers from our group,[8,9,44,86,87,109] it is sometimes necessary to adapt these well-known equations in order to extract accurate rotational constants and/or rotational populations based on the experimental methods (*e.g.* pump-probe,[44,45] transient grating,[86,87] four-wave mixing,[109] and multiphoton ionization[8,9]).

Rotati

polarization ve

(⊥) to each o

isotropic contr

anisotropic con

perpendicular tr

For simplicity t

be written as I_t a

obtained by the s

Gordon noted tha

defined in Equatio

contributions and

rotational anisotro

The simplicity of t

absolute dynamics

measurements whe

signal is the parti

experiments, or a m

Rotational anisotropy is typically measured by obtaining transients with the polarization vectors of the pump and probe beams oriented parallel (||) or perpendicular (⊥) to each other, $I_{\|}(t)$ and $I_{\perp}(t)$ respectively. The difference, $I_{\|}(t) - I_{\perp}(t)$, contains isotropic contributions in addition to the time-dependent anisotropy.[123] The pure anisotropic component of the signal is obtained by subtraction of the parallel and perpendicular transients and division by the purely isotropic component of the signal, I_{iso}. (For simplicity in the equations that follow, the parallel and perpendicular transients will be written as $I_{\|}$ and $I_{\perp}$.) Based on the work of Gordon[123], the isotropic component can be obtained by the sum

$$I_{iso} = I_{\|} + 2I_{\perp}. \tag{3.1}$$

Gordon noted that dividing the difference by the isotropic component of the signal as defined in Equation (3.1) leads to a measurement that is independent of isotropic contributions and experimental parameters such as the relative signal intensity. Thus, the rotational anisotropy could be obtained according to the formula[33,123]

$$r(t) = \frac{I_{\|} - I_{\perp}}{I_{\|} + 2I_{\perp}}. \tag{3.2}$$

The simplicity of this formula is misleading. In fact, it applies only to a subset of the ultrafast dynamics detection techniques. Equation (3.2) is applicable only for measurements where Equation (3.1) is true. Among these are experiments where the signal is the partial absorption of the probe, a common setup for liquid phase experiments, or a measure of fluorescence depletion caused by the probe.

In a

interactions

10^{-5} W cm^{-1}

field-induce

must be in

saturation.

may includ

standpoint,

given expe

the time-re

we observ

not reprod

derived fr

reflect the

In

formula

does not

interchan

spaces.

phase

a plan

the

In addition, the anisotropy formulae were originally derived assuming weak-field interactions.[123] The peak intensities of femtosecond laser pulses can typically approach 10^{12} W/cm^2 levels; therefore, it is important to consider the role of saturation and other field-induced effects on anisotropy measurements and how these nonlinear phenomena must be included in the analysis to extract accurate information. In the case of severe saturation, other photophysical and photochemical pathways become available. These may include multiphoton excitation, ionization, and dissociation. From a theoretical standpoint, the rotational anisotropy at time zero and time infinity are well defined for a given experiment.[21,44] We had observed that as the intensity of our pump laser increased, the time-resolved measurements no longer reflected these theoretical values. In addition, we observed a number of examples in the literature where these theoretical values were not reproduced experimentally. This shortcoming implies that quantitative information derived from ultrafast rotational anisotropy (URA) measurements may not truthfully reflect the rotational populations and dynamics of the system when the laser intensity is high.

In this study we explore the applicability of the typical rotational anisotropy formula (Equation (3.2)) to ultrafast measurements where the signal arises from probe laser induced fluorescence (LIF). In particular we explore the effect of unidirectional detection of the fluorescence signal taking into account the *f*-number of the collection optics. This experimental configuration is one of the most common in time-resolved gas-phase measurements. We also present experimental URA data for gas-phase iodine using a pump laser that is adjusted over three orders of magnitude in intensity, from no saturation to highly nonlinear saturation of the B←X transition. We develop a correction

to the model b

become quant

typically mea

determine the

error. Here w

treatment cor

applicable to

observed. In

dynamics, dis

3.2.1. Pur

Ani

Th

rotational

pulse selec

between t

As the dis

other pa

molecules

fluoresce

to the model based on saturation and other nonlinear effects and demonstrate that all data become quantitatively correct. Ultrafast rotational anisotropy measurements are not typically meant to provide highly accurate temperatures; they are usually used to determine the temperature of products from chemical reactions within a 10% margin of error. Here we show that this wide margin cannot be achieved if saturation occurs. Our treatment concerns the first picoseconds of the URA measurements; however, they are applicable to all time domains where rotational quantum recurrences or revivals are observed. Implications of these measurements to the characterization of rotational dynamics, distributions, and temperatures are discussed.

3.2. THEORY

3.2.1. Pump-Probe Technique for Studying Rotations (Rotational Anisotropy Measurements)

The pump-probe technique has been described earlier. The time evolution of the rotational alignment is measured with linearly polarized lasers. Excitation by the pump pulse selects an initial population distribution described by $\cos^2\theta$ where θ is the angle between the transition dipole and the pump laser polarization vector.[124] (See Figure 2.3.) As the distribution dephases due to rotations of the molecules, the probe pulse (polarized either parallel or perpendicular to the excitation pulse) is unable to excite all the molecules to another state, resulting in a decrease in the fluorescence from that state. This fluorescence is monitored as a function of time delay between pump and probe pulses.

The time-res

and $\perp$ (perpen

pump and prob

in this case, and

3.2.2. Iodine

Molecu

reached met

experiments r

molecules tha

in the excited

$f_{\parallel}(t)$ and $f_{\perp}(t)$

the laser inc

nm, 134.135 un

in Figure 3.

accessible u

The time-resolved data for each polarization arrangement ($I_{\parallel}$ and $I_{\perp}$, where || (parallel) and ⊥ (perpendicular) refer to the relative orientation of the polarization vectors of the pump and probe pulses) contain an isotropic component, reflecting molecular vibrations in this case, and an anisotropic component, reflecting rotational dephasing.

3.2.2. Iodine Sample

Molecular iodine is one of the most extensively studied molecules by time-resolved methods. (See References 34,100,125-129 and 107 for example.) The experiments measure the initial alignment and subsequent rotational dephasing of iodine molecules that absorb a photon in a parallel transition from the ground X ($^1\Sigma_{0+g}$) state[130] to the excited B ($^3\Pi_{o+u}$) state.[131] The probe laser excites molecules in the B state to the E (0^+_g) and f (0^+_g) ion pair states.[132-135] The signal for the measurements presented here is the laser induced fluorescence (LIF) from the f ion pair state to the B state at 340 nm[134,135] unless otherwise noted. The potential energy curves for these states are shown in Figure 3.1. As will be discussed in detail later, the A ($^3\Pi_{1u}$) and β (1_g) states are also accessible with the pump and probe lasers and are also shown in Figure 3.1.

Figure 3.1.
be excited
transition) v
induce a tra
beams) and
beams). In

3.2.3. Rota

The d

ransitions ha

luorescence

irection). one

ube configura

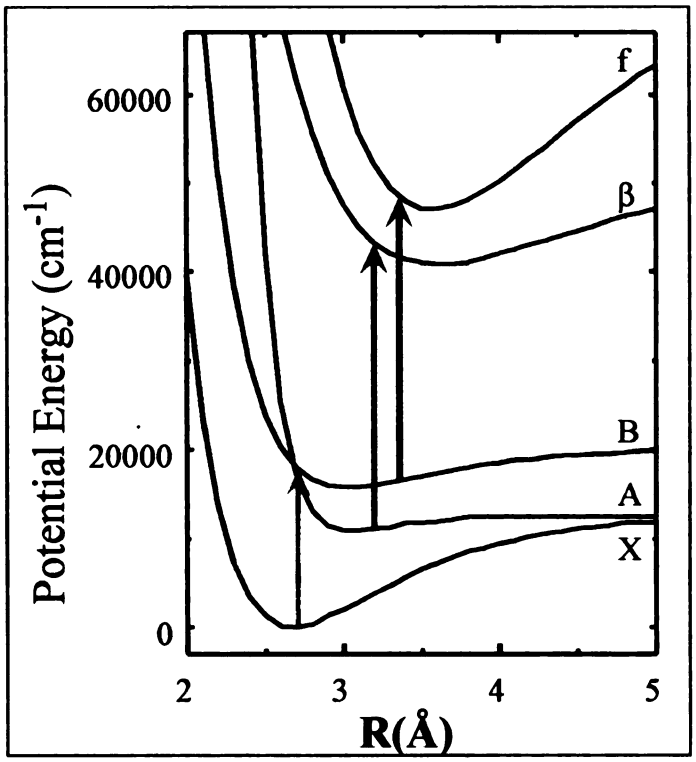

Figure 3.1. Relevant potential energy curves for I_2. Molecules in the X state can be excited to the B state (parallel transition) and the A state (perpendicular transition) with 622 nm laser pulses. Excitation with 311 nm probe pulses will induce a transition between the B and f states (favored by parallel pump-probe beams) and between the A and β states (favored by perpendicular pump-probe beams). In both cases, LIF (f → B, β → A) at 340 nm is detected.

3.2.3. Rotational Anisotropy Formulation: All-Direction Detection

The dependence of URA measurements on the polarization of the pump-probe transitions has been discussed by Baskin and Zewail.[21] For the case when the fluorescence collection is proportional to the whole distribution (*i.e.* all-direction detection), one can consider the experimental signal for parallel and perpendicular pump-probe configurations to be of the form,[21]

where A

isotropic

such as c

semiclassic

effective r

Substitutio

which the

having I_{sc}

depends onl

3.2.4. Rotat

A cent

Equation (3.1)

experiments w

condensed-phas

experimental se

induced LIF, an

of collection ge

$$I_{\parallel} = C \cdot A(t) \cdot (1 + 2\cos^2 \omega t) \text{ and} \tag{3.3a}$$

$$I_{\perp} = C \cdot A(t) \cdot (2 - \cos^2 \omega t) \tag{3.3b}$$

where $A(t)$ represents the time-dependent absorption probability of the probe beams (all isotropic), C is a proportionality constant that takes into account experimental conditions such as collection efficiency and spectroscopic parameters, and $\cos^2 \omega t$ represents the semiclassical time-dependent rotational dynamics where $\omega = 4\pi B_{eff} j$ and B_{eff} is the effective rotational constant of the molecule. (For linear molecules, B_{eff} equals B.) Substitution of Equations (3.3a) and (3.3b) into Equation (3.1) yields an expression in which the semiclassical time-dependent rotational dynamics terms ($\cos^2 \omega t$) cancel leaving I_{iso} proportional to $C \cdot A(t)$. These terms cancel in Equation (3.2). Thus $r(t)$ depends only on the rotational population and the rotational constants of the molecule.

3.2.4. Rotational Anisotropy Formulation: Unidirectional Detection

A central aspect for the above analysis is that the experimental setup must satisfy Equation (3.1), namely that the denominator must be truly isotropic. This is the case for experiments where absorption of the probe laser is measured, as in most time-resolved condensed-phase experiments. We need to consider one of the most common experimental setups used for gas-phase measurements, unidirectional detection of probe induced LIF, and determine whether or not Equation (3.1) is fulfilled. While the effects of collection geometry have been noted before,[21] the implications have not been

explored. Be

of the optic

number co'le

3.2.4.1.

For

from either

proportion

UF at a rig

be shown ar

For these

polarizatio

explored. Below, we first assume a large *f* number collection (*f* number is the focal length of the optic divided by the diameter of the optic); then we examine differences for small *f* number collection.

3.2.4.1. Large *f* number collection

For unidirectional detection experiments, fluorescence collection favors signals from either parallel or perpendicular probing configurations; thus, the signal is not proportional to the whole distribution. A common example is collecting probe induced LIF at a right angle to the laser (*e.g.* X-direction) as shown in Figure 2.3. This point can be shown analytically using the equations for the signals as given in Reference 21

$$S_{\|X} = S_{\|Y} = \frac{2C}{105}(1+2\cos^2\omega t), \tag{3.4a}$$

$$S_{\|Z} = \frac{C}{35}(1+2\cos^2\omega t), \tag{3.4b}$$

$$S_{\perp Y} = \frac{C}{105}(3-\cos^2\omega t), \text{ and} \tag{3.4c}$$

$$S_{\perp X} = S_{\perp Z} = \frac{C}{210}(11-6\cos^2\omega t). \tag{3.4d}$$

For these expressions, the polarization vector of the probe is fixed along the Z-axis; the polarization vector of the pump is oriented along the Z- or X-axes for parallel or

perpendic

the polariz

the signal

radiation c

unidirectio

perpendicul

detection d

important e

and $I_{\perp}$ for λ

cancellation

molecular ori

formulae are

detection can

perpendicular measurements respectively. The LIF signal arises from the components of the polarization dipole along each of the lab-fixed axes. For example, S_X corresponds to the signal that is radiated by a dipole that is oriented along the X-axis. Note that this radiation can not be observed along the X-axis itself. This is one of the reasons why unidirectional detection can over- or under-estimate the ratio between parallel and perpendicular signals. Equations (3.4a)-(3.4d) are used to calculate $I_{\parallel}$ and $I_{\perp}$ for different detection directions. These expressions are shown in Table I in addition to other important equations and values in anisotropic measurements. Clearly the addition of $I_{\parallel}$ and $I_{\perp}$ for X-detection ($I = S_Y + S_Z$) according to Equation (3.1) does not lead to the cancellation of the rotational term. Because the goal is to render the sum independent of molecular orientation, one can easily deduce the correct expression by substitution; these formulae are shown in Table I. As shown in the table, the experimental $r(t)$ for X-detection can be calculated from the data using

$$r(t)_X = \frac{I_{\parallel} - I_{\perp}}{I_{\parallel} + \frac{5}{2} I_{\perp}} . \tag{3.5}$$

Table I. Semiclassical time-resolved anisotropy expressions for unidirectional detection (parallel pump and probe transitions assumed) and large f number collection. Corrections for multiphoton pump or probe measurements can be made by using the formulae in Reference 9.

Table I. Semiclassical time-resolved anisotropy expressions for unidirectional detection (parallel pump and probe transitions assumed) and large *f* number collection. Corrections for multiphoton pump or probe measurements can be made by using the formulae in Reference 9.

	A	B	C	D
	All-direction detection $I = S_X + S_Y + S_Z$	X-detection $I = S_Y + S_Z$	Y-detection $I = S_X + S_Z$	Z-detection $I = S_X + S_Y$
$I_{\parallel}$	$\frac{C}{15}(2+\cos(2\omega t))$	$\frac{C}{21}(2+\cos(2\omega t))$	$\frac{C}{21}(2+\cos(2\omega t))$	$\frac{4C}{105}(2+\cos(2\omega t))$
$I_{\perp}$	$\frac{C}{15}\left(\frac{3}{2}-\frac{1}{2}\cos(2\omega t)\right)$	$\frac{C}{21}\left(\frac{13}{10}-\frac{2}{5}\cos(2\omega t)\right)$	$\frac{C}{21}\left(\frac{8}{5}-\frac{3}{5}\cos(2\omega t)\right)$	$\frac{4C}{105}\left(\frac{13}{8}-\frac{1}{2}\cos(2\omega t)\right)$
I_{iso}	$I_{\parallel}+2I_{\perp}$	$I_{\parallel}+\frac{5}{2}I_{\perp}$	$I_{\parallel}+\frac{5}{3}I_{\perp}$	$I_{\parallel}+2I_{\perp}$
$r(t)$	$\frac{I_{\parallel}-I_{\perp}}{I_{\parallel}+2I_{\perp}}$	$\frac{I_{\parallel}-I_{\perp}}{I_{\parallel}+\frac{5}{2}I_{\perp}}$	$\frac{I_{\parallel}-I_{\perp}}{I_{\parallel}+\frac{5}{3}I_{\perp}}$	$\frac{I_{\parallel}-I_{\perp}}{I_{\parallel}+2I_{\perp}}$
$r_f(t)$	$\frac{1}{10}(1+3\cos(2\omega t))$	$\frac{2}{15}(1+2\cos(2\omega t))$	$\frac{3}{35}(1+4\cos(2\omega t))$	$\frac{1}{14}(1+4\cos(2\omega t))$
$r(0)$	0.400	0.400	0.429	0.357
$r(\infty)$	0.100	0.133	0.086	0.071

3.2.

So

number is c

However, it

efficiency by

contributions

proper expre

anisotropy fo

the resulting c

3.2.4.2. *f* number dependence (small *f* number)

So far the discussion has been limited to large f number collection, where f number is defined as the focal length divided by the diameter of the collection optic. However, it is important to recognize that most experimentalists maximize the collection efficiency by reducing the f number of the collection optics. We calculated the relative contributions of Equations (3.4a)-(3.4d) as a function of f and again determined the proper expression for the $r(t)$ denominator by substitution. In the generalized rotational anisotropy formula

$$r(t) = \frac{I_{\parallel} - I_{\perp}}{I_{\parallel} + C(f) I_{\perp}}, \tag{3.6}$$

the resulting coefficients $C(f)$ as a function of f for X-, Y-, and Z-detection are

$$C_X(f) = \frac{5}{2} - \frac{7}{2(5+16f^2)}, \tag{3.7a}$$

$$C_Y(f) = \frac{5}{3} + \frac{7}{12(1+6f^2)}, \text{ and} \tag{3.7b}$$

$$C_Z(f) = 2 . \tag{3.7c}$$

From Equati

negligible. Even for l

and 7% for $f = 2$ and

such as optical mounts

= 1 collection difficult

is necessary for the uni

3.2.5. Evolution of t

In Figure 3.2

orientations, initially cos

defined as (A) initial

persistent alignment and

simulated using semiclass

rotational population can

From Equations (3.7a)-(3.7c), it is clear that for $f \geq 3$ the second term is negligible. Even for low f values, the deviation caused by the second term is small, 2% and 7% for $f = 2$ and $f = 1$ respectively for X-detection. In general physical constraints such as optical mounts, spatial filters, and spherical and chromatic aberrations make true $f = 1$ collection difficult. Therefore, for most URA measurements, no f number correction is necessary for the unidirectional equations in Table I.

3.2.5. Evolution of the $\cos^2\theta$ Distribution

In Figure 3.2 we have shown snapshots of the distribution of molecular orientations, initially $\cos^2\theta$, at certain characteristic points on the $r(t)$ graph. These can be defined as (A) initial alignment or full-recurrence, (B) isotropic distribution, (C) persistent alignment and (D) half-recurrence. The time-dependent evolution has been simulated using semiclassical methods and a visualization of the evolution for a thermal rotational population can be found at Reference 136.

Figure 3.2. (a) Simulated rotational anisotropy graph at shorter time delays. The distribution quickly changes from the initial alignment (A) to an isotropic distribution (B) to a persistent alignment (C). Drawings of these distributions as viewed from the X-Y plane are shown above the $r(t)$ graph. (b) Simulated $r(t)$ at longer time delays. After the persistent alignment, a half-recurrence (D) develops. The drawing of this distribution is shown from a view out of the X-Y plane so that the $\sin^2\theta$ shape (rotated around the Z-axis) is evident. Each $r(t)$ is labeled with the distributions that occur as time evolves.

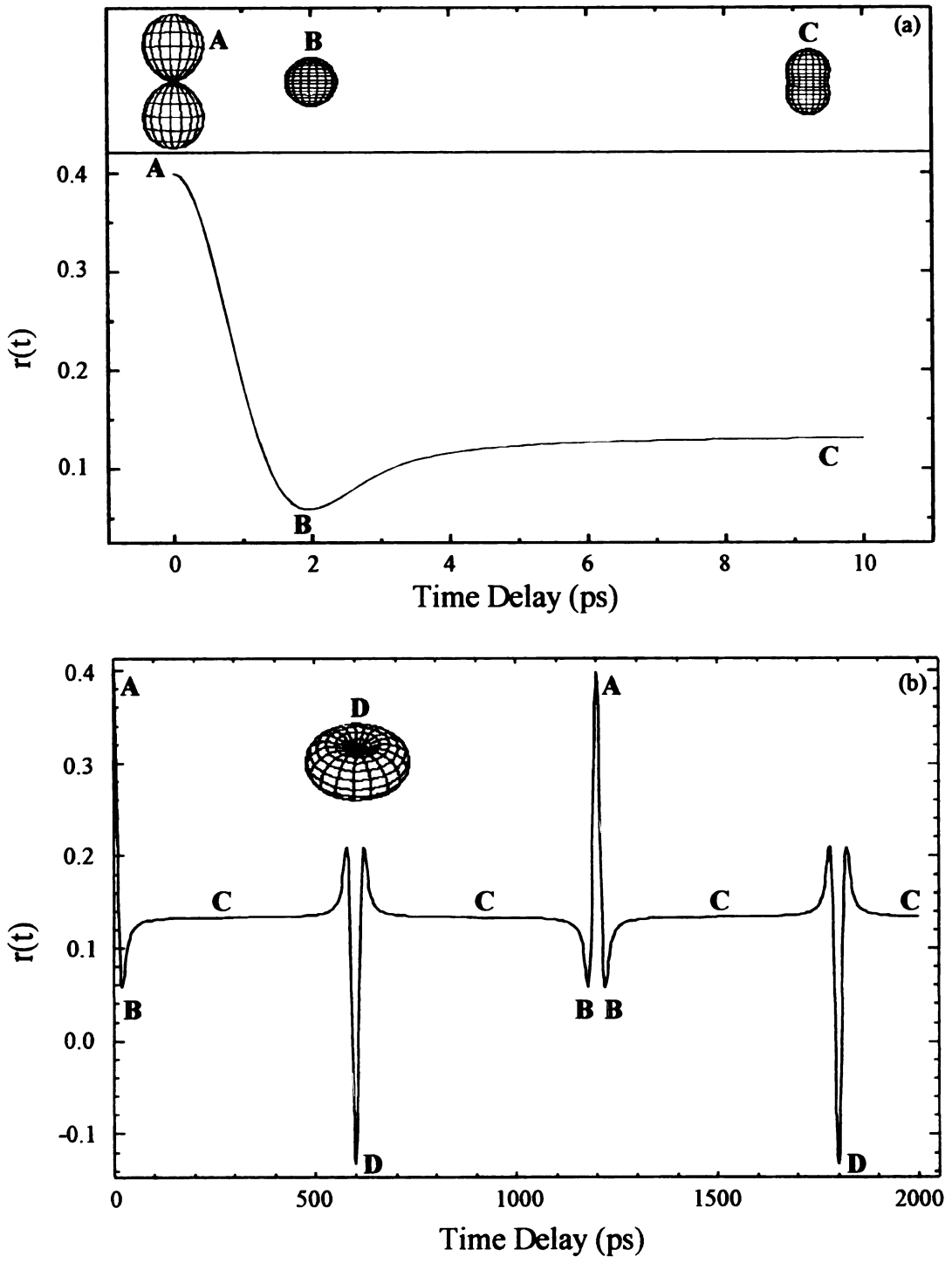
(a)
A
B
C
0.4
0.3
0.2
0.1
r(t)
0
2
4
6
8
10
Time Delay (ps)
(b)
D
0.0
-0.1
500
1000
1500
2000

Figure 3.2

In

persistent

transitions

detection

as one e

liquids. t

alignment

time infin

the differe

most UR

can make

3.2.6.

Sa

of the indiv

where $P(j)$ is the

distribution. The equa

In the absence of collisions, dilute gases for example, molecules exhibit a persistent alignment (C) that favors parallel over perpendicular probing (parallel transitions assumed). As a consequence fluorescence emission is anisotropic and the detection configuration influences the measurement. The loss of this persistent alignment as one enters the condensed phase is the subject of a paper from Zewail's group.[137] In liquids, the anisotropy values range from 0.4 at $r(0)$ to 0.0 at $r(\infty)$ because rotational alignment is relaxed by collisions. Table I shows the expected values at time zero and at time infinity for each detection direction for gas-phase experiments. Differences among the different detection geometries are significant and well above signal to noise ratios of most URA measurements. Having identified the type of collection in the experiment, one can make quantitative URA measurements.

3.2.6. Extracting Molecular Dynamics Information

Semiclassically, the rotational anisotropy, $r(t)$, can be written as a weighted sum of the individual rotational state anisotropies, $r(j,t)$,[21,33]

$$r(t) = \frac{\sum_j P(j) r(j,t)}{\sum_j P(j)} \tag{3.8}$$

where $P(j)$ is the product state distribution, for example a Boltzmann or Gaussian distribution. The equations defining $r(t)$ are adapted to the specific experimental method

used

the d

meas

tempe

3.2.7.

Th

nonresonar

Hershbach.

induced dip

leads to ali

induced a

ionization

et al. [40]

forced to

was impa

Demonstrat

and Felker

smaller nor

resonance

corresponding a

deformation of mo

used for the measurements.[9,21,44,87] Fits of the experimental $r(t)$ to Equation (3.8) lead to the determination of the experimental rotational distributions. For the room temperature measurements presented here, a Maxwell-Boltzmann distribution is assumed and a temperature is extracted to quantitate accuracy of the measurement (*vide infra*).

3.2.7. High Intensity Fields and Molecular Alignment

The observation of molecular alignment stemming from high intensity nonresonant laser excitation has been explored theoretically by Friedrich and Hershbach.[138,139] In the laser-induced alignment method, the intense laser field causes an induced dipole in polarizable molecules, which suppresses the rotational motion and leads to aligned pendular states.[138,139] Friedrich and Herschbach developed this laser-induced alignment theory based on earlier observations of dissociative multiphoton ionization experiments on CO and I_2 with intense infrared lasers conducted by Normand *et al.*[140] and Dietrich *et al.*,[141] respectively. In these cases, either the parent molecule was forced to align along the polarization vector of the laser before dissociation[140] or a torque was imparted on the molecule thereby causing a gain of angular momentum.[141] Demonstrations of the laser-induced alignment technique have been conducted by Kim and Felker on large nonpolar molecules[142,143] and by Stapelfeldt and coworkers on smaller nonpolar molecules.[144,145] Corkum and coworkers have combined intense off-resonance chirped circularly-polarized fields to induce rotational acceleration, thus constructing a molecular centrifuge.[146] Fujimura's group is currently exploring the deformation of molecules in the presence of strong-fields.[147] Experimental findings from

our gro

Those

observe

increase

intense a

period of

alignment is

also importa

the rotation

experiment.

were froze

molecules

align with

examined.

found that

Alig

Tamar Seid

strong ac

heavier molec

pulse duration

nonresonant electr

our group indicate that CS_2 molecules bend in the presence of strong off-resonance fields. Those experiments were carried out by measuring the field-free rotational recurrence observed ~76 ps after strong-field excitation in a transient grating experiment.[87,148]

In the laser-induced alignment method, increased alignment results from increased laser intensity and decreased initial rotational temperature. In addition to being intense and nonresonant, the pulses need to be relatively long (compared to the rotational period of the molecules). The experimental demonstrations have shown that the alignment is more successful if the initial rotational energy is reduced (< 10K).[144,145] It is also important to turn on the field adiabatically where the rise time is much longer that the rotational period of the molecule being aligned.[144] In the Corkum group's experiment, they noted that, with the use of intense femtosecond lasers, the I_2 molecules were frozen on the rotational time scale and the field only imparted a torque on the molecules to gain some angular momentum; however, the I_2 molecules would eventually align with the intense field if it lasted picoseconds.[141] Furthermore, Posthumus *et al.* have examined the multiphoton dissociative ionization of H_2, N_2 and I_2 with 50 fs pulses and found that only H_2 and N_2 show alignment characteristics.[149]

Alignment with resonant intense laser fields has been examined theoretically by Tamar Seideman. When on-resonance fields are used, the intensity does not have to be as strong as in off-resonance experiments to generate alignment.[150] She noted that for heavier molecules (which would correspond to greater rotational periods), a longer laser pulse duration is required to align the molecules; in addition, she also noted that nonresonant experiments may be more advantageous for these larger molecules under

low

align

Orig

molec

nonre

laser puls

conclusion

expected b

molecule, a

of this wo

influence r

3.2.8. E

As

experiments

the measure

RA measu

impulsively e

intensity of the

probability for stim

low initial rotational temperature conditions.[150] Finally in these experiments, the alignment survives and recurs at specific times after the field is turned off. Similarly, Ortigoso *et al.* have calculated the conditions (laser pulse and rotational constant of the molecule) for which recurrences of the laser-induced alignment can be expected with nonresonant short pulses.[151]

The experimental work presented here involves moderately intense femtosecond laser pulses that are resonant with the electronic transitions of I_2. Based on the results and conclusions of the above on- and off-resonance studies, adiabatic alignment is not expected because of the short duration of the laser pulses, the mass of the iodine molecule, and the warm initial rotational temperature of the molecules (294 K). The goal of this work is to explore how nonlinear processes brought about by resonant fields influence rotational anisotropy measurements.

3.2.8. Effects of Saturation

As we discussed above, we do not expect laser-induced alignment from these experiments. Another possibility is that the intense laser field will create a reduction in the measured URA. The goal is to explore how the intensity of the pump laser affects URA measurements because of saturation in the B←X transition. The initial population impulsively excited by the pump pulse has a $\cos^2\theta$ distribution. (See Figure 2.3.) As the intensity of the pump pulse increases, the population in the B state increases and the probability for stimulated emission increases as well. Hence saturation occurs. Those

molecu

emissio

with a l

the ove

anisotro

where $r_0(\lambda$

constant of

between 0 a

intensity in

anisotropy

molecules which are well aligned with the laser will be more susceptible to stimulated emission. Molecules with a smaller θ are more likely to experience saturation than those with a larger θ. Therefore the $\cos^2\theta$ distribution broadens. The end result is a reduction in the overall anisotropy. For these cases, we propose a modification of the state-resolved anisotropy equation (in the X-direction)[44] by including a saturation factor, A_S, to obtain

$$r_{A_S}(j,t) = (1 - A_S) r_0(j,t) = (1 - A_S)\frac{2}{15}(1 + 2\cos(2\omega t)) \qquad (3.9)$$

where $r_0(j,t)$ is the unperturbed rotational anisotropy, $\omega = 4\pi Bjc$, B is the rotational constant of the molecule, and c is the speed of light. The saturation parameter can vary between 0 and 1 (no saturation to severe saturation, respectively). As the pump laser intensity increases, A_S increases to take into account the reduction in the overall anisotropy.

Experim

and 340

- 340 nm

state: the

fluorescence

here, the pu

unpolarized

collection wa

The

Chapter 2

to explore

the laser int

pulse was in

thereby reduc

prepared on a

125 Torr at th

3.3. EXPERIMENTAL

For more specific experimental details of the pump-probe method, see Chapter 2. Experiments were carried out on gas-phase iodine with 622 nm pump – 311 nm probe and 340 nm fluorescence detection (622/311(340)) or with 550 nm pump – 311 nm probe – 340 nm detection (550/311(340)). The 622 nm (or 550 nm) pump excites I_2 to the B state; the 311 nm probe causes an excitation to the f state from which laser induced fluorescence (LIF) was collected at 340 nm (see Figure 3.1). For the results presented here, the pump and probe excitations are one-photon parallel transitions and the unpolarized LIF is collected perpendicular to the propagation of the lasers. The signal collection was restricted to $f = 3$.

The polarization of the pump and probe beams was ensured as described in Chapter 2. Neutral density filters were used to attenuate the pump laser intensity in order to explore the role of laser intensity on the molecular dynamics. For experiments where the laser intensity was 0.056×10^{12} and 0.27×10^{12} W/cm^2, the pulsewidth of the laser pulse was increased from 50 fs to 120 fs. This broadening reduced the peak intensity, thereby reducing nonlinear effects even further. A quartz cell containing iodine was prepared on a vacuum line and degassed to less than 10^{-6} Torr. The vapor pressure of I_2 is 0.25 Torr at the laboratory room temperature ($T_{RT} = 294 \pm 3$ K).

3.4.1.

the wea

signal pro

pplicable

time-resolve

with weak p

before the

correspond

Figure 3.1

and probe

the $f \leftarrow B$

between th

rotations of

correspond

vibrational

addition, w

corresponds to

system for the

rations for J and

3.4. RESULTS AND DISCUSSION

3.4.1. Unidirectional Detection at Weak Laser Intensities

In gas-phase molecular iodine, the B ← X and f ←B excitations resulting from the weak intensity pump and probe beams are one photon, parallel transitions. Only signal propagating at a right angle (X-direction) to the lasers is collected. The formulae applicable for this case are shown in column B of Table I. In Figure 3.3 we present I_2 time-resolved measurements ($I_{\parallel}$ and $I_{\perp}$) for 550/311(340) and for 622/311(340) obtained with weak pump and probe laser beams. At negative time delays, the probe pulse arrives before the pump (311 nm before 622 (550) nm); this sequence of pulses does not correspond to an excitation pathway that would produce 340 nm fluorescence (refer to Figure 3.1). Thus, no signal is observed. At positive time delays (or time zero), the pump and probe pulses arrive in the correct order (or at the same time) for excitation through the f ← B ← X pathway resulting in LIF at 340 nm as noted above. As the time delay between the pump and probe pulses changes, the LIF varies due to vibrations and rotations of the I_2 molecules in the B state. In these transients, the oscillations in the LIF correspond to the vibrations of iodine molecules (about 300 fs). Notice that these vibrational oscillations are similar in the parallel and perpendicular transients. In addition, underneath the vibrational oscillations is a more slowly changing signal that corresponds to the rotations of the iodine molecules. Notice that this rotational signal is different for the parallel and perpendicular transients as indicated by the theoretical equations for $I_{\parallel}$ and $I_{\perp}$ in Table I.

Figure 3.3. (a) $I_{\parallel}$ and I
for I_2 with 622/311(340
different vibrational lev
excitation wavelengths
same reason, the rotati
resulting in a slight diffe

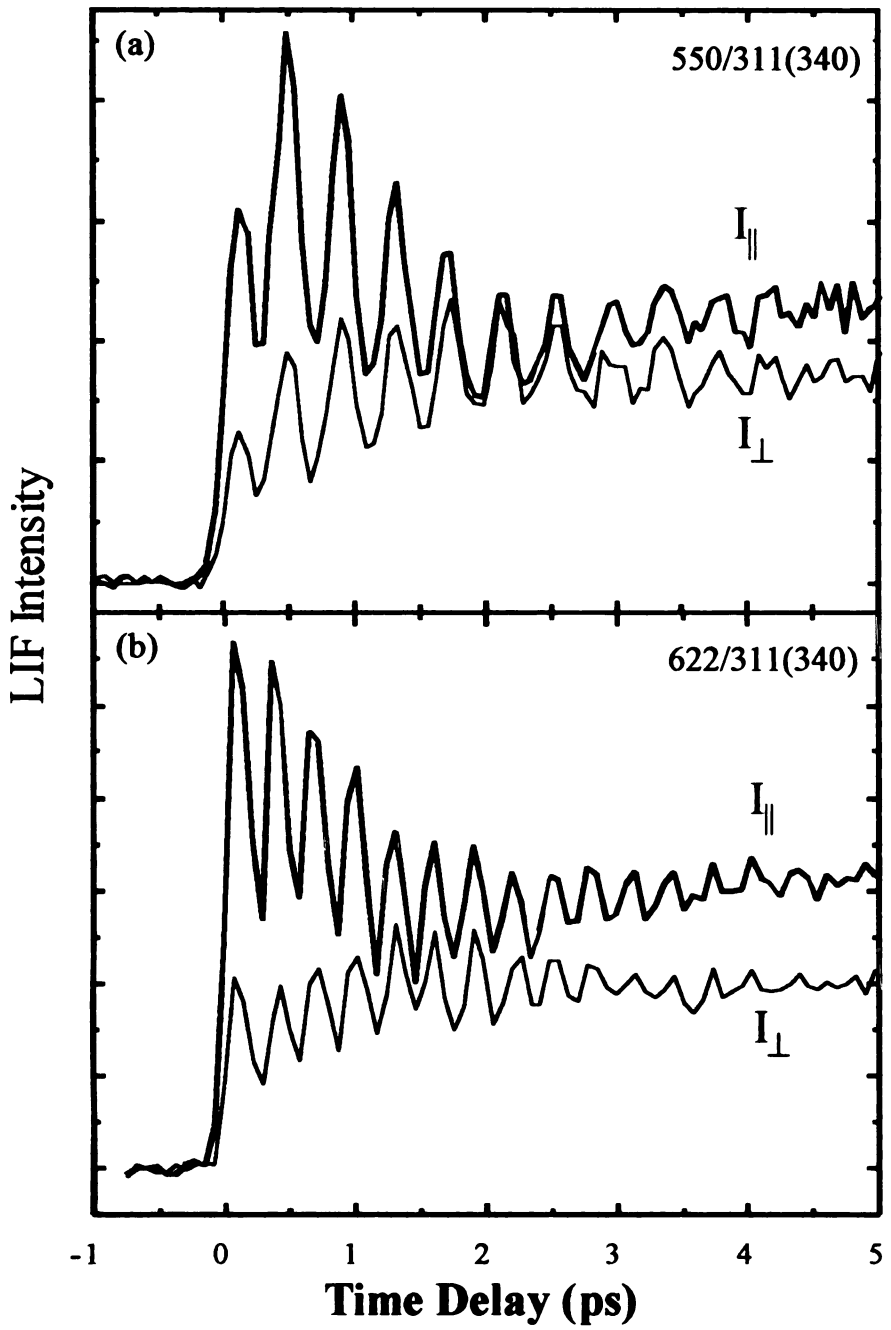

Figure 3.3. (a) $I_{\parallel}$ and $I_{\perp}$ transients for I_2 with 550/311(340). (b) $I_{\parallel}$ and $I_{\perp}$ transient for I_2 with 622/311(340). Vibrations are clear in both sets of transients. Because different vibrational levels are reached on the anharmonic B state by the two excitation wavelengths, (b) shows faster vibrational dynamics than (a). For the same reason, the rotational constants are also different for the two data sets resulting in a slight difference in the rotational dynamics.

The transien

intensity laser beam

Saturation effects or

measurements are p

resolved transients.

pump-probe time del

for parallel transient

Equation (3.5). (The

and $I_{\perp}$ as the time de

observed that using

and fitting routine ch

temperature). Equatio

constants obtained fr

temperature as the on

(solid lines). The exper

isotropic. The data at t

r(z) with great accura

does show a slight decr

play a role in the exci

populations of 294 ± 12

intensity = 0.056 x 10^{12}

x 10^{12} W cm^{-2}. These ter

±3 K. The deviation obs

The transients used for these URA measurements were obtained with low intensity laser beams to minimize saturation effects on the anisotropy measurement. Saturation effects on anisotropy measurements are discussed below. Experimental URA measurements are presented in Figure 3.4 and Figure 3.5 (scattered points). The time-resolved transients, $I_{\parallel}$ and $I_{\perp}$, have been normalized such that the intensity at negative pump-probe time delays is 0 and the intensity at 6 ps (approaching time infinity) equals 2 for parallel transients and 1.3 for perpendicular transients before calculating $r(t)$ using Equation (3.5). (These values are obtained by examining the theoretical equations for $I_{\parallel}$ and $I_{\perp}$ as the time delay approaches infinity. See Table I for the relevant equations.) We observed that using normalized versus unnormalized data in the anisotropy calculation and fitting routine changes the results only slightly (±3% for the rotational population temperature). Equation (3.8) is used in the fitting program (see Appendices) with B constants obtained from Reference 34. The fits to the normalized data sets, with temperature as the only adjustable parameter, are shown in Figure 3.4 and Figure 3.5 (solid lines). The experimental URA data are devoid of vibrational oscillations, which are isotropic. The data at these lower intensities reproduce the theoretical values for $r(0)$ and $r(\infty)$ with great accuracy. The higher intensity URA measurement (0.27×10^{12} W/cm^2) does show a slight decrease from the theoretical $r(0)$ value of 0.4 as saturation begins to play a role in the excitation process (*vide infra*). In addition, the fits reflect thermal populations of 294 ± 12 K with 550 nm pump; 302 ± 22 K with 622 nm pump, laser intensity = 0.056×10^{12} W/cm^2; and 290 ± 12 K with 622 nm pump, laser intensity = 0.27×10^{12} W/cm^2. These temperature fits agree with the temperature in the laboratory, 294 ± 3 K. The deviation observed in the weaker intensity transient is probably caused by the

much lo

obtained

obtained

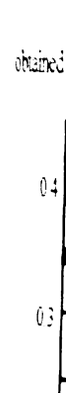

Figure 3.4
values cal
shown as t
shown as t
234 ± 12 K

much lower signal-to-noise ratio of the data. Thus, accurate rotational temperatures are obtained when using the appropriate equations in Table I to evaluate URA measurements obtained from probe induced LIF with a particular detection geometry.

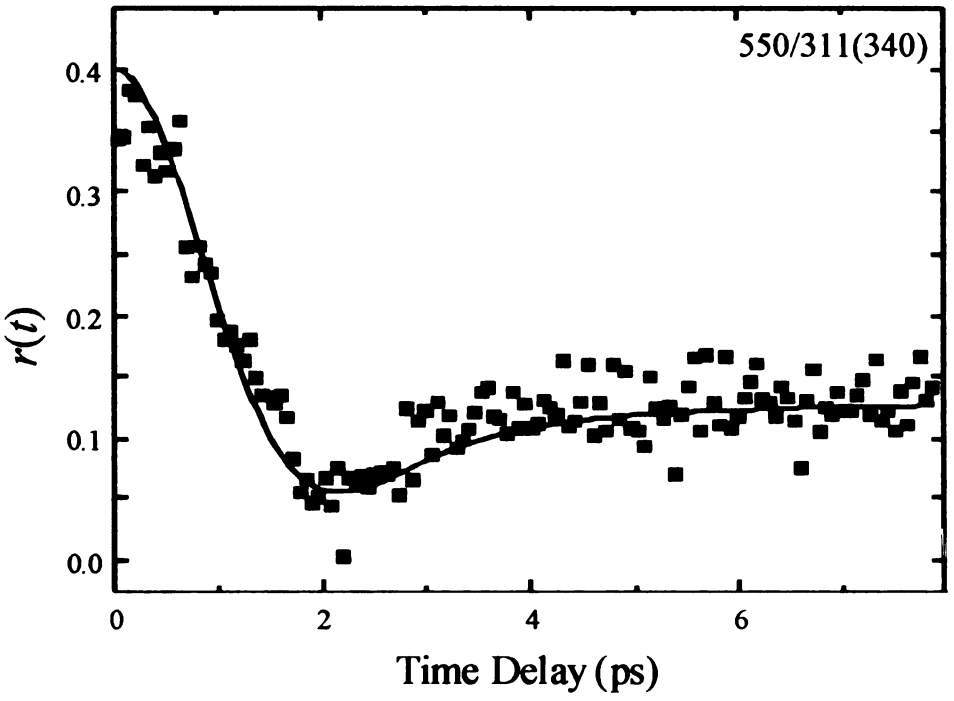

Figure 3.4. URA measurements for 550/311(340) on I_2. Rotational anisotropy values calculated from normalized experimental data and Equation (3.5) are shown as the scattered points. Fits to these values using Equation (3.8) are shown as the solid lines. The measurement is best fit by a thermal distribution of 294 ± 12 K. Note that temperature is the only adjustable parameter.

Figure 3.5
Experimen
are shown
parameter
best fit by t
that temper

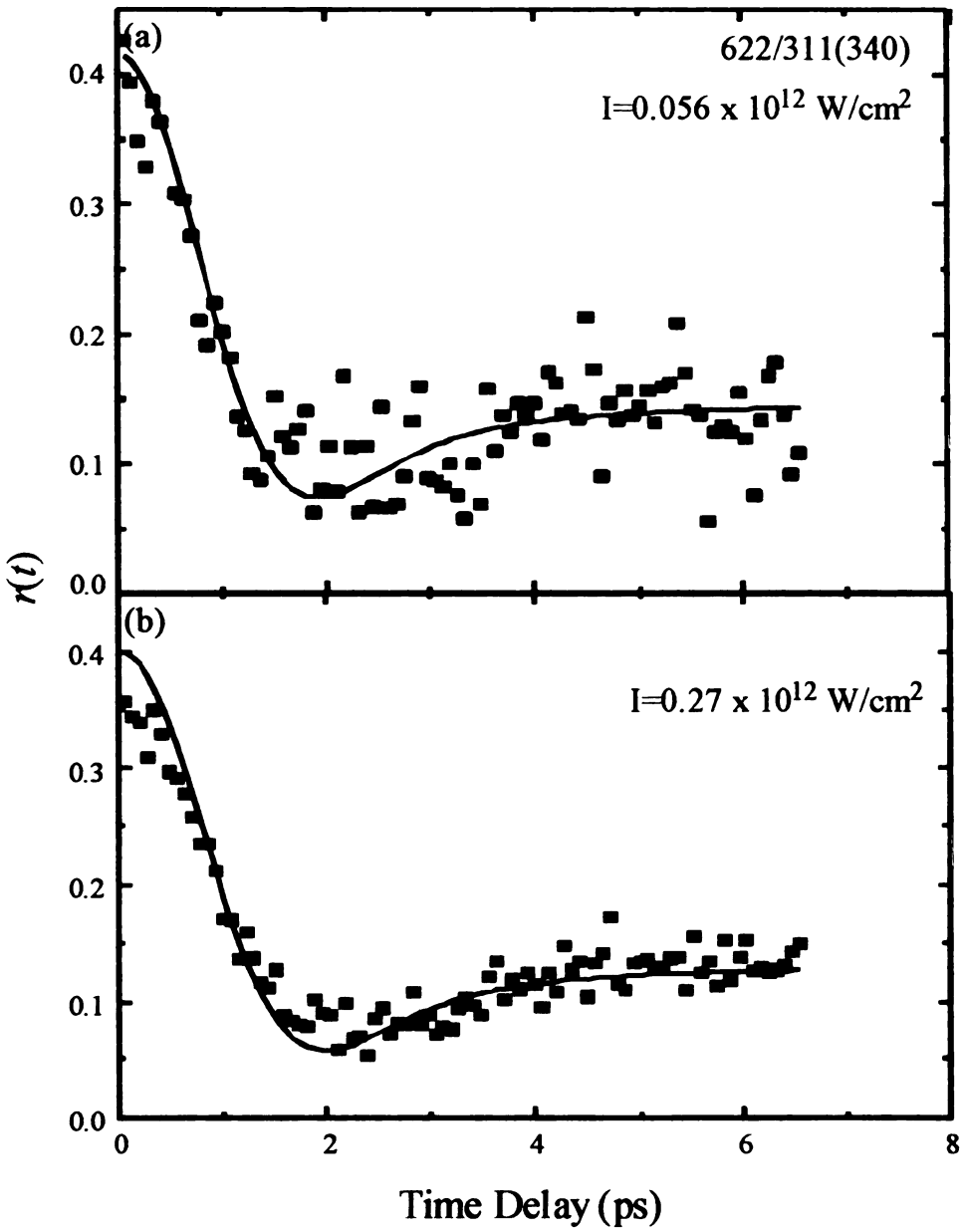

Figure 3.5. Rotational anisotropy of I_2 in the low pump laser intensity regime. Experimental data are shown by the square data points and the temperature fits are shown with the lines. These URA measurements are fit without the saturation parameter and accurately reflect the shape of the data. The measurements are best fit by thermal distributions of 302 ± 22 K and 290 ± 12K respectively. Note that temperature is the only adjustable parameter.

3.4.2 Laser Intensi

One of the goa

rotational distribution

strong-field effects. T

carried out at room t

each URA measureme

the experimental rota

(3.5), conducting a

Equation (3.8) where

to vary. The backgrou

the best fit to the exp

evaluate the quality of

3.4.2.1.

Parallel and pe

intensities from 0.056

corresponding to each

at zero and varying onl

the two lowest laser int

deviation between T_{fit} a

pump laser intensities d

3.4.2. Laser Intensity Effects

One of the goals of this study was to determine how the accuracy in determining rotational distributions or rotational temperatures is compromised by saturation and other strong-field effects. To this end, all the laser intensity dependence measurements were carried out at room temperature, T_{RT}. The rotational temperature obtained from fitting each URA measurement, T_{fit}, was compared with T_{RT}. Each fit was found by calculating the experimental rotational anisotropy from the experimental transients using Equation (3.5), conducting a linear squares regression on the experimental $r(t)$, fitting it to Equation (3.8) where $r(j,t)$ is defined in Equation (3.9), and allowing the temperature, T_{fit}, to vary. The background and the saturation parameter, A_S, were also optimized to obtain the best fit to the experimental data. The agreement between T_{fit} and T_{RT} was used to evaluate the quality of the model.

3.4.2.1. Ultrafast rotational anisotropy: Weak-field model

Parallel and perpendicular transients were measured over a range of pump laser intensities from 0.056 x 10^{12} W/cm^2 to 62 x 10^{12} W/cm^2. The URA measurement corresponding to each intensity was fit as described above, keeping the saturation factor at zero and varying only the temperature and background. As can be seen in Table IIA, at the two lowest laser intensities, the agreement with theory is very good with 1.4 to 2.7 % deviation between T_{fit} and T_{RT}. However, the URA measurements obtained with higher pump laser intensities do not fit the conventional theory (up to 58 % deviation) because

of saturation effects. These two lowest laser intensity URA measurements are shown in Figure 3.5 (data and fits) and are discussed in detail in the above section.

Table II. Rotational temperatures (T_{fit}) resulting from the fits based on Equation (3.3) (A) without the saturation parameter and (B) with the saturation parameter at different pump laser intensities. Note that parentheses around a percentage indicate that the calculated temperature is below the actual temperature.

Intensity (10^{12}W/cm^2)	A. No Saturation Parameter (A_s=1.0)		B. Saturation Parameter		
	T_{fit} (K)	% Error	A_s	T_{fit} (K)	% Error
0.056	302 ± 22	2.7%	---	--- ---	
0.27	290 ± 12	(1.4%)	---	--- ---	
1.4	379 ± 23	29%	0.23	325 ± 22	11%
8.5	325 ± 22	11%	0.36	243 ± 15	(17%)
19	433 ± 34	47%	0.46	276 ± 17	(6.1%)
37	446 ± 47	52%	0.59	243 ± 22	(17%)
62	464 ± 55	58%	0.65	228 ± 30	(22%)

3.4.2.2. Ultrafast rotational anisotropy: Saturation effects

The experimental URA data (squares) for strong-field excitation are shown in Figure 3.6. Notice the overall reduction in anisotropy and the appearance of a dip around time zero, $t < 500$ fs. In these cases, the saturation parameter, A_S, in addition to T_{fit} and the background were allowed to vary in the fitting procedure as described above. The results from these fits are shown in Table IIB. The fits give temperatures that do not correspond to T_{RT} (6.1 – 22 % deviation) but are more accurate than the temperatures obtained without the saturation parameter (see above). From Figure 3.6, it is evident that the rotational temperature fits (lines) do not model the early time behavior properly

because of the a

the fit at the bott

model the data v

simple saturation

temperatures. Th

anisotropy for wh

because of the appearance of a dip in the experimental URA measurement. In addition, the fit at the bottom of the rotational anisotropy curve (near t = 2 ps) does not appear to model the data very well. The depletion feature near time zero cannot be addressed by the simple saturation model, leading to improper fits and resulting in inaccurate rotational temperatures. Therefore, a different process is responsible for these changes in the anisotropy for which the simple saturation model cannot account.

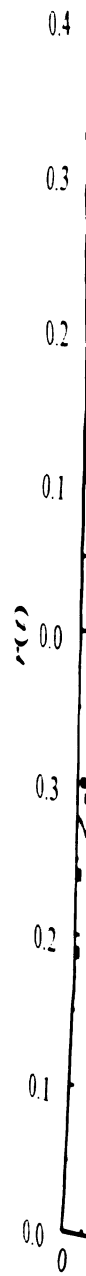

Figure 3.6. Ro
These URA m
saturation mod
and yields rotat

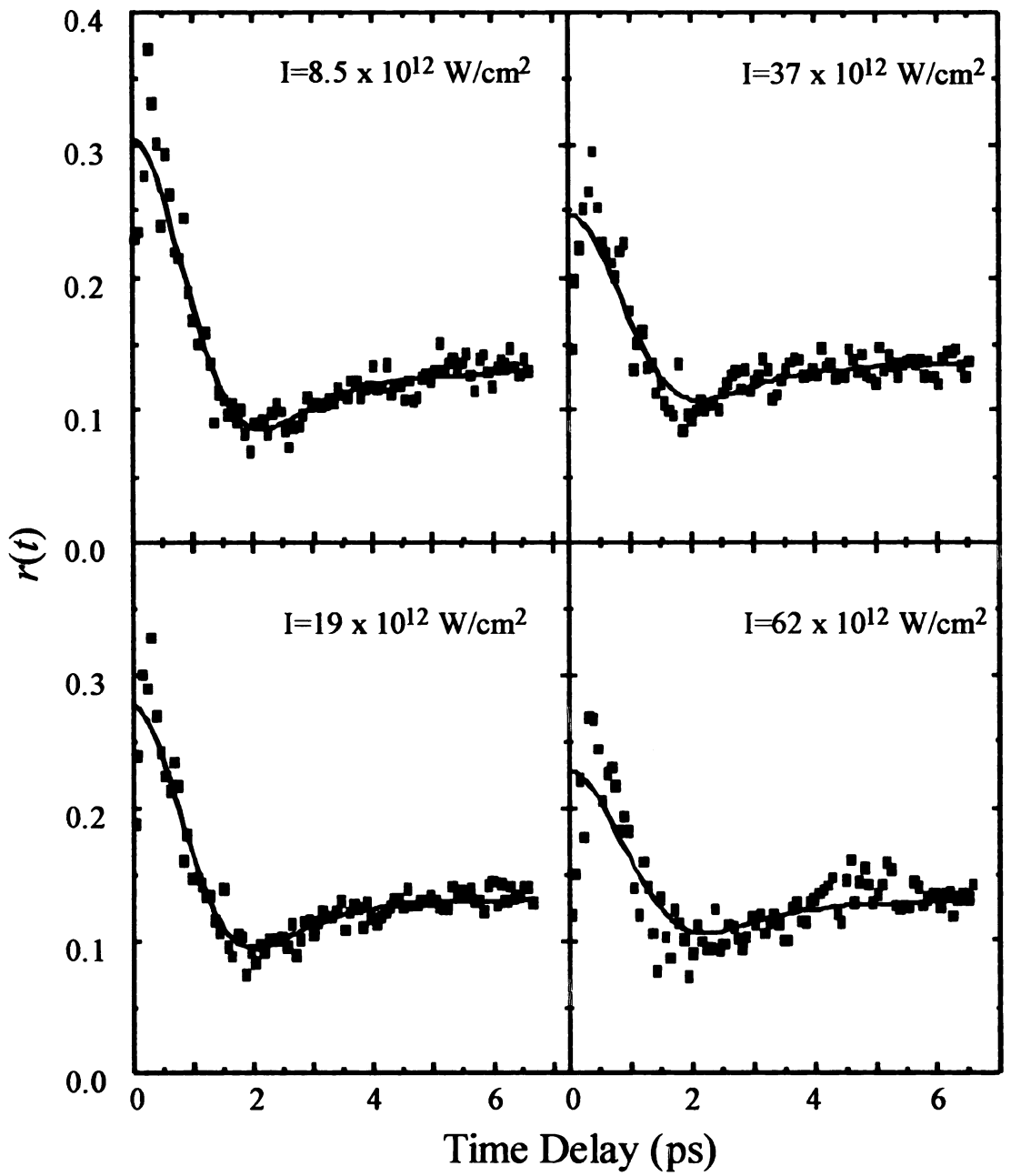

Figure 3.6. Rotational anisotropy of I_2 in the high pump laser intensity regime. These URA measurements are fit with the saturation parameter, A_S. This simple saturation model does not predict the observed dip in the data near time zero and yields rotational temperatures with 6 - 22 % error.

3.4.2.3

In the

emission but als

other states, et

($^1\Pi_u$) state is

lived wave pac

laser: this is a p

f → B transitio

surfaces. At hig

a steeply repuls

Therefore, as th

transition begin

characteristics o

beams, the B st

state is probed

pump-probe arra

intensities (*vide i*

We have

oscillation (neares

follow it, particu

3.4.2.3. Ultrafast rotational anisotropy: Saturation and reactive pathway

In the case of iodine, high pump laser intensities allow not only stimulated emission but also the possibility of other pathways, *e. g.* multiphoton excitation, access to other states, etc. At the excitation wavelength of 622 nm, the repulsive wall of the A ($^3\Pi_{1u}$) state is accessible through the A ← X perpendicular transition.[152,153] The short-lived wave packet on the A state can be excited to the β (1_g) state by the 311 nm probe laser; this is a parallel transition. Interestingly, the β → A fluorescence coincides with the f → B transition at 340 nm.[154-156] Refer to Figure 3.1 for the relevant potential energy surfaces. At high intensities, the B state saturates; however, the A state, being reached at a steeply repulsive region, has a short-lived transition state and is not easily saturated. Therefore, as the B state becomes saturated at higher intensities, the weaker A state transition begins to play an important role in the excitation process. Based on the characteristics of the transitions (parallel or perpendicular), with parallel pump-probe beams, the B state is primarily observed; with perpendicular pump-probe beams, the A state is probed preferentially. The short-lived signal, arising from the perpendicular pump-probe arrangement, explains the dip in the URA observed near t = 0 fs at higher intensities (*vide infra)*.

We have observed in our measured data ($I_{\parallel}$ and $I_{\perp}$) that the first vibrational oscillation (nearest to t = 0) in the $I_{\perp}$ transients is more intense than the oscillations that follow it, particularly for the highest pump laser intensities. These perpendicular

transients at differ

left-side shows th

above.) The $I_{\parallel}$ tra

the first vibrationa

predicted based on

(51 L mol^{-1} cm^{-1})

the dissociation en

spontaneous emissi

s^{-1} and $\beta \rightarrow A$ at

parameter that dep

$\beta \leftarrow A \leftarrow X$ versu

saturation while $I_{\perp}$

probed in the perpe

the numerator of Eq

only be observed at

in 200-300 fs (as

stages).[157,158] There

= 0 for perpendicu

becomes larger wit

intensity of the first

intensity.

transients at different pump laser intensities are shown on the right-side of Figure 3.7; the left-side shows the parallel transients. (These transients were normalized as described above.) The $I_{\parallel}$ transients do not exhibit a similar significant increase in the intensity of the first vibrational oscillation as compared to the subsequent ones. This effect can be predicted based on the extinction coefficients of the A-X (23.9 L mol^{-1} cm^{-1}) and the B-X (51 L mol^{-1} cm^{-1}) transitions[153] and the short lifetime of the wave packet excited above the dissociation energy of the A state. The Einstein coefficients are similar for the two spontaneous emission processes following the probe pulse: f → B at 341 nm is 712 x 10^5 s^{-1} and β → A at 341 nm is 745 x 10^5 s^{-1}.[156] These values allow us to calculate a parameter that depends on the ratio of the probability for probing these two pathways (β ← A ← X versus f ← B ← X), $A_{A/B}$ = 0.49. At high intensities, $I_{\parallel}$ decreases from saturation while $I_{\perp}$ increases from the contribution from the A state that is preferentially probed in the perpendicular configuration near t = 0. Therefore, the expression ($I_{\parallel}$ - $I_{\perp}$) in the numerator of Equation (3.5) becomes much smaller and $r(t)$ decreases. This effect can only be observed at short time delays because molecules reaching the A state dissociate in 200-300 fs (as measured by Zewail and coworkers who studied I_2 in solvent cages).[157,158] Therefore, the additional signal (a fast decaying, almost delta function) at t = 0 for perpendicular transients causes the dip in the URA measurements. This dip becomes larger with higher pump intensities and can be predicted by examining the intensity of the first oscillation in the perpendicular transients as a function of pump laser intensity.

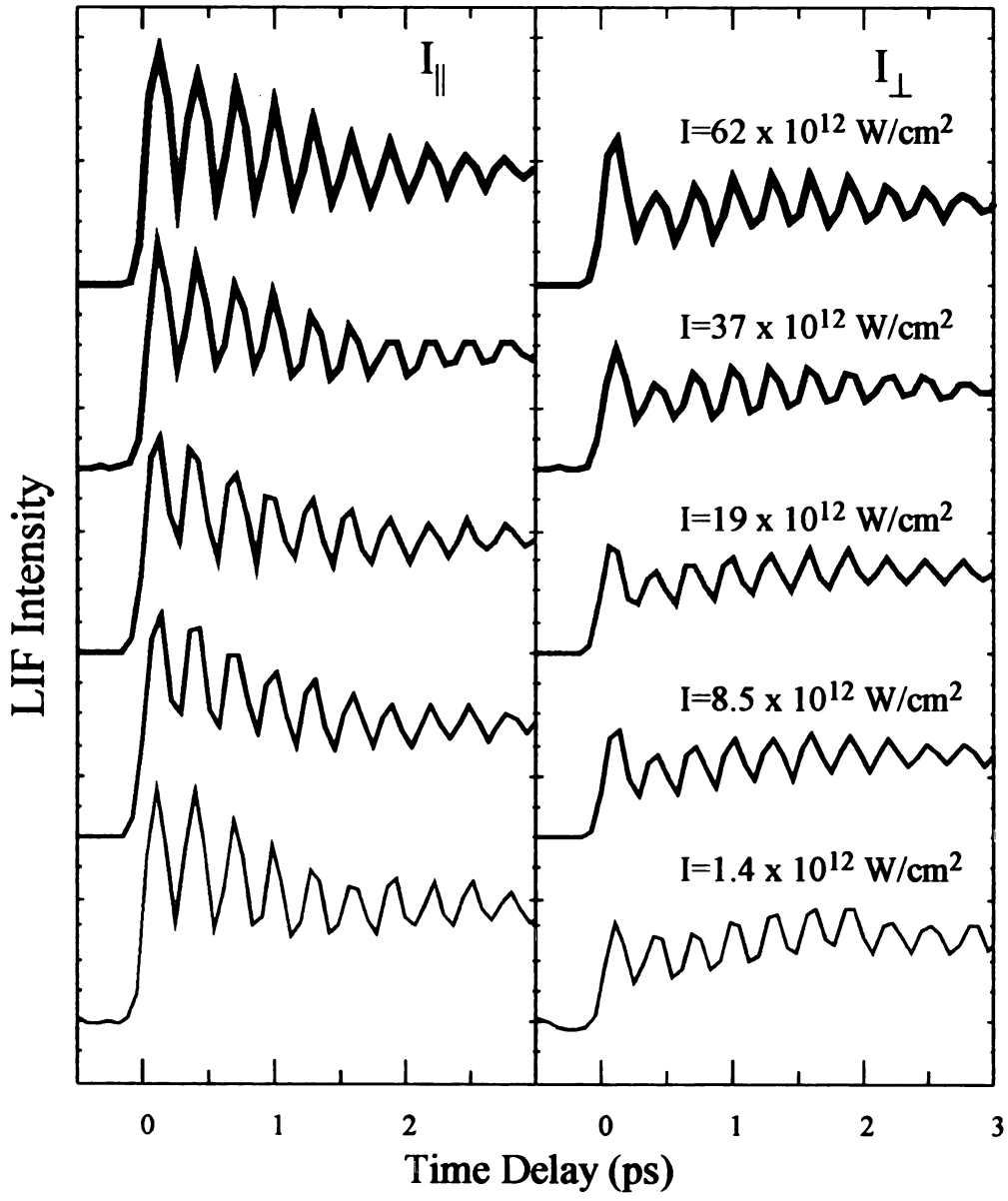

Figure 3.7. Parallel and perpendicular experimental transients obtained with different pump laser intensities. As the laser intensity increases, there is a significant increase in the LIF intensity of the first vibrational oscillation in the perpendicular transients. The parallel transients do not show this pattern. This increase is due to the contribution from the β-A-X excitation pathway at high laser intensities when the polarization of the beams is perpendicular.

This part

account equation

states to I_A and I

state. In Figure

shown for unidi

contribution only

and B states as

increase significa

not affected as

experimental perp

intensity due to a

observed when th

magnitude of thi

populations of the

calculation that as

the nature of th

population of the

effective of the ex

This pattern can also be examined with semiclassical calculations that take into account equations for $I_{\parallel}$ and $I_{\perp}$ as defined in Table I, the contributions from the A and B states to $I_{\parallel}$ and $I_{\perp}$, the Einstein coefficients for the two states, and the lifetime of the A state. In Figure 3.8a, the typical $I_{\parallel}$ and $I_{\perp}$ transients (rotational contribution) and $r(t)$ are shown for unidirectional X-detection, with a one photon parallel transition (*i. e.* B state contribution only). Then $I_{\parallel}$ and $I_{\perp}$ can be calculated by including the contribution of the A and B states as described above and are shown in Figure 3.8b. Notice that $I_{\perp}$ transients increase significantly near time zero due to the A state preferential probing; whereas, $I_{\parallel}$ is not affected as much. These theoretical calculations support the observations in the experimental perpendicular transients (Figure 3.7) where the first oscillation is higher in intensity due to a change in the rotational contribution to the signal. Therefore, the dip is observed when the rotational anisotropy is calculated from these rotational transients. The magnitude of this dip is influence by the intensity of the laser as well as the relative populations of the A and B states. The thin line in the $r(t)$ plot in Figure 3.8b shows the calculation that assumes A and B have the same populations, which does not reflect the true nature of the system; the thick line shows the calculation assuming that the population of the A state is equal to one-third of the population of the B state, more reflective of the experimental system.

Figure 3.8.
perpendicu
only the f-B
laser intens
pathways as
of the A stat
in the signal
calculated ro
populations

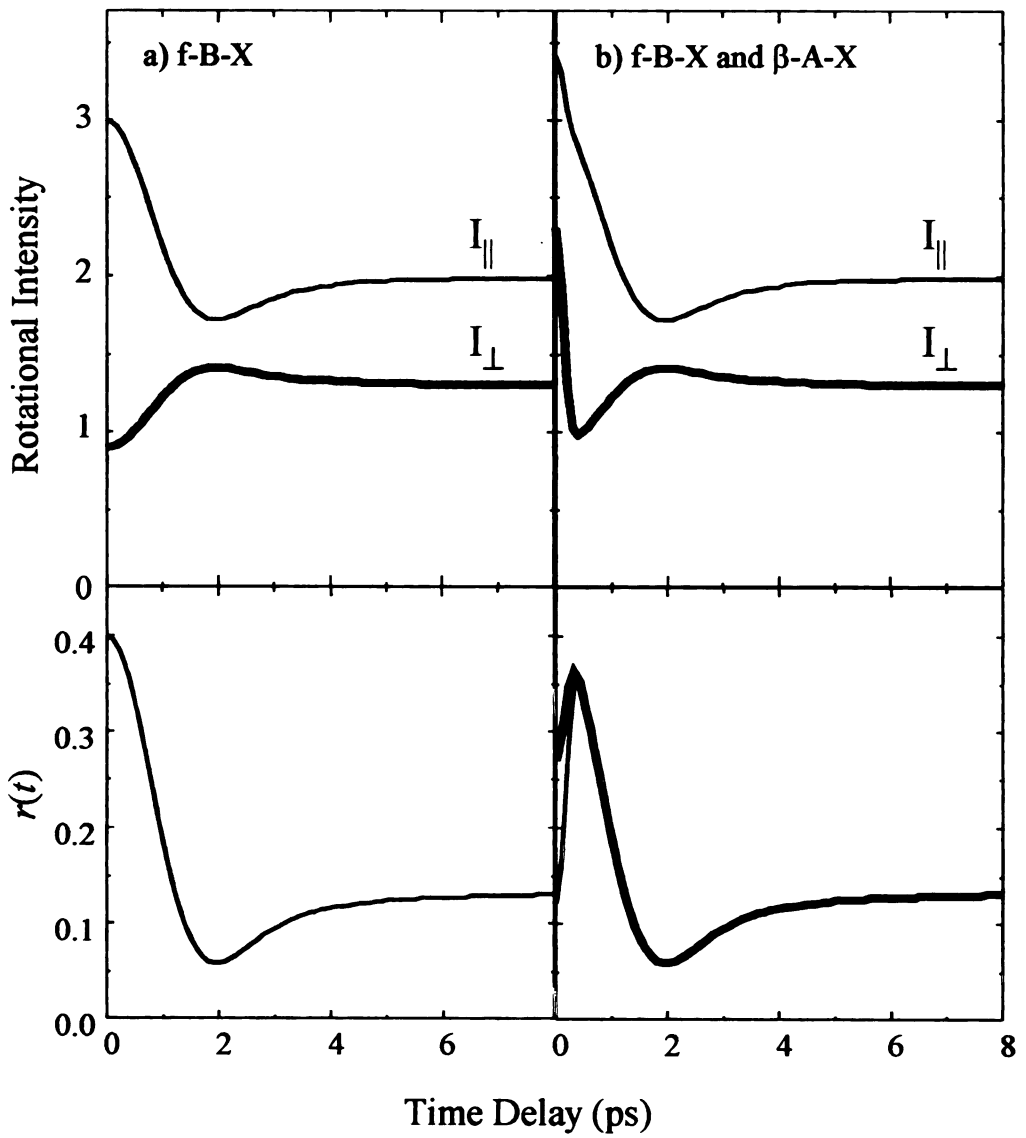

Figure 3.8. Semiclassical calculations of the rotational component of parallel and perpendicular transients and rotational anisotropy. (a) These calculations include only the f-B-X excitation pathway (typical pump-probe experiment) with weak laser intensity. (b) These calculations include both the f-B-X and β-A-X excitation pathways as is possible here with strong laser intensity. The preferential probing of the A state in the perpendicular pump-probe arrangement leads to an increase in the signal near time zero. This creates the dip that is observed in the calculated rotational anisotropy. The thin *r*(*t*) line was calculated assuming equal populations of A and B states; the thick line assumed a larger B state population.

To accou

for the state-resolv

where the first te

of the B-X transi

times caused by t

population in the

window of the pr

The expe

are shown in Fig

$\eta(J)$ is defined b

In Equation (3.1

convoluted with

times) yield the

LIRA measurem

intensities: 14 %

results). See Tab

rise near time ze

curve reflects th

(compare Figure

To account for the additional state interaction, we propose the following model for the state-resolved rotational anisotropy,

$$r_{A_S,\perp}(j,t) = (1 - A_S) r_0(j,t) - A_\perp e^{-(t/\tau)^2} \tag{3.10}$$

where the first term describes the reduction in the overall anisotropy caused by saturation of the B-X transition as in Equation (3.9) and the second term describes the dip at early times caused by the interaction of the repulsive A perpendicular state. $A_\perp$ accounts for the population in the A state and the Gaussian function accounts for the Gaussian spectral window of the probe and the temporal convolution of the laser pulses.

The experimental URA data (squares) obtained with high pump laser intensities are shown in Figure 3.9. In this case, the fits were obtained using Equation (3.8), where $r(j,t)$ is defined by Equation (3.10), and allowing A_S, $A_\perp$, T_{fit}, and the background to vary. In Equation (3.10), τ was set equal to 180 fs which corresponds to the fast dissociation convoluted with the cross correlation of our laser system for these measurements. The fits (lines) yield thermal populations that accurately reflect the laboratory temperature for all URA measurements at higher laser intensities (3.7 – 8.5 % deviation for the strongest intensities; 14 % for a moderate intensity, where Equation (3.9) yielded more accurate results). See Table III for the temperatures obtained with the fits. The dip and subsequent rise near time zero in the data for each intensity is modeled well and the entire fit of the curve reflects the data more accurately as compared to the fits that do not include $A_\perp$ (compare Figure 3.6 and Figure 3.9).

Figure 3.
The fits fo
reactive s
model. Th
shown are

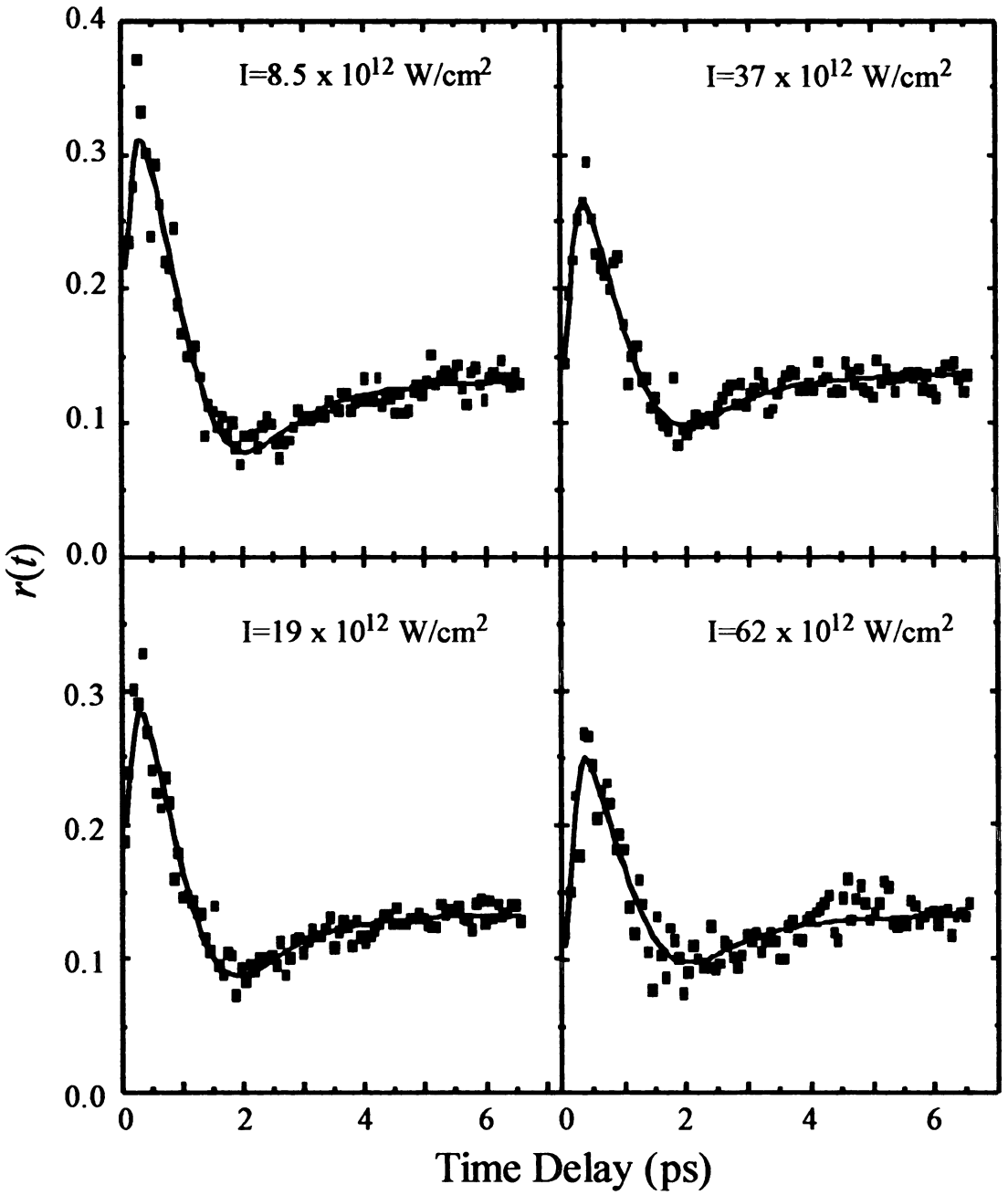

Figure 3.9. Rotational anisotropy of I_2 in the high pump laser intensity regime. The fits for these URA measurements include both the saturation effect, A_S, and reactive state interaction, $A_\perp$. The early time behavior is reflected well in this model. The rotational temperatures for the data at the four laser intensities shown are within 3.7 – 8.5 % of the laboratory temperature.

Table III. Rot
Equation (3.4
path parame
calculated te

Intensity (10^{12}W/cm^2)	
1.4	
8.5	
19	
37	
62	

The tren

broad gray line

dark gray squa

intense fields. T

closer to the lab

that incorporates

A-X transition (E

Table III. Rotational temperature fits (T_{fit}) at different pump laser intensities using Equation (3.4) which includes both the saturation parameter (A_S) and the reactive path parameter ($A_\perp$). Parentheses around a percentage indicate that the calculated temperature is below the actual temperature.

Intensity (10^{12}W/cm^2)	Saturation + Perpendicular Parameter			
	A_s	$A_\perp$	T_{fit} (K)	% Error
1.4	0.18	0.042	336 ± 23	14%
8.5	0.24	0.14	269 ± 11	(8.5%)
19	0.34	0.12	309 ± 12	5.1%
37	0.45	0.15	283 ± 13	(3.7%)
62	0.49	0.17	273 ± 18	(7.1%)

The trends in T_{fit} obtained with the three models are displayed in Figure 3.10; the broad gray line is T_{RT} (294 ± 3 K). As has been noted above, the no saturation model (dark gray squares) yields T_{fit} values that are much higher than the T_{RT} for the most intense fields. The simple saturation model (light gray triangles) leads to temperatures closer to the laboratory temperature but are too low at the highest intensities. The model that incorporates both the saturation of the B-X transition and the reactive path from the A-X transition (black circles) results in temperatures closest to the actual temperature.

Figure 3.10. R
fit the experim
294 ± 3K is sh
standard devia
included (squa
well, the high i
temperature. W
the temperatur
presence of the
the actual temp

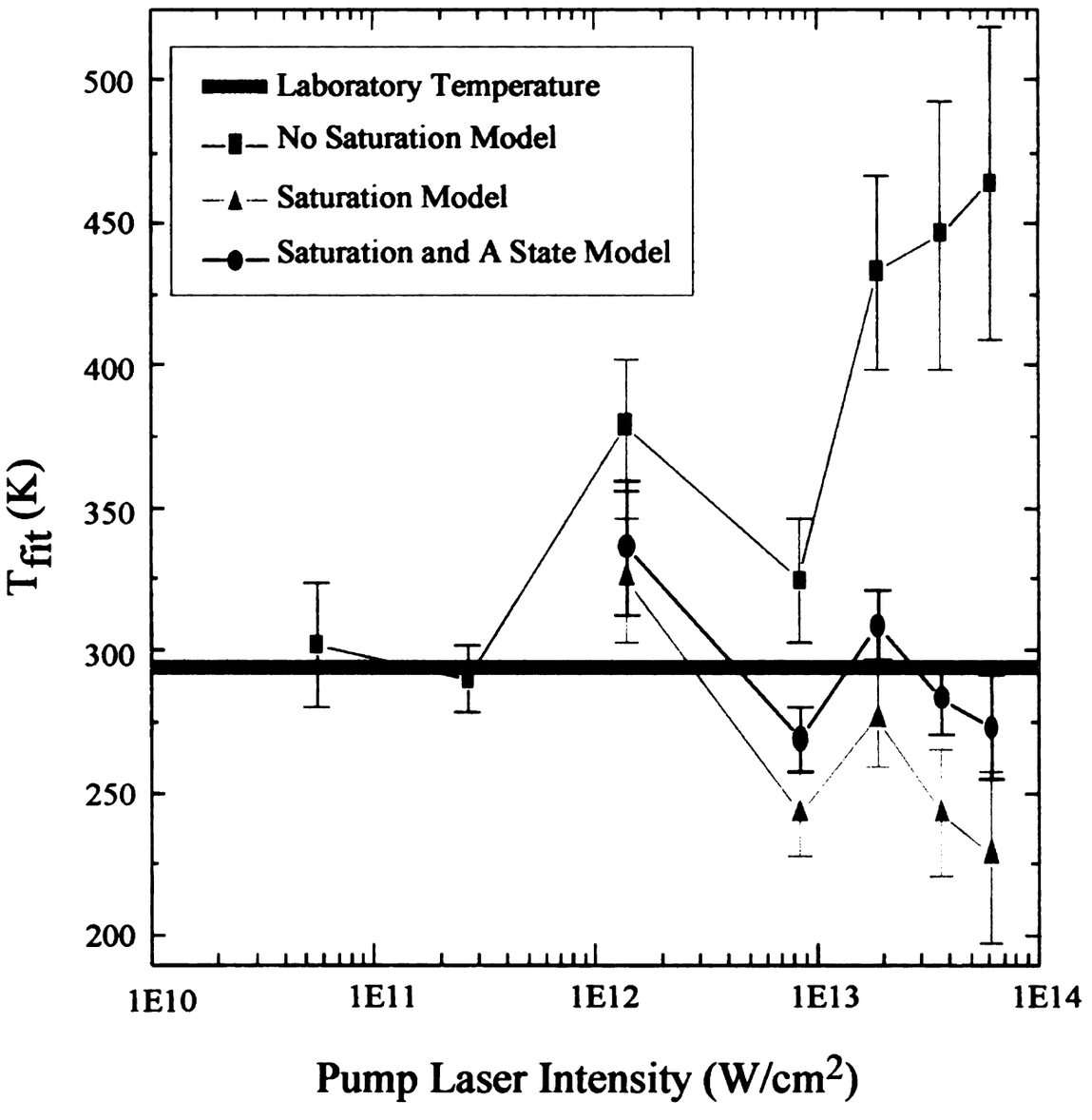

Figure 3.10. Rotational temperatures, T_{fit}, obtained from the three models used to fit the experimental rotational anisotropy data. The laboratory temperature, T_{RT} = 294 ± 3K is shown as the broad gray line. Error bars, corresponding to one standard deviation, are shown for each fitted temperature. When saturation is not included (squares), the model predicts only low intensity regime temperatures well; the high intensity regime temperatures deviate far above the actual temperature. When the model is based on the saturation of the B←X transition, the temperatures are too low. When both saturation of the B←X transition and the presence of the A state reactive path are included, the fitted temperatures reflect the actual temperature (< 10% error) in the high intensity regime.

Base

parameter va

parameter (.

determined t

follow an ex

data point w

reasonable to

values for the

Figure 3.11.
parameters o
with similar va

Based on the modified rotational anisotropy equation (Equation (3.10)) and the parameter values in Table III, as the intensity of the field increases, both the saturation parameter (A_S) and the perpendicular state parameter ($A_\perp$) increase. We have empirically determined the relationship between these parameters and the pump laser intensity. Both follow an exponential model as shown in Figure 3.11. (For the $A_\perp$ trend line, the second data point was not used in the fit because of its deviation from the rest of the data.) It is reasonable to expect a simple relationship between the two parameters. Notice that the values for the saturation intensity (I_0) are similar for these two trends.

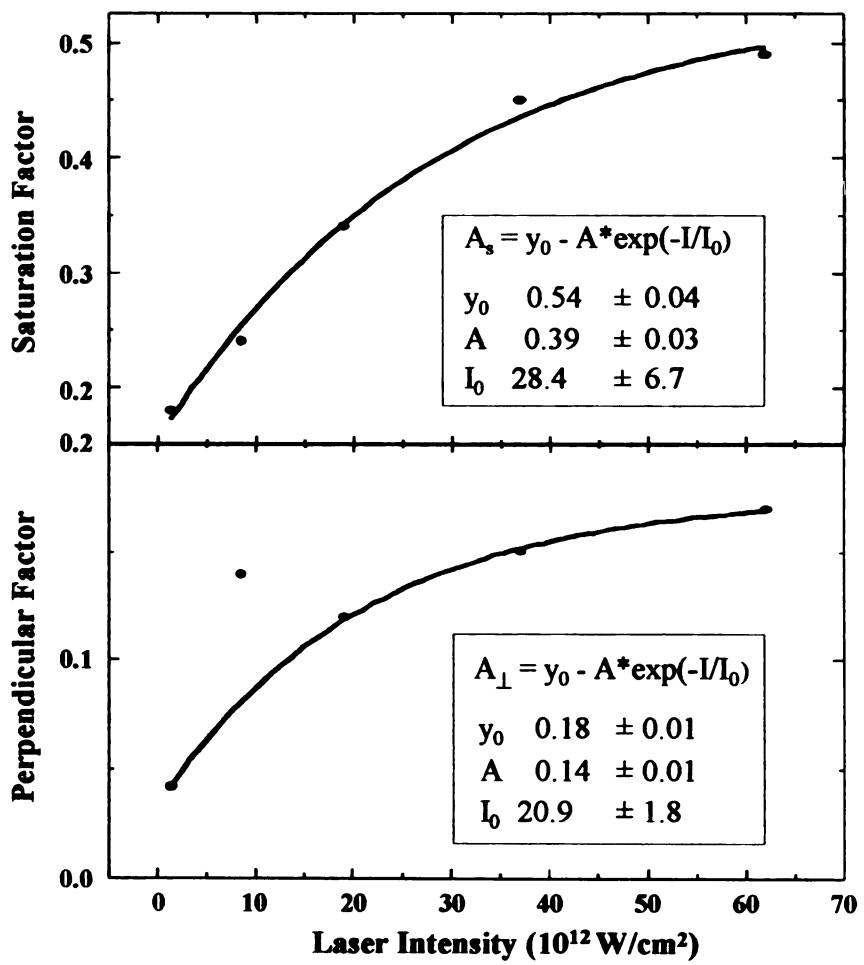

Figure 3.11. Dependence of the saturation (A_S) and perpendicular ($A_\perp$) parameters on the laser intensity. Both parameters show an exponential trend with similar values for the saturation intensity, I_0.

A unifying equation for modeling the rotational anisotropy can be obtained if we assume that the ratio of the probabilities for probing the two pathways (β←A←X and f←B←X) is fixed and corresponds to $A_{A/B}$ as discussed earlier. Under this assumption, we obtain the following expression for the rotational anisotropy,

$$r_{A_S,A_{A/B}}(j,t) = r_0(j,t) - A_S\left(r_0(j,t) + A_{A/B}e^{-(t/\tau)^2}\right) \tag{3.11}$$

where the saturation reduces the observed B-X anisotropy and, at the same time, increases the ability to see the A-X transition. Using Equation (3.11) in place of Equation (3.9) (or Equation (3.10)) in the fitting procedure described above, we have fit the data by varying A_S, T_{fit}, and the background and keeping the value of $A_{A/B}$ equal to 0.49. We have found satisfactory agreement between T_{fit} and T_{RT} with 1.7 – 16 % deviation (see Table IV).

Table IV. Rotational temperature fits (T_{fit}) at different pump laser intensities using Equation (3.11) which includes the saturation parameter (A_S) and the fixed $A_{A/B}$ parameter (which is 0.49). Parentheses around a percentage indicate that the calculated temperature is below the actual temperature.

Intensity (10^{12}W/cm^2)	Saturation + Perpendicular Parameter ($A_{A/B}$ = 0.490)		
	A_s	T_{fit} (K)	% Error
1.4	0.13	346 ± 20	16%
8.5	0.26	265 ± 10	(11%)
19	0.30	321 ± 11	8.1%
37	0.38	302 ± 12	1.7%
62	0.43	290 ± 16	(2.4%)

Ultrafast

rotational charac

reliably obtain q

from experiment

for unidirectiona

tools to properly

geometry. Secon

intensities contin

some of these m

for rotational ani

anisotropy caused

corresponds to a r

We have s

and competing rea

anisotropy data s

accurate quantitati

expanded to other

distributions and ten

3.5. CONCLUSIONS

Ultrafast rotational anisotropy measurements are important for determining the rotational characteristics of non-reactive and reactive systems. Therefore, being able to reliably obtain quantitative rotational temperatures or rotational population distributions from experimental data is essential. First, our results quantitatively reproduce the theory for unidirectional signal detection (X-direction). The equations in Table I provide the tools to properly analyze URA measurements given a particular experimental detection geometry. Second, as the availability of femtosecond laser systems with very high peak intensities continues to increase, it is important to understand how strong fields affect some of these measurements. Here we explore the effect of high pump laser intensities for rotational anisotropy measurements and give a formulation that includes the loss of anisotropy caused by saturation as well as an additional parameter that, in the case of I_2, corresponds to a reactive pathway.

We have shown here how experimental detection geometry, saturation effects, and competing reactive pathways can be taken into account in order to fit rotational anisotropy data spanning three orders of magnitude in laser intensities and obtain accurate quantitative measurements. This modified rotational anisotropy model can be expanded to other systems, including reactive systems, to obtain quantitative rotational distributions and temperatures when using intense laser fields.

4. TRA

MIXING T

ROTAT

The f

essential aspe

a sample; thi

the molecule

about the m

described he

explained in

The

parameters.

sample. The

transform o

vibrational d

broad spectr

information t

transformed

availability of

4. TRANSIENT GRATING AND THREE-PULSE FOUR-WAVE MIXING TECHNIQUES FOR EXTRACTING AND CONTROLLING ROTATIONAL AND VIBRATIONAL MOLECULAR DYNAMICS

4.1. INTRODUCTION

The four-wave mixing (FWM) technique has been described in Chapter 1. The essential aspect of this technique is that two fields interact to create a transient grating in a sample; this transient grating decays and reforms based on the molecular dynamics of the molecules in the sample. When a third field scatters off that grating, information about the molecular dynamics of the sample can be obtained. In all our experiments described here, we collect signal defined by the wave vector $\mathbf{k}_s = \mathbf{k}_a - \mathbf{k}_b + \mathbf{k}_c$ as explained in Chapter 1.

The time resolution of four-wave mixing measurements depends on two different parameters. The first is related to the time duration of the laser pulses interrogating the sample. The second is related to the coherence time of the laser pulses, *i.e.* the Fourier transform of the spectral width of the laser pulse.[78] The observation of femtosecond vibrational dynamics can be achieved with nanosecond laser pulses provided they have a broad spectral bandwidth.[159] Experiments using nanosecond sources obtain purely the information that is contained in the steady-state absorption spectrum, which is Fourier transformed and convolved by the coherence length of the light source. The easy availability of broad-band light sources with extremely short coherence lengths make

those kinds

spectroscopy.

experiments o

interrogation o

various dephas

measurements.

directly observe

electric fields ar

because of the r

chirps can be us

with the sample

transition states.

gained with ultra

Many pos

however, each

geometry. The si

wave vector $\mathbf{k}_s$ =

For most of our r

0). When fields E_s

known as a transie

that is referred to a

(RTG) measuremen

the excitation is res

those kinds of measurements, which are similar to Fourier transform infrared spectroscopy, very attractive.[159] However, it is worth noting the advantages of experiments obtained with femtosecond pulses. For these experiments, the laser interrogation of the sample is complete within a time-scale that is short compared to various dephasing mechanisms. Therefore, by using femtosecond pulses in FWM measurements, (a) the onset of electronic vibrational and rotational dephasing can be directly observed,[81] (b) there is a possibility to control the temporal ordering of the three electric fields and their relative phases,[103,104,107] (c) four-wave mixing is easily achieved because of the nonlinear dependence of these techniques on laser intensity, (d) frequency chirps can be used to control the wave packet that is launched by each laser interaction with the sample,[105,106] and (e) for chemical reactions one is able to interrogate the transition states, *i.e.* observe as the reactants become products. The additional sensitivity gained with ultrashort pulses makes off-resonant measurements easily accessible.

Many possible FWM signals can be formed in the forward box configuration; however, each one has a unique wave vector determined by the phase-matching geometry. The signal detected at the upper right corner of the box is identified by the wave vector $\mathbf{k}_s = \mathbf{k}_a - \mathbf{k}_b + \mathbf{k}_c$ and is the one we collect. (See Figure 1.2 and Figure 2.4.) For most of our measurements, two of the fields (E_a and E_b) are coincident in time ($\tau_{ab} = 0$). When fields E_a and E_b precede E_c, we refer to that as a positive time delay; this is also known as a transient grating (TG) measurement. When field E_c arrives before E_a and E_b, that is referred to as negative time delay; this is also known as a reverse transient grating (RTG) measurement. A TG measurement can be taken for each of our samples, whether the excitation is resonant or off-resonant. A RTG measurement can only be taken with

resonant exci

excitation of

overlapped i

fixed time de

measurement

Pulse Sequen

E_1 precedes

that the desig

or negative ti

equivalent. T

the first time

time delay (τ

E_2 precedes E

effect of cha

explored othe

these studies a

resonant excitation of a sample. For some of the measurements involving the resonant excitation of iodine, in addition to the TG and RTG measurements where E_a and E_b are overlapped in time, we also make measurements with E_a and E_b being separated by a fixed time delay ($\tau_{ab} \neq 0$) while E_c is scanned in time (τ). Furthermore with these resonant measurements on iodine with $\tau_{ab} \neq 0$, we have explored two different pulse sequences. In Pulse Sequence I (PS-I), fields E_a and E_b precede E_c; in Pulse Sequence II (PS-II), field E_c precedes E_b and E_a. (See Figure 4.1 for schematics of the pulse sequences.) Notice that the designations of PS-I and PS-II when $\tau_{ab} \neq 0$ are similar to the notation of positive or negative time delays when $\tau_{ab} = 0$. In the forward box geometry, fields E_a and E_c are equivalent. This implies that the only difference between PS-I and PS-II is that for PS-I the first time delay (τ_{ab}) is fixed and the second one (τ) is variable. For PS-II, the first time delay (τ) is variable and the second one (τ_{ab}) is fixed. Also notice that in PS-I, field E_a precedes E_b for $\tau_{ab} > 0$; in PS-II, field E_b precedes E_a for $\tau_{ab} > 0$. Here we explore the effect of changing τ_{ab} on the molecular dynamics observed in the sample. We have explored other pulse sequences in resonant three-pulse FWM measurements; results from these studies are published elsewhere.[103,106,107,109,160]

Figure 4.1. PS-I
time delay betw
E_b and E_c. PS-I
variable time de
between fields

Here we

experiments on

demonstrate the

formalism to e

optical signals.

third-order nonl

formulae are de

experimental tr

demonstrate on

be designed to

molecule.

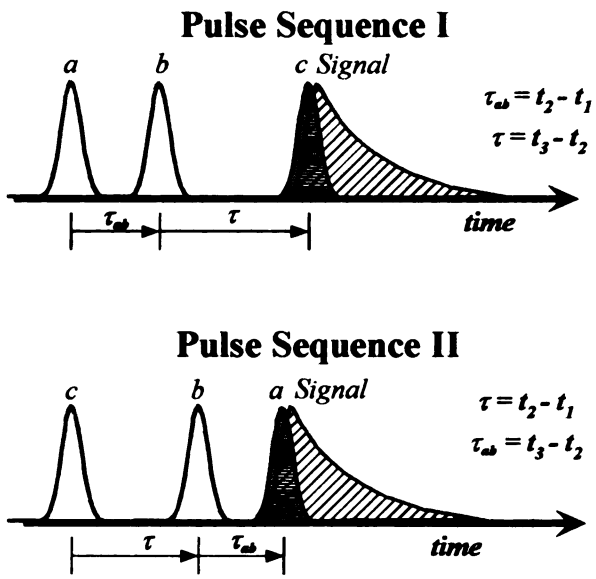

Figure 4.1. PS-I shown at the top for the three-pulse FWM process. τ_{ab} is a fixed time delay between fields E_a and E_b and τ is a variable time delay between fields E_b and E_c. PS-II shown at the bottom for the three-pulse FWM process. τ is a variable time delay between fields E_c and E_b and τ_{ab} is a fixed time delay between fields E_b and E_a.

Here we report a systematic study of femtosecond time-resolved transient-grating experiments on atomic, diatomic, triatomic and larger molecular systems. Our goal is to demonstrate the various types of molecular dynamics accessible and to provide a simple formalism to extract quantitative information from TG and related FWM nonlinear optical signals. A theoretical framework is included that takes into account the different third-order nonlinear processes that contribute to the observed signals. From this analysis formulae are derived to analyze the vibrational and rotational dynamics observed in the experimental transients for both resonant and off-resonant excitation. We also demonstrate on molecular iodine that pulse sequences in resonant three-pulse FWM can be designed to control the transition probability between two electronic states of a molecule.

The

in the literat

4.2.1. Gen

The

three inciden

where $P^{(}$

matching

measureme

where $\chi^{(}$

order to

susceptibil

possible be

Calcul

tensor requires

4.2. THEORY

Theoretical treatments of time-dependent four-wave mixing signals are abundant in the literature.[78,161] Here, a review of the results relevant to this study will be presented.

4.2.1. General Considerations

The FWM signal intensity, $I_{FWM}(\tau)$, resulting from the interaction between the three incident laser pulses and the sample medium, can be evaluated using[78,161,162]

$$I_{FWM}(\tau) = \int_{-\infty}^{\infty} \left| P^{(3)}(\mathbf{k}_S, t) \right|^2 dt \tag{4.1}$$

where $P^{(3)}(\mathbf{k}_s,t)$ represents the time-dependent third-order polarization for a given phase-matching condition. This equation is applicable for homodyne detection. For TG measurements with $\mathbf{k}_s = \mathbf{k}_a - \mathbf{k}_b + \mathbf{k}_c$, $P^{(3)}(\mathbf{k}_s,t)$ can be expressed as[78]

$$P^{(3)}(\mathbf{k}_S, t) = -E_2(t) \int_0^{\infty} \left| E_1(\tau - t') \right|^2 \chi^{(3)}(t')\, dt' \tag{4.2}$$

where $\chi^{(3)}(t)$ is the third-order susceptibility associated with the molecular system. In order to determine what type of information should be included in the molecular susceptibility term, it is important to first analyze the different interactions that are possible between the laser fields and the sample.

Calculation of the FWM signal polarization $P^{(3)}(\mathbf{k}_s,t)$ and associated susceptibility tensor requires knowledge of the third-order density operator $\rho^{(3)}(t)$.[78,161] The explicit

form of $\rho^{(}$

equation tha

incident ele

detailed des

the density

ground elec

ground state

electric field

excited (e) st

occurred. TH

(see Equatio

general an o

which is als

interactions v

vibrational le

the ro-vibrati

diagonal bloc

field involve

diagrams.[78,16

four-wave mix

Simpler diagra

describe differe

form of $\rho^{(3)}(t)$ follows from a perturbative solution of the quantum mechanical Liouville equation that describes the temporal evolution of the system under the influence of the incident electromagnetic fields and the intrinsic relaxation processes.[78,161] A more detailed description of this density matrix theory is published elsewhere.[103,163] Initially, the density matrix, $\rho^{(0)}$, corresponds to the population of the vibrational levels in the ground electronic state (upper diagonal block). In our calculation, we assume that the ground state vibrational levels are equally populated. After the first interaction with the electric field, the density matrix evolves into a coherence between the ground (g) and excited (e) states where all the diagonal terms are zero and no net population transfer has occurred. The interaction with a second electric field completes the population transfer (see Equation (1.11)) without electronic coherence between the $|g\rangle$ and $|e\rangle$ states. In general, an odd-number of interactions with the electric fields will produce a coherence, which is also a time-dependent polarization of the molecules. An even number of interactions will produce a population state that is characterized by the population of the vibrational levels in each electronic state (the diagonal terms in the diagonal blocks) and the ro-vibrational coherence within each electronic state (the off-diagonal terms in the diagonal blocks). The changes in the density matrix after each interaction with an electric field involve different processes that can be followed using double-sided Feynman diagrams.[78,161] For further information about these diagrams and their applications to four-wave mixing processes, the reader is referred to References 78,86,161,164 and 103. Simpler diagrams that alternate up and down transitions between two states fail to describe differences between populations and coherences.

4.2.2. Feynma

First we c

level system. The

of the density m

electric fields. Th

two <g| ton the r

bottom to the top

sample. Those p

pointing left cor

correspondence

conjugate prefact

center of the di

photon emission.

on both. Thus, w

only one side c

absorption or em

signal from a pa

shown in Figure

all diagrams field

field E_2 with a lef

4.2.2. Feynman Diagrams

First we consider the case in which the three laser fields are resonant with a two-level system. The diagrams shown in Figure 4.2 are representations of the time evolution of the density matrix operator ρ and its transformations by the interaction with the electric fields. The operator is denoted by the two parallel arrows which correspond to the *bra* $\langle g|$ (on the right) and the *ket* $|g\rangle$ (on the left) of the matrix. Time increases from the bottom to the top. Wavy arrows represent the interaction of each of the fields E_j with the sample. Those pointing towards the right correspond to $E_j \exp(-i\omega_j t + i\mathbf{k}_j \cdot \mathbf{r})$, while those pointing left correspond to $E_j^* \exp(i\omega_j t - i\mathbf{k}_j \cdot \mathbf{r})$. Because the *bra* and *ket* are in dual correspondence to each other – a complex prefactor on a *ket* appears as the complex conjugate prefactor on the corresponding *bra*.[165] Therefore, arrows pointing towards the center of the diagram indicate photon absorption while those pointing away indicate photon emission. An electric field interaction occurs on either the *bra* or the *ket*, but not on both. Thus, when only one electric field interacts with the system, a change occurs on only one side of the Feynman diagram (*bra* or *ket*) giving rise to a polarization; absorption or emission of a photon requires two electric field interactions. Detection of signal from a particular phase-matching configuration, for example $\mathbf{k}_s = \mathbf{k}_a - \mathbf{k}_b + \mathbf{k}_c$ as shown in Figure 1.2, determines the sign of the individual wave-vectors. Therefore, for all diagrams fields E_a and E_c must be represented with right pointing arrows, $+\mathbf{k}_j$, and field E_b with a left pointing arrow, $-\mathbf{k}_j$.

Figure 4.2. Double-sided Feynman diagrams corresponding to four-wave mixing processes observed for phase-matching condition $\mathbf{k_s} = \mathbf{k_a} - \mathbf{k_b} + \mathbf{k_c}$. In all cases the signal, emission from the *ket* side, has been omitted for clarity. Based on the experimental constraints of our measurements, beams E_a and E_b are overlapped in time and beam E_c can be delayed or advanced with respect to these beams. The label for each diagram, for example $\mathbf{ab_g}$, indicates the two beams that form the transient grating and the state in which the population is formed. The molecular response function (R_1, R_2, R_3, or R_4) corresponding to each Feynman diagram is also noted.[78,87] (a) For positive time delays, E_a and E_b form the grating and cause a transformation of $\rho^{(0)}_{gg}$ into $\rho^{(2)}_{g'g}$ or $\rho^{(2)}_{gg'}$. When E_c scatters from this grating, at positive time, ground state dynamics are obtained. (b) Here E_a and E_b form the grating and cause a transformation of $\rho^{(0)}_{gg}$ into $\rho^{(2)}_{ee'}$ or $\rho^{(2)}_{e'e}$. When E_c scatters from this grating, at positive time, excited state dynamics are obtained. (c) These diagrams contain beam E_c between fields E_a and E_b which are overlapped in time. Therefore signal is only observed only for times within the laser pulse duration. (d) For these diagrams E_c arrives first and, if resonant, forms a coherence between the ground and excited states of the form $\rho^{(1)}_{eg}$. The coherence is allowed to evolve for a time τ. The coherence dynamics are probed by the arrival of field E_b, which forms the grating, and field E_a that scatters from the grating.

Positive Time Delay (a) Ground and (b) Excited State Dynamics

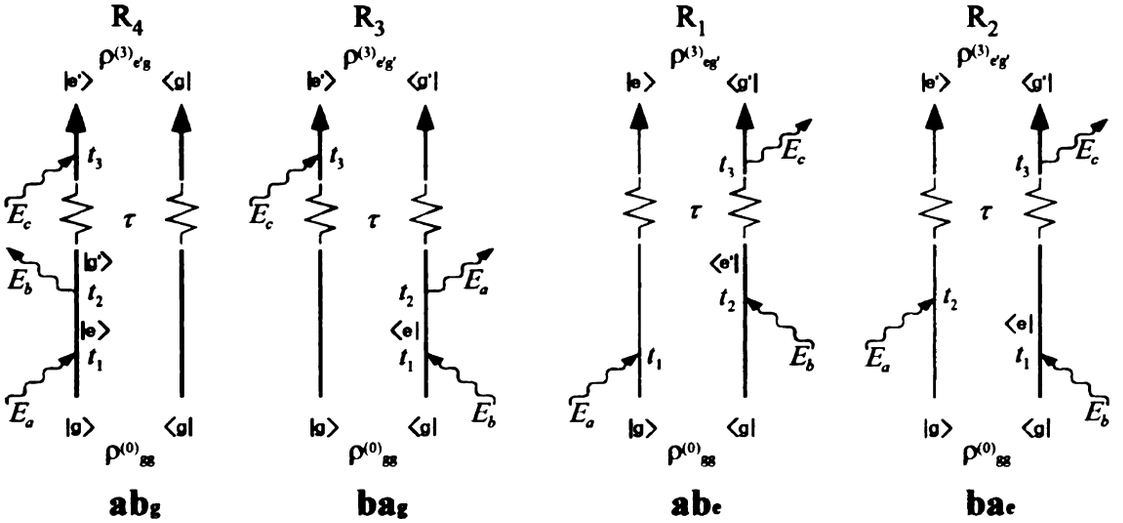

(c) Time zero contribution only

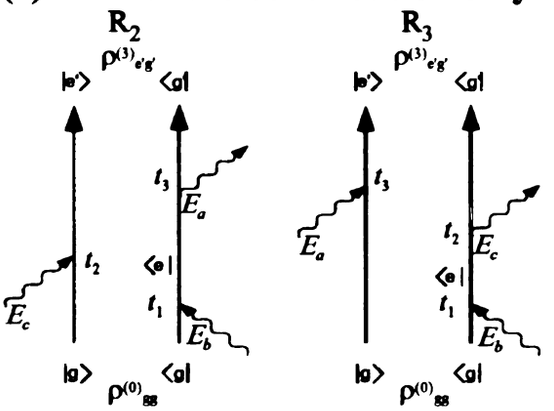

(d) Negative Time Delay - Coherence Dynamics

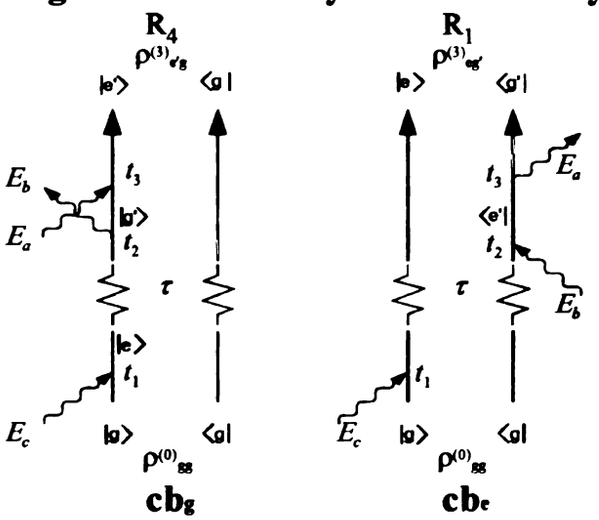

Figure 4.2

T

or *ket* si

either of

alternativ

forty-eigl

ground st

F

the obser

out most

$\frac{E_e - E_g}{\hbar}$

therefore.

field E_a a

proportio

zero. the

denomina

Contribut

neglected

diagrams

diagrams

been docu

The first field interaction may involve any one of the three fields acting on the *bra* or *ket* side. This results in six possible alternatives. The second interaction may involve either of the two remaining fields acting on the *bra* or *ket* side, giving a total of 6 x 4 alternatives. Finally the remaining field can act on the *bra* or *ket* side giving a total of forty-eight possible diagrams, representing the transformation of the initially incoherent ground state medium $\rho^{(0)}$ into $\rho^{(3)}(t)$ for this phase-matching condition.[78,161,164]

For resonant or near-resonant excitation, not all forty-eight diagrams contribute to the observed signal. In fact the rotating wave approximation (RWA) can be used to rule out most of these combinations.[166] First we define the transition frequency $\Omega_{eg} = \frac{E_e - E_g}{\hbar} = -\Omega_{ge}$ as the energy difference between the ground and the excited states; therefore, near-resonant excitation has $\omega_j \approx \Omega_{eg}$ where ω_j is the photon frequency. When field E_a acts on the *ket* at time t_1, the corresponding contribution to the polarizability is proportional to $\langle e|\mu \cdot E_a|g\rangle / (\Omega_{eg} - \omega_a)$. When the denominator is small, in this case near zero, the contribution is large. However, if E_a acts on the *bra* at time t_1, the corresponding denominator is $(\Omega_{ge} - \omega_a) = (-\Omega_{eg} - \omega_a)$, about twice the optical frequency. Contributions from these anti-rotating wave processes are very small and can be neglected for weak near-resonant fields. One can identify eight of the forty-eight diagrams in which all three field interactions satisfy the RWA and therefore these eight diagrams have a significant contribution to the polarizability. This selection process has been documented in the literature.[78,164,167]

states, l

are poin

vertical

the last

omitted

$\rho^{(3)}_{ge}$ fo

resonant

two leve

depicts t

nonlinear

fields car

Notice th

(42), the

N and the

nonlinear

formulae,

derive the

DFWM te

The diagrams shown in Figure 4.2 assume near-resonant excitation between two states, labeled here *g* and *e*. Some of the differences expected for non-resonant excitation are pointed out later in the discussion. Time ordering of each field is given by the relative vertical position of the wavy arrows and by the time labels t_1, t_2 and t_3. In all eight cases the last step, corresponding to emission of the signal field from the *ket* side, has been omitted to simplify these diagrams. The transformation of $\rho^{(0)}= |g\rangle\langle g|$, designated as $\rho^{(0)}_{gg}$, following each laser-sample interaction is labeled on the *bra* or the *ket* side. For resonant excitation it is important to illustrate how the susceptibility tensor for an isolated two level system depends on the laser's frequency. The first diagram ($\mathbf{ab_g}$) in Figure 4.2 depicts the transformation $\rho^{(0)}_{gg} \xrightarrow{E_a(t)} \rho^{(1)}_{eg} \xrightarrow{E_b(t)} \rho^{(2)}_{g'g} \xrightarrow{E_c(t)} \rho^{(3)}_{e'g}$. The nonlinear susceptibility associated with this particular interaction between the three laser fields can be expressed as

$$\chi^{(3)}_{ab_g} \propto N \sum_{gg',ee'} \rho^{(0)}_{gg} \frac{\langle g|\boldsymbol{\mu}\cdot\boldsymbol{E_s}^*|e'\rangle\langle e'|\boldsymbol{\mu}\cdot\boldsymbol{E_c}|g'\rangle\langle g'|\boldsymbol{\mu}\cdot\boldsymbol{E_b}^*|e\rangle\langle e|\boldsymbol{\mu}\cdot\boldsymbol{E_a}|g\rangle}{(\Omega_{eg}-\omega_a)(\Omega_{g'g}-\omega_a+\omega_b)(\Omega_{e'g}-\omega_a+\omega_b-\omega_c)}. \quad (4.3)$$

Notice that once this expression for the susceptibility is introduced in Equations (4.1) and (4.2), the overall FWM signal depends on the square of the number density of the sample *N* and the eighth power of the transition dipole μ. Similar equations can be written for the nonlinear susceptibilities associated with the other Feynman diagrams. However, these formulae, which are usually used for frequency-resolved techniques, are not used to derive the formalism used to simulate our time-resolved experiments. Frequency-resolved DFWM techniques have been proven to yield very high-resolution spectra, especially for

Dopp

enhan

Figure

state

associ

diagra

$\rho^{(}_{gg}$

a pola

beam

differe

E_c is n

the pul

E_c in t

on the

ab_g Fey

State dy

State is

near-res

transien

Doppler-free configurations, taking advantage of the very large resonant enhancement.[84,168]

The eight diagrams have been divided into four groups. The first group, shown in Figure 4.2a, represents the four-wave mixing process allowing the observation of ground state population dynamics. The diagonal terms of the density matrix ρ_{gg} and ρ_{ee} are associated with populations while the off-diagonal terms represent coherences. The two diagrams, labeled $\mathbf{ab_g}$ and $\mathbf{ba_g}$, indicate transient grating formation in the ground state $\rho^{(2)}{}_{g'g}(t)$ or $\rho^{(2)}{}_{gg'}(t)$ by fields E_a and E_b with positive time delay (or PS-I). Field E_c induces a polarization after a time delay τ, indicated by a break in the time arrows, and the signal beam emitted by this polarization reveals ground state dynamics information. Two different diagrams describe this observation because the sequence between fields E_a and E_b is not defined for $\tau_{ab} = 0$. When fields E_a and E_b are separated in time, the sequence of the pulses better defines each process. For example, in Figure 4.2a, field E_a precedes field E_b in the diagram shown on the left side, while field E_b precedes field E_a in the diagram on the right side. Thus, when τ_{ab} is greater than the pulse duration of the laser, only the $\mathbf{ab_g}$ Feynman diagram applies.

The second group of diagrams in Figure 4.2b depicts the observation of excited state dynamics at positive time delays (or PS-I). This observation requires that the excited state is long-lived compared to the pulse width of the laser and that the laser pulses are near-resonant with the electronic transitions. For the two diagrams, labeled $\mathbf{ab_e}$ and $\mathbf{ba_e}$, transient grating formation in the excited state $\rho^{(2)}{}_{ee'}(t)$ or $\rho^{(2)}{}_{e'e}(t)$ by E_a and E_b. This time

the signal beam resulting from the polarization induced by E_c after a time delay τ reveals excited state dynamics. Again both diagrams contribute for τ_{ab} = 0, but only $\mathbf{ab_e}$ contributes to the signal for τ_{ab} is larger than the pulse duration. The top of Figure 4.1 shows the pulse sequence that gives the TG signals arising from the diagrams shown in Figure 4.2a and b.

The third group of diagrams in Figure 4.2c contains the two sequences in which E_c, the field that can be physically delayed in time in our experimental setup, interacts with the system after field E_b but before field E_a. The signal arising from these interactions, labeled $\mathbf{bc_e}$ and $\mathbf{bc_g}$, is therefore limited to near-zero time delays when τ_{ab} = 0 (with pulse sequence I). These diagrams show the nonlinear processes that are responsible for generating signal in a different pulse sequence; when field E_b is scanned in time and arrives before fields E_a and E_c we measure stimulated photon echo dynamics.[81,87,107]

The fourth group of diagrams in Figure 4.2d corresponds to observation of signal for negative time delays (or PS-II), *i.e.* when field E_c precedes the other two fields (see bottom of Figure 4.1 corresponding to the RTG pulse sequence). The first step in these two diagrams is the formation of a coherence (off-diagonal term in the density matrix) $\rho^{(1)}_{eg}(t)$ between the ground and excited states. After a time delay τ a transient grating population is formed by field E_b in the ground $\rho^{(2)}_{g'g}(t)$ or excited $\rho^{(2)}_{ee'}(t)$ states. The signal is created when E_a induces a polarization after time τ_{ab} following the formation of the transient grating. Notice that diagrams $\mathbf{cb_g}$ and $\mathbf{cb_e}$ are identical to $\mathbf{ab_g}$ and $\mathbf{ab_e}$ except

for th

(PS-I

exci

grou

cohe

invo

liter

cor

co

re

be

tir

da

th

th

fi

n

e

li

d

n

for the labeling of fields E_a and E_c and thus the relative time ordering of τ. Unlike TG (PS-I) measurements where the signal reveals the population dynamics in the ground or excited states, RTG (PS-II) measurements reveal an electronic coherence between the ground and excited states. Note that both $\mathbf{cb_g}$ and $\mathbf{cb_e}$ diagrams apply for $\tau_{ab} \geq 0$. The coherence signal decays according to the electronic dephasing time between the states involved, *i.e.* a T_2 type measurement. In most cases T_2 is very different than T_1, the lifetime of the excited state.[81]

The observation of coherence dynamics for negative time delays (or PS-II) is not common to all FWM experiments because it depends on the phase-matching configuration, on the polarization of the three incident fields, and on the existence of a resonant or near-resonant state. For experimental arrangements where all three incident beams are in one plane, the direction of the signal wave vector for positive and negative time delays, determined by the phase-matching geometry, may be different.[169] The detection geometry can be used to discriminate a particular phase-matching geometry. In the forward box arrangements, negative time delay signal is possible (see Figure 1.2) for the pulse sequence discussed here and for other sequences.[68,70] When the three incident fields have the same polarization, as in the near-resonant experiment discussed here, the negative time delay signal can be observed. For cases involving non-resonant excitation, excitation of repulsive states, or condensed-phase measurements, a very short coherence lifetime ($\sim 10^{-14}$ s) is expected. Therefore, little or no dynamics are observed for time delays exceeding the laser pulse duration for these systems. Additional discussion on the negative time delay signals can be found in References 85,170 and 171.

A different diagram classification than the one discussed so far is possible. Notice that for diagrams $\mathbf{ba}_g$, $\mathbf{ba}_e$, $\mathbf{bc}_e$ and $\mathbf{bc}_g$, the first step involves formation of a coherence $\rho^{(1)}_{ge}$. The time evolution of the coherence involves dephasing processes. The dephasing dynamics can be reversed by interaction with the third electric field forming $\rho^{(3)}_{eg}$. This reversal, analogous to the $\pi/2$ pulses in nuclear magnetic resonance (NMR), leads to the formation of an echo. Photon echo measurements are extremely useful in the measurement of coherence life times and have been used primarily in the study of relaxation dynamics in condensed phases. For reviews on these studies see References 172 and 173. These types of measurements require a controlled arrival of field E_b with respect to fields E_a and E_c. Experiments of this kind involving different pulse sequences have been carried out in our group recently and will be published elsewhere.[107,109]

4.2.3. Off-Resonant Excitation

Far from resonance both RWA $\left(\Omega_{eg}-\omega_j\right)$ and anti-RWA $\left(\Omega_{eg}+\omega_j\right)$ terms become comparable making the selection of the active Feynman diagrams more difficult. For the particular arrangement discussed here with fields E_a and E_b overlapped in time, diagrams $\mathbf{ab}_g$ and $\mathbf{ba}_g$ in Figure 4.2 illustrate the nonlinear processes responsible for the off-resonant transients. The general principle hinges on impulsive excitation of rotational and vibrational states in the ground state. The polarizability response function of isolated molecules for off-resonant excitation can be expressed as a combination of correlation functions of the effective polarizability of the molecule $\tilde{\alpha}$,[174]

where

The pol

with res

The firs

isotropi

$\beta \equiv (\alpha$

polariz

leads t

vibrati

zero in

equilib

therefo

where

consta

orient

contri

$$\chi^{(3)}(t) = \chi_{\alpha\alpha}(t) = \left\langle \frac{i}{\hbar}[\tilde{\alpha}(t), \tilde{\alpha}(0)] \right\rangle \tag{4.4}$$

where $\chi_{\alpha\alpha}$ is the linear response function associated with the molecular polarizability. The polarizability tensor can be expressed by expanding each element in a Taylor series with respect to the normal coordinates of vibration q_i as

$$\tilde{\alpha} = \tilde{\alpha}_0 + \sum_{i=1}^{3n-5 or 3n-6} \left[\frac{\partial \tilde{\alpha}}{\partial q_i}\right]_0 q_i + \frac{1}{2} \sum_{i,k}^{3n-5 or 3n-6} \left[\frac{\partial^2 \tilde{\alpha}}{\partial q_i \partial q_k}\right]_0 q_i q_k + \cdots \quad . \tag{4.5}$$

The first term corresponds to the equilibrium polarizability and can be separated into its isotropic and anisotropic contributions by using the definitions $\alpha \equiv \frac{1}{3}(\alpha_{\parallel} + 2\alpha_{\perp})$ and $\beta \equiv (\alpha_{\parallel} - \alpha_{\perp})$. Here $\alpha_{\parallel}$ and $\alpha_{\perp}$ are the parallel and perpendicular components of the polarizability with respect to the principal symmetry axis of the molecule. This separation leads to two contributions. The equilibrium isotropic term, having no orientation or vibrational dependence, does not contribute to the observed dynamics except for a time-zero instantaneous response (*vide infra*). The second contribution, corresponding to the equilibrium anisotropic polarizability, depends on the molecular orientation and is therefore responsible for the rotational component which has been expressed as

$$\chi^{R}(t) = -\frac{4N\beta^2}{45k_B T} \frac{\partial}{\partial t} \left\langle P_2[\cos\theta(t)] \right\rangle, \tag{4.6}$$

where N denotes sample density, T is the sample temperature, and k_B is the Boltzmann constant.[174-176] For spherically symmetric molecules having $\beta = \alpha_{\parallel} - \alpha_{\perp} = 0$, the pure orientational contribution vanishes. Note that the derivative arises from the fact that contributions to the time-dependent polarizability are purely imaginary for off-resonant

excitation (purely real in the frequency domain). The above expression is relevant for the case discussed here where all beams are linearly polarized in the same direction. Different polarization arrangements are discussed elsewhere.[84,174,175] By expressing the ensemble average and the second-order Legendre polynomial as done by Zewail and coworkers,[21,32,33] the last term in Equation (4.6) can be evaluated using

$$\frac{d}{dt}\left\langle P_2\left[\cos\theta(t)\right]\right\rangle = \frac{d}{dt}\frac{\sum_J P(J)\frac{1}{2}\left[3\cos^2\omega_J t - 1\right]}{\sum_J P(J)} = -\frac{3}{2}\frac{\sum_J P(J)\ \omega_J \sin 2\omega_J t}{\sum_J P(J)} \quad . \tag{4.7}$$

The effects on the rotational recurrences caused by nuclear spin and centrifugal distortion are discussed in the Results section.

The second term in Equation (4.5), corresponding to the derivative of the polarizability in terms of the vibrational coordinates, can be expanded in terms of isotropic and anisotropic contributions. This separation yields[174]

$$\chi_{iso}(t) = \sum_{i=1}^{3n-5\,or\,3n-6}\left[\frac{\partial\alpha}{\partial q_i}\right]_0^2\left\langle\frac{i}{\hbar}\left[q_i(t), q_i(0)\right]\right\rangle \text{ and} \tag{4.8a}$$

$$\chi_{aniso}(t) = \left\langle P_2\left[\cos\theta(t)\right]\right\rangle\sum_{i=1}^{3n-5\,or\,3n-6}\left[\frac{\partial\beta}{\partial q_i}\right]_0^2\left\langle\frac{i}{\hbar}\left[q_i(t), q_i(0)\right]\right\rangle \tag{4.8b}$$

where the first-order expansion terms are given by $\left[\partial\alpha/\partial q_i\right]_0$ and $\left[\partial\beta/\partial q_i\right]_0$ at the equilibrium internuclear separation. Both of these expressions give the ro-vibrational dependence of the polarizability. The different isotropic and anisotropic contributions for each normal mode can be sorted by experiments that are sensitive to the polarization of the signal beam for different incoming polarizations.[53,78,84,164,177-183] The focus of our study is on the molecular dynamics; no effort has been made to sort the isotropic and anisotropic components as shown in Equations (4.8a) and (4.8b).

Because the correlation function for a coherent superposition of vibrational modes is sinusoidal in time, the vibrational contribution $\chi^v(t)$ of Equations (4.8a) and (4.8b) can be modeled as a summation of sine functions,[42]

$$\chi^v(t) = \sum_{i=1}^{3n-5 or 3n-6} B_i \sin\left(\omega_i t + \phi_i\right) \tag{4.9}$$

where B_i and ϕ_i are time independent constants for the i^{th} vibrational mode and ω_i is the fundamental frequency of the i^{th} normal mode. Notice that in Equation (4.9) we have omitted the orientational term due to the anisotropic susceptibility in Equation (4.8b). We have also omitted the anharmonic contributions that result from the higher-order terms in Equation (4.5). For the different samples studied here, we found this level of approximation to be satisfactory. Additional terms can be introduced when the harmonic approximation is not sufficient to model the experimental data. The amplitude and phase of each vibrational motion in the ground or excited state are left as fitting parameters to be determined during the analysis of the experimental data. Thus by combining the rotational and vibrational contributions, the overall expression for $\chi_{\alpha\alpha}(t)$ becomes

$$\chi_{\alpha\alpha}(t) = \sum_{i=1}^{3n-5 or 3n-6} B_i \sin(\omega_i t + \phi_i) + \beta^2 \frac{\sum_J P(J)\ \omega_J \sin 2\omega_J t}{\sum_J P(J)}. \qquad (4.10)$$

Equation (4.10) reflects a separation of rotational and vibrational contributions to the anisotropy (at least to first order approximation), a fact that has long been recognized in Raman spectroscopy.[184,185] For time-resolved FWM experiments with homodyne detection, Equation (4.10) leads to cross terms between the rotational and vibrational contributions as will be shown later. Heterodyne detection would give a signal proportional to $P^{(3)}(\mathbf{k}_s,t)$ rather than its square, which would be free from cross-terms of the kind referred to above.[78,176] It is interesting to note that for time-resolved pump-probe experiments the rotational and vibrational contributions are multiplied.[21,32,33] The purely rotational component of the signal is typically isolated by the use of the anisotropy measurement as defined in Chapter 3. For example, Equation (3.2) indicates that the orientation dependence multiplies the isotropic molecular dynamics.[32,33,123] For the time-resolved FWM presented here, we demonstrate that this multiplication is not applicable for the separation of isotropic and anisotropic contributions to the signal.

For polyatomics, if the polarizability varies as the atoms are displaced collectively along a given normal coordinate, the normal mode is observable by its contribution to $\chi^V(t)$. For linear triatomics of the type ABA, the symmetric stretch satisfies this condition while the antisymmetric stretch and the bend do not. The latter modes are infrared active but are not Raman active. In general, Raman active modes can be observed by four-wave mixing techniques. This point is illustrated in the result section for HgI_2.

The vibrational selection rules for Raman transitions are determined by integrals of the form

$$\int \psi_{v'}^{*} \alpha_{g,g'} \psi_{v''} d\tau \tag{4.11}$$

where g, g' = x, y, or z, $\alpha_{g,g'}$ is one of the components of the polarizability, and $\psi_{v'}$ and $\psi_{v''}$ refer to the vibrational wave functions in the initial and final states, respectively.[186,187] These integrals vanish unless the vibrational normal mode involved belongs to the same representation as one or more of the six components of the polarizability tensor of the molecule, *e.g.* α_{xx}, α_{xy}.[188] The rotational Raman selection rule is that the molecule must be anisotropically polarizable (*i.e.* $\beta = \alpha_{\parallel} - \alpha_{\perp} \neq 0$). In addition, for linear molecules ΔJ equals 0, ±2 and for nonlinear molecules ΔJ can equal 0, ±1, ±2.[186]

The observation of rotational and vibrational dynamics for off-resonant measurements depends on the impulsive excitation of vibrational and rotational levels in the ground state, which are overlapped by the frequency bandwidth of the laser pulse. When the vibrational period is shorter than the coherence time of the laser pulse or when all molecules are not vibrating in-phase, the nonlinear response averages to zero and does not contribute to the overall signal. The short pulses employed in this study are nearly transform limited and have a pulse width of approximately 50 fs. The availability of 5 fs

laser pulses[30,189] will extend these types of studies by opening the possibility for observing the real-time dynamics of all but C–H, N–H and O–H chemical bonds.

Equation (4.10) gives a satisfactory expression for the susceptibility that can be convolved by the electric fields and squared according to Equations (4.1) and (4.2) in order to simulate the data. However, in the impulsive limit, when the laser pulse width can be neglected in comparison to the rotational and vibrational periods, the electric field envelopes can be treated essentially as Dirac-delta functions and the FWM signal intensity simply reduces to[78]

$$I_{FWM}(\tau) = \left|\chi_{\alpha\alpha}(\tau)\right|^2. \tag{4.12}$$

In FWM experiments, when all three fields are present near time zero, a condition of temporal degeneracy arises. During this time multiple nonlinear processes occur. The observed signal enhancement near time zero, arising from the coherent interaction of the three light fields with the medium, has been called the coherence coupling artifact or the coherence spike.[52,78,190-192] The coherent spike is typically symmetric about time zero and in many cases can be removed by the antisymmetrization technique described by Eisenthal, Fleming and their coworkers.[192,193] In the absence of chirp, the coherent spike can be described as the square of the electric field autocorrelation of the incident laser pulses. This is because the major contribution comes from the equilibrium isotropic polarizability (α_0) which has an instantaneous response limited to when the three fields are overlapped in time. For most femtosecond measurements this feature can be approximated by a Gaussian or hyperbolic-secant-squared function. Thus, by considering

the coherent spike as a Gaussian function with amplitude A primarily depending on α_0 and using Equations (4.10) and (4.12), the FWM signal intensity can be modeled as

$$I_{FWM}(\tau) = \left| Ae^{-\tau^2/\Delta^2} + \sum_{i=1}^{3n-5 or 3n-6} B_i \sin(\omega_i \tau + \phi_i) + C\beta^2 \frac{\sum_J P(J)\ \omega_J \sin 2\omega_J \tau}{\sum_J P(J)} \right|^2 \tag{4.13}$$

where Δ corresponds to the full-width at half-maximum (FWHM) of the coherence time of the laser pulses, *i.e.* the pulse width divided by $2\sqrt{\ln 2}$ (for Gaussian pulses) and C is a proportionality constant.[194] For most cases convolution by the temporal response of the laser system can be carried out easily when necessary. This formula is convenient for the analysis of off-resonance TG data. Note that we have not included the inverse-squared dependence of the off-resonance signal on temperature.

This formulation allows the quantitative interpretation of the vibrational and rotational characteristics of the TG off-resonant signals obtained. Atomic species exhibit signals exclusively at time zero because of their instantaneous polarizability. Diatomics and polyatomics exhibit, for positive time delays, ground state rotational (as long as $\beta \neq 0$) and vibrational dynamics. The vibrational modes must be Raman active and have a vibrational period that is longer than the coherence time of the laser system to be observed. In the results and discussion section, experimental data is presented to illustrate the different cases discussed. Of particular interest is the experimental observation of the cross terms that arise upon squaring the sum of rotational and vibrational contributions to

th

FV

ob

be

an

4.2

grou

pola

diag

(PS-

I) bo

are g

molec

the s

molec

studie

researc

study o

the signal according to Equation (4.13). As we will demonstrate later, the off-resonance FWM transients show rotational recurrence features that are quite different from those observed by laser induced fluorescence (LIF).[21,32,33,120,195] Most of the differences can be explained in terms of the modulus square and the time derivative in Equations (4.1) and (4.6).

4.2.4. Resonant Excitation

We now turn our attention to the types of molecular dynamics that are observed in ground and excited states and how they are manifested in the induced molecular polarization with resonant FWM. From the discussion in Section 4.2.2 (Feynman diagrams), we know to expect ground and excited state signal at both positive time delays (PS-I) and negative time delays (PS-II). For resonant TG experiments (or when using PS-I) both ground state and excited state wave packets are formed. The rotational dynamics are given by the time-dependent evolution of the population excited at $t = 0$. The molecular orientations are averaged starting with the usual classical expression based on the second Legendre polynomial $P_2[\cos\theta(t)]$ where $\theta(t)$ is the angle between the molecular axis at time t and that at time zero.[124] This evolution has been extensively studied in the time domain for pump-probe time-resolved gas-phase studies by Zewail's research group.[21,32,33] A simple semiclassical expression can be used for the quantitative study of the orientational dependent susceptibility and is given by

wher

and

2=[4

molec

each

groun

Anhar

frequer

observ

square

Therefo

$$\chi^R(t) = \frac{\sum_J P(J)\ \frac{1}{2}(3\cos^2\omega_J t - 1)}{\sum_J P(J)} = \frac{\sum_J P(J)\ \frac{1}{4}(1+3\cos 2\omega_J t)}{\sum_J P(J)} \qquad (4.14)$$

where $P(J)$ represents the distribution of rotational levels for the molecules being probed and the rotational frequency ω_J is given by $2\pi[2Bc(J+1)]$ for $\Delta J = \pm 1$ and $2\pi[4Bc(J+3/2)]$ for $\Delta J = \pm 2$ transitions where B is the rotational constant of the molecule.

The vibrational dynamics can be easily modeled by a sum of cosine functions each representing the frequency difference between adjacent vibrational levels of the ground or excited states.[42] The dependence of the susceptibility on vibrational motion is

$$\chi^v(t) = \sum_{i=1}^{3n-5 or 3n-6} B_i \cos(\omega_i t + \phi_i). \qquad (4.15)$$

Anharmonicity of each vibrational mode can be included by explicitly adding the frequency of all overtones that are populated in the excitation process. Note that the observation of real-time vibrations hinges on the frequency bandwidth of the laser pulses.

In the limit of very short laser pulses, the resonant FWM signal is equal to the square of the sum of the different components of the susceptibility (*vide supra*). Therefore, the third-order resonant TG signal is of the form

$$I_{Resonant}(\tau)=\left|Ae^{-\tau^2/\Delta^2}+\sum_{i=1}^{3n-5or3n-6}B_i\cos(\omega_i\tau+\phi_i)+C\beta^2\frac{\sum_J P(J)\ \frac{1}{4}(1+3\cos 2\omega_J\tau)}{\sum_J P(J)}\right|^2 \tag{4.16}$$

where A is the amplitude of the time-zero feature that is caused by a contribution from all eight diagrams in Figure 4.2. The second and third terms correspond to vibrational and rotational contributions to the signal. Note that both ground and excited states have to be taken into account for the resonant TG measurements.

For RTG measurements (or when using PS-II), the dynamics probed involve a coherence between the ground and excited states as discussed earlier. However, based on the Condon approximation,[78] applicable for resonance excitation only, one can demonstrate that the signal from RTG measurements tracks primarily the excited state. For reverse transient gratings, the signals can be modeled by Equation (4.16) given for TG measurements. The contribution for the excited state is expected to be about an order of magnitude greater than that of the ground state. An additional term needs to be added to account for the electronic dephasing time T_2 which is long in the gas phase (10^{-12}-10^{-9} s) and very short in condensed phases (10^{-15}-10^{-13} s).

4.2.

4.2.5. Controlling Observation of Molecular Dynamics in Iodine

For the resonant excitation of iodine, we used two different pulse sequences PS-I and PS-II (see Figure 4.1) to investigate the differences in the observed molecular dynamics when fields E_a and E_b are separated in time. We continue to detect signal in the phase-matching direction $\mathbf{k}_s = \mathbf{k}_a - \mathbf{k}_b + \mathbf{k}_c$. For PS-I (fixed time delay between E_a and E_b followed by E_c at a variable time delay), when $\tau_{ab} > 0$, only nonlinear processes shown in diagrams $\mathbf{ab_e}$ and $\mathbf{ab_g}$ in Figure 4.2 are possible. When $\tau_{ab} > 0$ for PS-II (E_c arriving at a variable time delay before E_b which is followed by E_a at a fixed time delay), only nonlinear processes represented in diagrams $\mathbf{cb_e}$ and $\mathbf{cb_g}$ in Figure 4.2 are possible. Our goal is to find the proper selection of τ_{ab} that would yield signal predominately from the excited state (*i.e.* $\mathbf{ab_e}$ or $\mathbf{cb_e}$) or from the ground state (*i.e.* $\mathbf{ab_g}$ or $\mathbf{cb_g}$). We also explore which pulse sequence allows more control over obtaining molecular dynamics predominately from one state.

A more complete description of the density matrix theory that describes the control of the molecular dynamics can be found in Reference 103. The density matrix elements after two electric field interactions contain a dependence on τ_{ab} and this parameter can be used to control the transition probability from the ground to the excited state.[103,105,106] After the second pulse is applied, the population transfer between the ground and excited states is given by

$$\sum_e \rho_{ee}^{(2)} - \sum_g \rho_{gg}^{(2)} \propto \cos\left(\frac{\omega_e \tau_{ab}}{2}\right)\cos\left(\frac{\omega_g \tau_{ab}}{2}\right)\cos\left(\omega\tau_{ab} - (\mathbf{k_a} - \mathbf{k_b})\mathbf{r}\right) \qquad (4.17)$$

where ω_g and ω_e are the vibrational frequencies of the ground and excited states, respectively. After the third pulse is applied at time $\tau_{ab} + \tau$, the signal is a sum of two contributions – one from molecules that remain in the ground state after two interactions with the electric fields,

$$S_g \propto \sum_{\substack{g,g' \\ g \neq g'}} \left| \tilde{\rho}_{gg}^{(2)} - \tilde{\rho}_{g'g}^{(2)} \right|^2 \propto \left(1+\cos\left(\omega_e \tau_{ab}\right)\right)\left(1+\cos\left(\omega_g \tau\right)\right), \qquad (4.18a)$$

and the other from molecules in the excited state,

$$S_e \propto \sum_{\substack{e,e' \\ e \neq e'}} \left| \tilde{\rho}_{ee}^{(2)} + \tilde{\rho}_{ee'}^{(2)} \right|^2 \propto \left(1+\cos\left(\omega_g \tau_{ab}\right)\right)\left(1+\cos\left(\omega_e \tau\right)\right), \qquad (4.18b)$$

where $\tilde{\rho}^{(2)}$ indicates only the terms of $\rho^{(2)}$ that satisfy our phase-matching condition. If we define $\tau_e = 2\pi/\omega_e$ (and $\tau_g = 2\pi/\omega_g$), at a time delay $\tau_{ab} = \tau_e(n+½)$, the signal for the ground state goes to zero. When $\tau_{ab} = \tau_e n$, the signal for the ground state reaches a maximum. Similarly $\tau_{ab} = \tau_g(n+½)$ and $\tau_{ab} = \tau_g n$ correspond to minimum and maximum signal from the excited state, respectively. Maximum control can be achieved for values of τ_{ab} that maximize one contribution and, at the same time, minimize the other. These values can always be found provided $\omega_g \neq \omega_e$. In the Results section, we will show that the time delay τ_{ab} can be used to discriminate among the processes that lead to the observation of ground state or excited state dynamics.

4.3. EXPERIMENTAL

For more specific details on the four-wave mixing method, see Chapter 2. Experiments were carried out on 30-760 Torr on gas-phase samples (or neat vapors for liquid samples) at room temperature unless otherwise noted. Three 622 nm beams were crossed in the forward box geometry producing a signal beam at the upper right corner of the box, identified by the wave vector $\mathbf{k}_s = \mathbf{k}_a - \mathbf{k}_b + \mathbf{k}_c$, which we collected. For most of our samples, we made off-resonant measurements. Iodine was the only sample that underwent resonant excitation with 622 nm incident light. The three beams were either fixed in time (E_a) or variable in time - either manually (E_b) or computer controlled (E_c) as described earlier. Sweeping the time delay between field E_c and the other two fields yielded transients reflecting the temporal evolution of the dynamics. Typical transients were obtained with 150-200 different time delays and 10-20 scans were averaged.

4.4. RESULTS AND DISCUSSION

4.4.1. Off-Resonance Excitation

4.4.1.1. Atomic Response

Transient grating data have been obtained for the atomic species argon and xenon at 1 atm pressure. The results are presented in Figure 4.3. A single peak is observed in each scan which can be fit by a Gaussian function with the center at zero time delay and with a FWHM of 131 fs for Ar and 139 fs for Xe corresponding to the third-order auto correlation of our laser system. The FWM response of these samples is only present while the three laser pulses are temporally overlapped. At time zero, the intensity of the FWM signal from Xe is about 14 times stronger than that from Ar. The ratio between the linear polarizabilities of Xe and Ar is about 2.45.[196-198] This ratio appears to indicate a cubic dependence on the linear polarizability (α) for the time-zero signal. The signal observed at time zero results from a non-resonant instantaneous polarizability. The absence of signal away from time zero is to be expected in spherically symmetric samples and in the absence of vibrations (see Equation (4.13)).

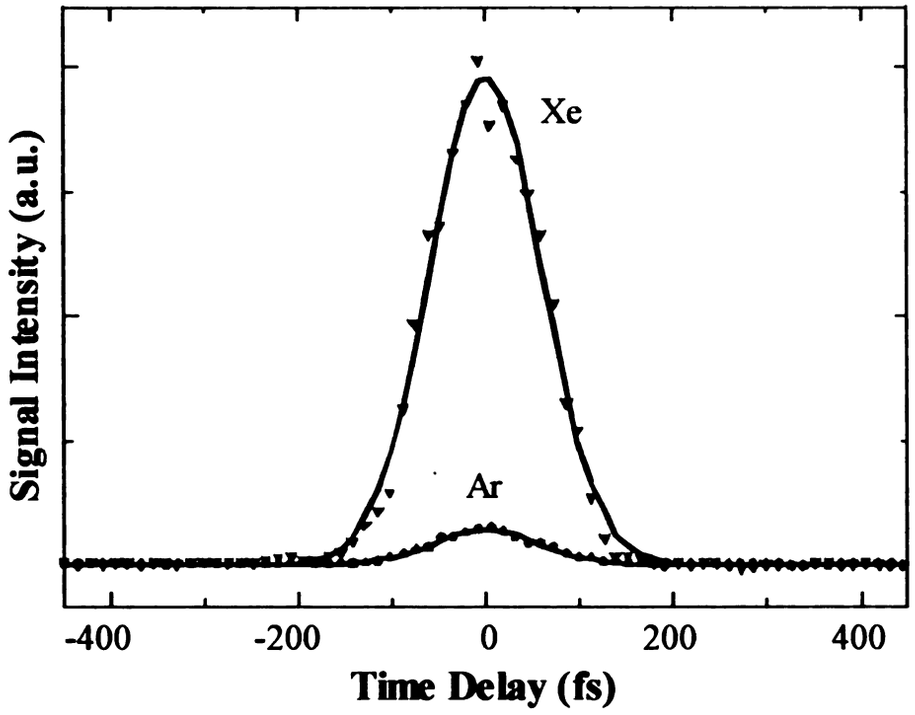

Figure 4.3. FWM signal from xenon and argon samples at 1 atm pressure. The data are represented by triangles for Xe and by circles for Ar. The black lines show Gaussian fits to the data. FWM signal from Xe is 14 times greater than from Ar because of the increase in polarizability of Xe over Ar. The width of the Gaussian fits for Ar is 131 fs and 139 fs for Xe.

4.4.1.2. Rotational Contribution

The data in Figure 4.4 (top) show the TG signal obtained for air. The nonlinear process responsible for the signal are illustrated in diagrams $\mathbf{ab}_g$ and $\mathbf{ba}_g$ in Figure 4.2a. The features in the air transient are interpreted as the rotational recurrences[37] of the constituent molecules of air.[199] TG transients for pure nitrogen and for pure oxygen molecules, each at 1 atm pressure, were also taken. The results are also presented in Figure 4.4 (middle and bottom) for comparison. Based on the rotational constants of nitrogen and oxygen (2.010 and 1.44566 cm^{-1} respectively) and the $\Delta J = \pm 2$ selection

rule, full recurrences are expected and are observed at 4.15 and 5.77 ps intervals respectively. Recurrences have a period of $(2\omega_J)^{-1}$; thus, half recurrences are expected at intervals $1/(8Bc)$ and full recurrences at $1/(4Bc)$. The alternation in heights between the half and full recurrences are caused by nuclear spin statistics. Whenever there is an interchange of equivalent nuclei in a rotation, the Pauli principle defines that only certain rotational states are populated. For molecules with a $\sum_g^+$ ground state, the ratio of the population of odd J states to the population of even J states (nuclear statistics) is defined by $(I+1)/I$ for fermions and by $I/(I+1)$ for bosons where I is the nuclear spin.[186] Therefore, for N_2 with integral spin equal to one, even J states are populated twice as much as odd J states. The nuclear spin of O_2 is zero. However, because the ground state of O_2 is $\sum_g^-$, only odd J states are populated; whereas, for CS_2 with zero nuclear spin and ground state $\sum_g^+$, only even J states are populated.

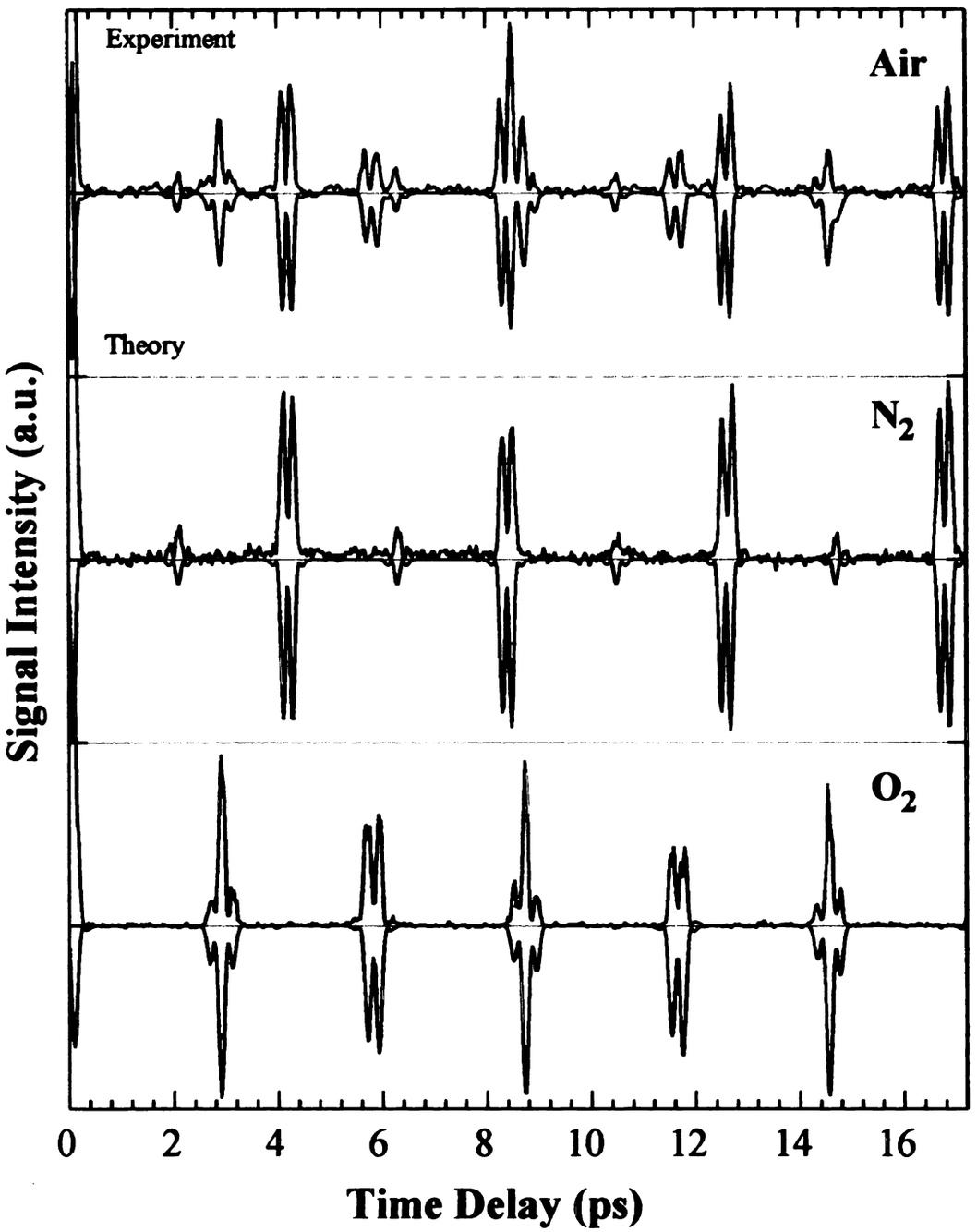

Figure 4.4. Experimental (positive) and theoretical (negative) TG transients of air, nitrogen, and oxygen. Full rotational recurrences are observed at 4.15 ps for N_2 and at 5.77 ps for O_2. Half recurrences are also observed. The peaks in the air transient directly correspond to recurrences in the N_2 and O_2 scans. Simulated TG signals for these samples were calculated using Equation (4.13) and are shown as the negative mirror image of the experimental data. Note that in the simulations, the full and half recurrences are reproduced at the same recurrence times and with the same intensity and shape as in the experimental signal.

All features in the transient in Figure 4.4 can be identified and simulated using Equation (4.13). In Figure 4.4 the simulations appear as negative reflections of the experimental transients in the top, middle and bottom sections. As can be seen in the figure, Equation (4.13) predicts the rotational recurrences for N_2 and O_2 and the relative peak heights and shape in each half and full recurrence accurately. Because of the square in Equation (4.13), TG transients look very different from LIF measurements.[21,32,33] By adding the simulated transients of N_2 and O_2, the experimental TG signal from air is reproduced.

Time-resolved TG experiments on carbon disulfide, CS_2, (300 Torr) yielded several transients showing multiple rotational recurrences, as depicted in Figure 4.5. This molecule has been studied extensively using nonlinear techniques because of its high degree of nonlinear polarizability.[46,200-207] Its $\chi^{(3)}$ is 23×10^{-14} esu.[208] Heritage and coworkers observed short birefringence at 38 and 76 ps after excitation with a picosecond pulse and verified these positions for CS_2 theoretically.[46,209] The data in Figure 4.5 allow accurate molecular constants to be extracted for this molecule. As can be seen, the half recurrence appears at 38.2 ps and the full recurrence occurs at 76.4 ps. For O_2, N_2, and CS_2, it is important to include centrifugal distortion in Equation (4.13) to reproduce the TG signal well. In these cases, ω_J is replaced by $2\pi c[(4B-6D)(J+\frac{3}{2})-8D(J+\frac{3}{2})^3]$ where D is the centrifugal distortion constant. From the positions of the first two rotational recurrences, the rotational constant, B = 0.10912 ± 0.00002 cm^{-1}, and centrifugal distortion constant, $D = 6.4 \times 10^{-9} \pm 0.2 \times 10^{-9}$ cm^{-1}, are obtained for CS_2. The effective rotational constant, before the centrifugal distortion effect is incorporated, is

0.10907 ± 0.00002 cm^{-1}. From the literature, the rotational constant for CS_2 is 0.10910 cm^{-1} and the centrifugal distortion is $1.0x10^{-8}$ cm^{-1}.[210]

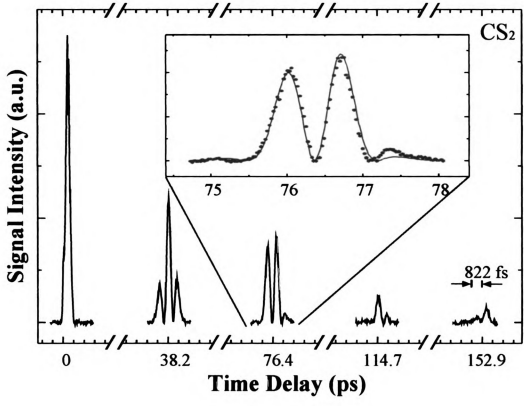

Figure 4.5. TG transient of carbon disulfide. The half and full rotational recurrences are observed at 38.2 and 76.4 ps respectively. The inset shows a magnification of the first full rotational recurrence (circles) with the simulation calculated using Equation (4.13) (solid line). Notice that the x-axis is not continuous; there are 30 ps gaps between each recurrence and the tick size is 822 fs for each expanded region. The decrease in signal as a function of time delay gives the overall rotational dephasing due to inelastic collisions (see text).

The determination of highly accurate rotational constants for polyatomic species by time-resolved coherence techniques is by now a well-known method (see for example References 37 and 42). Because these data were obtained over hundreds of picoseconds using a 10 inch long translation stage with a resolution of 0.2 μm/step, the equivalent

resolution in time delay can be estimated to be about one part per million. In principle, this resolution translates into measurements of rotational constants with six significant digits. To experimentally achieve this accuracy, it is important to meticulously align and calibrate the translation stage, interferometrically or with a well-known standard, and to take into account the index of refraction of air at the wavelength of the laser fields.

The inset in Figure 4.5 also shows a simulation of the first full recurrence calculated with Equation (4.13) and the parameters obtained above. As can be seen in the figure, Equation (4.13) reproduces the experimental signal well, missing only in the height of the last undulatory feature. The amplitude of the rotational recurrences in Figure 4.5 was found to decrease exponentially. A fit to the average intensity of the rotational recurrences gives a single exponential decay corresponding to a dephasing time of 62 ± 5 ps. By comparison, using Raman-induced polarization spectroscopy (RIPS) Chen and coworkers obtained dephasing times of 175 ps and 154 ps for the smaller molecules O_2 and N_2 respectively.[199] The observed decay time for CS_2 implies a cross section for rotational dephasing of 4 nm^2 equivalent to a 11.3 Å diameter assuming hard sphere collisions.[199] This cross section appears to be very large and to depend on the rotational angular momentum, leading to the distortion of the rotational recurrences that is not accounted by the centrifugal term, especially those at later times in Figure 4.5. This J dependent coherence relaxation is similar to the recent work on SF_6 published by Vasilenko *et. al.*[211] A study of the inelastic collisions leading to the rotational coherence dephasing based on measurements at different pressures seems warranted.

4.4.1.3. Vibrational Contribution

The TG transient obtained for mercuric iodide, HgI_2, heated to 280°C (150 Torr), is presented in Figure 4.6. Notice that the data contain a strong and broad feature near 500 fs with 211 fs oscillations. This feature is due to the rotational and vibrational coherence prepared in this large triatomic molecule. The Fourier transform of the experimental transient is shown as line (b) in the inset. The top Fourier transform (a) is obtained from the original experimental transient with the time-zero feature removed. As can be seen there are three major features in both transforms – one large peak at 19.7 $\pm$ 0.1 and a set of two peaks at 148.4 $\pm$ 0.2 and 167.9 $\pm$ 0.2 cm^{-1}. These peaks were fit with Gaussian functions to determine the center position and uncertainty. The sloping feature at low frequencies in the raw Fourier transform (b) results from the time-zero coherence artifact; as can be seen in the upper Fourier transform, removing this time-zero spike by subtraction eliminates this sloping background and more clearly shows the three main features. A small peak (157.7 cm^{-1}) between the pair of peaks in (a) seems to appear as a result of removing the coherence artifact spike; this small peak is absent in the raw data Fourier transform. We checked the possibility that this small peak is due to a cross term between the first and second terms in Equation (4.13). Our simulations did not support this argument probably because the equilibrium isotropic polarizability contributes only during the first 150 fs of the data. For experiments using nanosecond broad band lasers, this cross term becomes important.

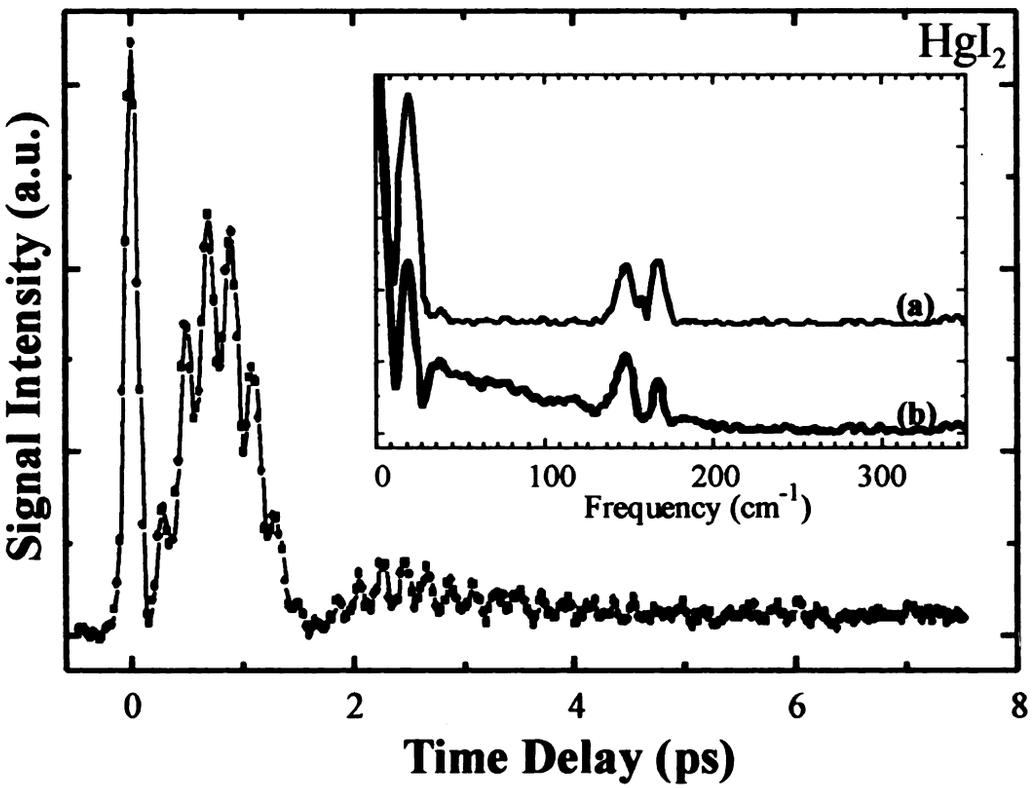

Figure 4.6. Bottom: TG transient of mercury(II) iodide. Ground state vibrations and rotations can clearly be seen in the transient. Inset: The Fourier transform of the experimental transient is shown as line (b). The top Fourier transform (a) corresponds to the experimental transient with the coherence spike subtracted. The symmetric stretch of HgI_2 has a frequency of 158.2 cm^{-1}. The cross term resulting from Equations (4.13) causes the Fourier transform to have peaks corresponding to $2\omega_R$ (19.7 ± 0.1 cm^{-1}), $\omega_V - \omega_R$ (148.4 ± 0.2 cm^{-1}), and $\omega_V + \omega_R$, (167.9 ± 0.2 cm^{-1}) as seen. The $2\omega_V$ peak is probably masked by the high frequencies from the experimental noise because of the low signal to noise ratio.

The frequency exactly between the latter two peaks at 158.2 ± 0.2 cm^{-1} corresponds to the symmetric stretch, 158.4 cm^{-1} determined by gas-phase Raman spectroscopy.[212] Vibrational frequencies have also been obtained for gas-phase HgI_2 using electron diffraction yielding 156 cm^{-1} for the symmetric stretch, 235 cm^{-1} for the antisymmetric stretch, and 49 cm^{-1} for the bending mode.[213] As can be seen in Figure 4.6, frequencies corresponding to the antisymmetric stretch and bending are not observed;

these two modes are not Raman active in a linear triatomic molecule so bands for these normal modes should not be observed for HgI_2. The results from the Fourier transform will be discussed in more detail below.

As was shown above, Equation (4.13) can be used to simulate the rotational dynamics for N_2, O_2, and CS_2. The HgI_2 data allows us to examine the separation of vibrational and rotational components in TG transients where the two are summed and to compare with the analysis of rotational anisotropy in pump-probe transients where the two are multiplied (see theory section). Figure 4.7 shows the HgI_2 experimental data (top), a transient simulated by $\chi_{\alpha\alpha}(t)$ having a vibrational contribution of the formula given in Equation (4.9) added to a rotational component according to Equation (4.6), $\chi_{\alpha\alpha}(t) = \chi^{v}(t) + \chi^{R}(t)$ (middle), and a transient simulated by multiplying the vibrational and rotational components, $\chi_{\alpha\alpha}(t) = \chi^{v}(t)\chi^{R}(t)$ (bottom). As can be seen in the figure, the product of rotations and vibrations produces a series of oscillations that is out-of-phase with the experimental data between 1.7 to 4.5 ps. However, the sum of rotations and vibrations produces a series of oscillations that corresponds in-phase to the vibrational oscillations of the data for all times.

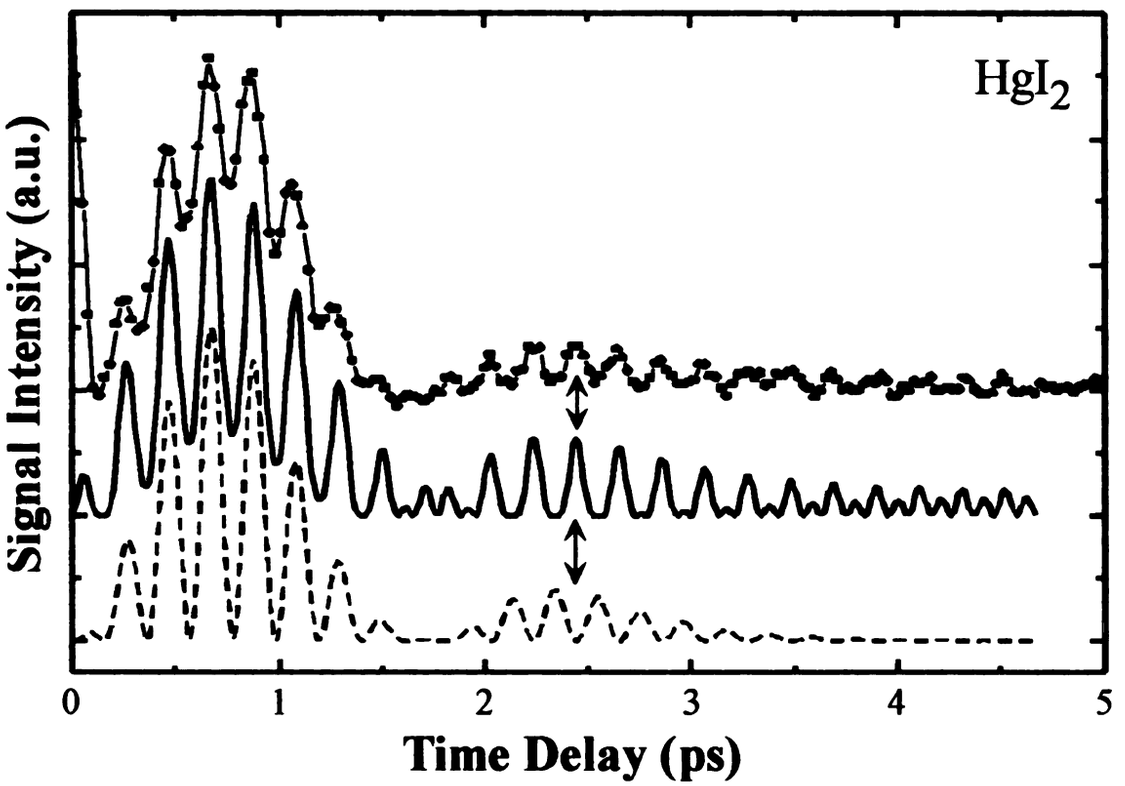

Figure 4.7. Top: Experimental TG transient of HgI_2. Middle: Transient resulting from $\chi_{aa}(t)$ equal to the sum of $\chi^R(t)$ and $\chi^V(t)$. Bottom: Transient resulting from $\chi_{aa}(t)$ equal to the product of $\chi^R(t)$ and $\chi^V(t)$. Notice that the product transient (bottom) is out-of-phase with the experimental data but the summation transient (middle) is in-phase with the experimental data for all times (see text).

The summation of the vibrational and rotational components of the polarizability provides the correct phase relationship in the data because of the cross term that is obtained from the square of the sum of sine functions. As is seen in the bottom simulation in Figure 4.7, the effect of the cross term is to invert the phase of the vibrations near $\tau >$ 1.7 ps and to cause a doubling of the vibrational frequency for $\tau > 3.5$ ps. The Fourier transform shown in Figure 4.6 confirms the validity of this model. The Fourier transform should contain peaks corresponding to $2\omega_v$, $2\omega_R$, $\omega_v + \omega_R$, and $\omega_v - \omega_R$, where ω_R and ω_v

are the average rotational and vibrational frequencies respectively. Note that the square of the summation of cosines also yields a constant term which causes a peak at zero frequency in the Fourier transform as seen in Figure 4.6 for both transforms.

Looking at Figure 4.6, a splitting around the symmetric stretching vibrational frequency (ω_v = 158.2 cm^{-1}) is evident; thus $\omega_v - \omega_R$ (148.4 cm^{-1}) and $\omega_v + \omega_R$, (167.9 cm^{-1}) are obtained. In addition, there is a peak corresponding to $2\omega_R$ (19.7 cm^{-1}) reflecting the 1.7 ps modulation. This corresponds to twice the average rotational frequency that arises from the sum of all the rotational levels (third term in Equation (4.13)). The $2\omega_v$ peak, corresponding to periodic oscillations of 105.4 fs, is not observed. This is probably because of a lack of time resolution as determined by the FWHM of the coherent spike, 138 fs for this transient. It is also possible that χ^v is small compared to the other terms that enter Equation (4.13). The summation of the equilibrium anisotropic polarizability (responsible for rotational dynamics) and the derivative of the polarizability with respect to the vibrational coordinates is consistent with Raman scattering theory.[184,185] The HgI_2 experimental data confirms that the analysis of time-resolved molecular dynamics by TG requires a summation of rotational and vibrational components and this is in contrast to the analysis of time-resolved pump-probe transients.

4.4.1.4. Early time response and comparison to liquid data

The results presented in Figure 4.8 compare the early time TG response for two gem-dihalomethane molecules, CH_2Cl_2 (340 Torr) and CH_2Br_2 (40 Torr). The two transients can be described by a time-zero coherence spike followed by a rotational coherence feature. As expected, based on the rotational moment of inertia, the dichloro compound has a faster rotational dephasing component. The dibromo compound is much slower. In both cases the rotational dephasing and time-zero coherence spike can be simulated using Equation (4.13) and the rotational constants for these compounds are recuperated, 0.12 and 0.050 cm^{-1} for CH_2Cl_2 and CH_2Br_2 respectively. The rotational constants calculated from moments of inertia are 1.1, 0.106 and 0.10 cm^{-1} for CH_2Cl_2 and 0.88, 0.0412 and 0.041 cm^{-1} for CH_2Br_2.[214] The *B* rotational constants for each molecule are close to the values we found; however, because CH_2Cl_2 and CH_2Br_2 are not symmetric tops, the measured rotational constant is a combination of the three rotational constants. From these early time TG signals, we observe that even in the absence of rotational recurrences, the initial dephasing is sufficient to determine the rotational constant of a molecule with two-digit accuracy or the rotational temperature of a known molecule or product of the reaction.

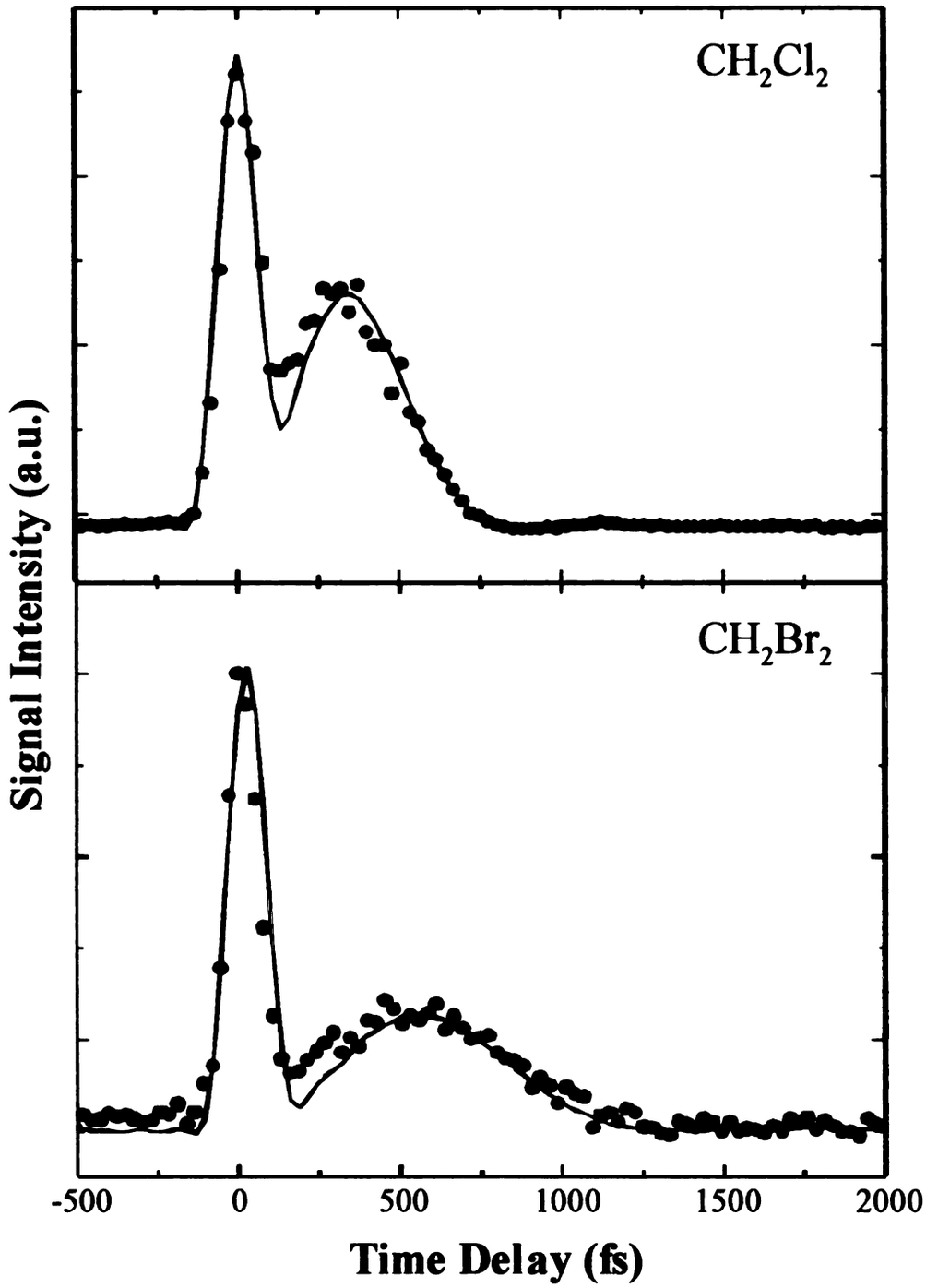

Figure 4.8. TG transients of methylene chloride (upper) and methylene bromide (lower). The experimental data are shown as circles and the simulations calculated using Equation (4.13) are shown by the solid line. In both scans, the time-zero coherence spike is observed and is more intense than the rotational dephasing. As expected, the rotational recurrence is faster in CH_2Cl_2 than in CH_2Br_2.

oscil

confi

moti

meas

bend

in th

polar

respe

0.18

cons

0.19

symm

is no

valu

rotat

agre

In addition to the rotational dephasing, the data on CH_2Br_2 contains a weak oscillatory modulation with a period of 190 fs. The frequency of this oscillation, confirmed by Fourier transformation of the data, corresponds to the Br-C-Br bending motion frequency around 173 cm^{-1}.[215] Impulsive stimulated Raman scattering measurements by Ruhman *et al.* on CH_2Br_2 have demonstrated the persistence of this bending motion for several picoseconds in the liquid phase.[216]

Figure 4.9 compares the early time TG response for larger polyatomic molecules, in this case benzene (90 Torr) and toluene (30 Torr). These molecules are highly polarizable with $\chi^{(3)}$ coefficients of 10.1 and 9.81 $x10^{-14}$ esu for benzene and toluene, respectively.[208] Simulations to the data using Equation (4.13) yield rotational constants of 0.1896 for benzene and 0.146 cm^{-1} for toluene. In the literature, the three rotational constants for benzene are 0.18960, 0.18960 and 0.09480 cm^{-1},[217] and for toluene are 0.19106, 0.08397 and 0.05834 cm^{-1}.[218] Our rotational constant for benzene, an oblate symmetric top, is in excellent agreement with the literature value for *B*. Because toluene is not a symmetric top, the *B* value from the literature is not corresponding well with the value we determined. However, if the reduced moment of inertia is used to calculate the rotational constant for toluene,[214] the rotational constant becomes 0.146 cm^{-1} which does agree well with our value.

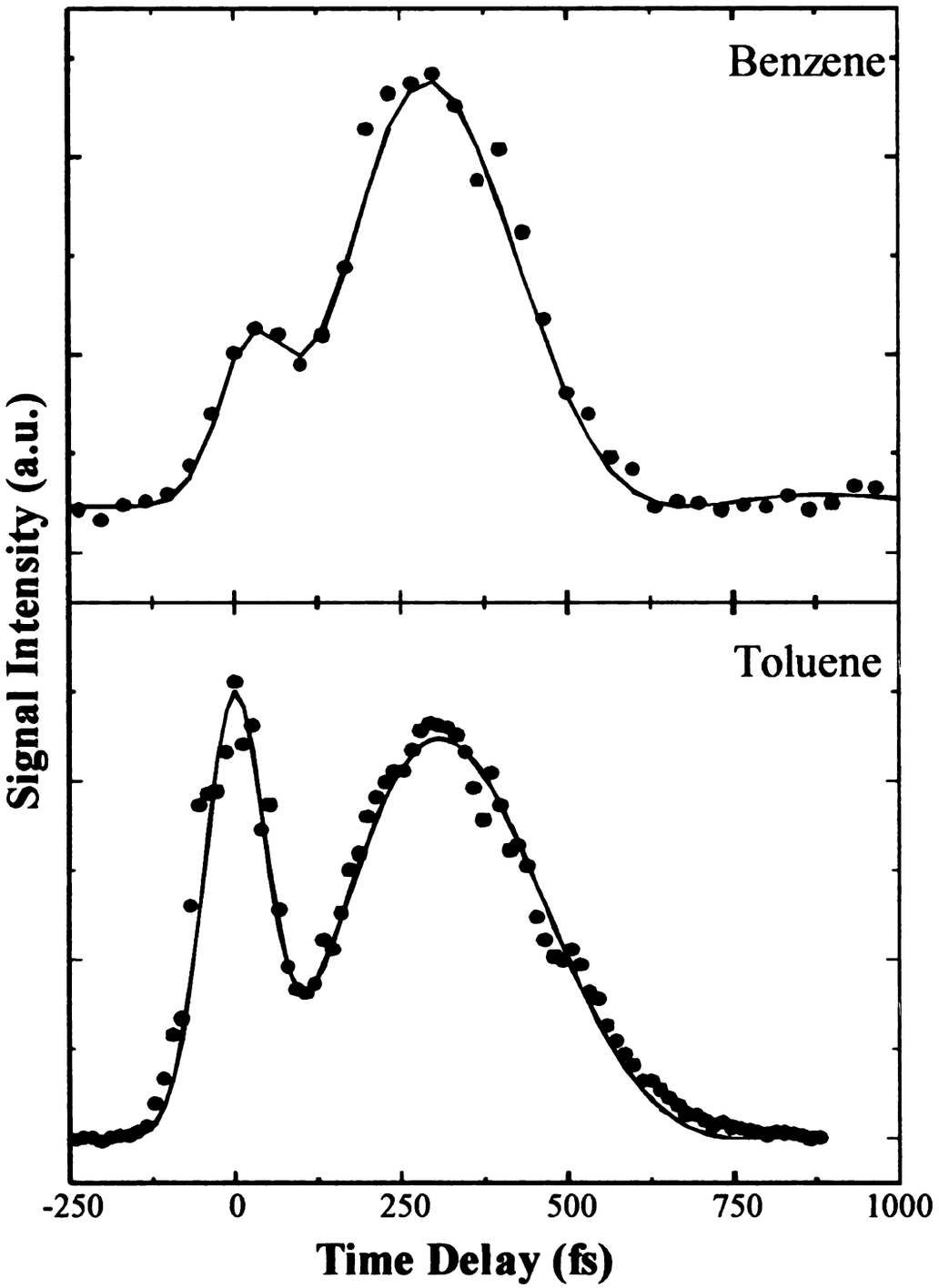

Figure 4.9. TG transients of benzene (upper) and toluene (lower). The experimental data are shown as circles and the solid line shows the simulations from Equation (4.13). The intensity of the rotational dephasing in benzene is stronger than the time-zero spike. However, in toluene the intensities of the rotational recurrence and the time-zero spike are about equal. The rotational recurrence time is similar for both compounds as expected from their rotational constants.

The femtosecond gas-phase CARS measurement by Hayden and Chandler on benzene gives the overall 12 ps rotational dephasing signal.[67] Our transient (in Figure 4.9) gives the early (first 500 fs) dynamics where the initial rotational dephasing is observed; a subsequent oscillation of the rotational coherence has also been observed at 1.2 ps (not shown). The data of Hayden and Chandler show the 1.2 ps feature as well as one at 4 ps and one at 8 ps.[67]

In benzene, the rotational dephasing component of the signal is more intense than the coherent spike at time zero. A similar effect for the relative intensities of time zero and the rotational dephasing was also observed for CS_2 and is expected for molecules with large anisotropic polarizabilities. For toluene, the relative intensities of the coherent spike and the rotational dephasing are about equal. At time zero, the signal results from the coherence coupling artifact through the instantaneous polarizability of the equilibrium isotropic component as well as other combinations of interactions between the three electric fields as discussed in the Theory section; the anisotropic orientational dependence contribution $\chi^R(t)$ in Equation (4.6) is zero at time zero. For positive times, only $\chi^R(t)$ contributes to the TG signal observed for these off-resonant transients. Both normal mode dependent contributions, Equations (4.8a) and (4.8b), average to zero because of the very fast vibrational frequencies in comparison to the coherence length of our laser pulses.

The gas-phase measurements presented in this study provide the isolated molecular response of the material. When compared to condensed-phase measurements, one can immediately recognize the intermolecular influence on the polarizability of the

system

measur

our da

group

semiem

from N

simulati

dephasi

molecul

time con

slow dif

coherenc

has a fast

system. In Figure 4.10 (top) we present both the early time response of gas-phase CS_2 measured in our laboratory and the simulation from Equation (4.13). In order to compare our data with liquid-phase measurements, we have simulated the data from Nelson's group on CS_2 obtained by impulsive stimulated Raman scattering using the same semiempirical formula used to simulate their data.[56,219] This simulation of the liquid data from Nelson's group is presented as the solid line in the bottom of Figure 4.10. In their simulation, three time scales were identified: (i) a fast component due to inhomogeneous dephasing, (ii) a fast emergence of an ensemble of aligned and coherently librating molecules, and (iii) a slow diffusional dephasing of the orientational anisotropy. The fast time constants in the simulation were given 1/e values of 114 and 102 fs respectively, the slow diffusional dephasing was simulated by a time constant of 1.37 ps, and the coherence coupling artifact was ignored.[56,219] It is clear that the condensed-phase data has a fast initial dephasing rate followed by a much slower decaying component.

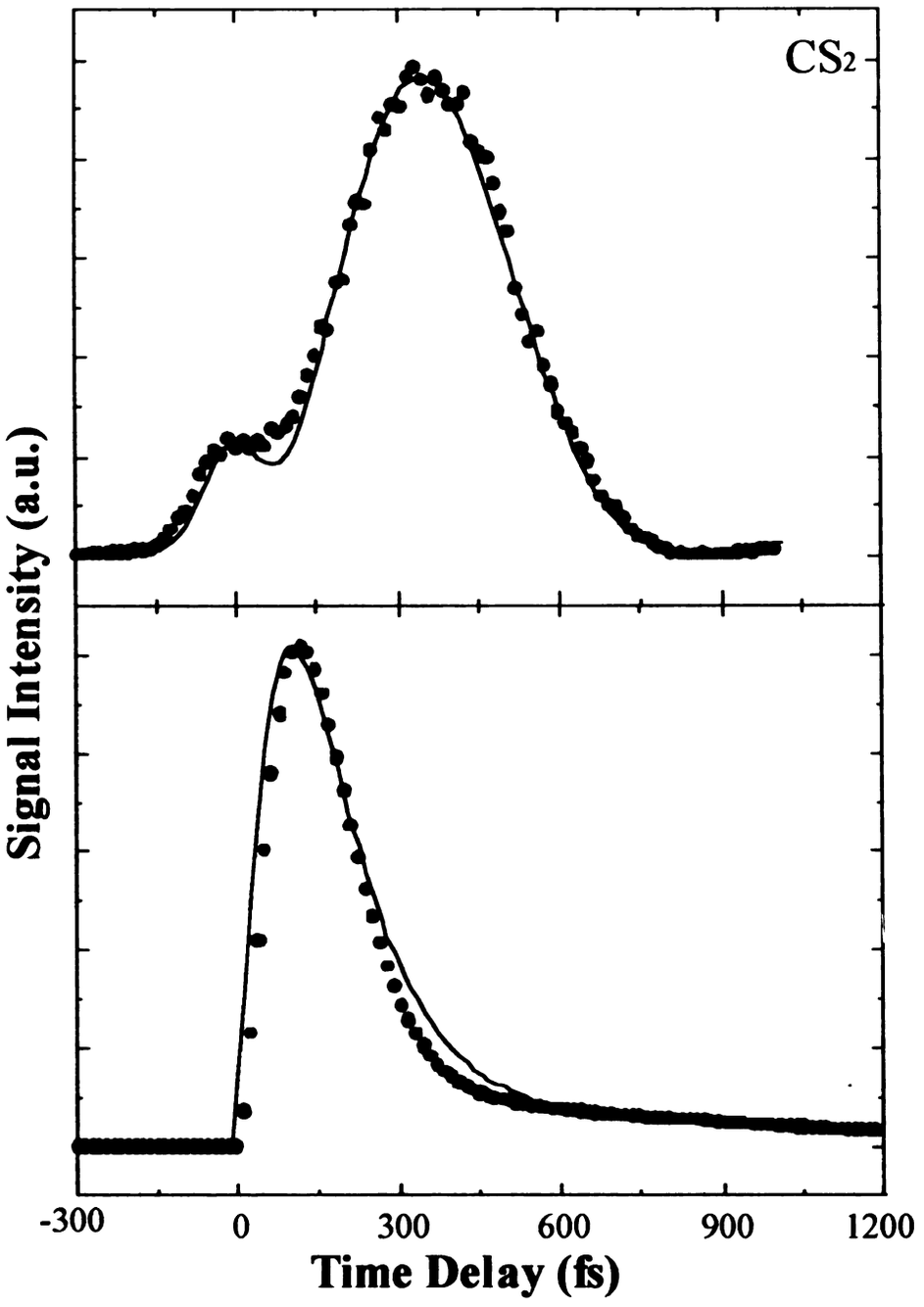

Figure 4.10. Top: TG transient obtained for CS_2 near time zero. The experimental data (circles) contain a very small coherence coupling artifact followed by a large rotational dephasing component. The data has been simulated using Equation (4.13) as shown by the solid line. Bottom: The curve with the circles corresponds to the simulation of our gas-phase TG signal for CS_2 multiplied by a fast decaying function which simulates inhomogeneous dephasing and by a slow decay function which simulates diffusional dephasing (see text). The smooth line corresponds to a simulation curve used by Nelson and coworkers to fit the liquid-phase experiments (see References 56 and 219).

Based on the simulation of the gas-phase data, we have attempted to reconstruct the condensed-phase measurements. Our simulation is achieved by multiplying our gas-phase simulation for CS_2 (from Equation (4.13)) with a function that includes both a fast decay time of 65 fs to simulate the inhomogeneous dephasing and a slow decaying component to incorporate the diffusive reorientational dephasing of 1.37 ps. The resulting curve, shown by the connected circles in the bottom of Figure 4.10, is very similar to the one generated by Nelson and coworkers. The differences between the two curves are a slight delay in the peak of the transient and a dip at ~ 420 fs. These differences may provide a more accurate simulation to the data presented in their publication.[56,219] The position where the signal achieves its maximum value is very sensitive to the fast decay which simulates the inhomogeneous broadening. Liquid-phase measurements have found that upon dilution the inhomogeneous decay rate decreases because the CS_2-alkane interactions are weaker than those between CS_2 molecules.[205,220,221] These findings are consistent with a physical description in which a weakening of the intermolecular interactions leads to dynamics that more closely mimic a gas-phase environment. Based on our preliminary model, only the inhomogeneous dephasing rate would need to be modified to simulate such behavior. The preliminary analysis presented here indicates that gas-phase dynamics can be used to provide a starting point toward the simulation of liquid-phase dynamics, especially during the first picosecond before dephasing is complete.

4.4.2. Resonant Excitation

4.4.2.1. Rotational and Vibrational Response ($\tau_{ab} = 0$)

The transient grating data (positive time delay with $\tau_{ab} = 0$) and reverse transient grating data (negative time delay with $\tau_{ab} = 0$) obtained from an iodine sample heated to 130-140°C (160 Torr) are shown in Figure 4.11. The long undulation (~1.5 ps) corresponds to the early dephasing in the rotational anisotropy. The fast oscillation corresponds to ground and excited state vibrations, which are excited impulsively by the short pulse lasers. Unlike the previous experimental transients, both excited and ground state dynamics of I_2 are observed. The difference stems from whether or not the TG interactions are resonant with the appropriate electronic transitions of the molecule in question. In this case, all three fields are resonant with transitions between the X ($^1\sum_g^+$) and the B ($^3\prod_{0^+u}$) states.[130,131,222,223] Transitions to other states with smaller transition probabilities at the wavelength of excitation, such as the A_{1u} state, are not observed because of the μ^8 dependence of the signal. All eight diagrams in Figure 4.2 contribute to the observed signal. In Figure 4.11, ground state and excited state dynamics are clearly obtained by FWM with three resonant beams. Schmitt *et al.* have carried out CARS and DFWM measurements on this molecule showing both ground and excited state dynamics, evident in the Fourier transform of data from positive time delays.[69,70] Below we present the analyses of our iodine experimental data for positive and negative time delays separately.

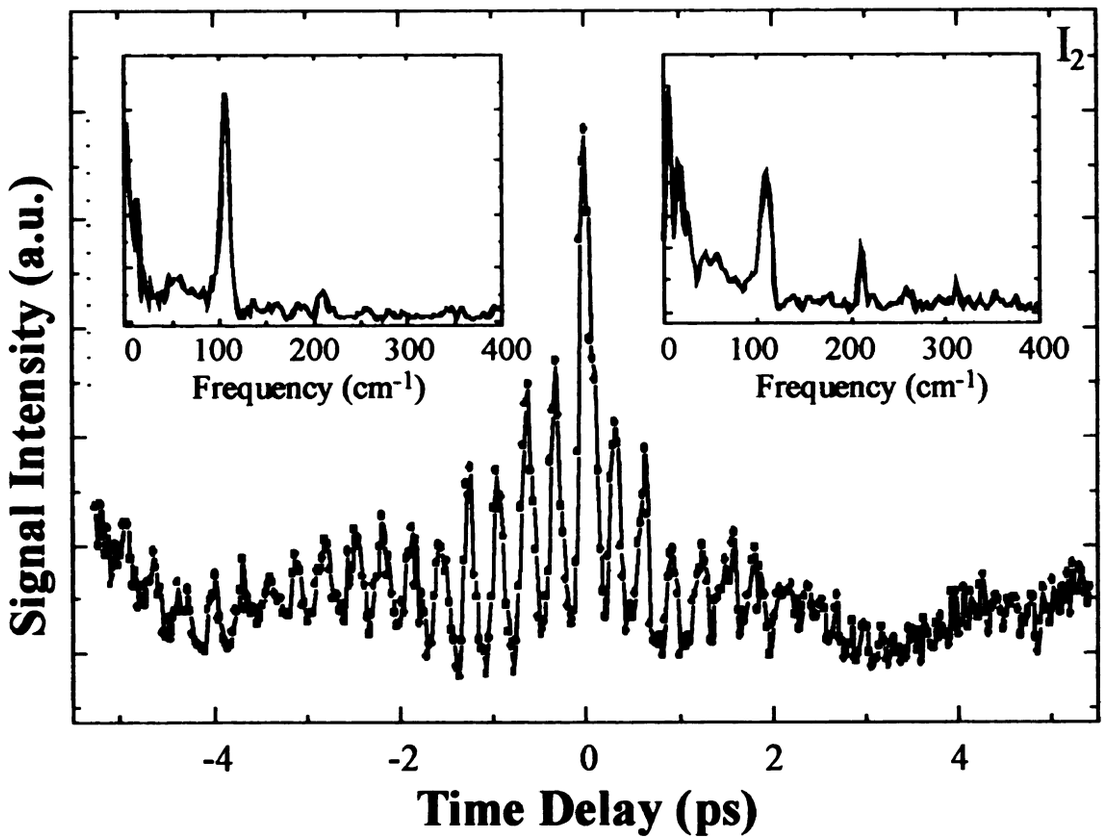

Figure 4.11. Bottom: TG and RTG transient of iodine. Vibrations can clearly be seen at both negative (left) and positive (right) time delays. Lasers with central wavelength of 622 nm are resonant with the X ↔ B electronic transition. Left inset: Fourier transform of the data at negative delay times. There is one main peak at 107.1 ± 0.3 cm^{-1} and another smaller peak at 209.9 ± 0.3 cm^{-1}. Right inset: Fourier transform of the data at positive delay times. The frequencies of the three main peaks are 107.8 ± 0.4, 210.8 ± 0.1, and 312.0 ± 0.2 cm^{-1}. Taking these values and accounting for the combination frequencies that should be observed in each Fourier transform because of the summation of cosines, values for the excited vibrational frequency (105 cm^{-1}), ground vibrational frequency (208 cm^{-1}), and average rotational frequency (3 cm^{-1}) can be obtained.

For positive time delays (Figure 4.11 - right) the dynamics arise from wave packets formed in the ground state (diagrams $\mathbf{ab_g}$ and $\mathbf{ba_g}$ in Figure 4.2a) and in the excited state (diagrams $\mathbf{ab_e}$ and $\mathbf{ba_e}$ in Figure 4.2b). It has been shown that vibrational levels v' = 7–12 form the coherent superposition in the B excited state following excitation with 620 nm pulses.[34,38,42,126] Each population in the ground and excited states

contributes vibrational and rotational dynamics to the signal. To simulate the experimental data, it is best to include each frequency component explicitly in Equation (4.16); however, for simplicity we can understand the data if we assume average frequencies for the excited and ground states. Thus we have two vibrational frequencies (ω_v'' and ω_v') and two rotational frequencies (ω_R'' and ω_R') which we know from the literature for the ground and excited states respectively.[130,131,222-224] When these four terms are introduced in Equation (4.16), the squaring results in a total of sixteen terms. The first four terms give dynamics proportional to $2\omega_R''$, $2\omega_R'$, $(\omega_R'' + \omega_R')$ and $|\omega_R'' - \omega_R'|$, all in the range of 0-50 cm^{-1}. The next four terms give frequencies proportional to $2\omega_v' \sim 220$ cm^{-1}, $2\omega_v'' \sim 420$ cm^{-1} (not observed), $(\omega_v'' + \omega_v') \sim 310$ cm^{-1} and $|\omega_v'' - \omega_v'| \sim 105$ cm^{-1}. The remaining eight terms correspond to the sums and differences arising from the four cross terms between vibrations and rotations. Because the rotational frequencies are very small compared to the vibrational frequencies only two peaks from these cross terms are expected, one at $\omega_v'' \sim 210$ cm^{-1} and the other at $\omega_v' \sim 110$ cm^{-1}. The Fourier transform (right inset) shows the low frequency rotational contributions and the three peaks at 107.8 ± 0.4, 210.8 ± 0.1 and 312.0 ± 0.2 cm^{-1}. Taking these values and accounting for the combination frequencies that should be observed in each Fourier transform because of the summation of cosines, values for the average excited vibrational frequency (105 cm^{-1}), average ground vibrational frequency (208 cm^{-1}), and average rotational frequency, $J_{ave}B_{ave}$ (3 cm^{-1}) can be obtained. Here B_{ave} is the average of the ground and excited rotational constants and J_{ave} is the average J level ($\approx$100). These values agree well with the available spectroscopic data of I_2 for the ground and excited states.[130,131,222-224] Based on the spectrum of our pulses, the sample temperature, and the

Frank-Condon factors, we can determine which states contribute to the ground and excited state dynamics. For the ground state, the observed motion arises from a linear superposition of states v'' = 2-4 with a collective frequency of 160 fs. Although levels v'' = 0 and 1 are the ones which are most populated in the sample at 140 °C before the interaction with the laser pulses, the Frank-Condon overlap between these levels and the excited state at 620 nm is very small.[223] For the excited state, the observed motion arises from a linear superposition of states v' = 6-11 in the B state, corresponding to a vibrational time period of 307 fs.[34,126]

An accurate determination of the magnitude of each of the contributions mentioned is not possible with the available data. Typically the anisotropic equilibrium polarizability (leading to the observation of rotations) is larger than the derivative of the polarizability (vibrational dependence), therefore rotational-vibrational cross terms are expected to have a major contribution. Quantum calculations have also been performed in connection to the phase-locked experiments by Scherer *et al.* on I_2 where the time dependence of the ground and excited state coherence was critical to their interpretation.[225] The ground state motion has been studied quantum mechanically by Jonas *et al.*[226] and Smith *et al.*[227]

Based on the guidelines in the theory section, a semiclassical calculation (using Equation (4.16)) can be performed that takes into account the rotational and vibrational contributions to the TG signal from ground and excited states as well as the coherent-coupling term, which contributes near time zero. In Figure 4.12, we show the simulated transient and corresponding Fourier transforms. The calculated transient looks similar to

the positive time experimental data. The Fourier transform shows peaks of similar position and shape to those obtained from the experimental data. The finite pulse duration in the experiments causes a loss of resolution for the high frequency components. We have not included convolution in the simulation; most likely this explains why the heights of the high frequency components are higher in the simulation Fourier transform than in the experimental one. If the parameters of the simulation, such as the magnitude and phase of each contribution (each vibrational level in the ground and excited states), were optimized by a fitting routine, an even better agreement could have been obtained.

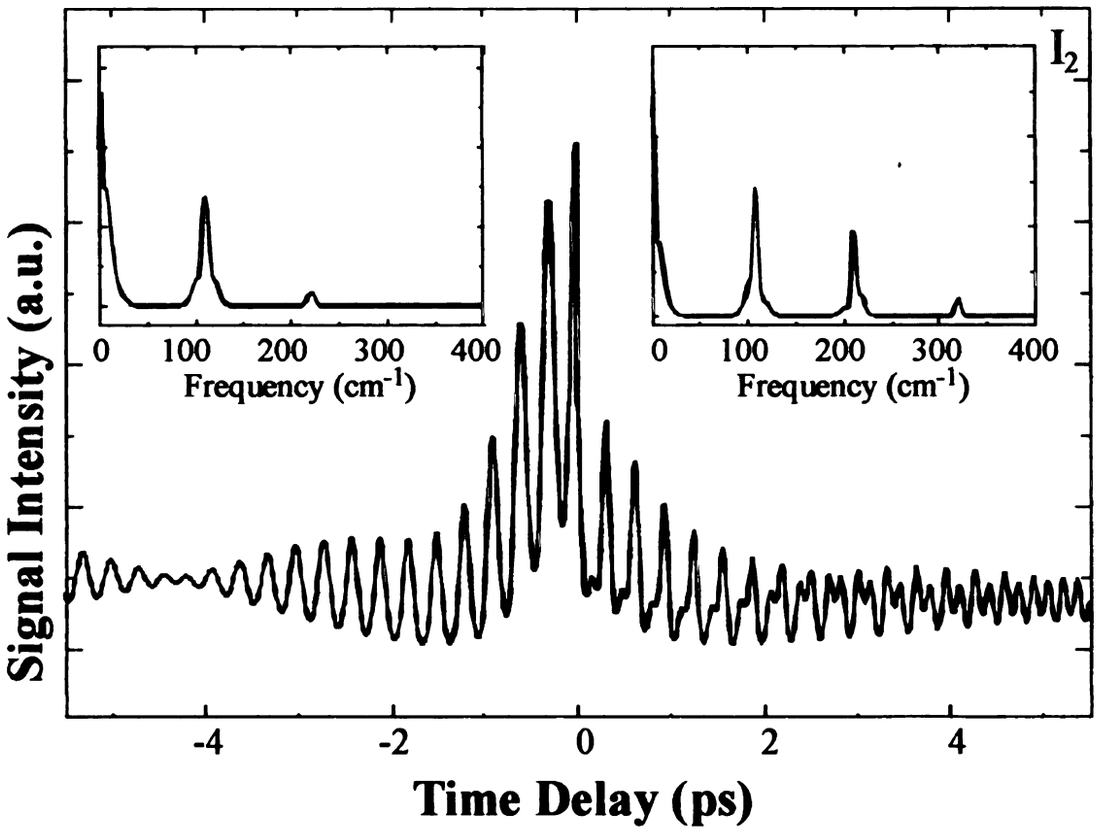

Figure 4.12. Semiclassical simulation of the iodine signal for positive and negative time delays (see text). The insets show the corresponding Fourier transforms. The simulations agree well with the experimental results presented in Figure 4.11.

The negative-time signal in Figure 4.11 (left) is observed when field E_c precedes fields E_a and E_b. Notice that the labels of the fields are arbitrary except for the fact that E_c is the only field that we delay or advance in time. The term "negative time delay" does not imply that E_c is scattered towards the detector before grating formation E_a and E_b has occurred. When E_c precedes the other two fields, (see bottom of Figure 4.1 and diagrams $\mathbf{cb_g}$ and $\mathbf{cb_e}$ in Figure 4.2d), an electronic coherence between the ground and excited states is formed (see Theory section). The time dependence of this electronic coherence is probed by the formation of a transient grating by E_b and scattering of E_a from the grating into the direction of the signal detector. In the absence of collisions, the coherence persists for long times and yields coherence decay information. Our group has investigated the relaxation times of this coherence in iodine at different temperatures with different FWM pulse sequences.[81]

The Fourier transform of the negative time delay experimental transient (Figure 4.11 - left inset) shows frequencies in the 0-10 cm^{-1} range as well as a strong component at 107.1 $\pm$ 0.3 cm^{-1} and a weaker peak at 209.9 $\pm$ 0.3 cm^{-1}. As indicated earlier, the coherence probed in the RTG measurement contains primarily a contribution from the excited state. This can be understood by considering the wave function launched by the first pulse as a coherent superposition of vibrational eigenfunctions from the ground and excited states. The signal is proportional to the overlap between the initial wave function $\Psi(t = 0)$ and the wave function at later times $\Psi(t)$. For iodine the range of motion (center of mass) of the ground state components has been found to be 0.12 Å, while that of the B excited state is 0.6 Å and it is significantly displaced from the ground state equilibrium

geometry.[34,226,227] Therefore, the signal observed is dominated by the dynamics on the excited state. This point was tested with a calculation of the overlap between two ground and excited state model oscillators and it is a manifestation of the Condon approximation.[78]

The rotational component of the signal depends on the rotational dynamics of the coherence. When the excited state vibrational dynamics, the time-zero component, and the rotational dephasing terms are introduced in Equation (4.16), one obtains a transient that is very similar to the observed data. The simulated transient and its Fourier transform at negative time delays, shown in Figure 4.12, are in good agreement with the experimental observations (Figure 4.11). Convolution of the simulated transient, not included for this figure, reduces the relative height of the high frequency component near 210 cm^{-1}.

Other sources for the negative time signal have been considered. Most importantly we can rule out the possibility of a two-photon resonant excitation by which other potential energy curves are probed. For gas-phase iodine the only two-photon allowed transition is to a repulsive state.[38,228] Repulsive states can only contribute to the observed signal within the first $\tau < 100$ fs. In the liquid phase, the ion pair states of iodine are solvated and can be reached by two photons with wavelength in the visible. These states have been implicated in the studies from Fleming's group on phase locked dynamics of molecular iodine.[229] The contribution of ion pair states in the data presented here is ruled out because for gas-phase iodine three photons are required to reach them. Most importantly, the simple semiclassical calculations presented here, involving the B

and X states closely reproduce the data and its Fourier transform. The observation of coherence dynamics for negative time delays in four-wave mixing has been discussed theoretically by Mukamel *et al.*[85,170,171] and has been observed in the gas phase by M. Schmitt *et al.* (for I_2) and by Motzkus *et al.* (for Na_2).[68,70]

4.4.2.2. Control of Molecular Dynamics ($\tau_{ab} \neq 0$)

Now we turn to examining the molecular dynamics of iodine obtained when E_a and E_b are not overlapped in time. First we consider Pulse Sequence I. When field E_a acts on the sample before field E_b, the sample has a certain amount of time (τ_{ab}) to evolve. We have explored how to use the time dependence of the molecular system for controlling the excitation process. The two transients shown in Figure 4.13 and Figure 4.14 were collected consecutively under identical conditions. The only difference between them was the time delay (τ_{ab}) between the first two pulses. Based on the theory, various multiples of the ground or excited state vibrational periods can be used to achieve control over the population transfer.[103] We have tried a number of combinations with great success. We have chosen to use 460 fs ($3/2\,\tau_e$) and 614 fs ($2\,\tau_e$) which correspond to times when the ground state population is at a minimum and a maximum respectively. We chose $2n\,\tau_e$ rather than $(n + \frac{1}{2})\,\tau_g$ in order to maximize the ground state contribution.[103]

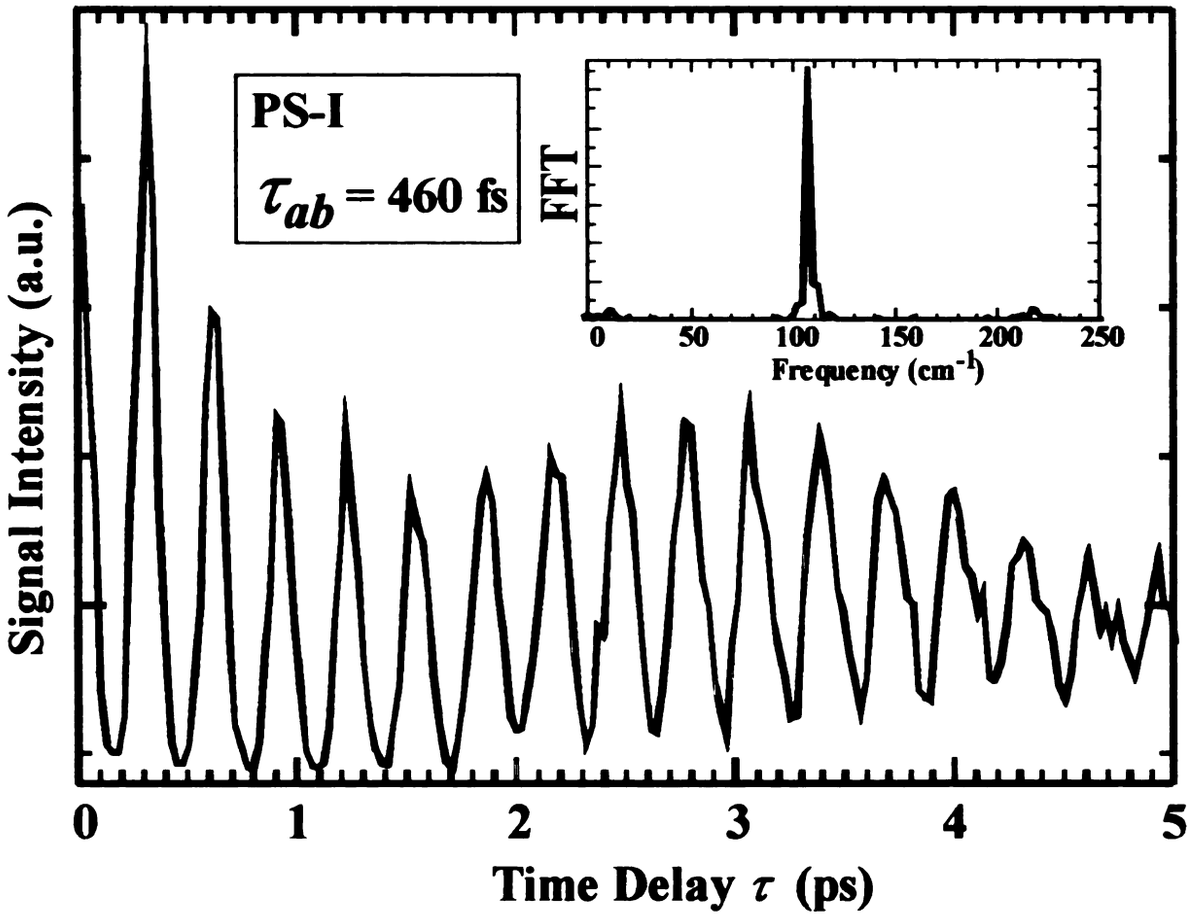

Figure 4.13. Experimental transient for PS-I (only the first 5 ps are shown) where τ_{ab} = 460 fs corresponding to one and a half vibrational periods of iodine in the excited state (3/2 τ_e). Observed vibrations have a period of about 307 fs. The power FFT of the transient shows a predominant frequency of 107.7 ± 0.2 cm^{-1} corresponding to vibrations of the excited B $^3\Pi_{o,u}$ state of molecular iodine. It reflects that the detected FWM signal is exclusively from the excited state. The slow modulation with a dip near 1 ps is due to rotational dephasing.

Figure 4.13 shows the three-pulse FWM signal obtained with τ_{ab} = 460 ± 10 fs (3/2 τ_e). The transient shows vibrational oscillations with a period of 307 fs corresponding to dynamics in the B $^3\Pi_{o+u}$ state involving vibrational levels v' = 6-11. Also observed is a long undulation dipping around 1 ps. The power FFT of the transient is shown in the inset of the figure. The most prominent peak is centered at 107.7 ± 0.2 cm^{-1} and corresponds to vibrations of the excited state. A small peak centered at 218.2 ±

0.2 cm^{-1} is the second harmonic of the excited state signal and is not a contribution from the ground state.[103] The small peak centered at 10.8 ± 0.5 cm^{-1} corresponds to the rotational dephasing dynamics.[86] The dynamics observed are consistent with the excited B $^3\Pi_{o+u}$ state. By comparing the FFTs in Figure 4.11 and Figure 4.13, we can see that the ground state molecular dynamics are suppressed (*i. e.* no peak at 208 cm^{-1}) with this selection of τ_{ab}.

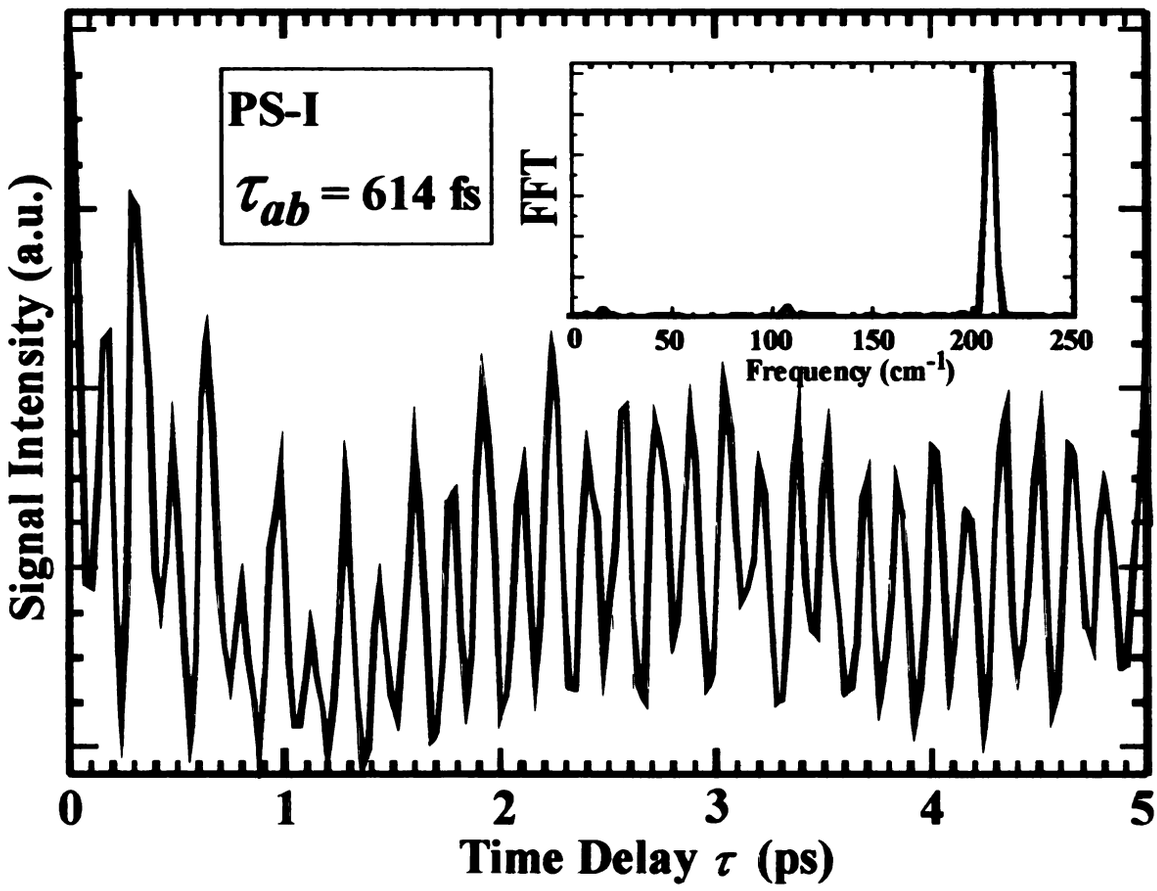

Figure 4.14. Experimental transient for PS-I where τ_{ab} = 614 fs (only the first 5 ps are shown). This value of τ_{ab} is equivalent to two vibrational periods of the excited state of iodine ($2\tau_e$). Observed vibrations have a period of 160 fs. The power FFT of the transient shows a predominant frequency of 208.3 ± 0.1 cm^{-1} corresponding to vibrations of the ground X $^1\Sigma_{0+g}$ state of molecular iodine. It depicts that the detected FWM signal is predominately from the ground state. There is a minor peak at 107.1 ± 0.1 cm^{-1} corresponding to a small contribution from the excited state. Note that the slow dip in modulation around 1.5 ps is due to rotational dephasing.

Figure 4.14 shows the three-pulse FWM signal obtained for τ_{ab} = 614 ± 10 fs ($2\tau_e$). Notice the large change in the experimental transients that occurs with this change in τ_{ab} (compare to Figure 4.13). The transient shows vibrational oscillations with a period of 160 fs corresponding to dynamics in the X $^1\Sigma_{0+g}$ state involving vibrational levels v'' = 3,4. Also apparent in the transient is a slow undulation with a dip around 1.5 ps. The power FFT of the transient is shown in the inset. The most prominent peak is centered at 208.3 ± 0.1 cm^{-1} and corresponds to the vibrational frequency of the ground state. By examining the pattern of vibrational oscillations in these two transients (τ_{ab} = 460 and 614 fs cases), a clear mismatch is observed; this confirms that the dynamics in the τ_{ab} = 614 fs case are not caused by a doubling of the excited state frequency and are ground state dynamics.[103] A smaller peak centered at 107.1 ± 0.1 cm^{-1} corresponds to a minor contribution from the excited state which is expected for this value of τ_{ab} (see Equations (4.18a and 4.18b)).[103] The small peak centered at 15.9 ± 0.4 cm^{-1} corresponds to the rotational dephasing dynamics. The observed dynamics correspond almost exclusively to the ground X $^1\Sigma_{0+g}$ state. Again by comparing the FFTs in Figure 4.11 and Figure 4.14, it is apparent that the excited state dynamics are greatly reduced with this section of τ_{ab}.

In Figure 4.15 we examine the difference in the Fourier transforms for τ_{ab} = 460 fs and 614 fs as shown in Figure 4.13 and Figure 4.14. We first highlight the selectivity of this method for detecting ground or excited state dynamics. For τ_{ab} = 460 fs, we observe a dominant peak at 108 cm^{-1} corresponding to the excited state; a small peak at 218 cm^{-1} is most certainly due to the second harmonic of the same dynamics given that the FFT shows no amplitude at 208 cm^{-1}. For τ_{ab} = 614 fs, we observe a peak at 208 cm^{-1} that corresponds to the ground state vibrational frequency. For this time delay between

fields E_a and E_b, we also see a minor peak at 107 cm^{-1} that indicates a small contribution from the excited state. The insert shows the low frequency end of the Fourier transform with two distinguishable contributions. The moment of inertia of the X state is quite different from that of the B state; the rotational constants are 0.03696 and 0.02764 cm^{-1} respectively.[34,130] This difference is manifested in the low frequency components due to the differences in the rotational dephasing dynamics. The observed positions are 11 ± 1 and 16 ± 1 cm^{-1} respectively. The ratio between these positions is 1.5 ± 0.3 and the ratio of the rotational constants is 1.34; these are in fair agreement. This observation is further proof that the dynamics correspond primarily to the ground or the excited state. Based on these experimental data (Figure 4.11-Figure 4.15), we confirm that the time delay τ_{ab} can be used to control the transfer of population between the ground and excited states.

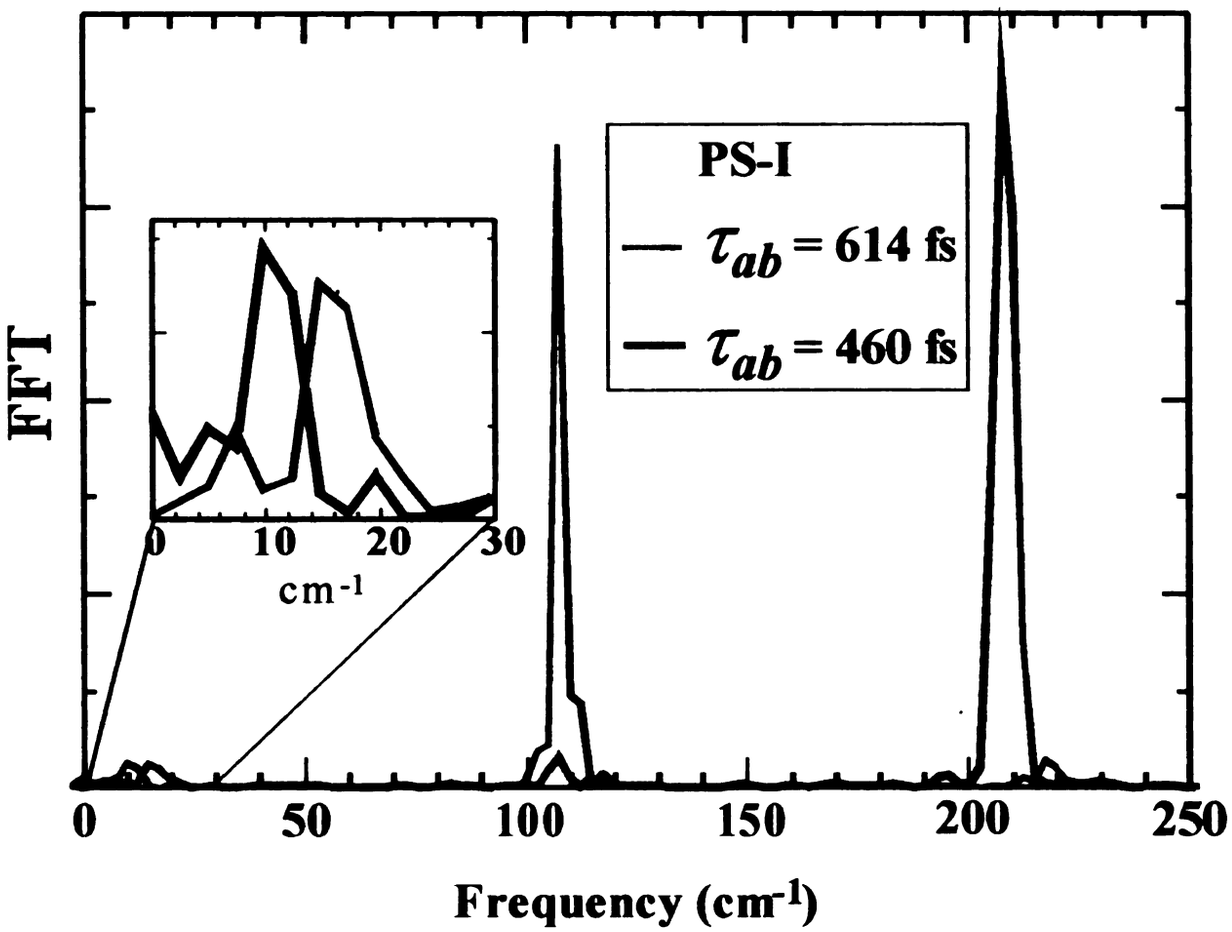

Figure 4.15. Close-up of the power FFT for the transients shown in Figure 4.13 and Figure 4.14. When τ_{ab} = 614 fs (gray line), the data show a small contribution at 107 cm^{-1} and a prominent peak at 208 cm^{-1}, corresponding to the vibrational frequency of the ground state. When τ_{ab} = 460 fs (black line), the data show a prominent peak at 108 cm^{-1}, corresponding to the vibrational frequency of the excited state, and a minor peak at 218 cm^{-1} which is most likely a second harmonic of the 108 cm^{-1} peak. The insert shows the enlarged region at low frequencies with peaks at 16 ± 1 and 11 ± 1 cm^{-1}. These correspond to the different rotational dephasing dynamics occurring in the X state (τ_{ab} = 614 fs) and the B state (τ_{ab} = 460 fs), respectively. The difference in the frequency is caused by the difference in the moment of inertia between these two states. These data confirm the ability to select ground or excited state dynamics based on the choice of τ_{ab} in three-pulse FWM.

The

first two p

ground sta

of the sys

process. I

between g

can carry

with the

system (

practica

and E_a

corresp

Conve

the de

PS-II

last t

the s

conve

use th

The previous data in Figure 4.11-Figure 4.15 show how the delay between the first two pulses in PS-I can be used to control what type of dynamics are observed, ground state, excited state, or both. It is interesting to ask what are the relevant dynamics of the system after a single interaction with the electric field that influences the control process. In the Theory section, we theoretically discussed the coherence $\rho_{eg}^{(1)}$ formed between ground and excited states after a single interaction with the electric field E_a. One can carry out an experimental observation of these dynamics by having field E_c interact with the system and, after a variable time delay τ, have fields E_b and E_a interrogate the system (PS-II). Note that in our experiments, fields E_a and E_c are interchangeable; for practical reasons we have carried out measurements with beam E_c preceding beams E_b and E_a. Recall that the RTG measurement in Figure 4.11 shows 307 fs oscillations, corresponding to the vibrational frequency of the excited state, dominating the transient.

In the Theory section, we discussed the signal dependence on τ_{ab} and τ for PS-I. Converting the formalism to PS-II turns out to be quite simple. For this, we will maintain the definition of τ_{ab} as a fixed time delay and τ as the time that is scanned. Note that for PS-II, τ is the delay between the first two pulses (t_2-t_1) and τ_{ab} is the delay between the last two pulses (t_3-t_2). The expressions for the ground and excited state contributions to the signal need to be modified accordingly by interchanging τ_{ab} and τ. This modification converts the ground (excited) to an excited (ground) state contribution.[103] Thus, we can use the fixed delay τ_{ab} to 'filter' the ground and excited state dynamics.

delay t

The da

10 fs.

second

ps are

groun

is evi

Figur

used

in th

amon

In Figure 4.16 and Figure 4.17 we have explored the possibility of using the delay time τ_{ab} between beams E_b and E_a to filter the type of dynamics that are observed. The data in Figure 4.16 (only the first 5 ps are shown), which was taken with $\tau_{ab} = 460 \pm 10$ fs, show excited state dynamics. The small contribution at 218 cm^{-1} is due to the second harmonic of the excited state dynamics. The data in Figure 4.17 (only the first 5 ps are shown), which was taken with $\tau_{ab} = 614 \pm 10$ fs, show an increase in the amount of ground state contribution as compared to the contribution when $\tau_{ab} = 0$ fs. This difference is evident by comparing the 210 cm^{-1} peaks in the Fourier transforms in Figure 4.11 and Figure 4.17. These experiments show that the delay τ_{ab} between fields E_b and E_a can be used effectively to filter the relative contributions from ground or excited state dynamics in the initially prepared coherence. We note that this filter does not provide the same amount of control as can be achieved with PS-I.[103]

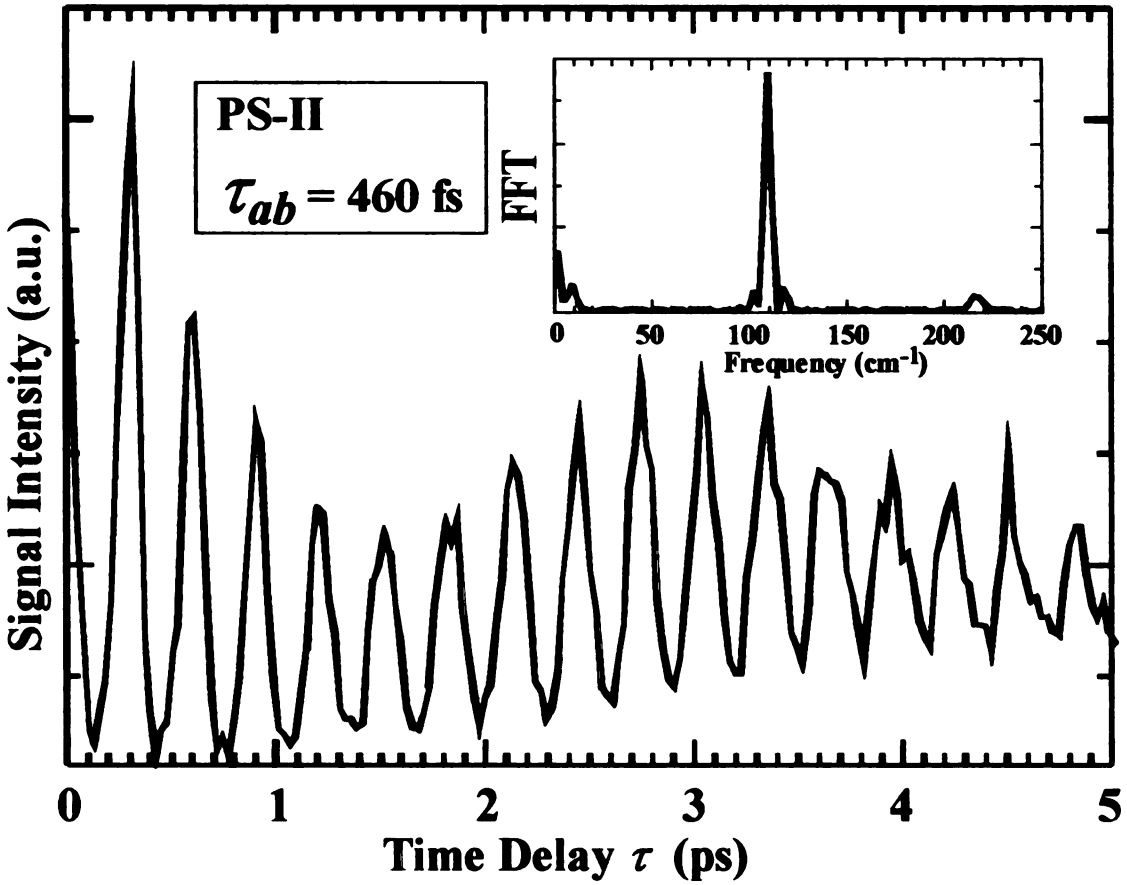

Figure 4.16. Experimental transient for PS-II where τ_{ab} = 460 fs (only the first 5 ps are shown). Notice the well-resolved oscillations with a period of 307 fs. The power FFT of this transient shows a predominant frequency of 108 cm^{-1} corresponding to vibrations of the excited state. A minor contribution at 218 cm^{-1} is most probably a second harmonic of the 108 cm^{-1} component.

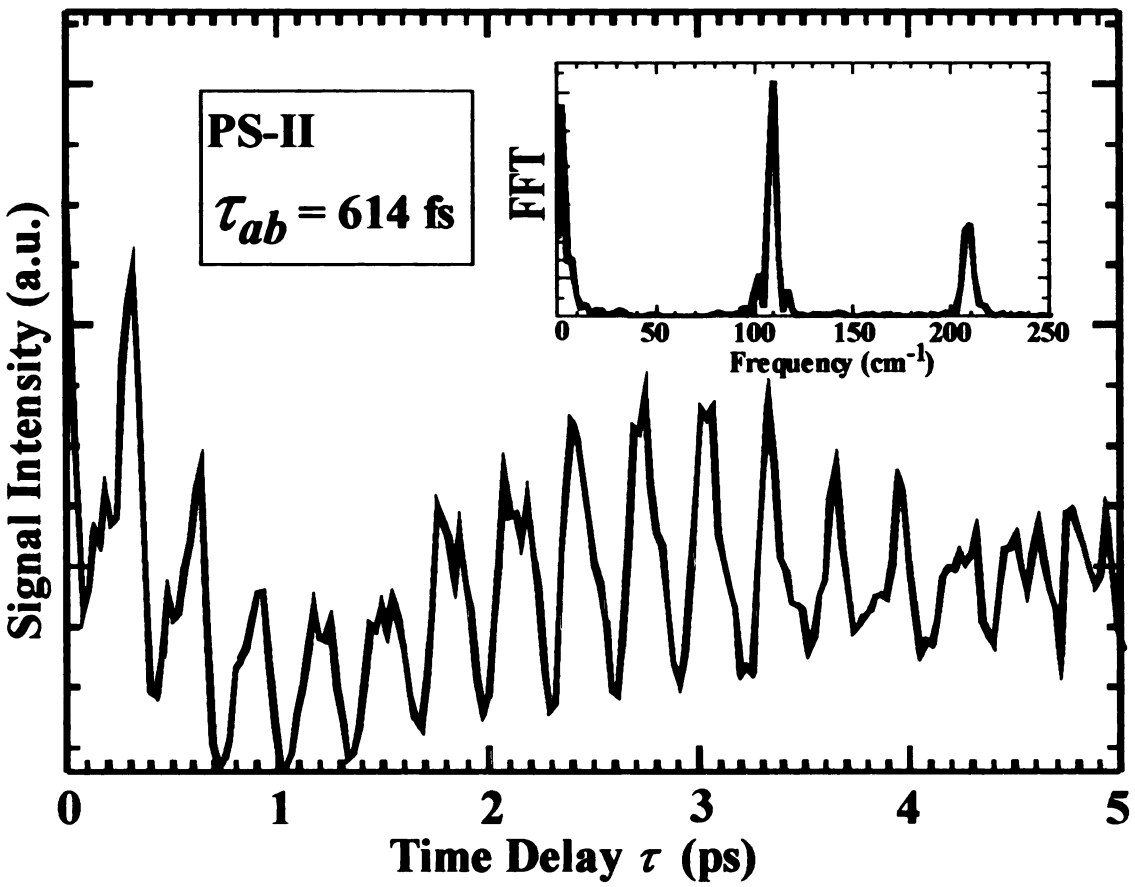

Figure 4.17. Experimental transient for PS-II where τ_{ab} = 614 fs (only the first 5 ps are shown). The power FFT of this transient shows frequencies at both 108 cm^{-1} and 208 cm^{-1}. Note that for this value of τ_{ab}, there is an increase in the amount of ground state contribution as compared to the case τ_{ab} = 0 fs (see Figure 4.11).

4.5. CONCLUSIONS

In summary, we have presented several types of femtosecond dynamic responses from atomic, diatomic and polyatomic gases. The nonlinear interactions between the laser fields and the sample have been sorted using double-sided Feynman diagrams. We have combined the quantum mechanical dependence of the molecular polarizability with the semiclassical expressions for the time-resolved rotational dynamics to arrive at a formula that describes the observed rotational dynamics in diatomic and polyatomic molecules as well as describing the vibrational dynamics. The experimental TG transients on atoms and molecules have been simulated using this formulation. The TG transient from air demonstrated the ability of Equation (4.13) for simulating rotational recurrences. Furthermore, it also demonstrated the capabilities for using TG techniques in the analysis of multiple component mixtures such as N_2 and O_2. Using the CS_2 transient, we demonstrated the accuracy that this time-resolved technique can achieve in the measurement of rotational temperature, rotational constants and centrifugal distortion directly from the time-dependent data without the need for Fourier transformation. For HgI_2, vibrational coherence from the symmetric stretch, which is the only Raman active mode, was observed. The cross terms arising from the sum of rotational and vibrational dependent terms on the molecular polarizability have been identified in the Fourier transform of the HgI_2 data. Vibrational and rotational dynamics from both the ground and B excited states of I_2 were obtained for positive time delays and are consistent with previous observations.[69,70,230] For negative time delays, corresponding to the RTG

configuration, coherence dynamics for I_2 were observed and simulated. The early time responses of polyatomic molecules including benzene, toluene and the dihalogenated methanes were investigated. Finally, for molecules with large anisotropic polarizability, we showed that the rotational dephasing signal may be stronger than the time-zero coherence spike. The understanding and analysis of these simpler non-reactive systems that we have developed here will aid us as we expand TG and FWM studies to reactive systems in the future.

We have also demonstrated that pulse sequences can be found for resonant three-pulse FWM experiments to optimize population transfer between two electronic states. For PS-I, the populations of the ground and excited states were controlled based on the time delay between the first two pulses. We showed that for τ_{ab} = 460 fs only excited state dynamics are observed, while for τ_{ab} = 614 fs primarily ground state dynamics are observed. In PS-II, we observed the time evolution of the coherence between the ground and excited states induced by one laser field interaction. In this case, we found that we changing τ_{ab} from 614 to 460 fs can increase or decrease (respectively) the contribution of the ground state to the FWM signal we collected; thus, we can isolate excited state dynamics in this case as well. We plan to expand these types of experiments to systems where it will be possible to control the outcome of chemical reactions.

The experimental data presented here show that the time delay between the first two pulses in a three-pulse FWM experiment can be used to control the population transfer between ground and excited states. We have used this technique in order to study the vibrational dephasing in the ground and excited states of iodine as a function of

temperature. By changing τ_{ab} we were able to obtain both separate values from the same setup.[81] The ability to transfer populations between different states is the chief tenet of the pump-dump control theory of Rice and Tannor.[231,232] With three-pulse FWM we have shown that this control can be achieved with great efficiency. This technique can be useful to study ultrafast dynamics involved in chemical reactions where one may want to follow processes that occur in the excited or ground state exclusively.

Experimental control using multiple laser pulse excitation has been explored by a number of groups.[88] While some of these experiments have been carried out without phase-locked pulses or phase-matching conditions,[68,233,234] the most striking control over the excitation process is observed for phase-matched or phase-locked setups. Scherer *et al.* measured this effect by observing a change in the total fluorescence of I_2.[96] Warren and Zewail used collinear phase-locked pulses to observe photon echos in I_2.[235] Pshenichnikov *et al.* used a phase-locked FWM arrangement where the grating and echo processes interfere constructively or destructively.[236] Time-delayed pulses can be combined to achieve population inversion by adiabatic passage.[237,238] From Equation (4.17), one can see that the population transfer is modulated by an electronic term with control parameter $\omega\tau_{ab}$, spatial condition $(\mathbf{k_a} - \mathbf{k_b})\mathbf{r}$, and phase-locking condition. The amplitude is further governed by the vibrational motion of both electronic states with control parameters $\omega_e\tau_{ab}$ and $\omega_g\tau_{ab}$. Our measurements use the vibrational time scale, which is independent of phase-locking, to achieve the control.

APPENDICES

5. APPENDICES

LabVIEW™ is a programming application based on the G graphical programming language and is offered by National Instruments.[239] Other text-based programming languages like Fortran, C, BASIC have lines of code that the programmer writes. The G graphical programming language has block diagrams that display the code written by the programmer. A program in G is called a VI, virtual instrument. This language can be used to write programs that collect data, analyze data, and store data just as text-based ones do. It also comes with a standard set of subroutines (subVIs) for many simple tasks, operations, and functions; in addition, manufacturers of scientific instruments or hardware also provide programs and/or subroutines to help facilitate writing programs to control their hardware. The "front panel" is what the user may see (it is hidden in some programs) and may look like the front of an instrument (buttons, knobs, switches, etc.). The front panel is not the program; it is the display of what the program needs as input or provides as output. The block diagram contains the graphical code. Various types of rectangles symbolize loops - "while" and "for-next" - and structures - "sequence", "true-false" or other "case" conditions, and formula calculations. The operations and tasks that should occur in these loops or structures are placed inside the rectangle. Wires show how information is transferred and flows from one part of the program to another. SubVIs are associated with an icon which may contain text and/or simple picture giving an idea of what that VI does. In addition, the icon shows input (left-side connections) and output (right-side connections) information of the subVI; this is called the connector pane. When a VI is written that calls upon a subVI, the icon of the subVI is shown on the block

diagram of the VI. In some cases, variables need to be defined and used across a number of subVIs. These variables are defined globally so they can be accessed by a number of VIs without the value changing or resetting between different VIs; these are called global definitions (global VIs) and are shown with a "world" or "globe" on the icon and block diagram.

There are two main programs that I wrote for acquiring data with our CPM laser system - a time transient scan (ftspgm) and a spectral wavelength scan (specpgm). I also wrote a small instrument control program (instrcontrol) for finding ideal settings on the scientific equipment. These three programs control a Standford Research 245 computer interface board[240], a SPEX 270 M monochromator,[241] and a Unidex 100 actuator.[242] The VIs that control the interface board and actuator are available from the Instrument Driver Network on the National Instruments web page.[239] The VIs that control the monochromator are available from the manufacturer.[241] Below are the hierarchical structures of the data acquisition programs. The VIs that I wrote/modified are indicated with a label, such as A.1 which correspond to the Appendix heading under which the documentation will appear (see below). The subVIs that are not labeled are either standard LabVIEW™ VIs or VIs distributed by the equipment manufacturers/National Instruments for the controlling the hardware. The VIs that control the equipment are easily identified by the text in the icon; the interface board VIs show "245", the monochromator VIs show "ISA" or "ISA Utils", and the actuator VIs show "U100". These hierarchies of the programs are followed by the LabVIEW™-generated documentation of the VIs I wrote. These are pages that contain the filenames, icons,

descriptions, connector panes, front panels, and block diagrams; the labels on the hierarchy correspond to the subheadings of these pages. (In a couple cases (A.5.1. B.5.1, D.3. and D.6.), I modified a standard VI from one of the instrument manufacturers and I have included that modified VI below.) The descriptions indicate the purpose of the VI. The overall structure of the two scanning programs is very similar. The documentation of these VIs for the programs are found in Sections A-D.

Another program used in this research is the fitting program for the rotational anisotropy measurements. This program is written in Fortran and was originally written by Una Marvet. I have modified it as needed for analyzing the unidirectional data and the pump intensity/saturation data on iodine. I have included the code for this program in the last Appendix section. In addition to this file, we also need a file containing the initial parameter values (rotational constants, saturation and perpendicular state parameters, temperature) and a file containing the rotational anisotropy data (time delays and fluorescence intensity) to conduct the fitting procedure of the data.

APPENDIX A

LABVIEW™ PROGRAM: TIME TRANSIENT DATA ACQUISITION

A. LabVIEW™ Program Time Transient Data Acquisition – TAKEFTS4.VI (Take Data)

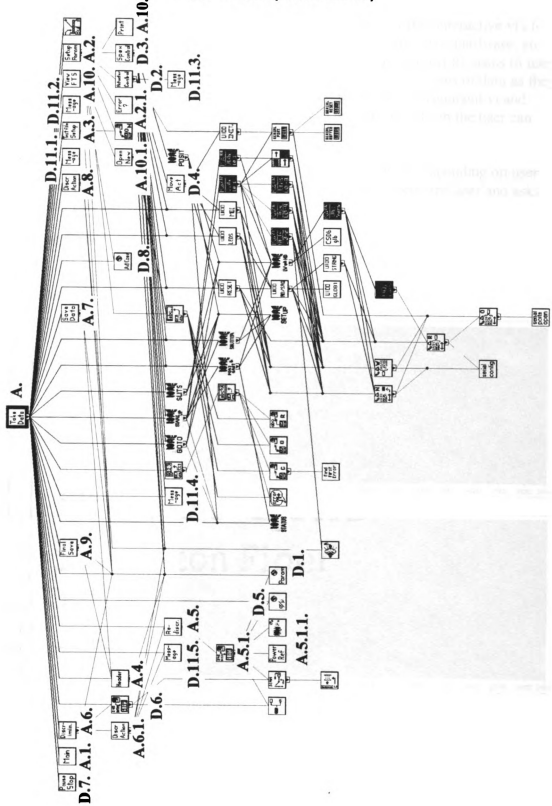

Take Data

This vi is the part that controls the taking of the data. It presents other interactive vi's to the user which are described elsewhere. These vi's are used to setup files, hardware, etc. This vi uses this info to then start fts scan, show summed and unsummed fts scans to user as they are taken, allow the user to pause/stop fts scan, and saves fts scans of data as they are successfully completed. This vi then sends this data to the file management vi and forces it to show the recorded data without input from user needed. Then the user can choose to take more data or to look at other files.

Within data acquisition, it can either discriminate or not discriminate depending on user preference and if a long wait or high %discarded shots occurs it alerts the user and asks for proper method to continue.

Connector Pane

Front Panel

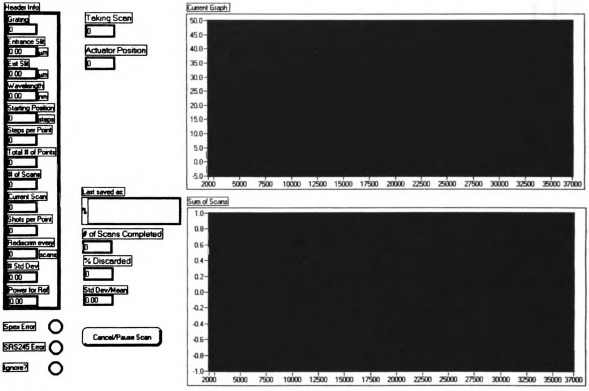

Take Data

Block Diagram

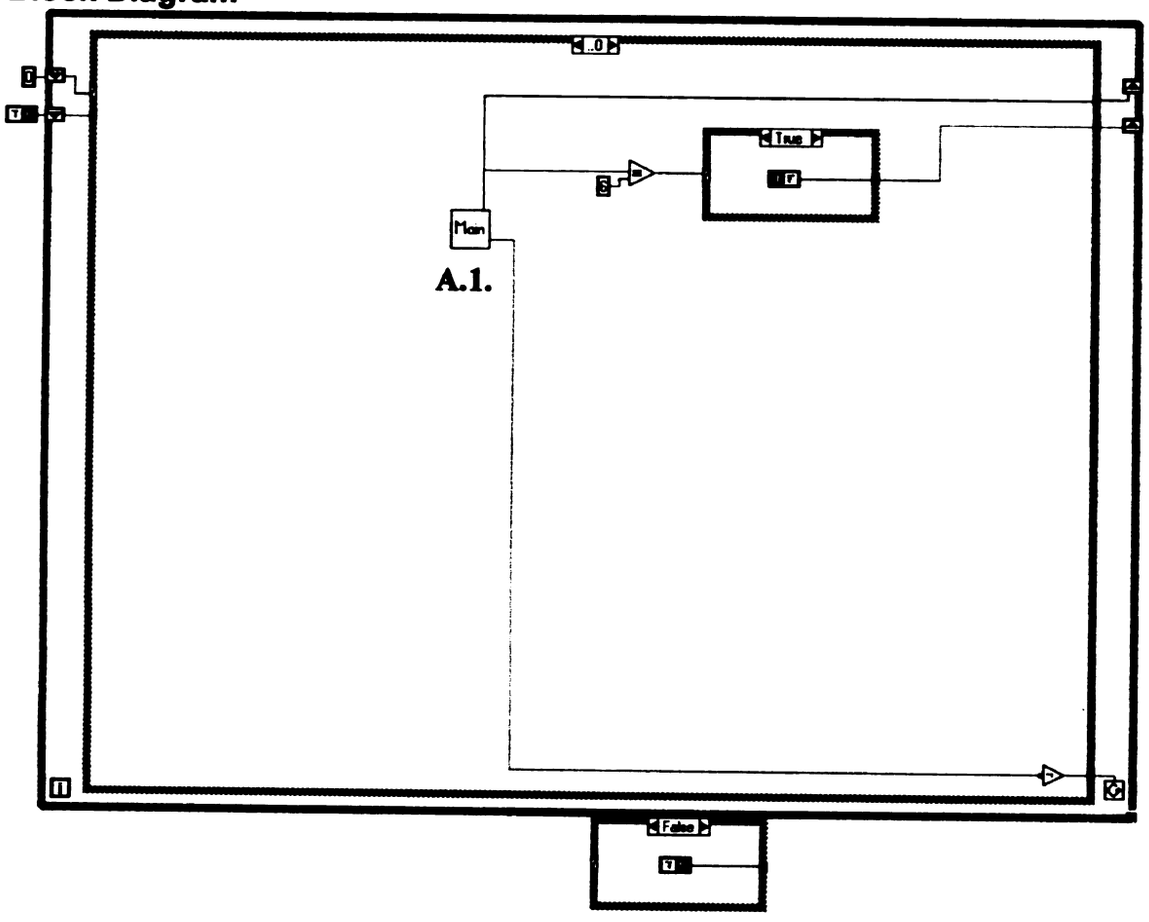

A.1.

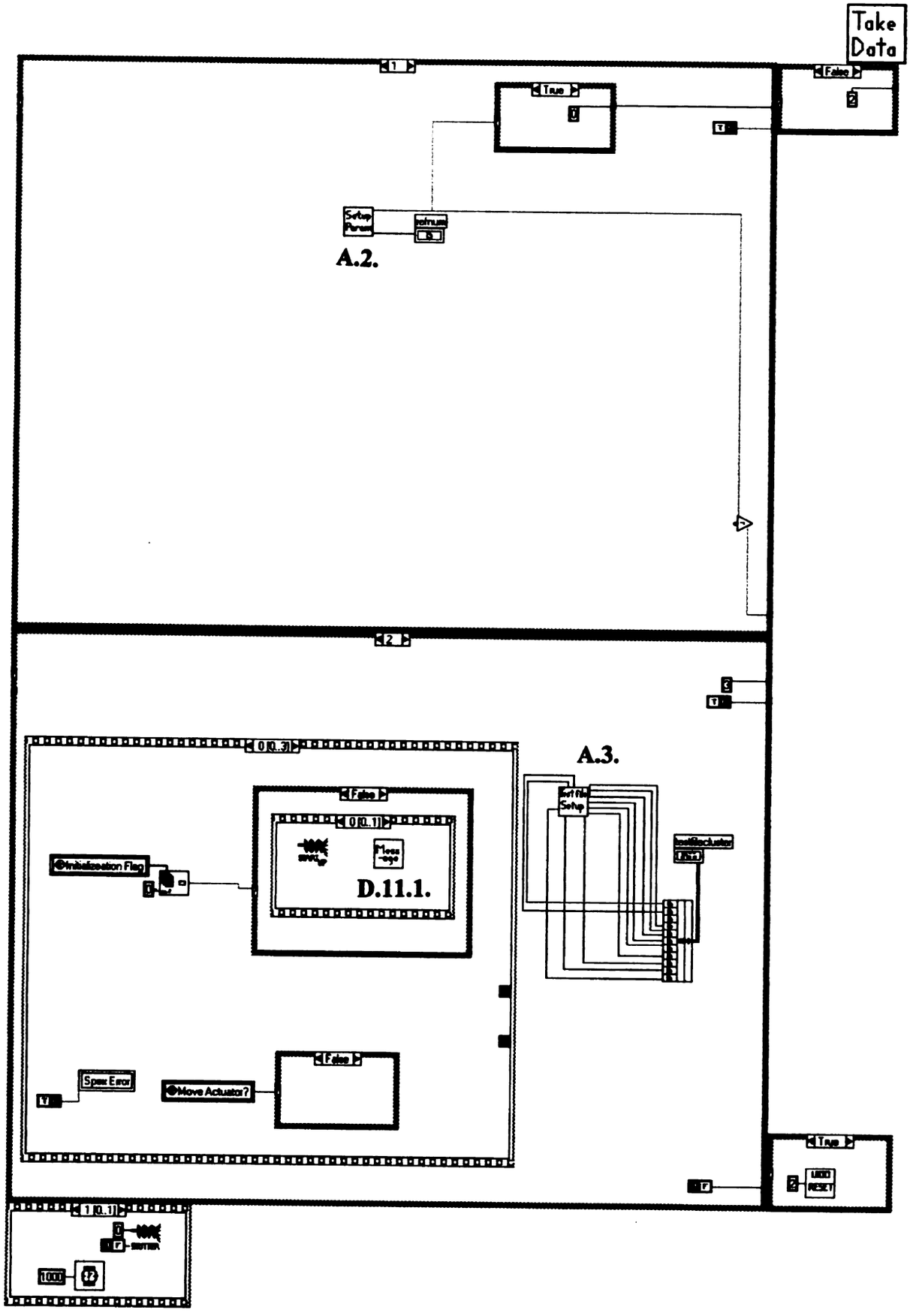
Take Data
A.2.
A.3.
D.11.1.
Move Actuator?

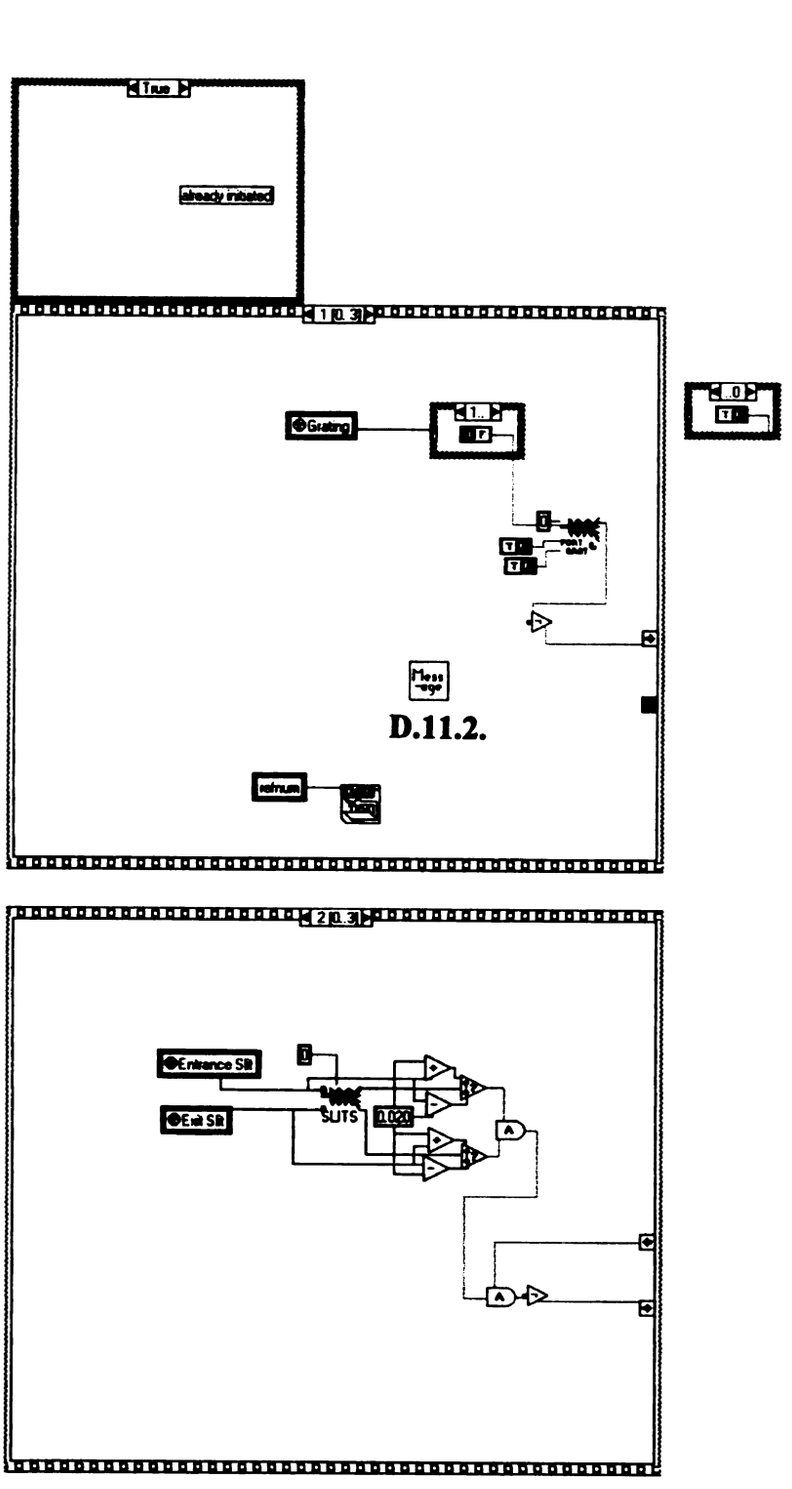
Take Data
True
already initated
1 [0..3]
Grating
0
Mess age
minum
2 [0..3]
Entrance SR
Exit SR
SLITS
0.020

D.11.2.

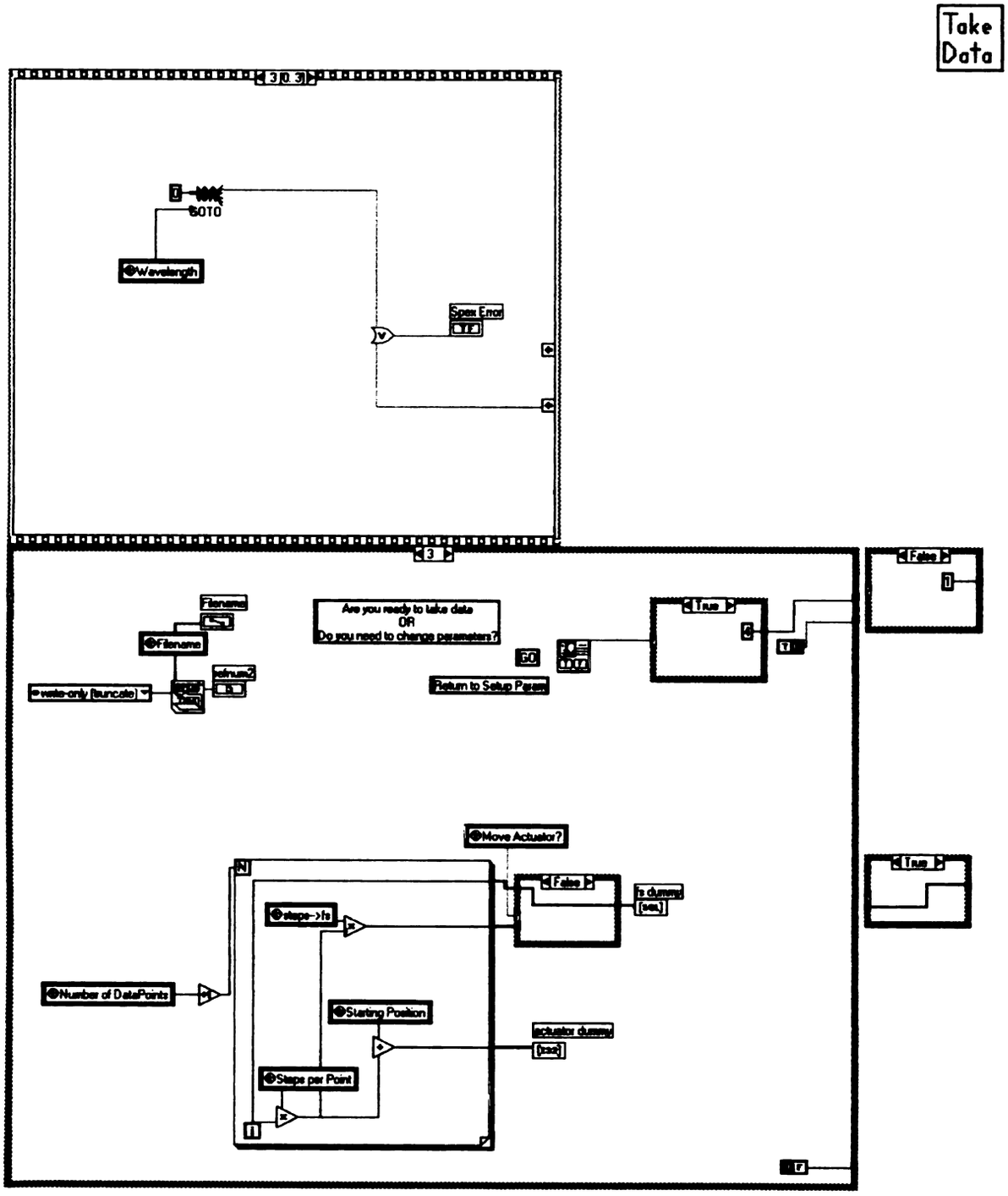
Take Data
3 0 3
GOTO
Wavelength
Spec Error
3
Filename
Are you ready to take data
OR
Do you need to change parameters?
GO
Return to Setup Panel
True
False
write-only (truncate)
Move Actuator?
False
True
steps->fs
Number of DataPoints
Starting Position
Steps per Point

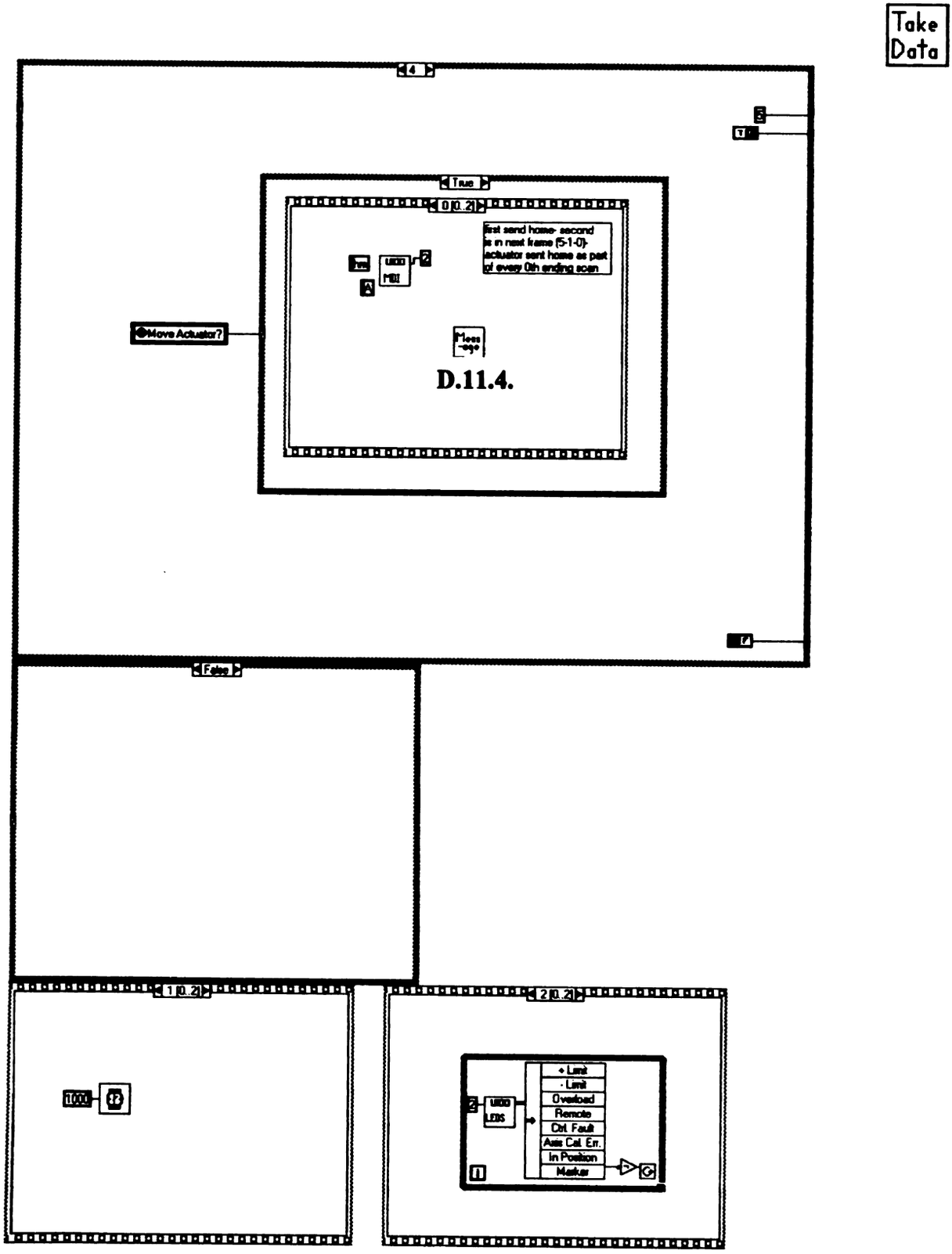
Take Data
4
True
0 [0..2]
first send home- second is in next frame (5-1-0)- actuator sent home as part of every 0th ending scan
Move Actuator?
D.11.4.
False
1 [0..2]
2 [0..2]
+ Limit
- Limit
Overload
Remote
Ctrl. Fault
Axis Cal. Err.
In Position
Master

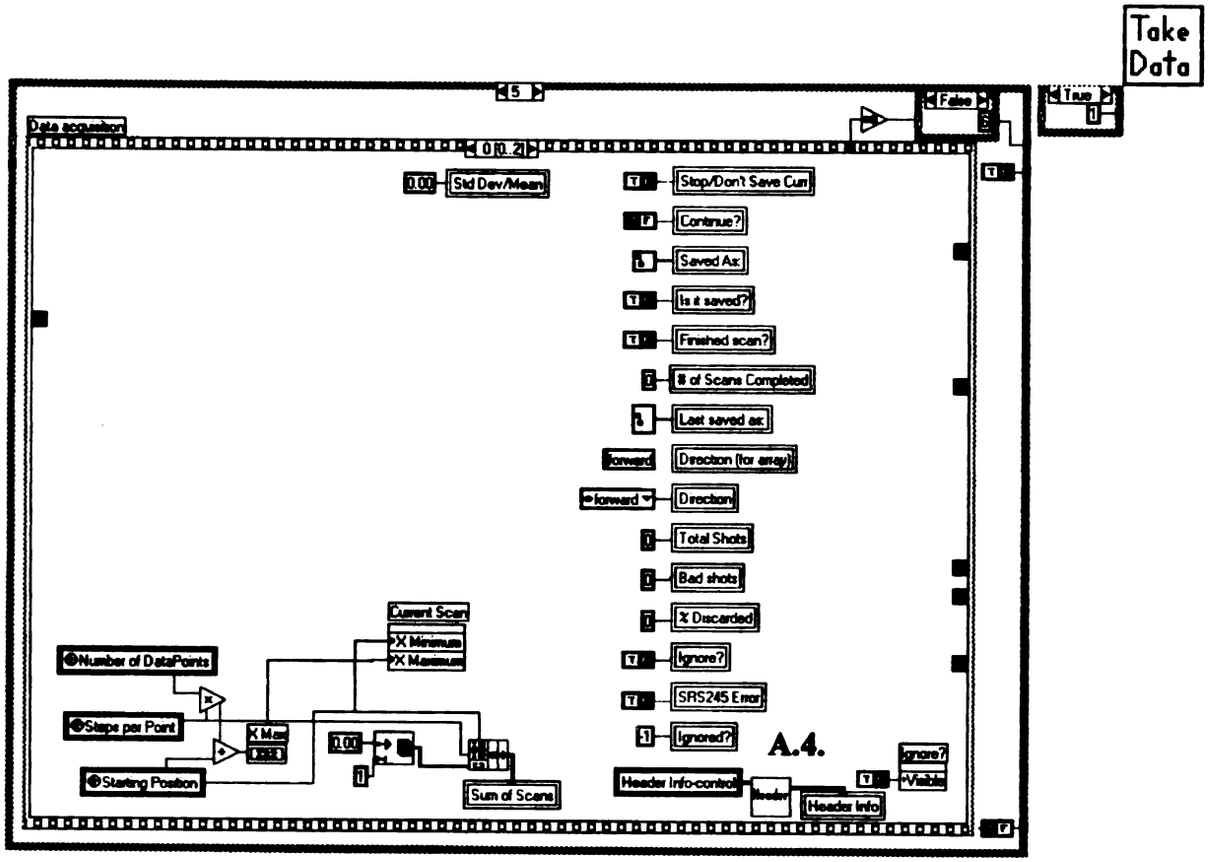
Take Data
Data acquisition
Std Dev/Mean
Stop/Don't Save Curr
Continue?
Saved As:
Is it saved?
Finished scan?
# of Scans Completed
Last saved as:
Direction (for array)
Direction
Total Shots
Bad shots
Discarded
Ignore?
SRS245 Error
Ignored?
Header Info-control
Header Info
Current Scan
Minimum
Maximum
Number of DataPoints
Steps per Point
Starting Position
Sum of Scans
A.4.

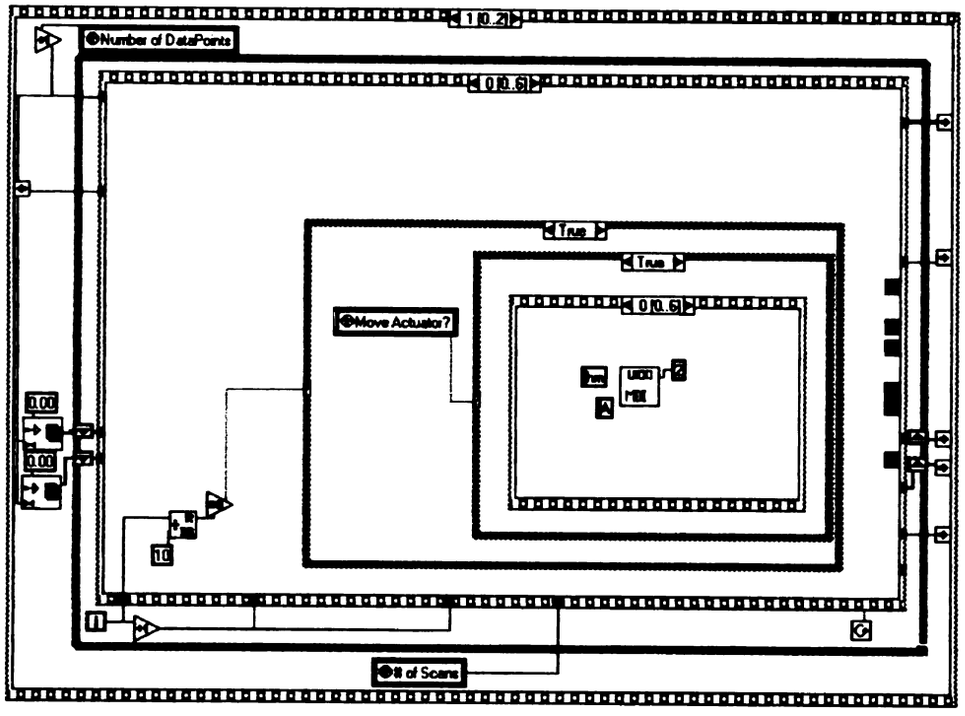
Number of DataPoints
True
Move Actuator?
# of Scans

Take Data

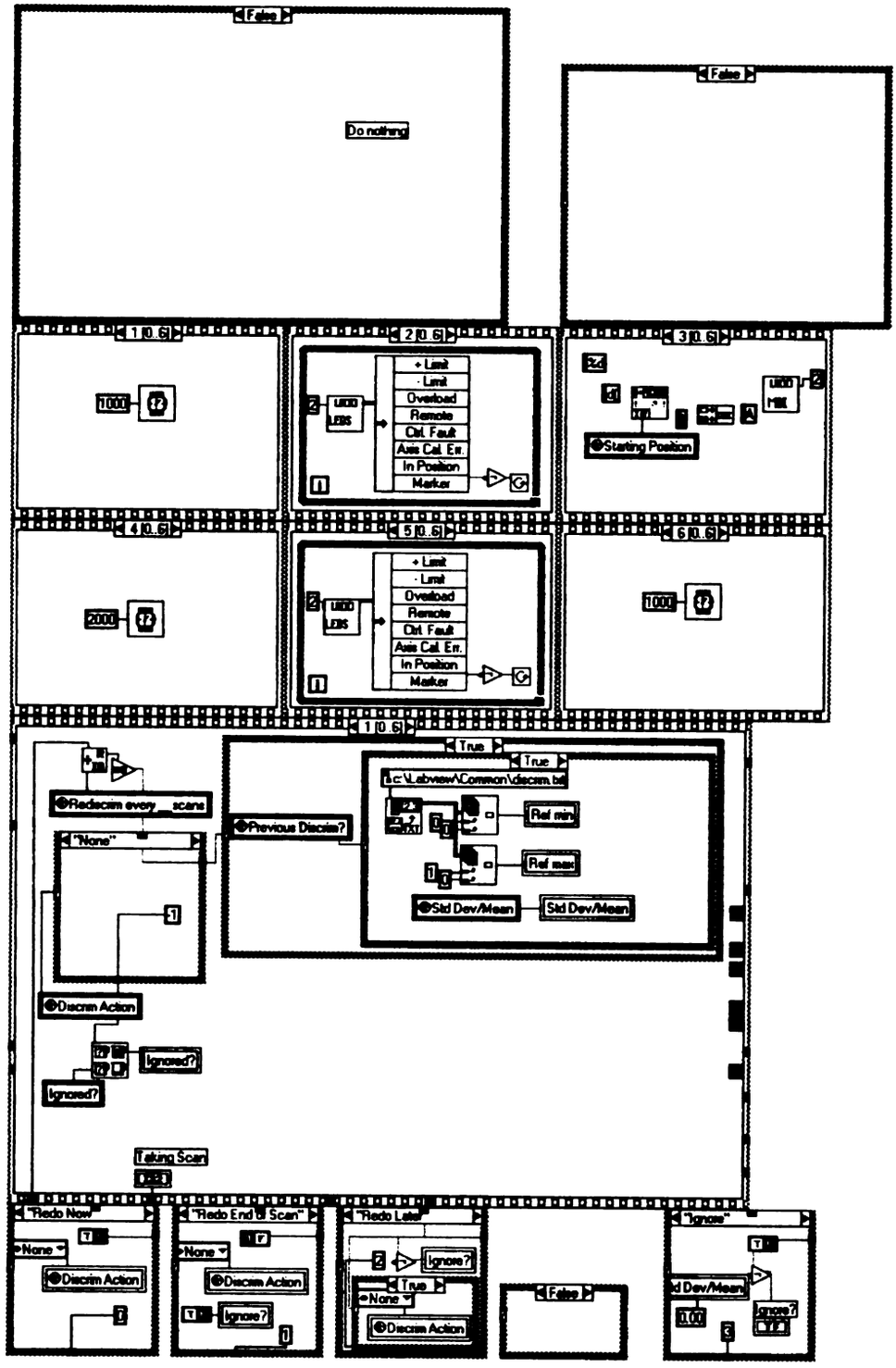
False
Do nothing
False
1 [0..6]
2 [0..6]
3 [0..6]
4 [0..6]
5 [0..6]
6 [0..6]
1000
2000
+ Limit
- Limit
Overload
Remote
Ctrl. Fault
Axis Cal. Err.
In Position
Marker
Starting Position
1 [0..6]
True
True
c:\Labview\Common\decrm.txt
Rediscrim every ___ scans
Previous Discrim?
"None"
-1
Ref min
Ref max
Std Dev/Mean
Std Dev/Mean
Discrim Action
Ignored?
Ignored?
Taking Scan
"Redo Now"
"Redo End Of Scan"
"Redo Level"
"Ignore"
None
Discrim Action
Ignore?
True
False

Take Data

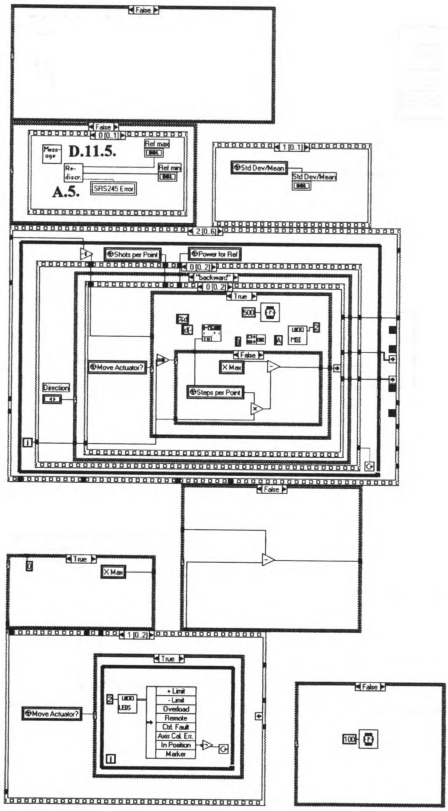
False
D.11.5.
A.5.
Std Dev/Mean
Shots per Point
Power for Ref
backward
True
Move Actuator?
X Max
Steps per Point
Direction
Move Actuator2
+ Limit
- Limit
Overload
Remote
Ctrl Fault
Axis Cal. En.
In Position
Marker

Take Data

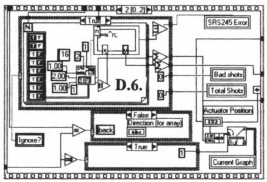
Take
SRS245 Error
Bad shots
Total Shots
Actuator Position
Current Graph
Ignore?
Direction (for Jenny)
Forward
Direction
Number of DataPoints
D.6.

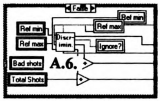
Refs
Ref min
Ref max
Ignore?
Bad shots
Total Shots
A.6.

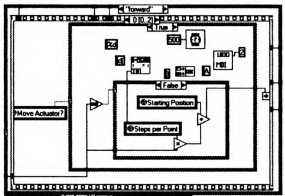
"forward"
Move Actuator?
Starting Position
Steps per Point

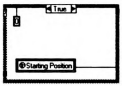
Starting Position

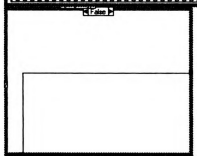

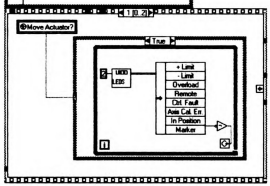
Move Actuator?
+ Limit
- Limit
Overload
Remote
Ctrl Fault
Axis Cal. Err
In Position
Marker

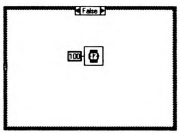

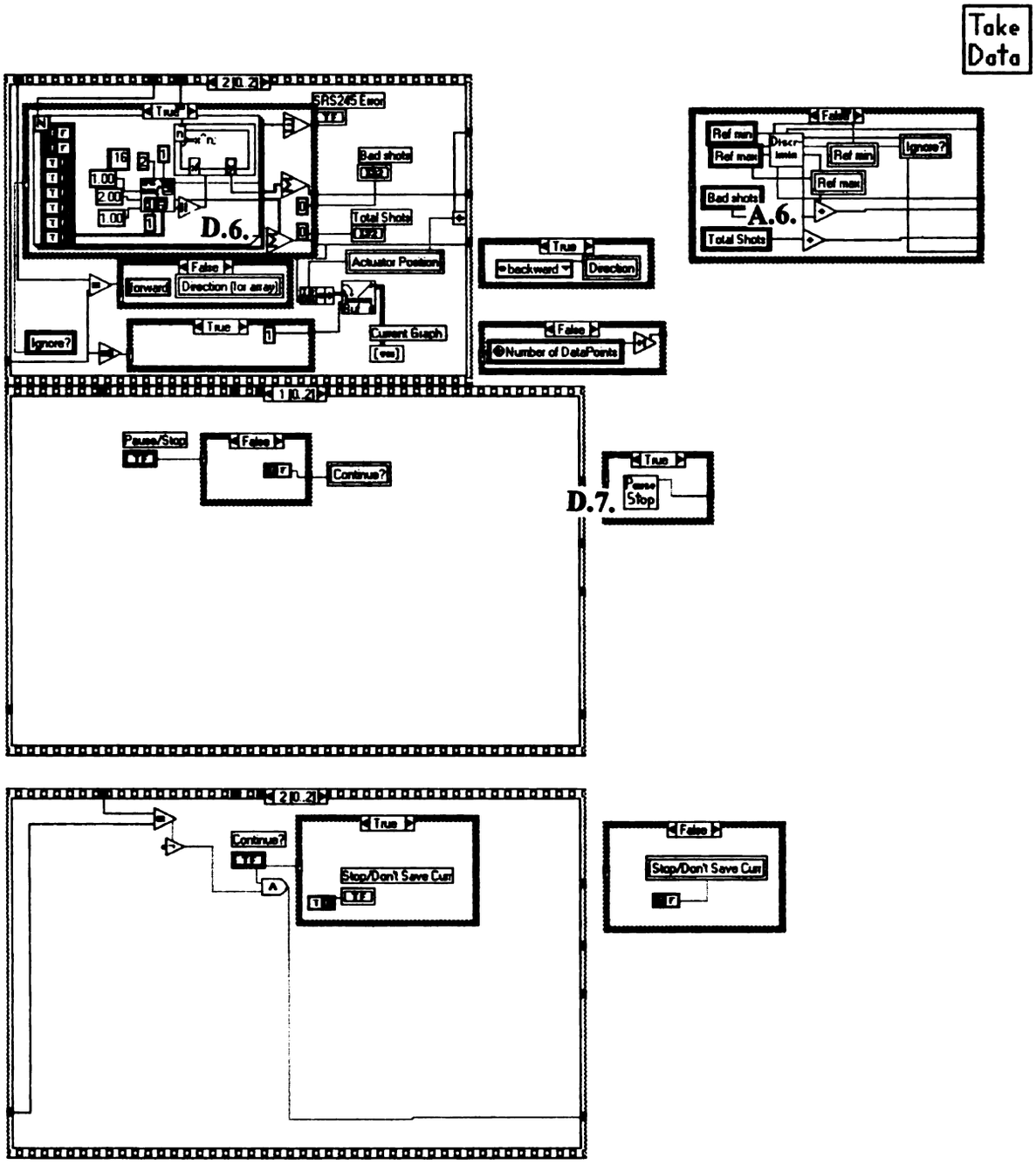
Take Data
SRS245 Error
Bad shots
Total Shots
Actuator Position
Current Graph
Direction (for array)
forward
backward
Direction
Number of DataPoints
Ignore?
Ref min
Ref max
Discr. levels
D.6.
A.6.
D.7.
Pause/Stop
Continue?
Stop/Don't Save Curr

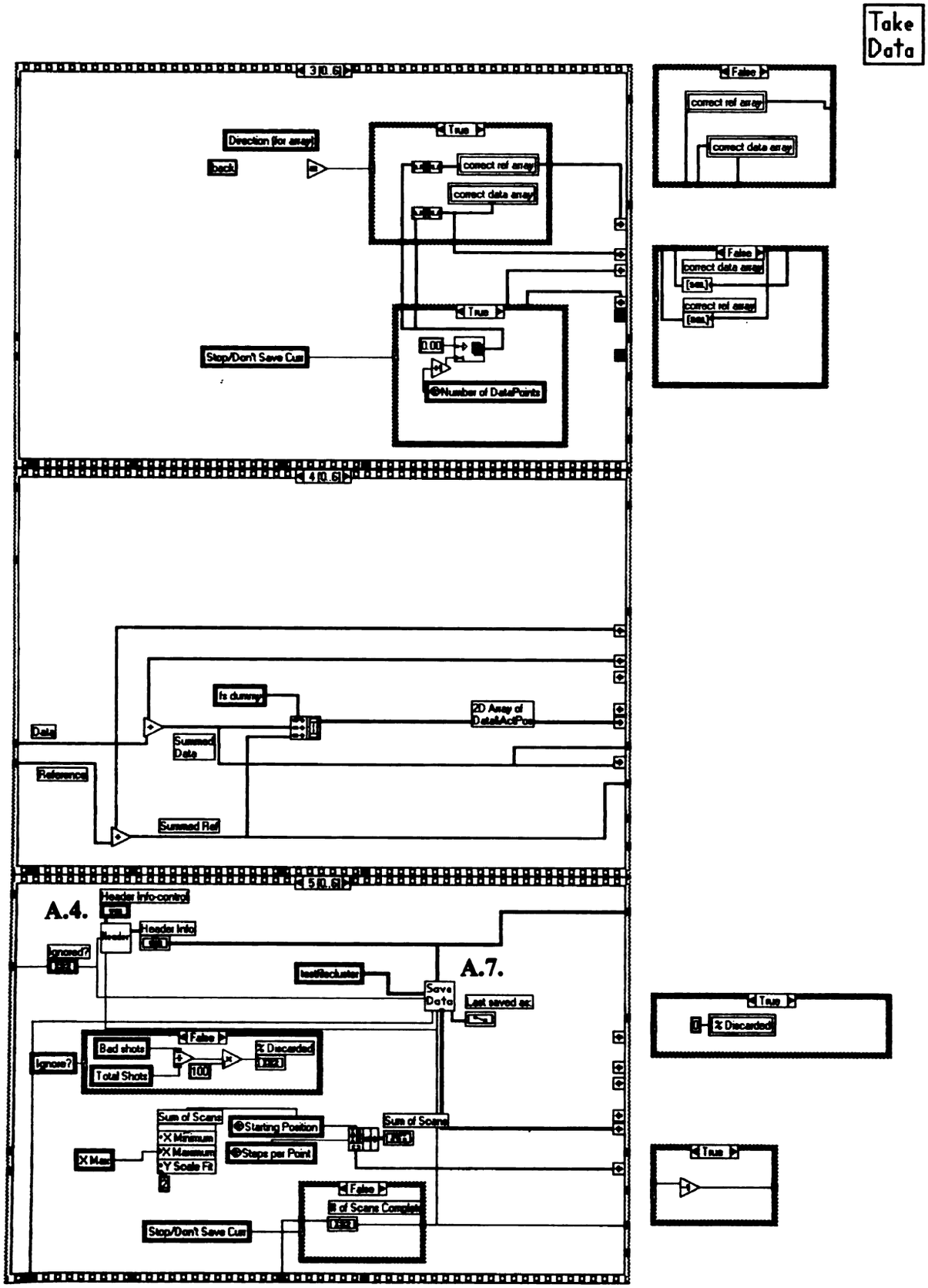
Take Data
3 [0..6]
Direction (for array)
back
True
correct ref array
correct data array
True
Stop/Don't Save Curr
1.00
Number of DataPoints
False
correct ref array
correct data array
False
correct data array
[val]
correct ref array
[val]
4 [0..6]
Is dummy?
2D Array of Data&AcqPos
Data
Summed Data
Reference
Summed Ref
5 [0..6]
A.4.
Header Info-control
Header Info
Ignored?
testRecruiter
A.7.
Save Data
Last saved as:
False
Bad shots
Total Shots
100
% Discarded
Ignore?
Sum of Scans
Starting Position
Steps per Point
Sum of Scans
X Minimum
X Maximum
Y Scale Fit
X Max
False
# of Scans Complete
Stop/Don't Save Curr
True
% Discarded
True

Take Data

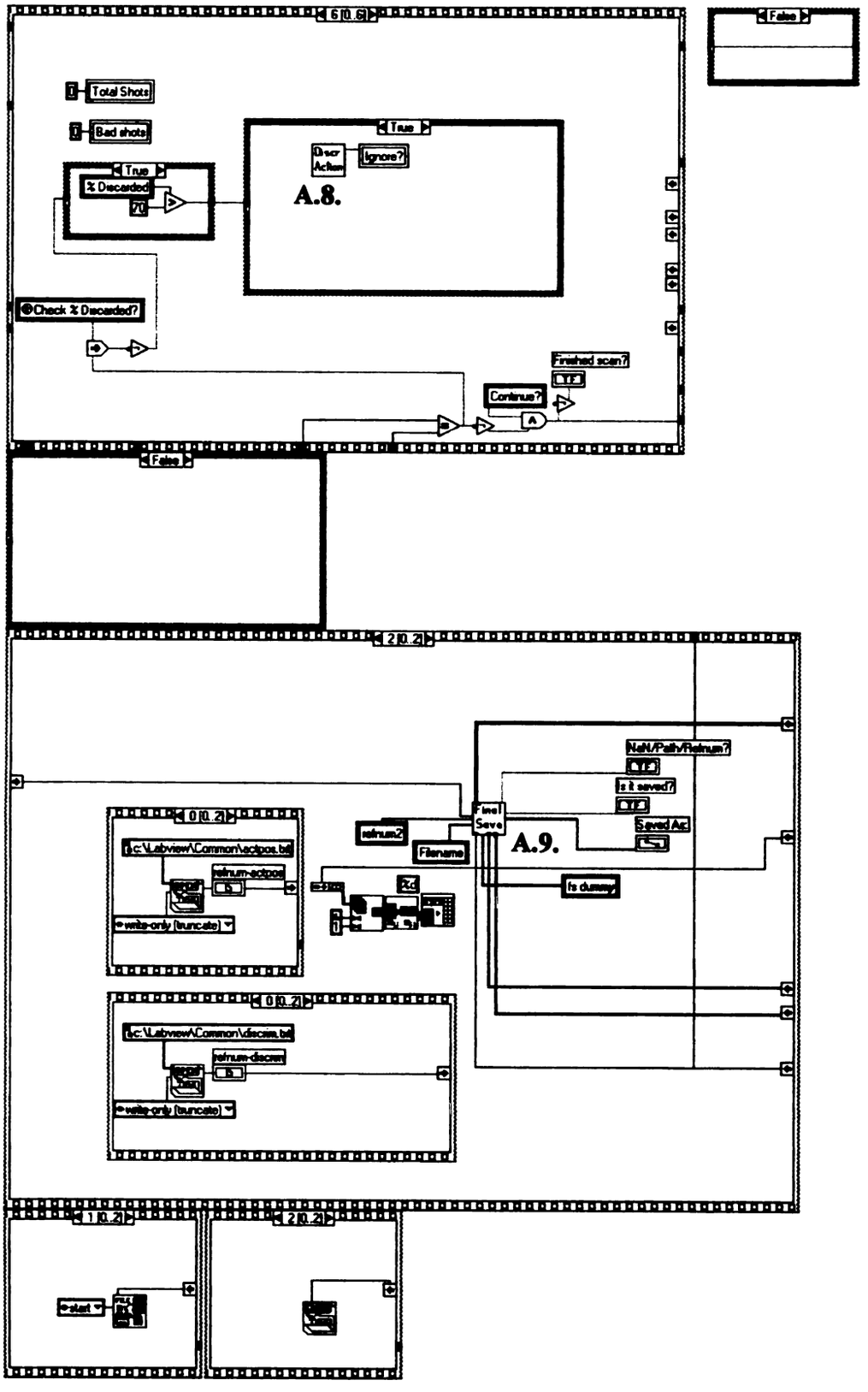
6 [0..6]
Total Shots
Bad shots
True
% Discarded
/0
True
Discr Action
Ignore?
A.8.
Check % Discarded?
Finished scan?
Continue?
A
False
2 [0..2]
NetV/Path/Retnum?
Is it saved?
Saved Ac
Final Save
A.9.
retnum2
Filename
Is dummy
0 [0..2]
c:\Labview\Common\ecdpos.txt
retnum-ecdpos
write-only (truncate)
2c
0 [0..2]
c:\Labview\Common\discexs.txt
retnum-discexs
write-only (truncate)
1 [0..2]
start
2 [0..2]

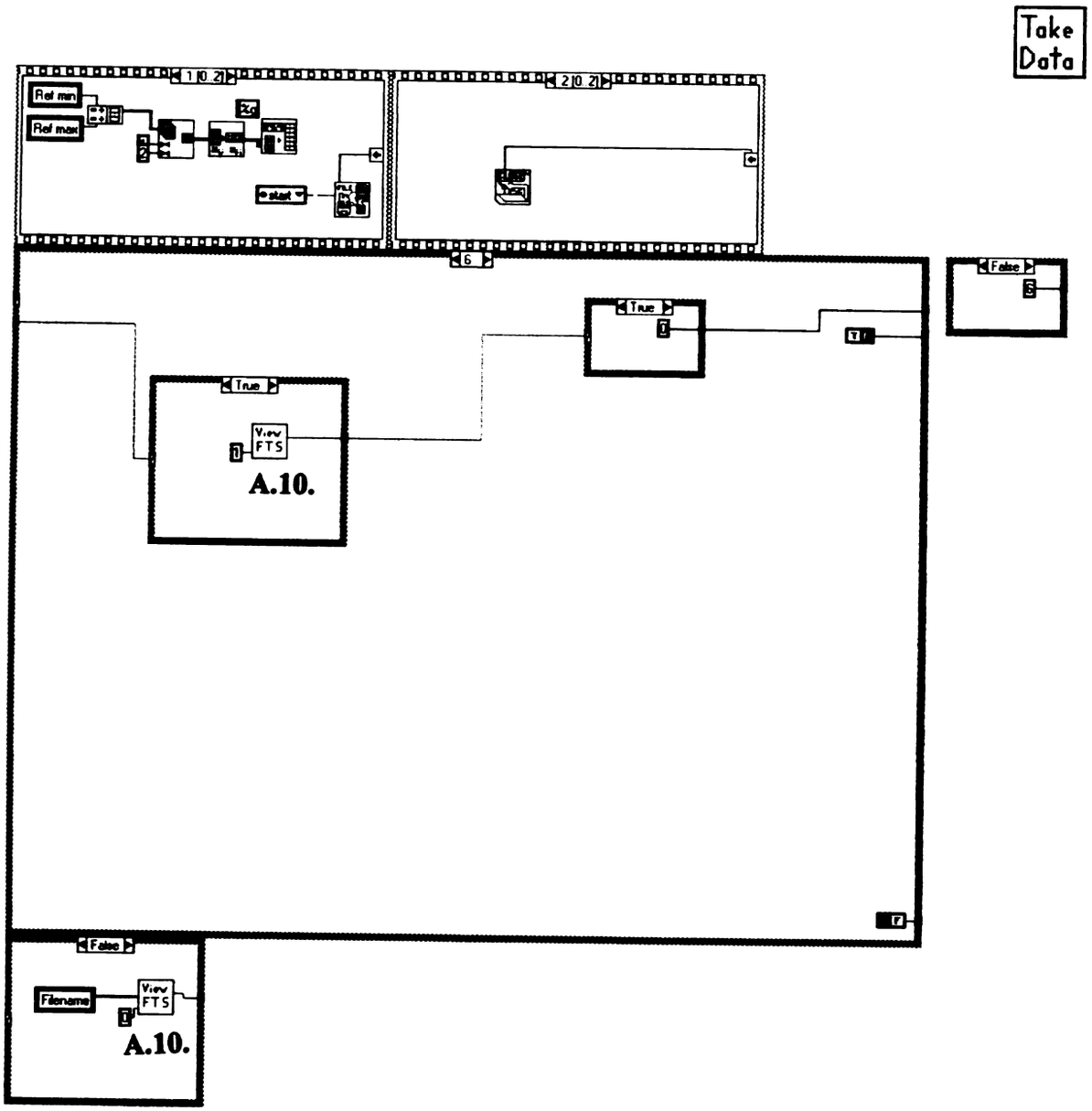
Take Data
Ref min
Ref max
start
True
View FTS
A.10.
False
Filename
View FTS
A.10.

A.1. ftspgm.vi (Main)

This vi is the starting point of the spectral scan program. The user decides between taking data and looking at previously taken spectra- either *.wnm or *.spc files. If the program is properly begun here, the user can go between both parts of the program easily. Ie. start with file management and then go to take data and back again, or start with take data and then go to file management and back again. (Or stay within one part of the program the whole time.)

Connector Pane

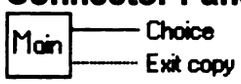

Front Panel

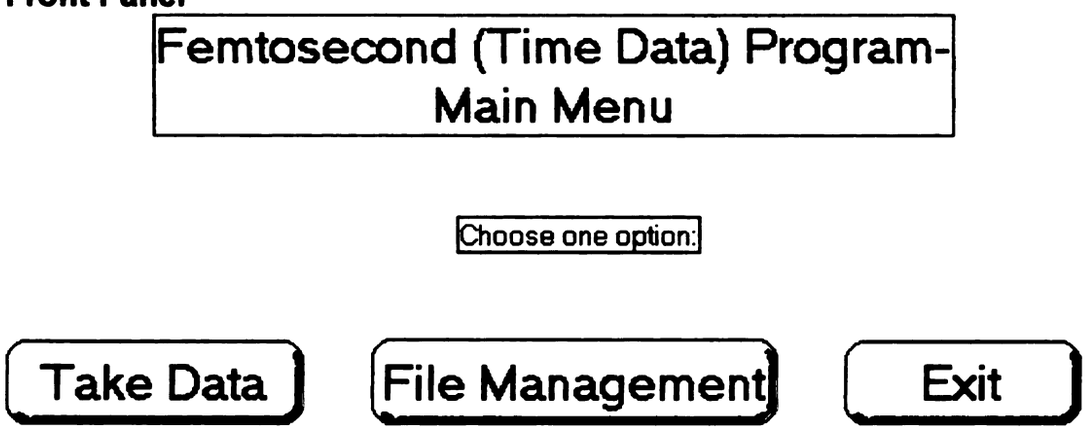

Main

Block Diagram

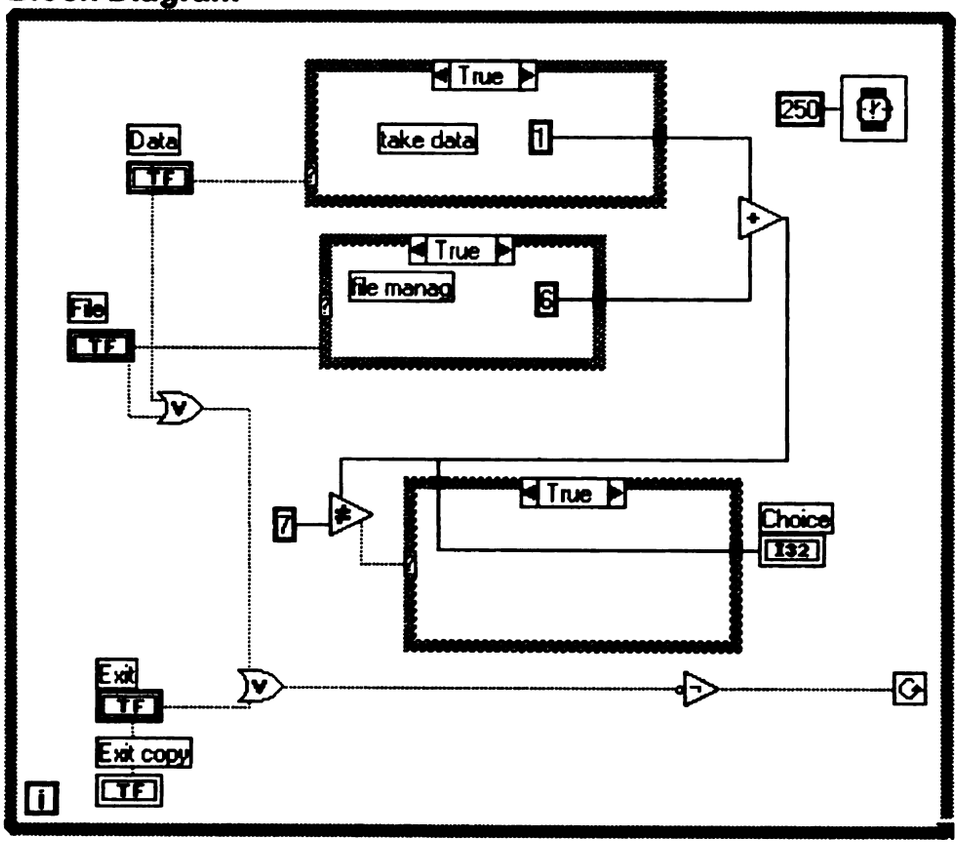

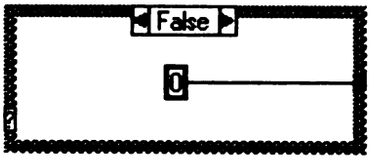

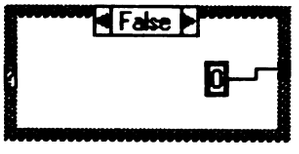

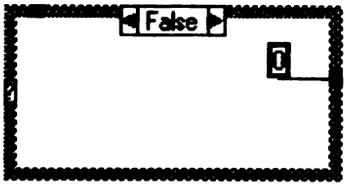

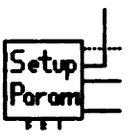

A.2. paramfts4.vi (Setup Param)

This vi writes the parameters to the global parameters vi so that all subsequent vi's have access to the initial conditions. If the program has been run earlier without Labview having been quit, the parameters from the previous run are shown on the screen (allowing the user to make only the necessary changes). The parameters are used to setup the resulting data file and data acquisition and setup the spectrometer and actuator. The user has the ability to control the spectrometer and the actuator during this screen in order to find the best locations. (OR use instrumental control vi to move/change settings).

Connector Pane

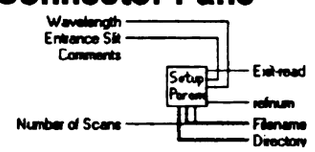

Front Panel

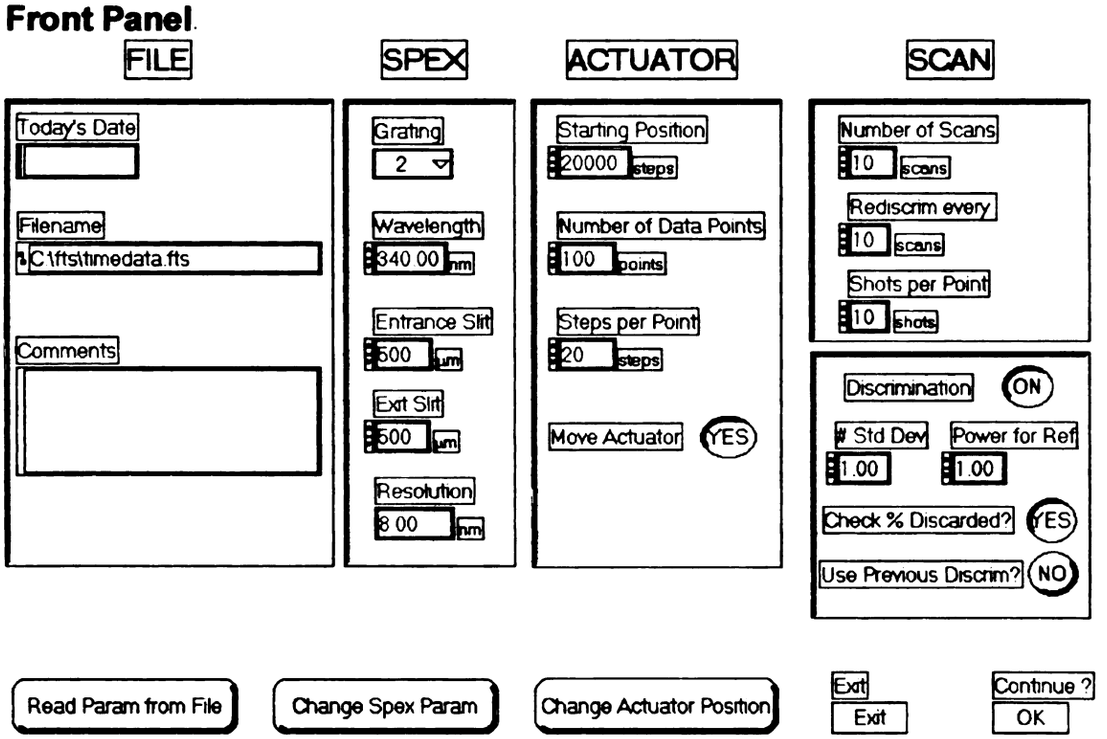

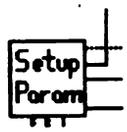

Block Diagram

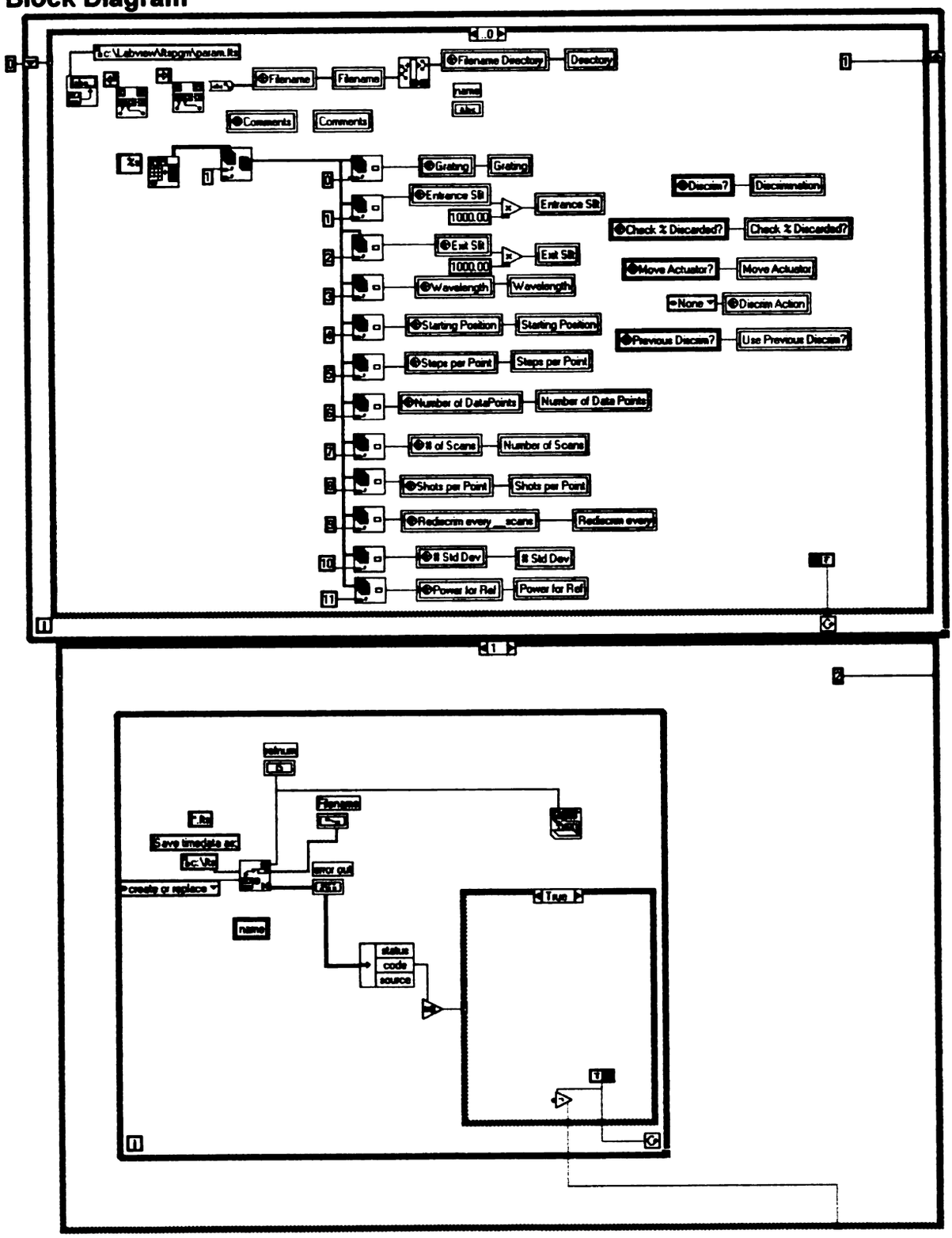

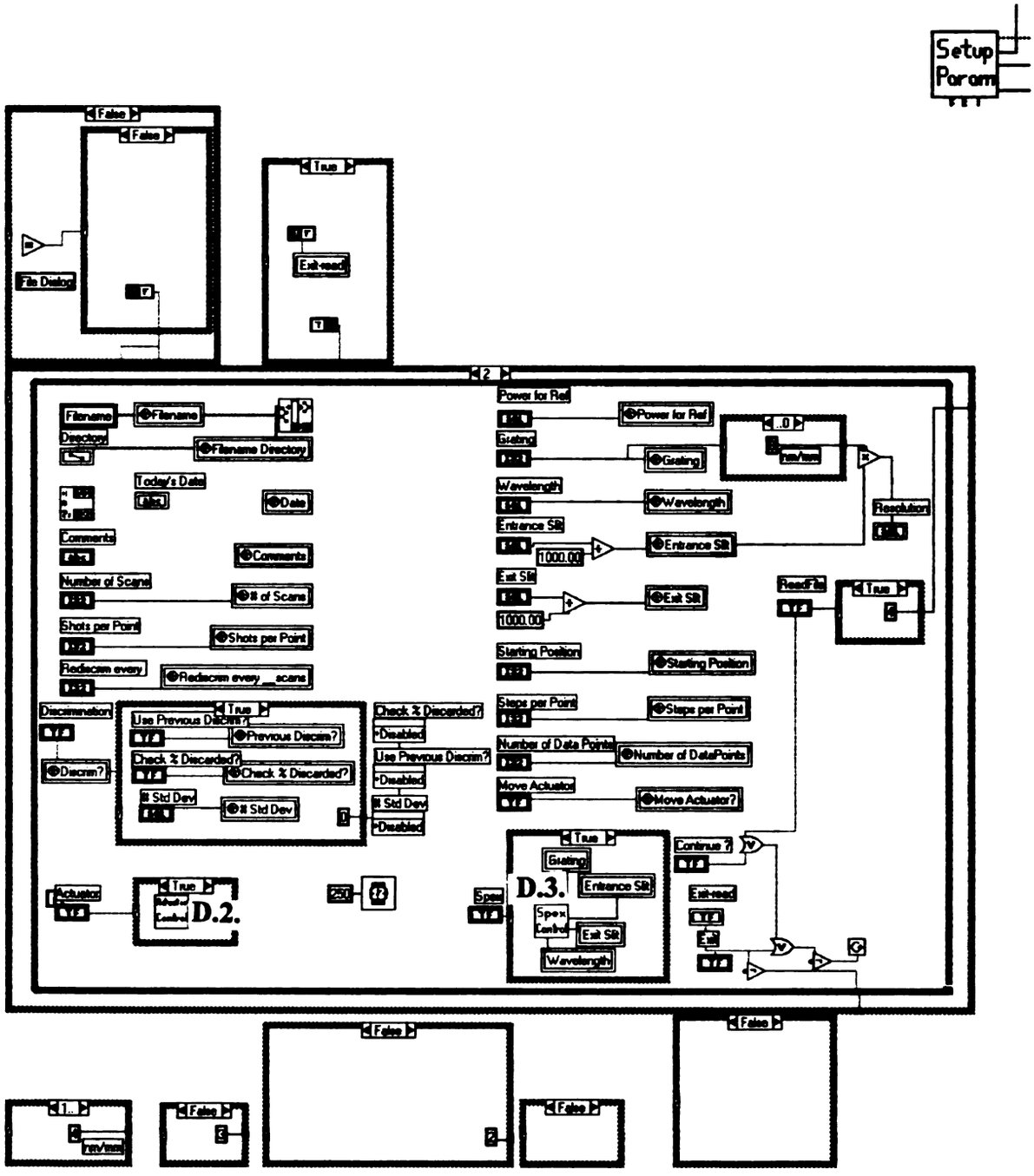
Setup Param
False
False
File Dialog
True
Exit read
2
Filename
Directory
Today's Date
Comments
Number of Scans
Shots per Point
Rediscrim every
Discrimination
Discrim?
Use Previous Discrim?
Check % Discarded?
Std Dev
Actuator
D.2.
250
Power for Ref
Grating
Wavelength
Entrance Slit
Exit Slit
1000.00
Starting Position
Steps per Point
Number of Data Points
Move Actuator?
Resolution
ReadFile
Continue ?
Exit read
Spex
D.3.
Exit Slit
Wavelength
False
False
False
False

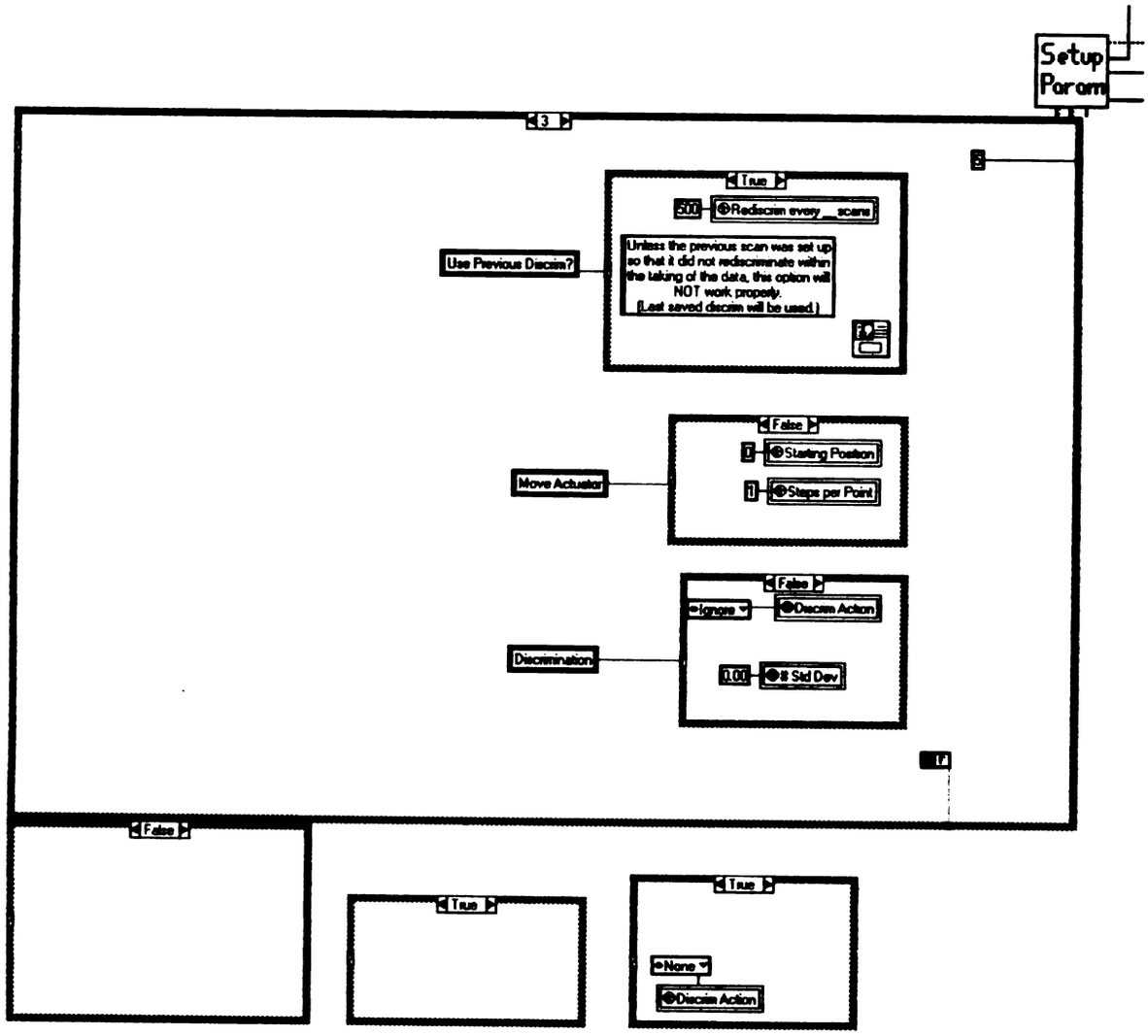
Setup Param
3
True
500
Rediscrim every __ scans
Unless the previous scan was set up so that it did not rediscriminate within the taking of the data, this option will NOT work properly.
(Last saved decrim will be used.)
Use Previous Discrim?
False
Starting Position
Steps per Point
Move Actuator
False
Ignore
Discrim Action
0.00
Std Dev
Discrimination
False
True
True
None
Discrim Action

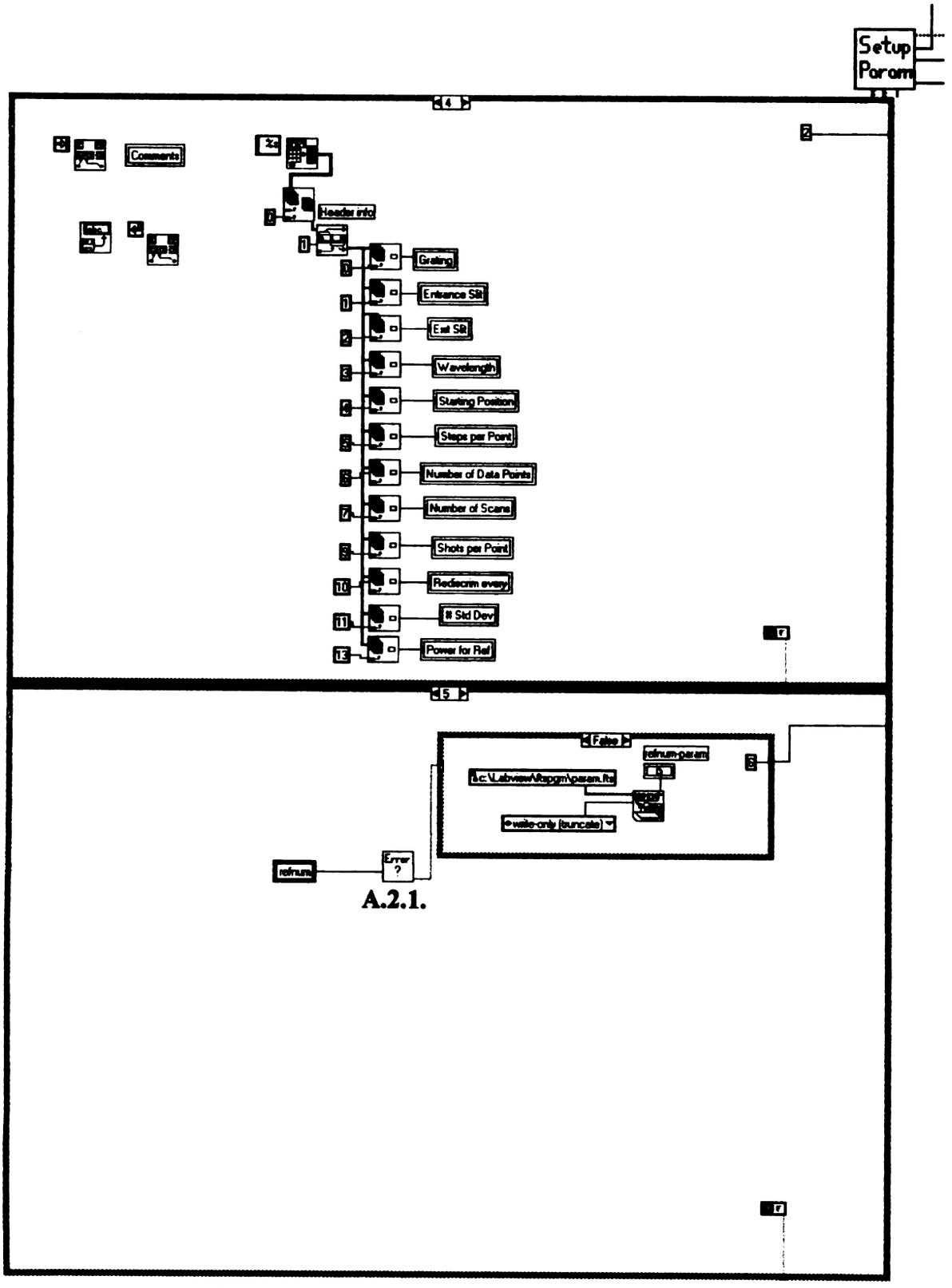
Setup Param
4
2
Comments
Header info
Grating
Entrance Slit
Exit Slit
Wavelength
Starting Position
Steps per Point
Number of Data Points
Number of Scans
Shots per Point
Rediscrm every
Std Dev
Power for Ref
5
False
refnum-param
c:\Labview\fitapgm\param.ttx
write-only (truncate)
refnum
Error ?

A.2.1.

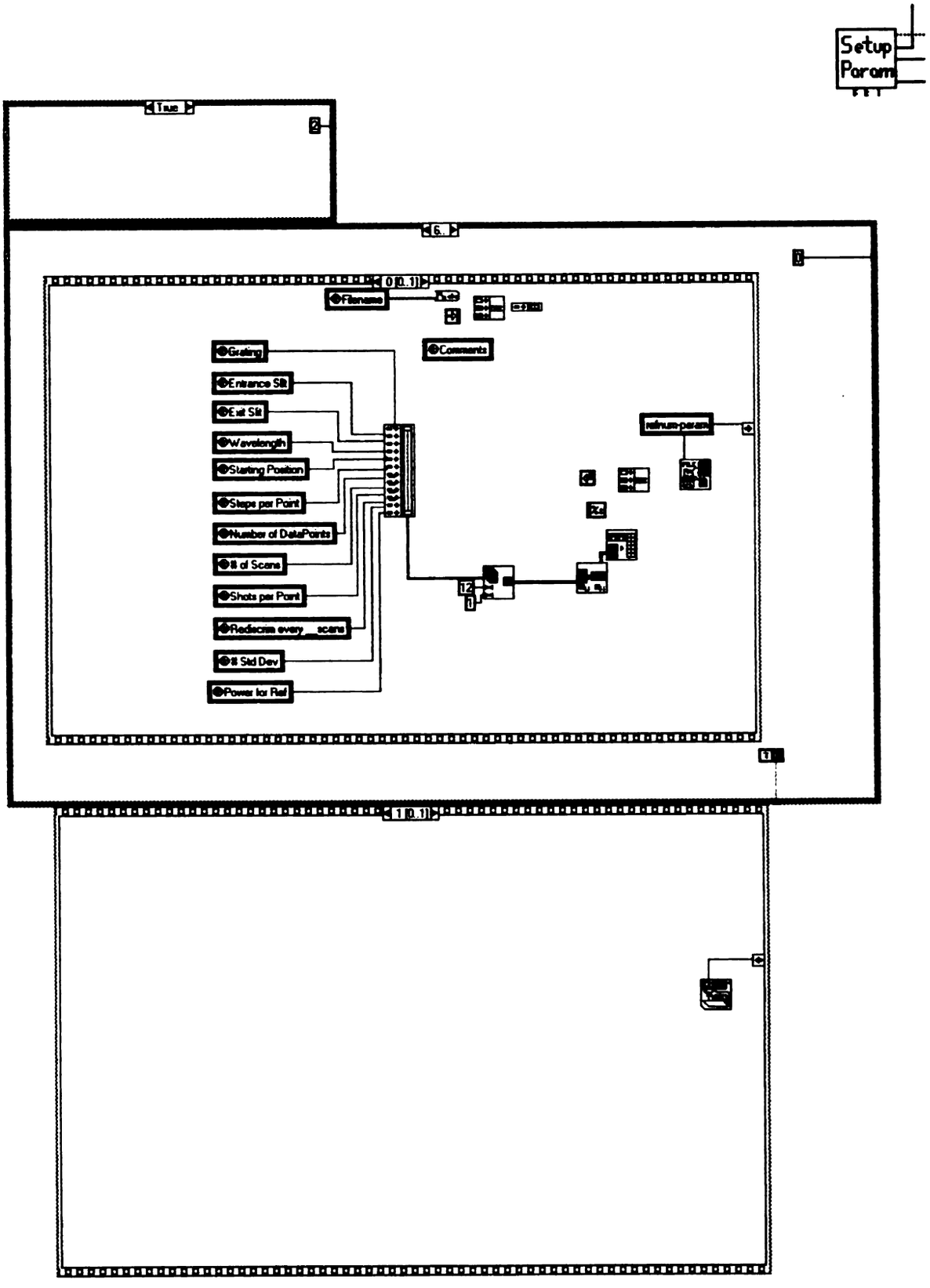
Setup Param
True
2
6
0 [0..1]
Filename
Comments
Grating
Entrance Slit
Exit Slit
Wavelength
Starting Position
Steps per Point
Number of DataPoints
# of Scans
Shots per Point
Rediscrim every __ scans
Std Dev
Power for Ref
retrieve-param
1
1 [0..1]

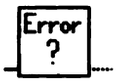

A.2.1. Errorfts.vi (Error ?)

This vi examines the setup parameters for any errors including too many scans, slit size out of usual range, wavelength range and/or grating error, max-min or increment problems. If there is a problem, this vi closes the opened file and the take data vi returns user to parameters setup screen to try again.

Connector Pane

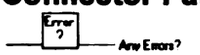

Front Panel

Block Diagram

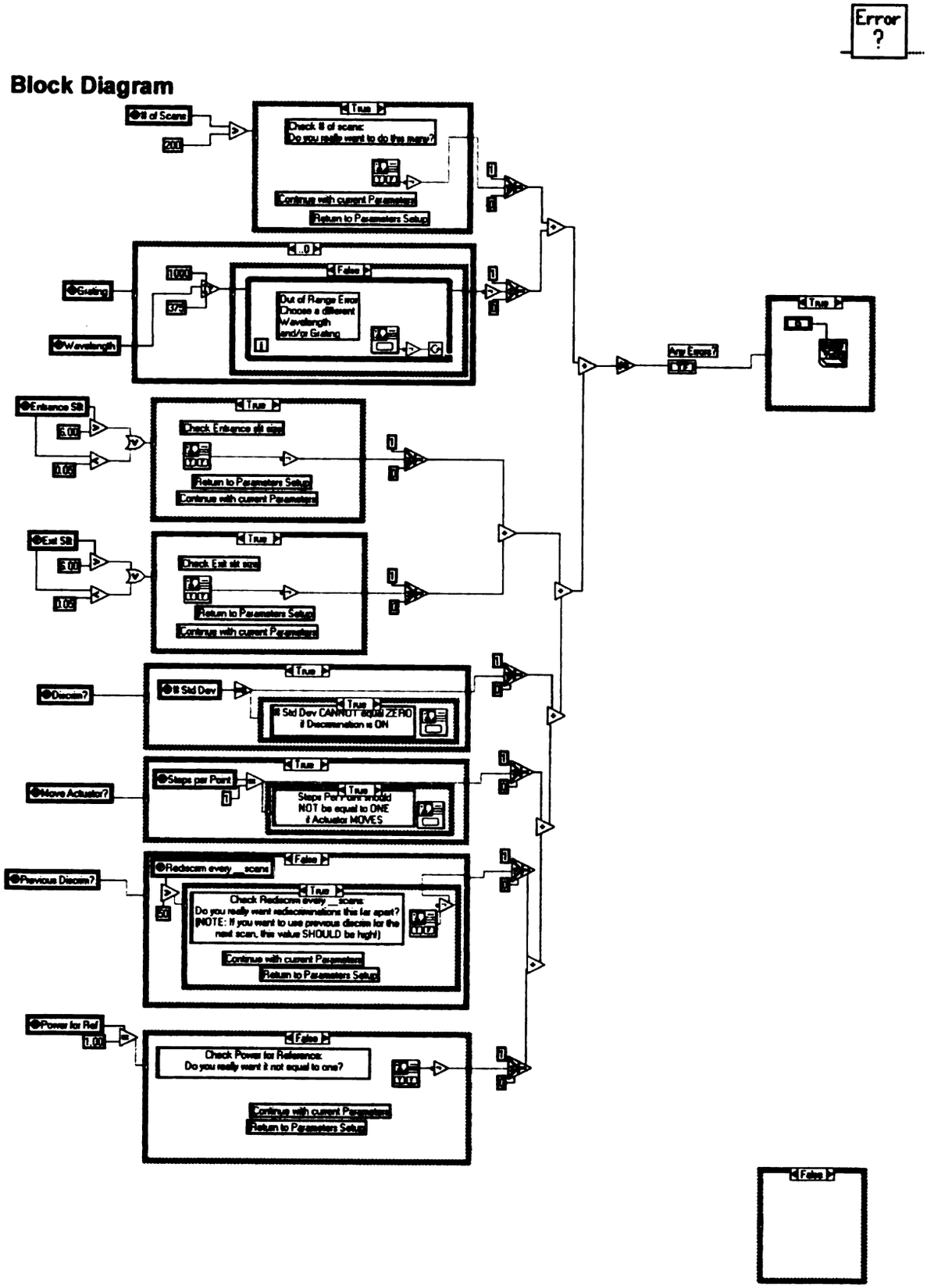

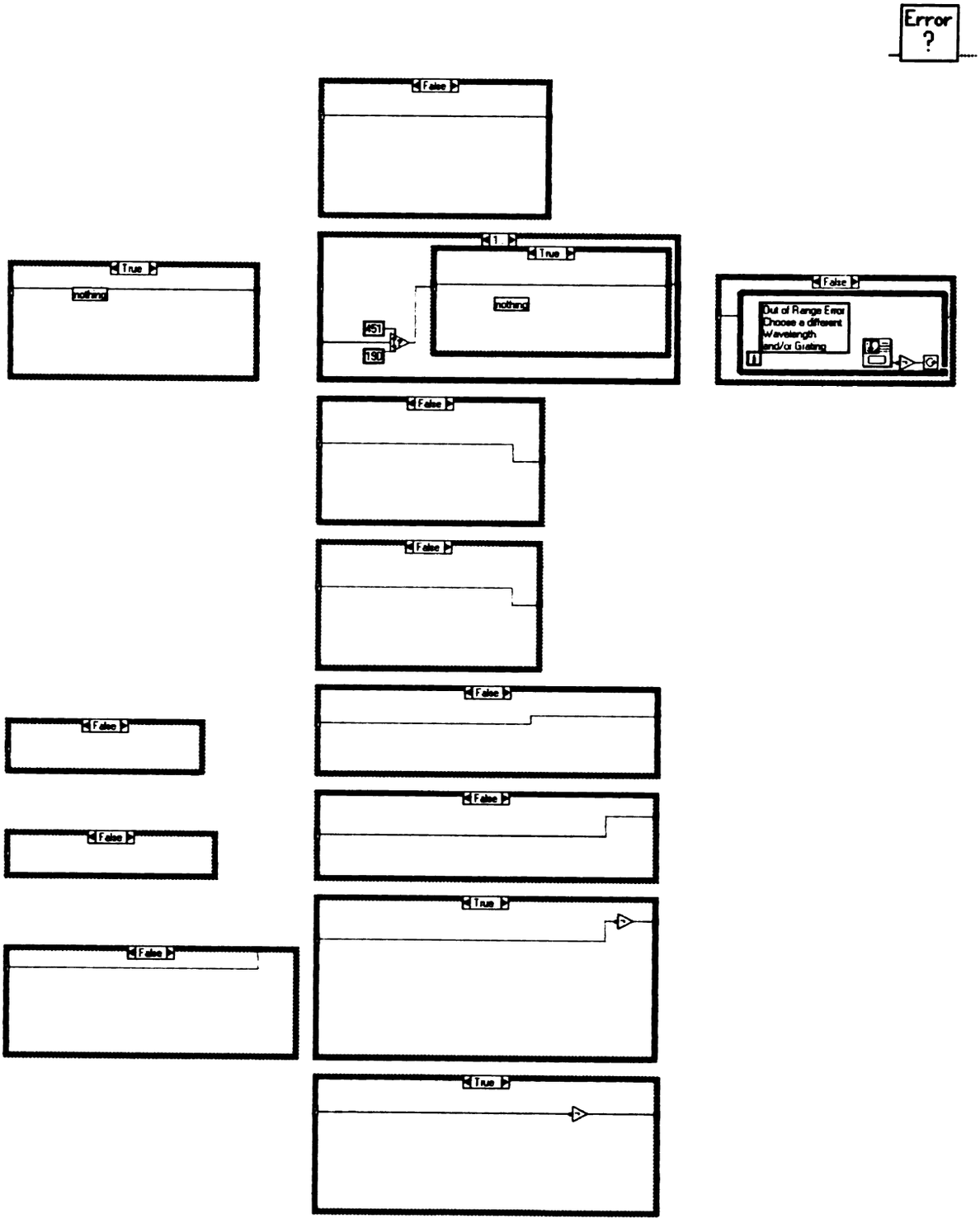
Error
?
False
True
nothing
1
True
nothing
451
191
False
Out of Range Error
Choose a different
Wavelength
and/or Grating
False
False
False
False
False
False
True
True

A.3. Testfts.vi (Test file Setup)

This vi opens the intermediate files (to save every 10 scans incrementally). It opens them, closes them and then opens them in the write-only truncate mode so that the file is overwritten each time a new scan completes successfully.

Connector Pane

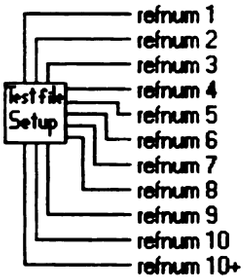

Front Panel

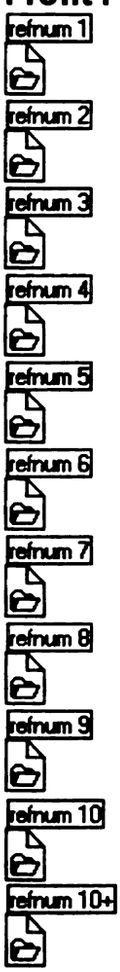

Block Diagram

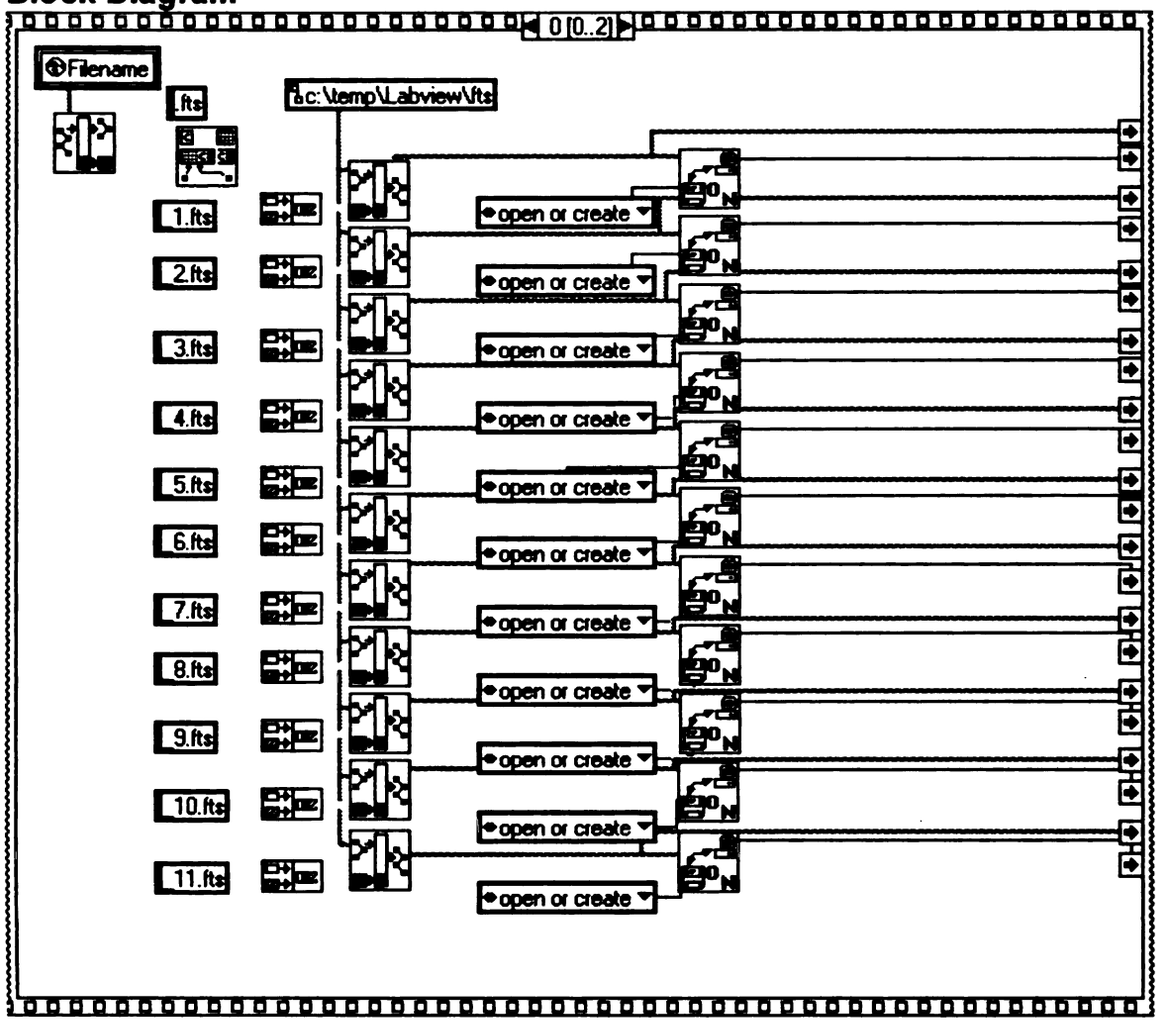

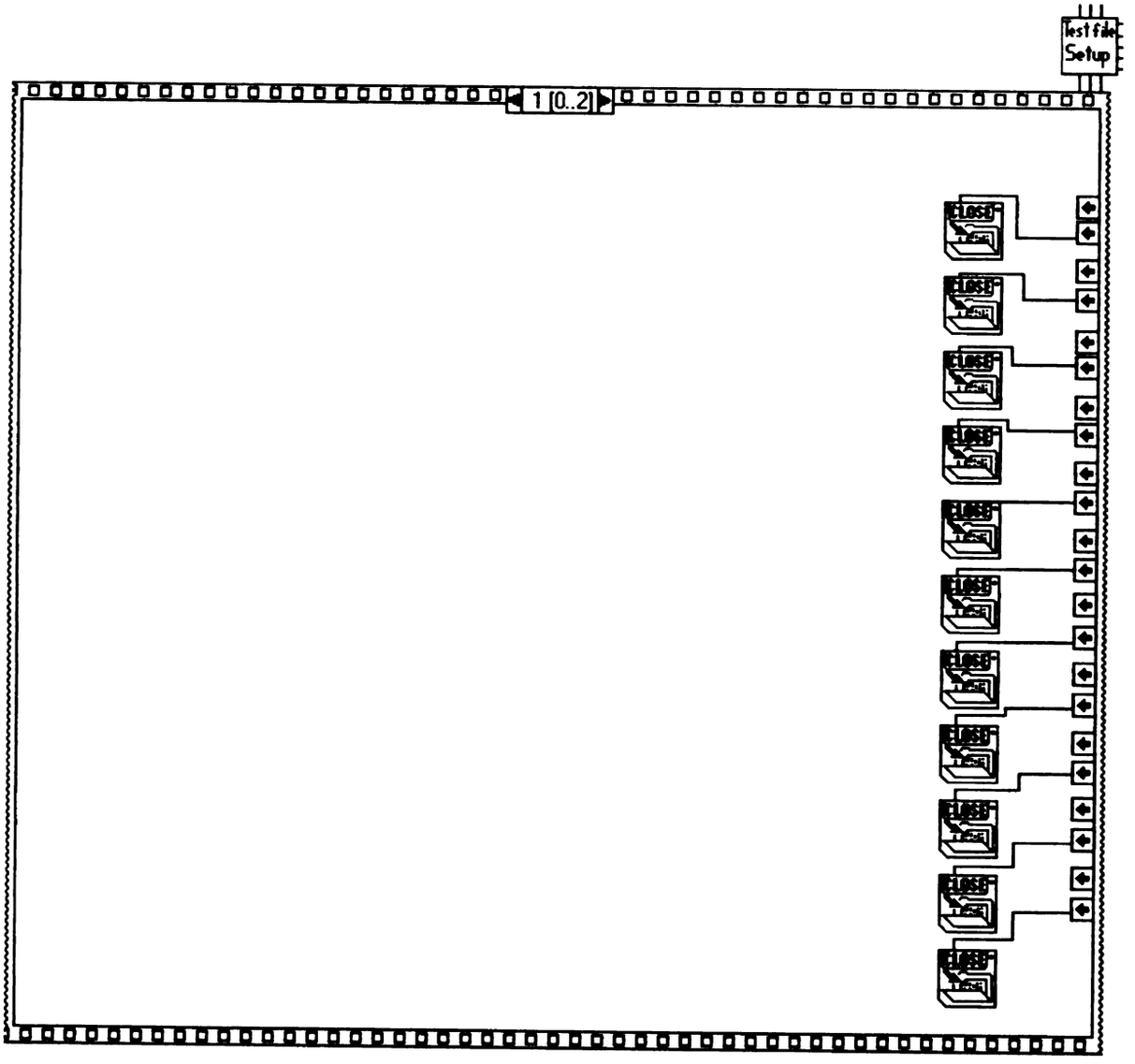
Test file
Setup
1 [0..2]

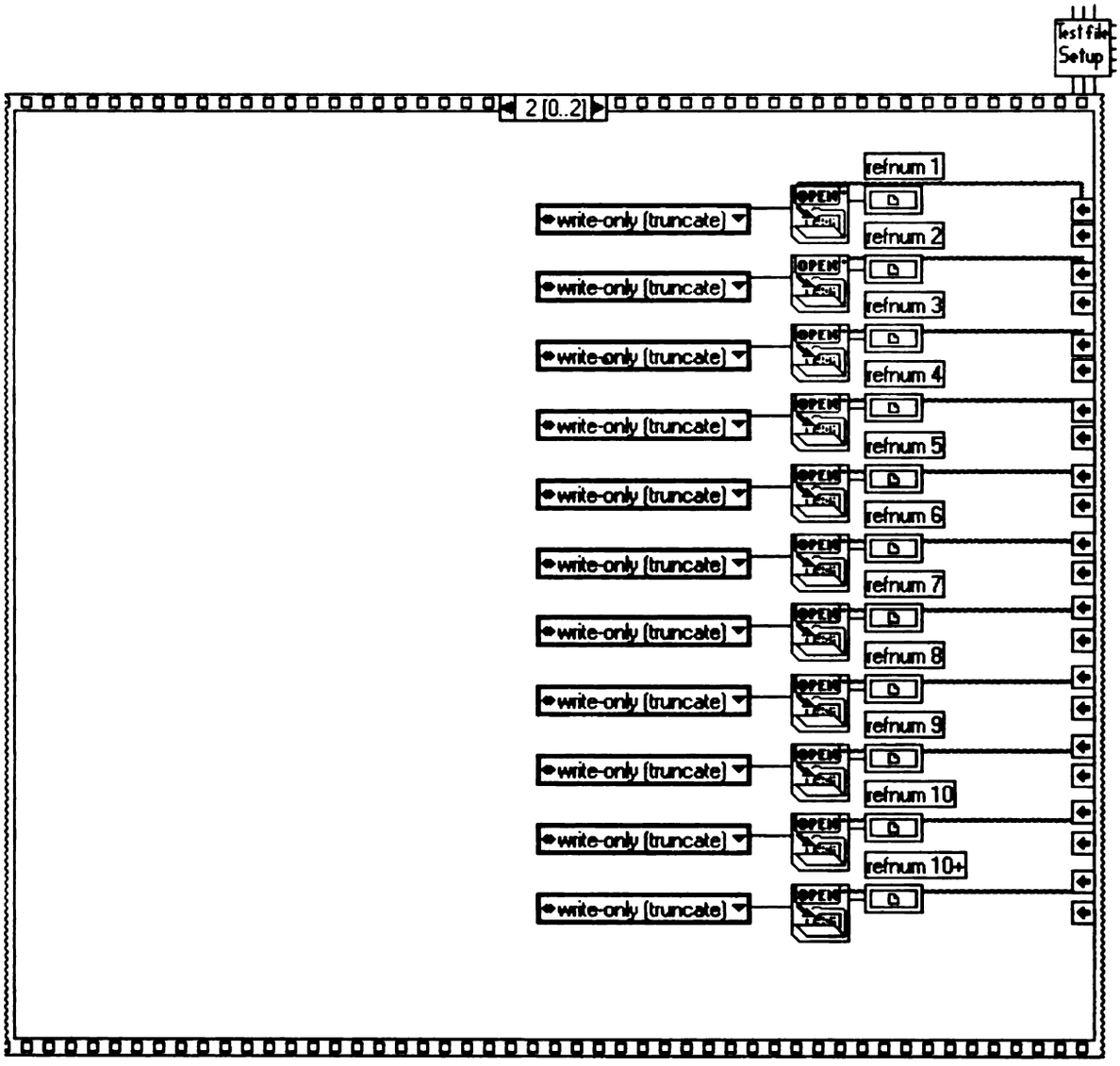
Test file Setup
2 [0..2]
write-only (truncate)
write-only (truncate)
write-only (truncate)
write-only (truncate)
write-only (truncate)
write-only (truncate)
write-only (truncate)
write-only (truncate)
write-only (truncate)
write-only (truncate)
write-only (truncate)
refnum 1
refnum 2
refnum 3
refnum 4
refnum 5
refnum 6
refnum 7
refnum 8
refnum 9
refnum 10
refnum 10+

A.4. Headerfts.vi (Header)

This vi assimilates the setup parameters into a header cluster that is used by other vi's.

Connector Pane

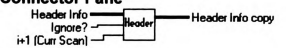

Front Panel

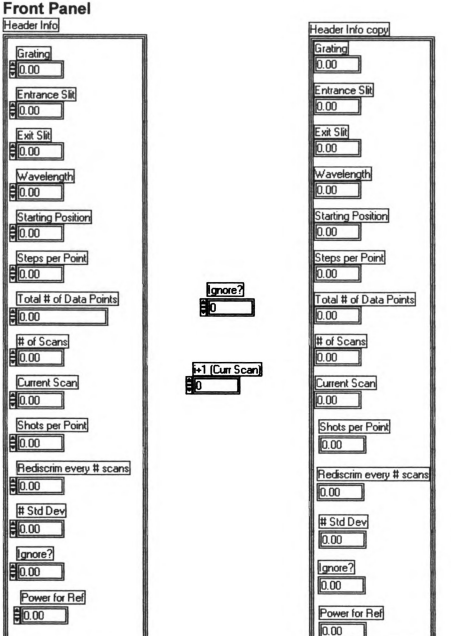

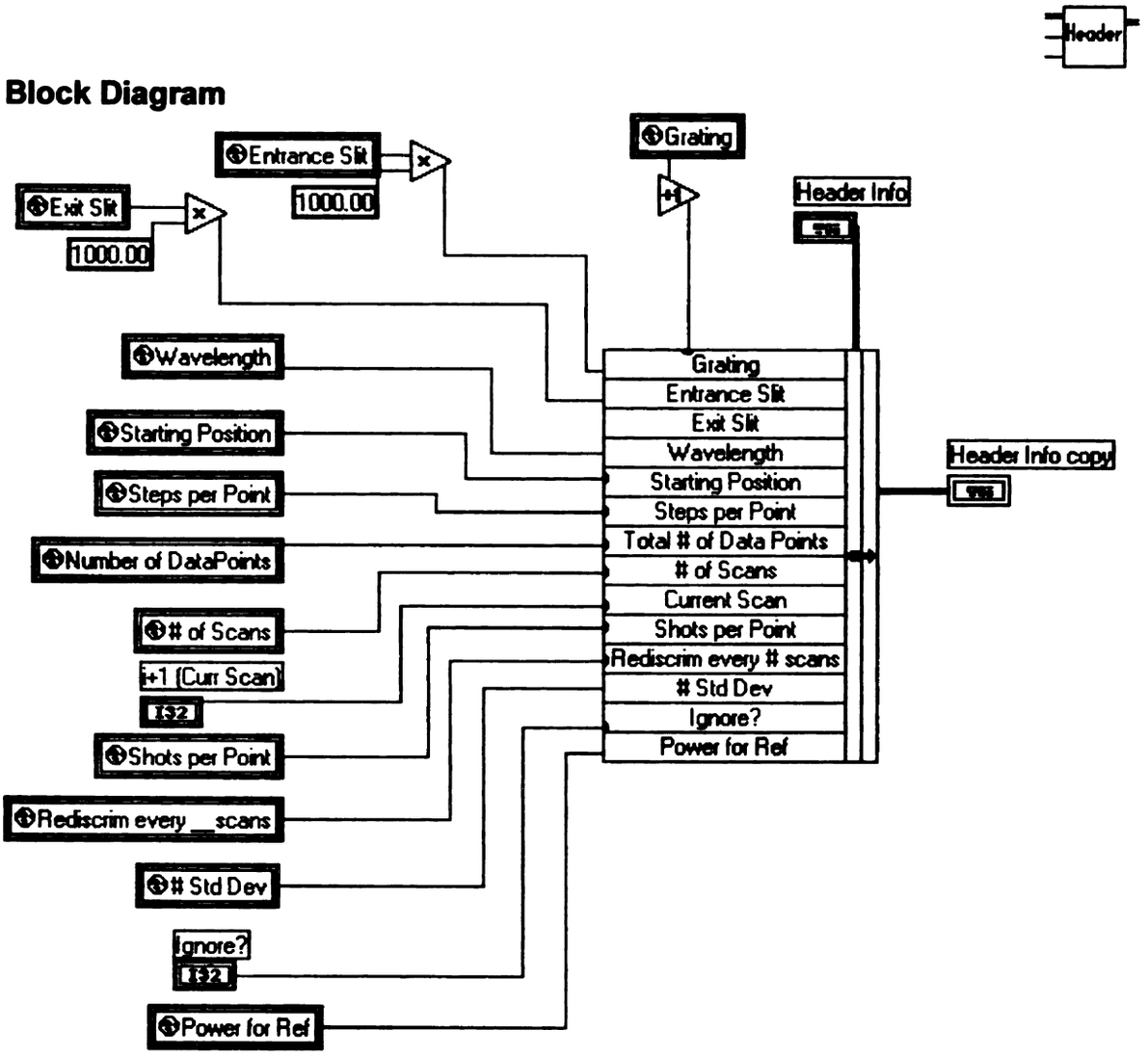
Header
Block Diagram
Entrance Slit
1000.00
Exit Slit
1000.00
Grating
Header Info
Wavelength
Starting Position
Steps per Point
Number of DataPoints
# of Scans
i+1 (Curr Scan)
I32
Shots per Point
Rediscrim every __ scans
Std Dev
Ignore?
I32
Power for Ref
Grating
Entrance Slit
Exit Slit
Wavelength
Starting Position
Steps per Point
Total # of Data Points
# of Scans
Current Scan
Shots per Point
Rediscrim every # scans
Std Dev
Ignore?
Power for Ref
Header Info copy

A.5. rediscrimfts.vi (Rediscr)

This vi takes 500 shots of data from the reference diode to determine the maximum and minimum values for the discrimination. The SRS 245 vi is written to compute max/min based on user preference for standard deviation. The max and min determined for discrimination is then passed back to takefts vi.

Connector Pane

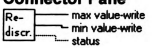

Front Panel

Block Diagram

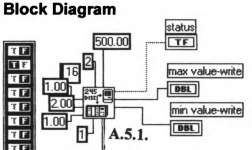

A.5.1. SR 245_rediscr_fts2.vi (245 DISC)

This vi is a variation on the SRS 245 vi from NI. This vi allows for input of GBIP, scan channels, # of scans, trigger setting and gives output of status and maximum and minimum values for discrimination. It determines these values from global variable defined by user for method of discrimination (standard deviation).

Connector Pane

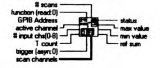

Front Panel

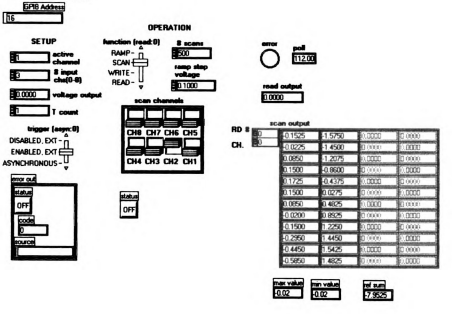

Block Diagram

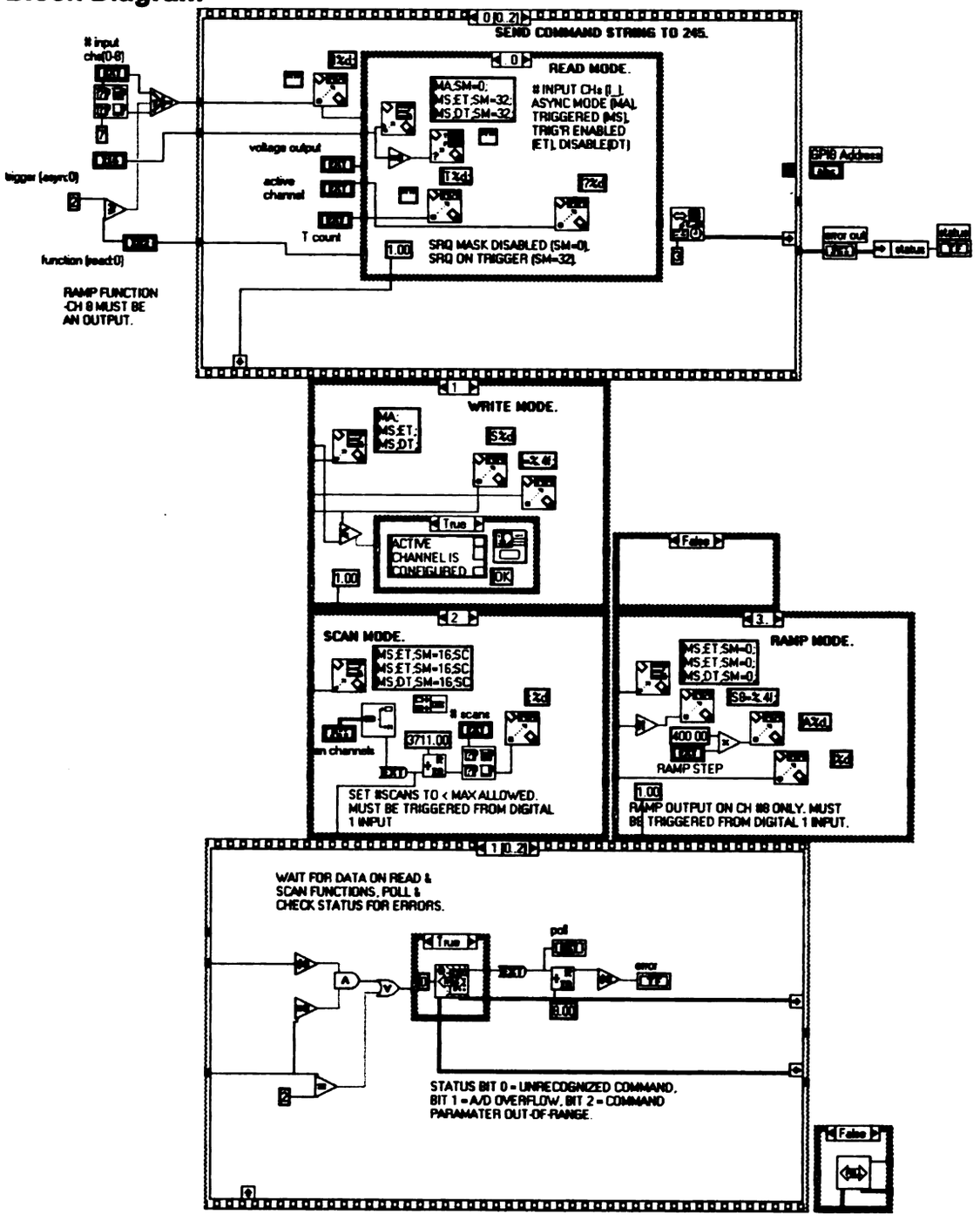

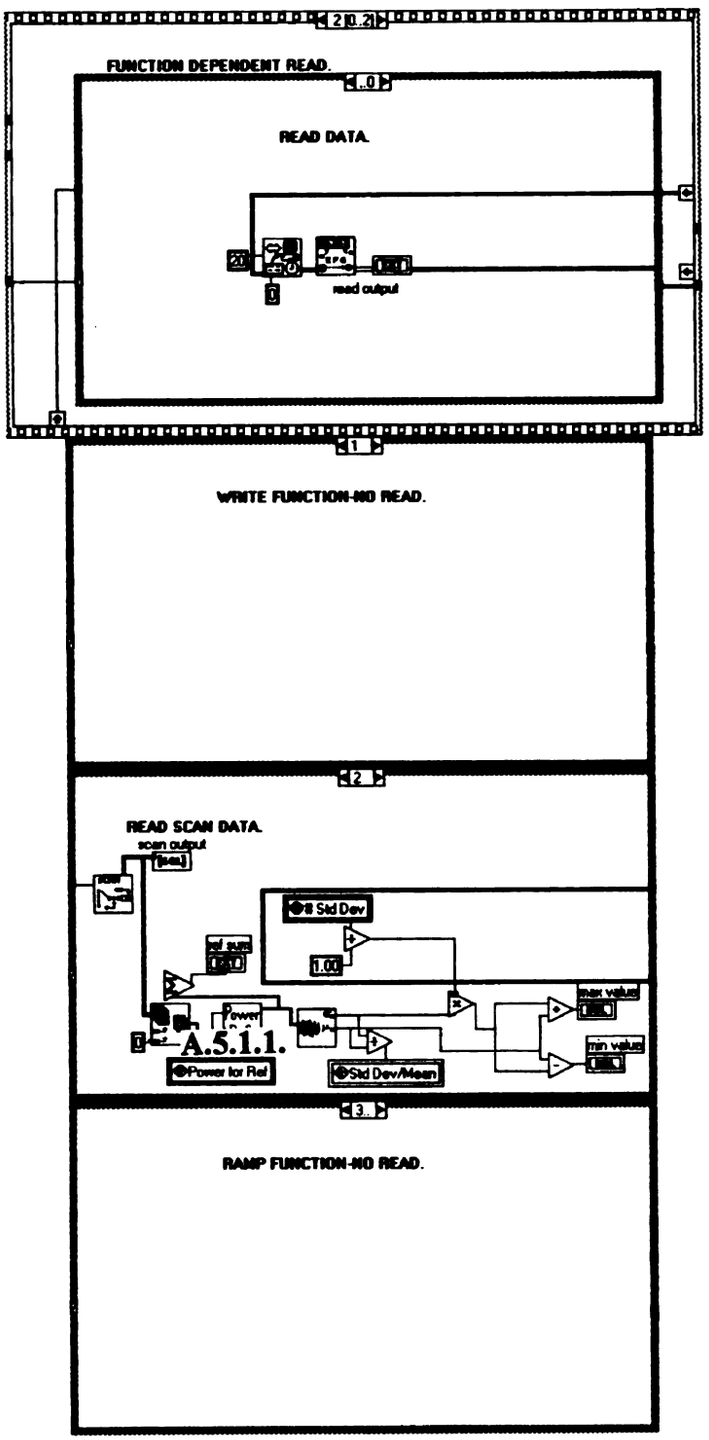
2 [0..2]
FUNCTION DEPENDENT READ.
..0
READ DATA.
20
0
read output
1
WRITE FUNCTION-NO READ.
2
READ SCAN DATA.
scan output
[beam]
ref num
0
Power
Power for Ref
A.5.1.1.
fit Std Dev
1.00
Std Dev/Mean
max value
min value
3..
RAMP FUNCTION-NO READ.

A.5.1.1. refpower.vi (Power Ref)

This vi allows for raising each data point to a particular power before summing the final transient. (This is important for multiphoton experiments - You cannot sum and then raise to a power.)

Connector Pane

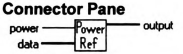

Front Panel

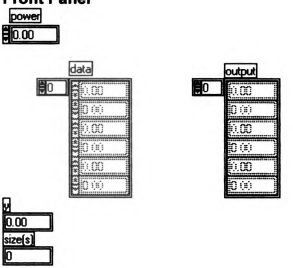

Block Diagram

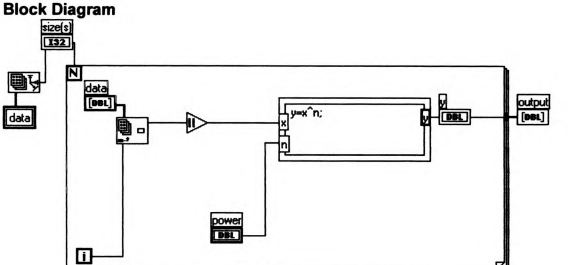

A.6. discrimdatafts2.vi (Discrimin)

This vi takes discriminated data (reference max/min determined by rediscrim vi). If a long wait occurs, vi asks user for action to take- ignore discrimination, ignore until next preset discrimination, ignore until end of scan then rediscriminate, or rediscriminate now. If the last option is chosen and a long wait occurs again, the computer alerts the user but will then take data by ignore discrimination until end of scan and then rediscriminate. If any ignore type options are chosen in the first screen, ignore becomes true within this vi and is transferred back to take data vi so that other data acquision vi (non-discrimination) is used until proper time for rediscrimination (depends on option chosen).

Connector Pane

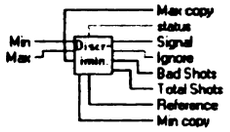

Front Panel

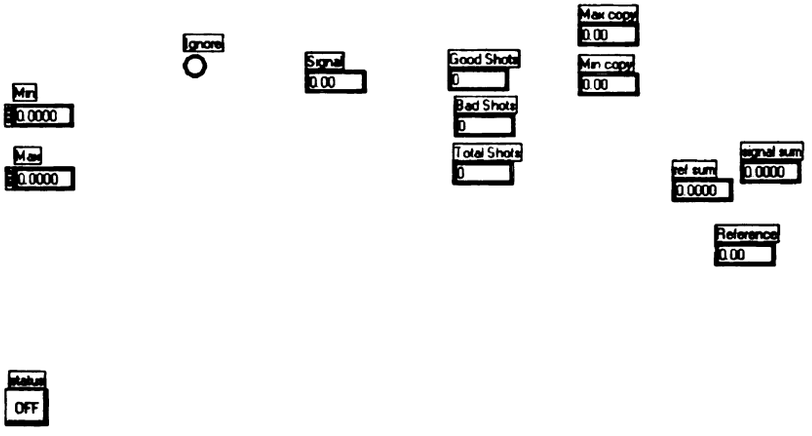

Discr-
imin.

Block Diagram

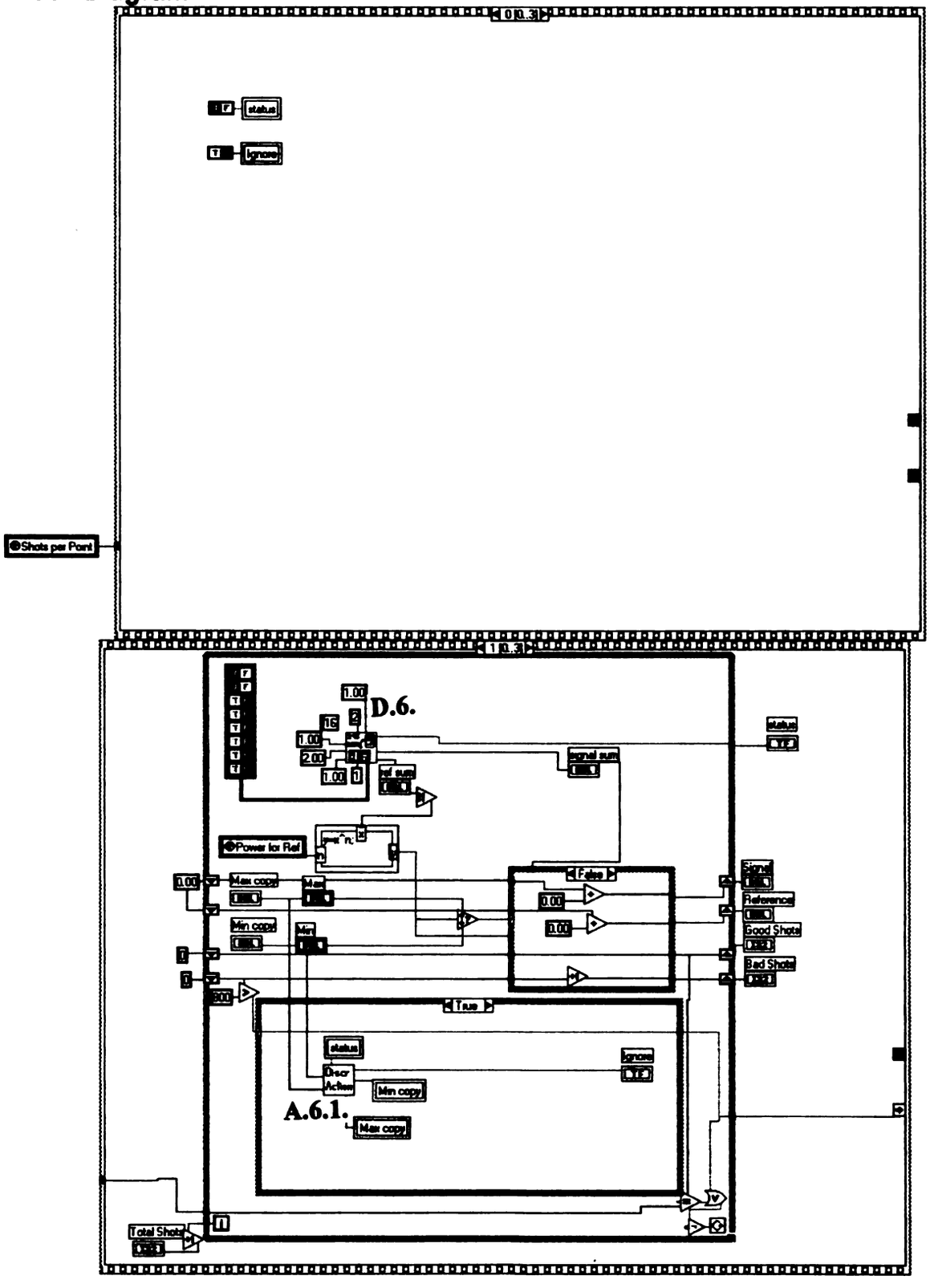

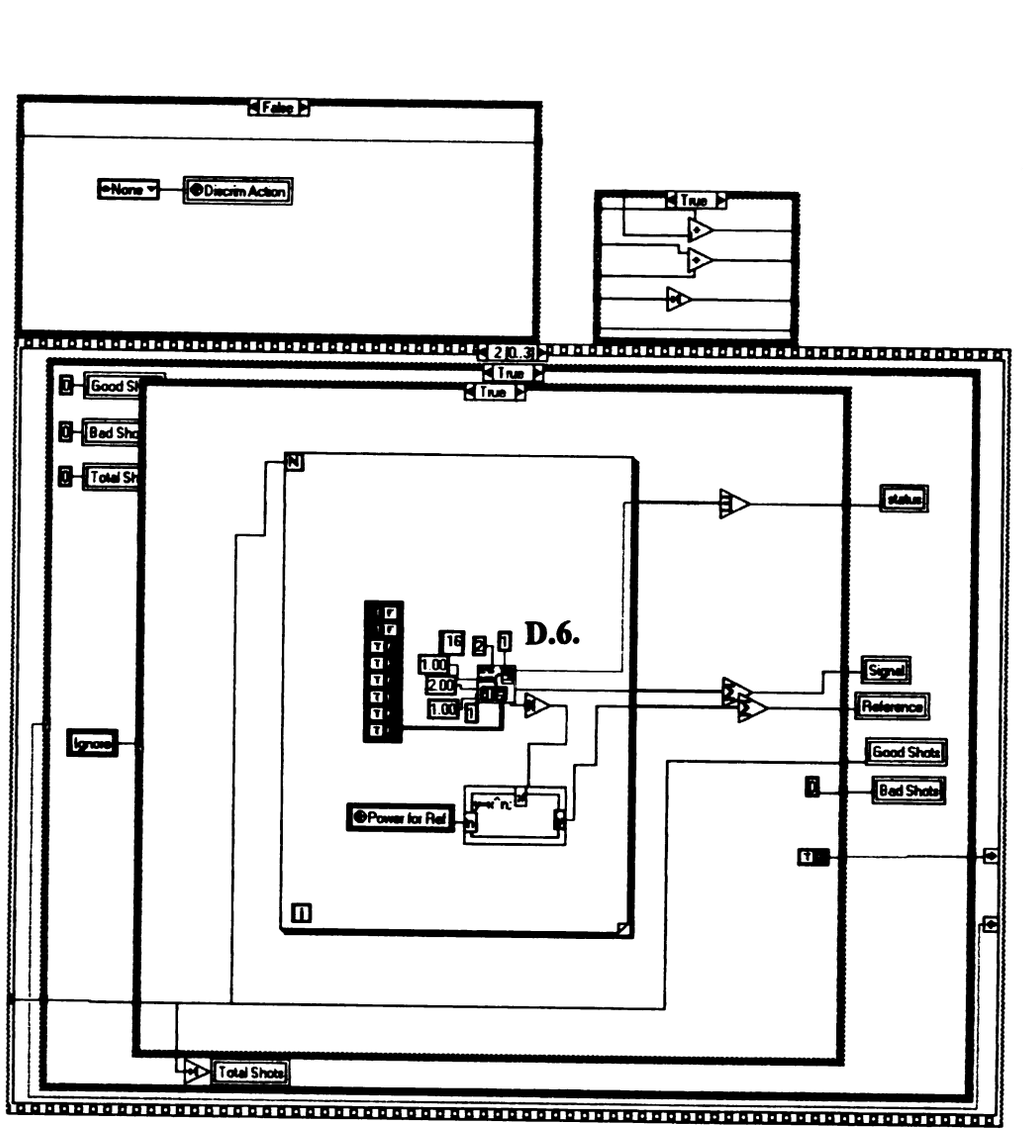
Discr-
imin.
False
None
Discrim Action
True
2 [0..3]
True
True
Good Sh
Bad Sho
Total Sh
status
D.6.
16
2
1
1.00
2.00
1.00
0
Signal
Reference
Ignore
Good Shots
Bad Shots
Power for Ref
N
i
Total Shots

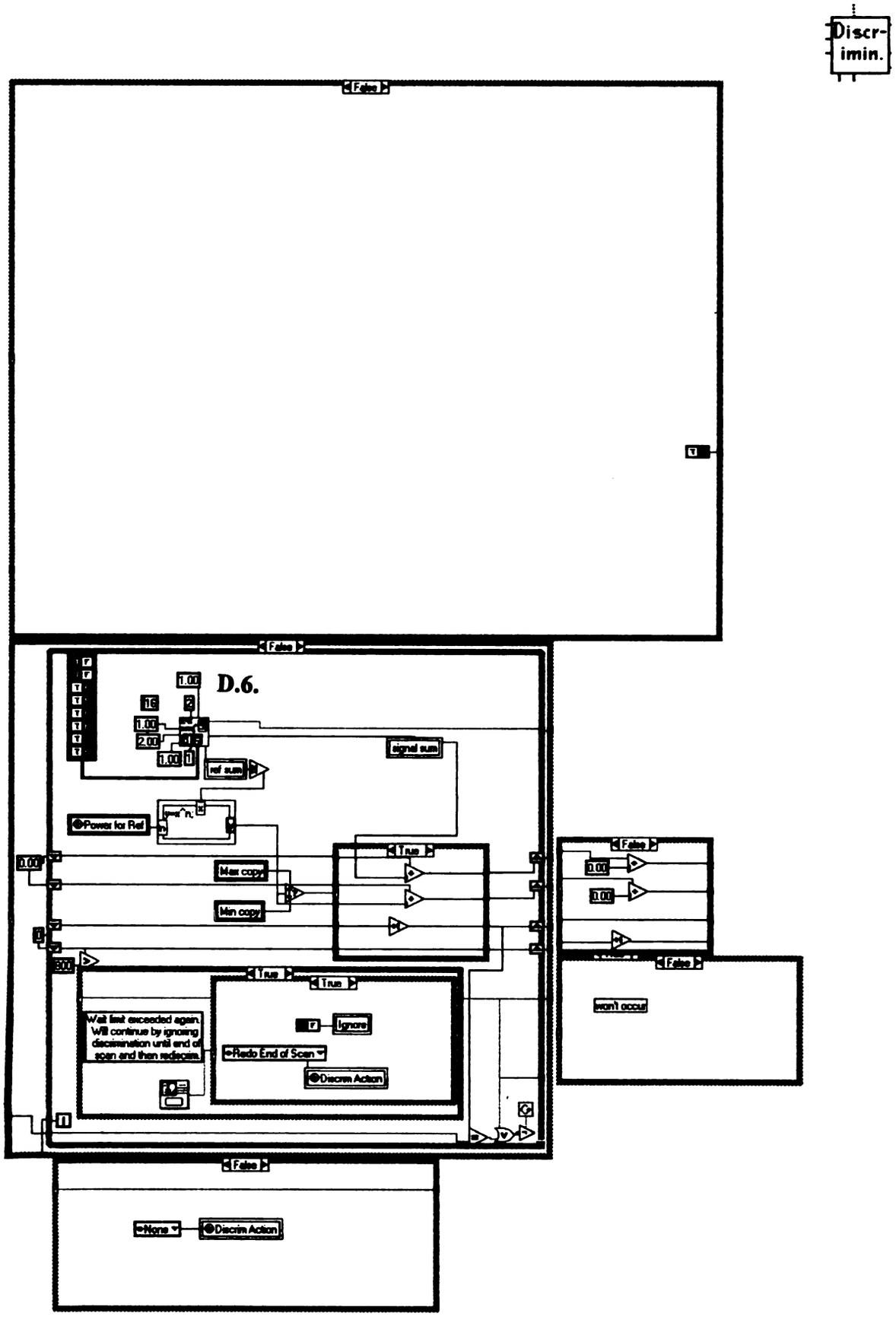
Discr-
imin.
False
D.6.
signal sum
ref sum
Power for Ref
Max copy
Min copy
True
False
won't occur
Wait last exceeded again.
Will continue by ignoring
discrimination until end of
scan and then redoscans.
Ignore
Redo End of Scan
Discrim Action
None
Discrim Action

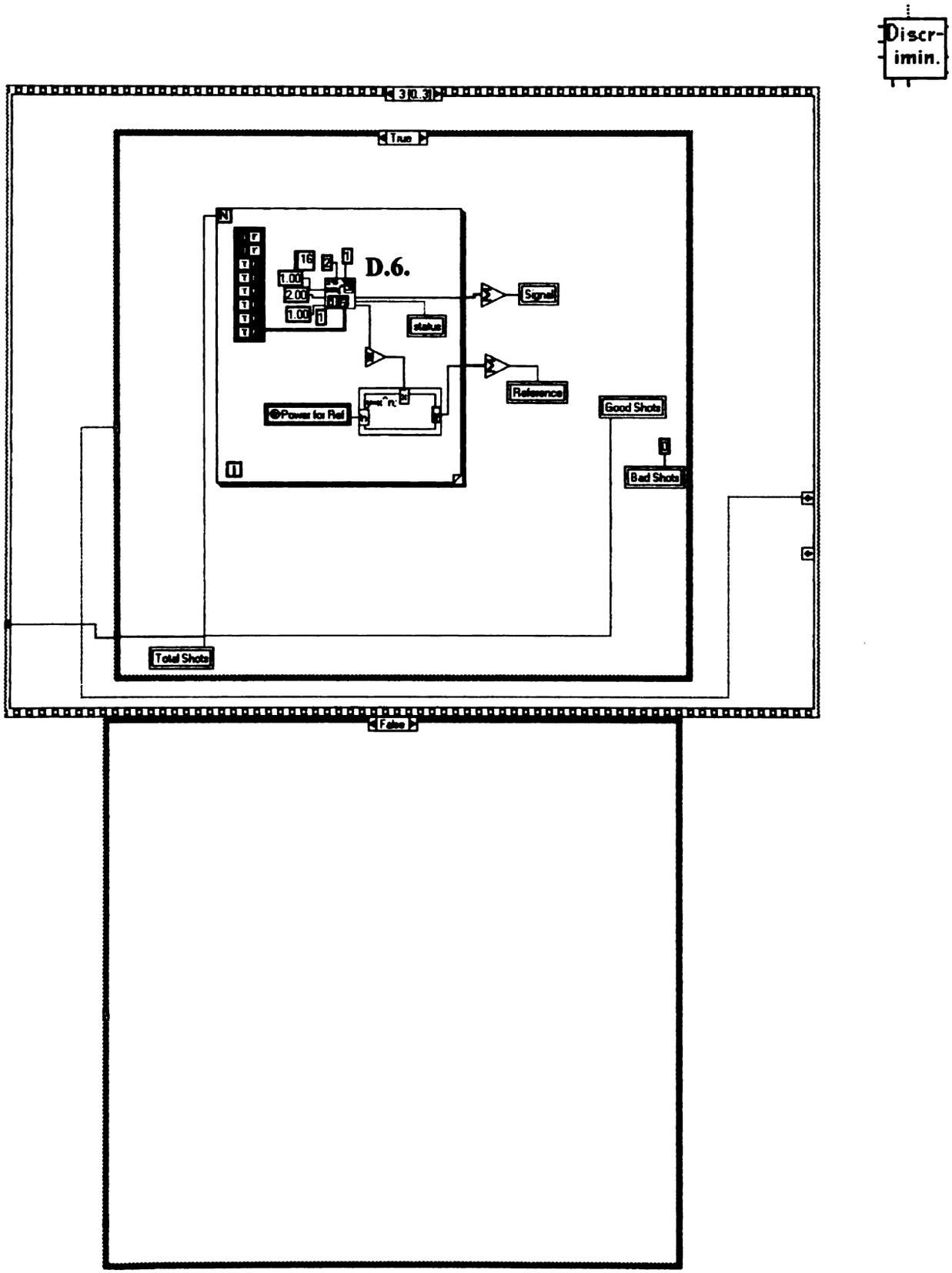
Discr-
imin.
3 [0..3]
True
D.6.
16
2
1.00
2.00
1.00
Signal
status
Reference
Power for Ref
Good Shots
1
Bad Shots
Total Shots
False

A.6.1. discrimactwaitfts.vi (Discr Action)

This is the vi that appears if there are too many bad shots in a row (called wait limit). This alerts user and waits for instruction on options. If redo now is called, this vi reruns rediscrim vi. For the other options, it sets the global variable to proper setting and returns to discrimdata vi.

Connector Pane

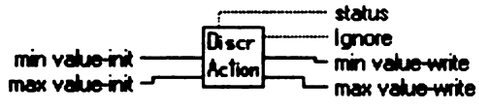

Front Panel

Wait limit exceeded- what would you like to do?

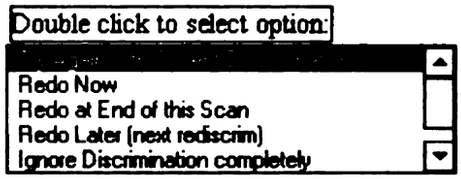

Block Diagram

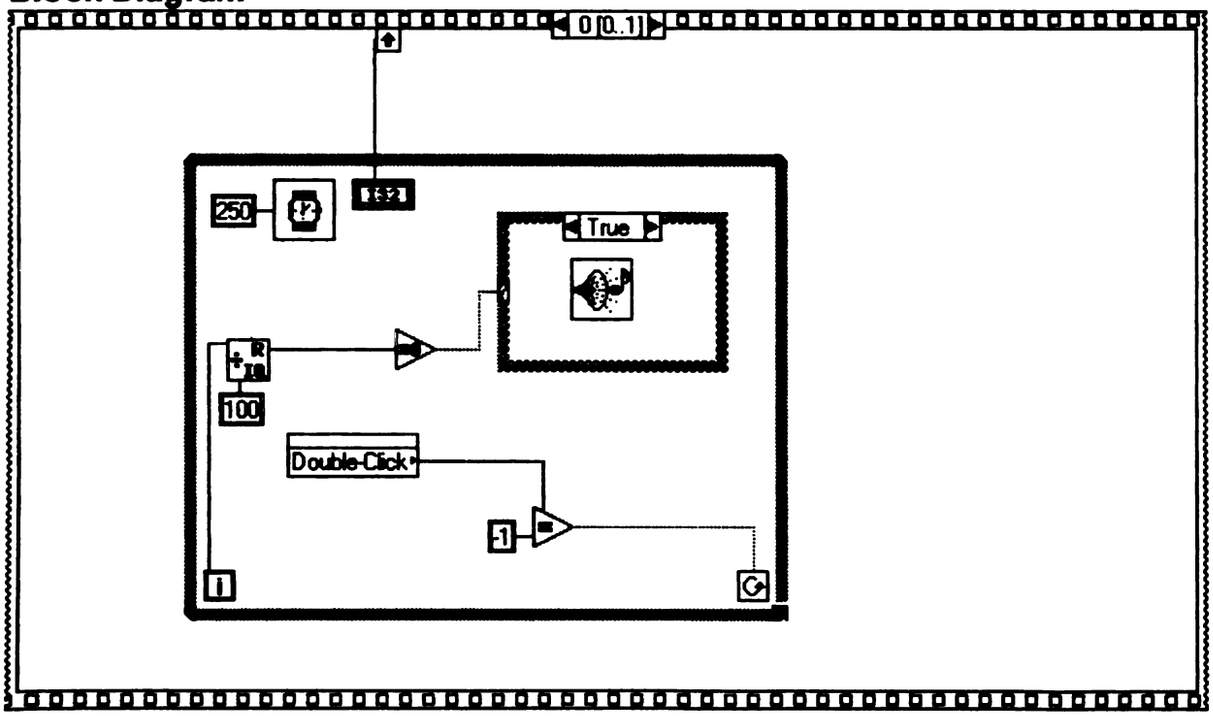

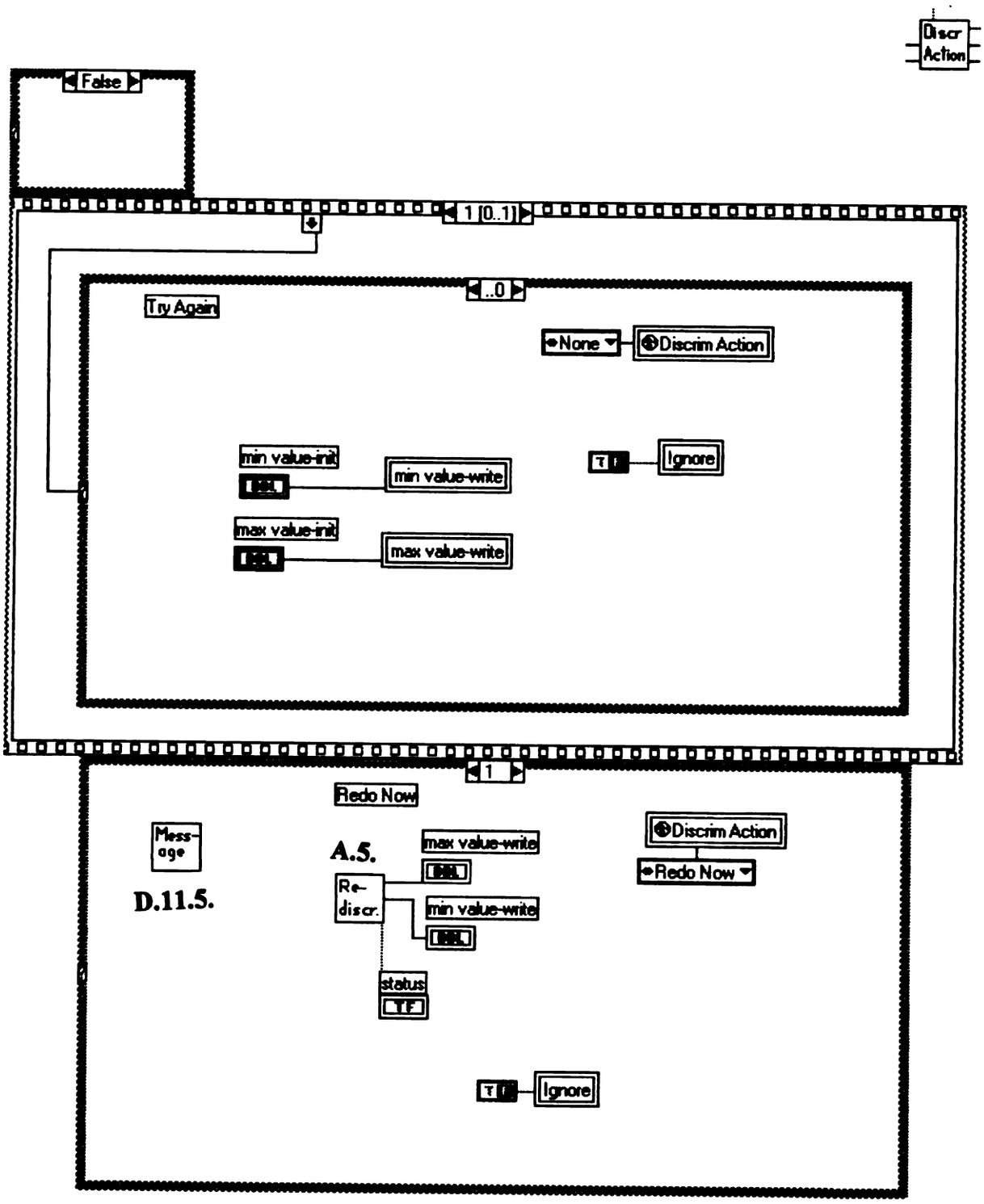
Discr Action
False
1 [0..1]
..0
Try Again
None
Discrim Action
min value-init
min value-write
Ignore
max value-init
max value-write
1
Redo Now
Mess-age
D.11.5.
A.5.
max value-write
Re-discr.
min value-write
status
TF
Discrim Action
Redo Now
Ignore

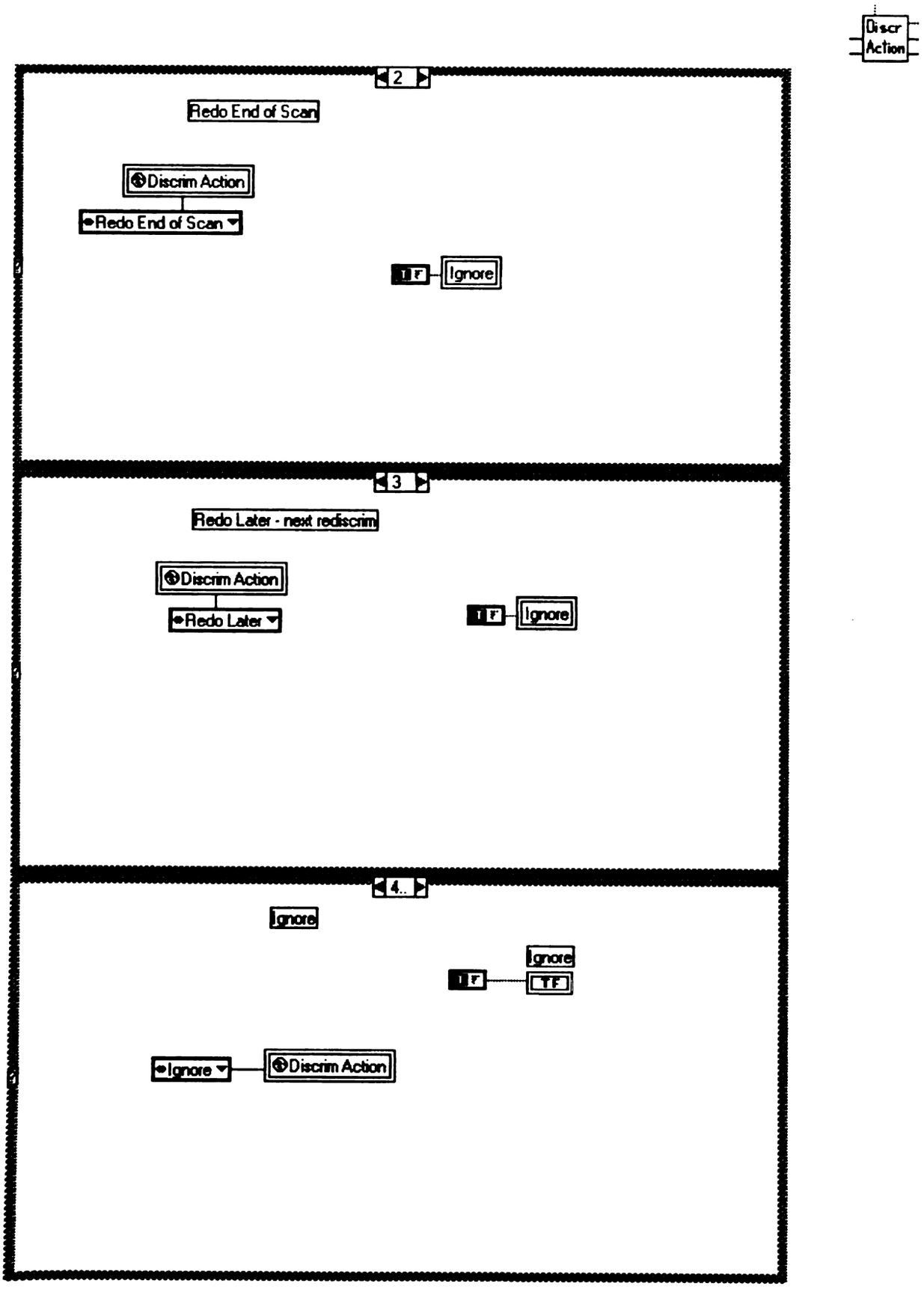
Discr Action
2
Redo End of Scan
Discrim Action
Redo End of Scan
Ignore
3
Redo Later - next rediscrim
Discrim Action
Redo Later
Ignore
4..
Ignore
Ignore
Ignore
Discrim Action

A.7. Savefts.vi (Save Data)

This vi saves the data after each scan completes successfully into one of the intermediate vi's. For example, if the user selects 50 scans total, test1.fts will contain the sum of scans 1-9, test2.fts will contain the sum of scans 1-19, test3.fts is the sum of scans 1-29, etc.

Connector Pane

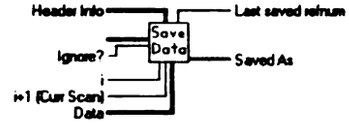

Front Panel

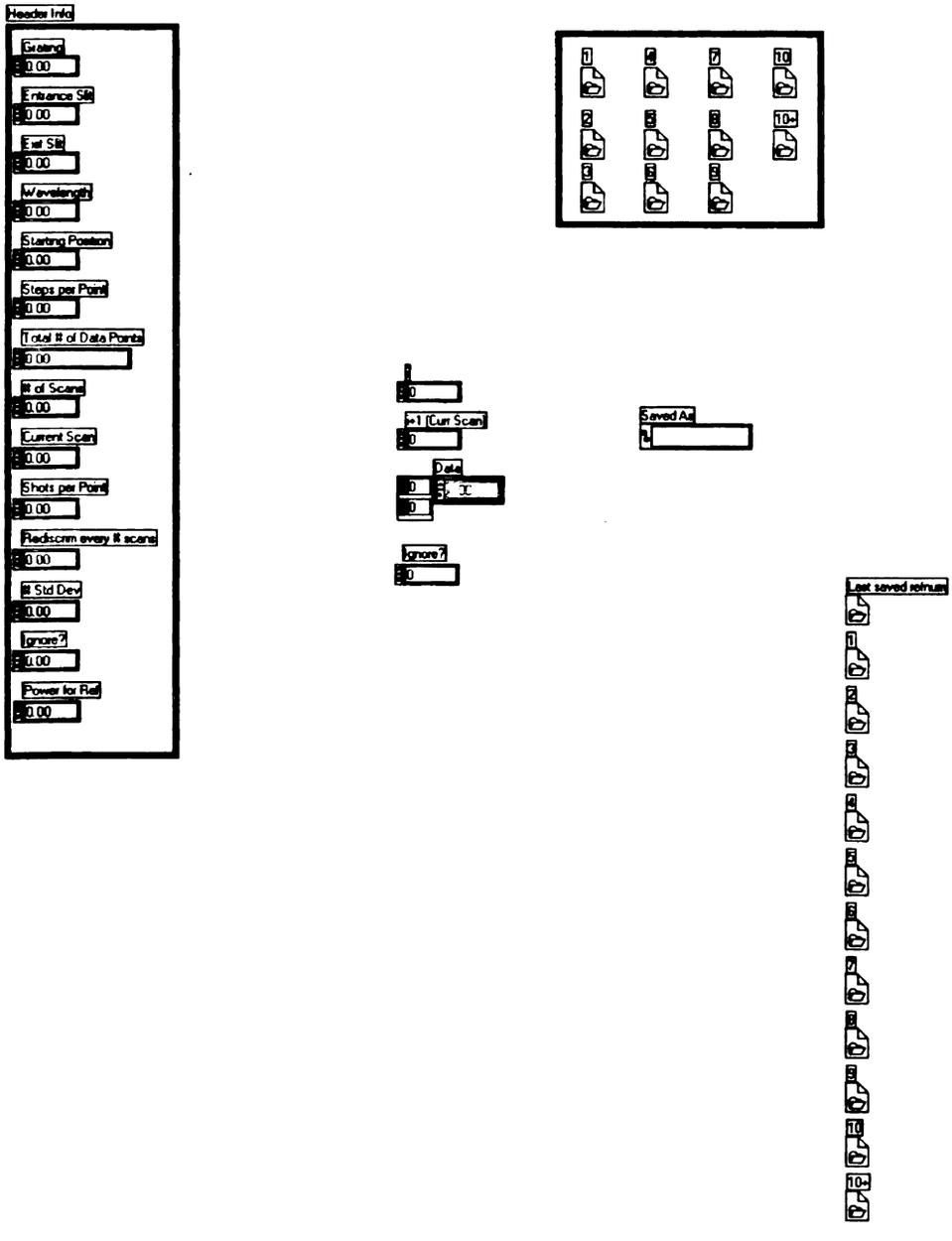

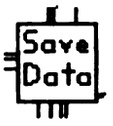

Block Diagram

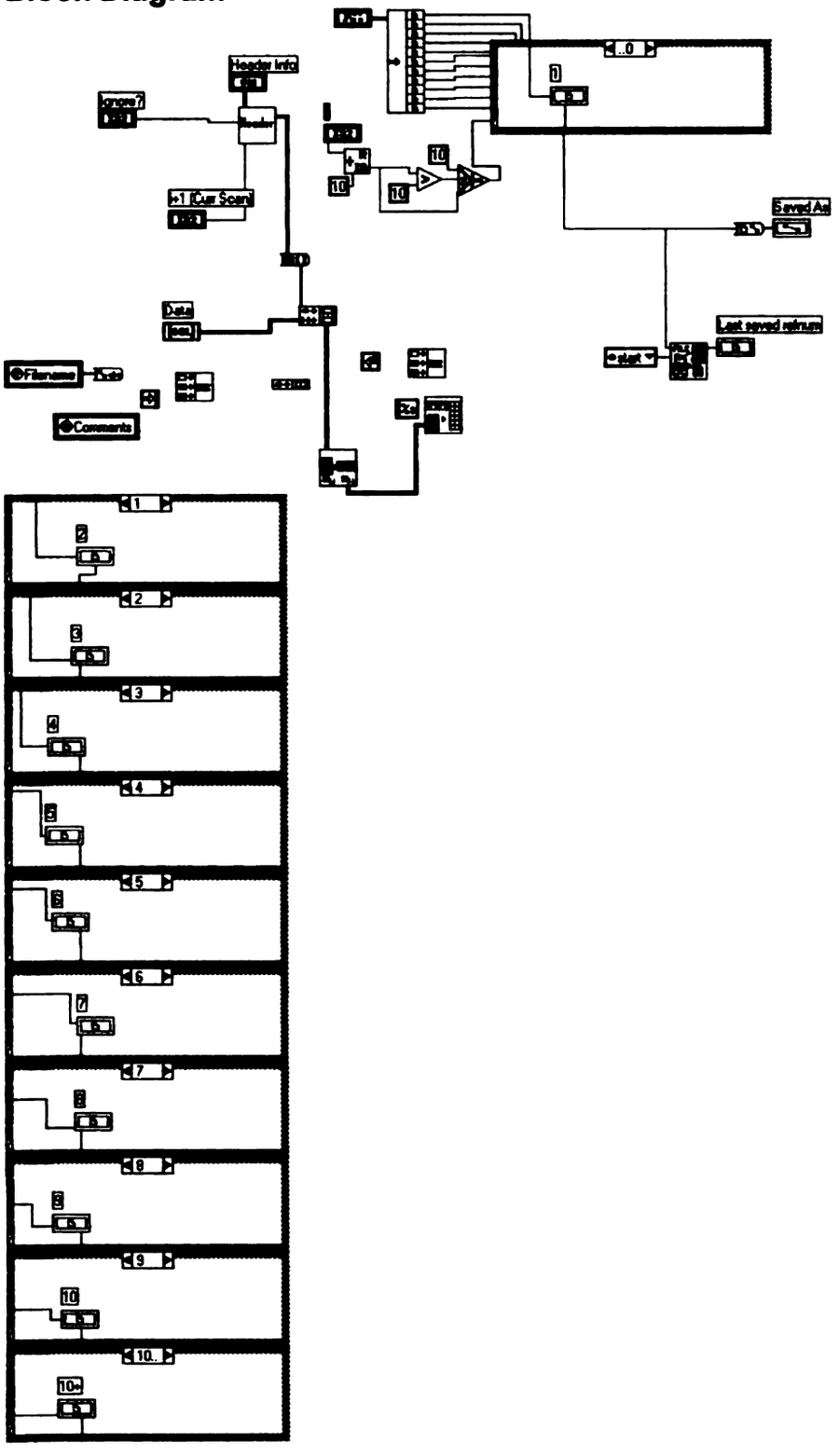

A.8. discrimactperfts.vi (Discr Action)

This is the vi that appears if the percentage discarded is too high. This alerts user and waits for instruction on options. For the options, it sets the global variable to proper setting and returns to discrimdata vi.

Connector Pane

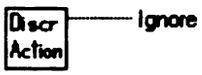

Front Panel

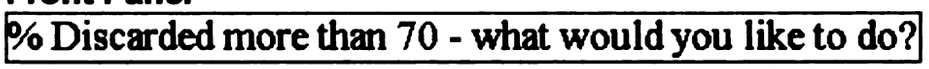

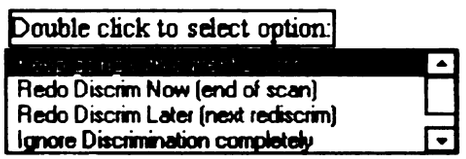

Block Diagram

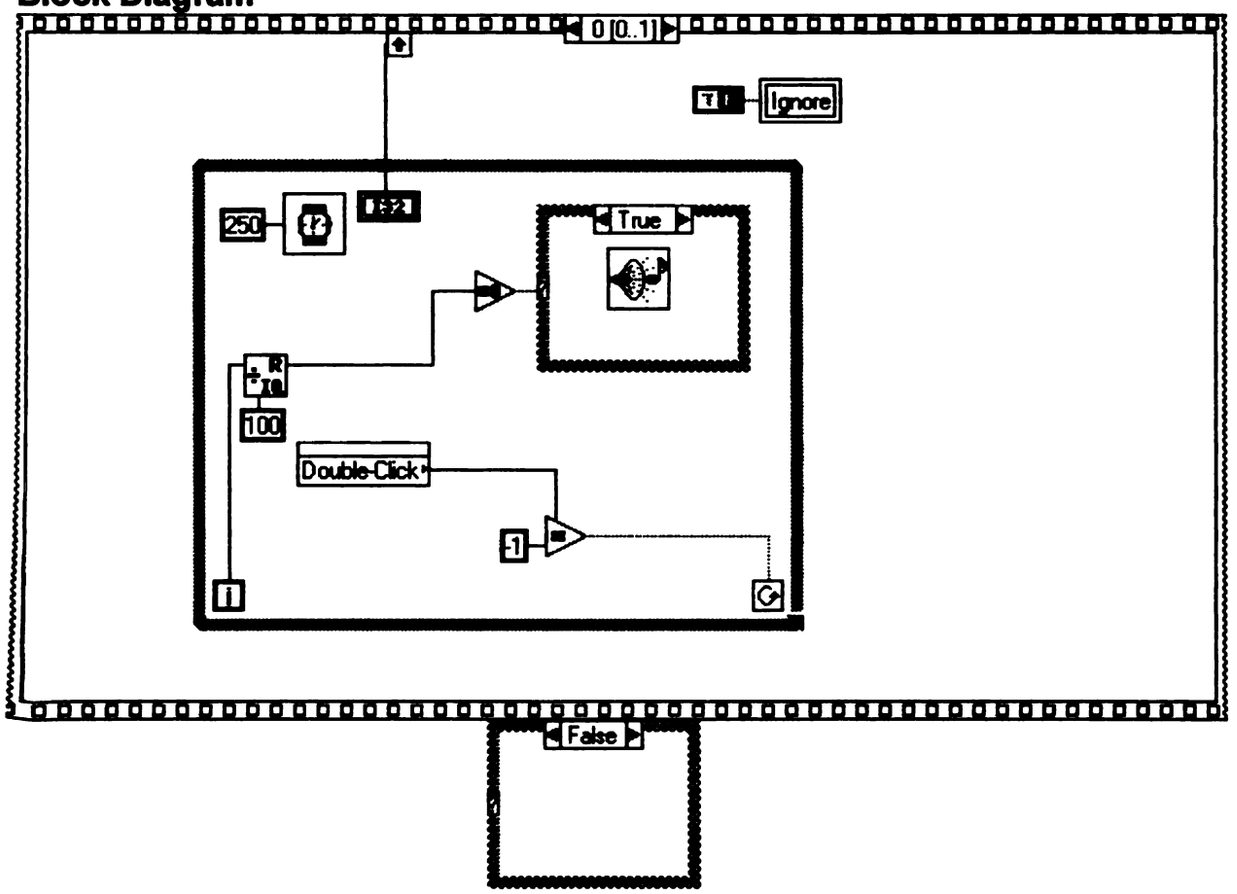

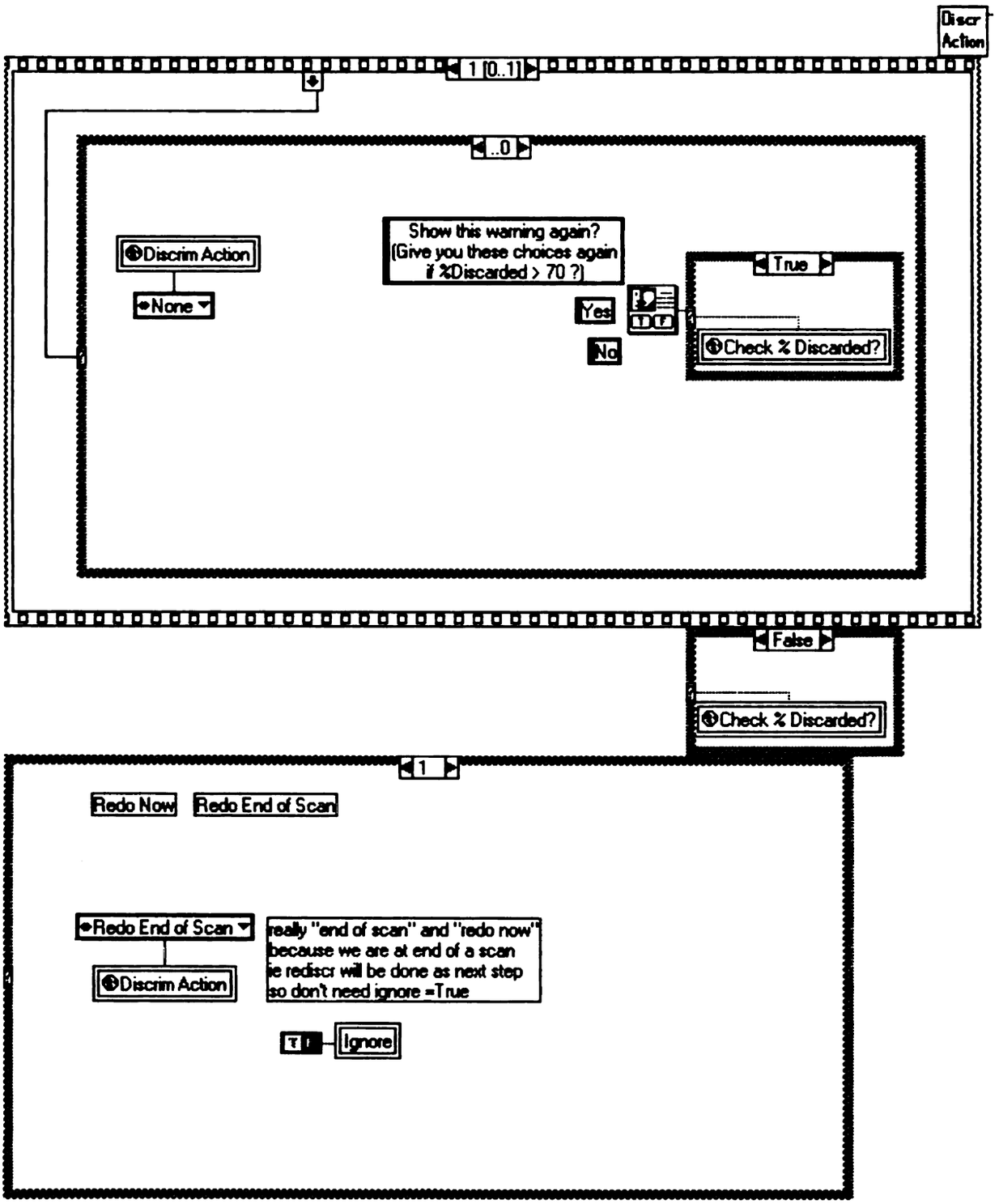
Discr Action
1 [0..1]
..0
Discrim Action
None
Show this warning again?
(Give you these choices again
if %Discarded > 70 ?)
Yes
No
True
Check % Discarded?
False
Check % Discarded?
1
Redo Now
Redo End of Scan
Redo End of Scan
Discrim Action
really "end of scan" and "redo now"
because we are at end of a scan
ie rediscr will be done as next step
so don't need ignore =True
Ignore

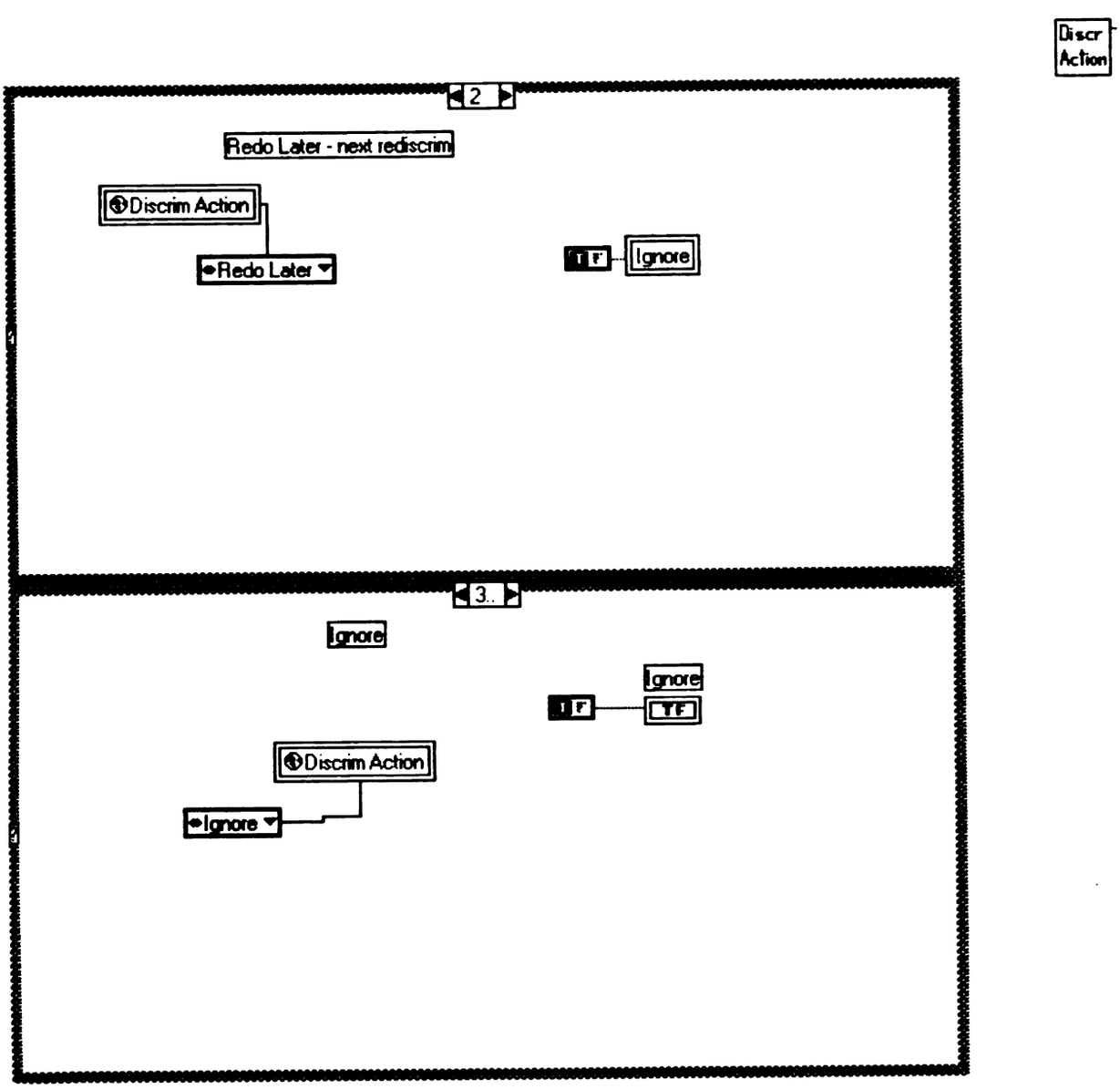
Discr Action
2
Redo Later - next rediscrim
Discrim Action
Redo Later
TF
Ignore
3..
Ignore
Ignore
TF
TF
Discrim Action
Ignore

A.9. Finalfts.vi (Final Save)

This vi saves the data under the filename given in the setup parameters. This save occurs whether the set of scans completes normally or is stopped in the middle using the pause/stop button on the screen. (This save will not occur if the hard stop at the top of the screen is used.)

Connector Pane

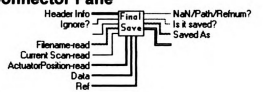

Front Panel

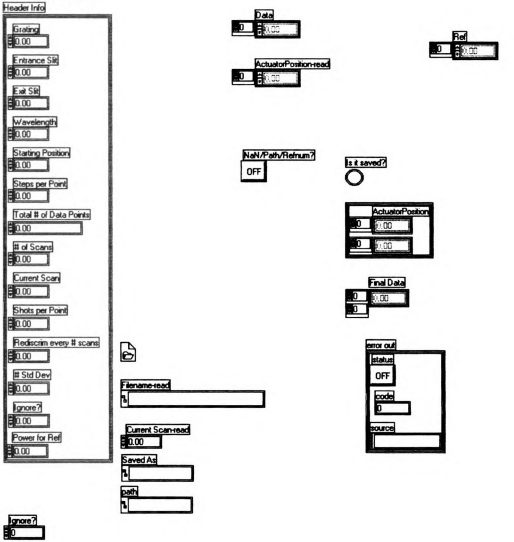

Final Save

Block Diagram

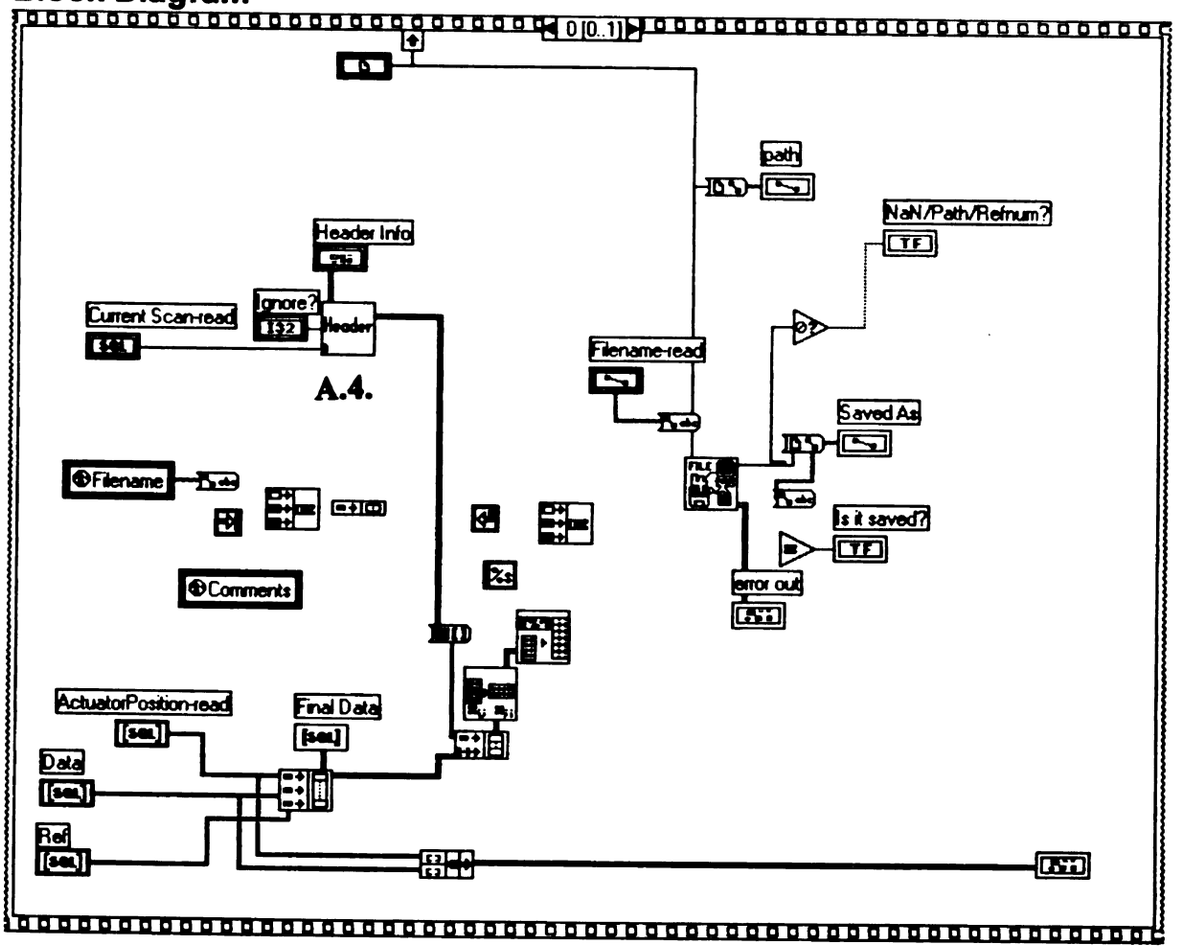

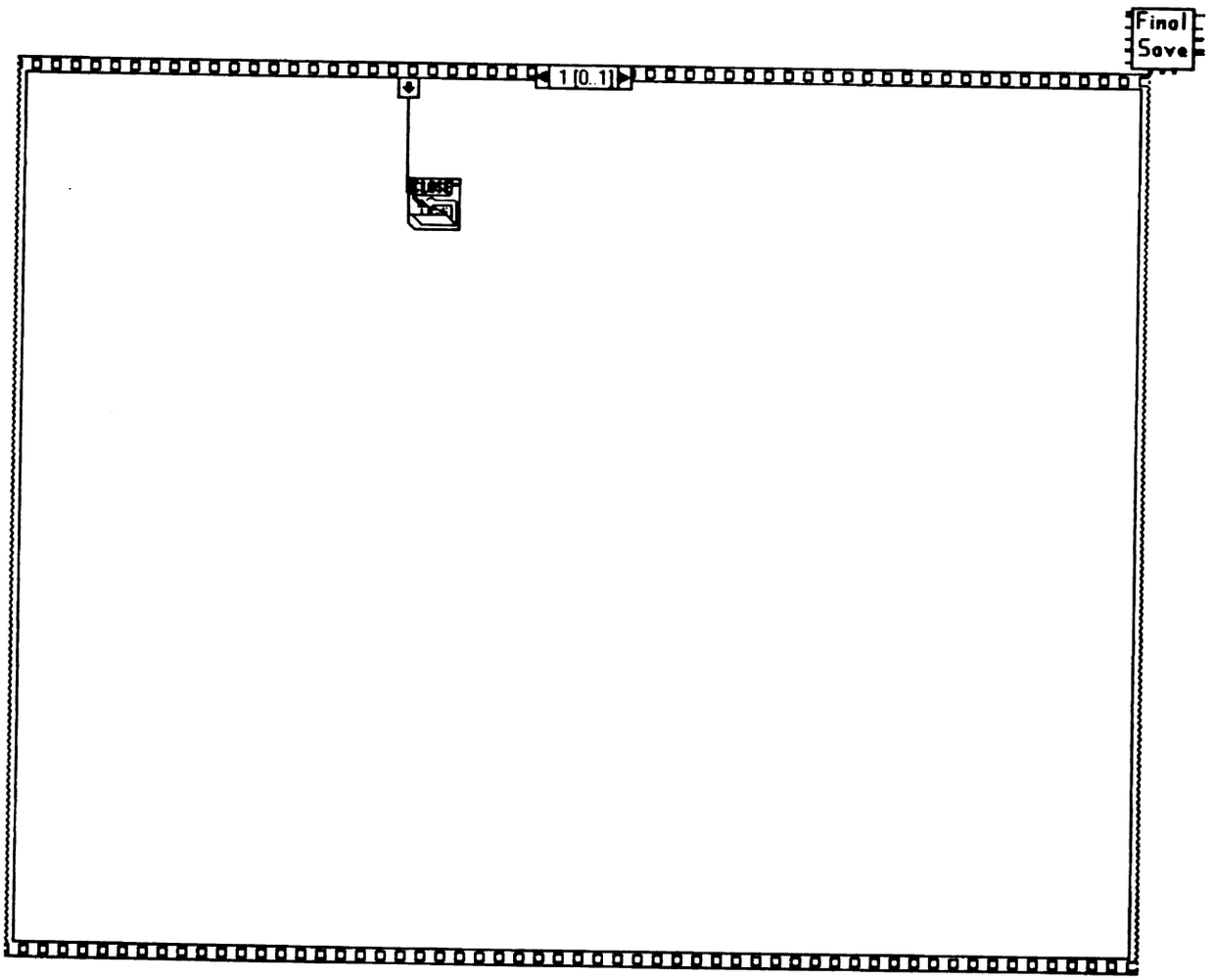
Final
Save
1 [0..1]

A.10. viewfts.vi (View FTS)

This vi will plot newer *.fts as well as older *.pts files (removed in recent versions). It allows the user to print the spectrum, choose another file to view, or to return to taking data. The exit returns the user to the initial fts program screen. The opennewfts and openoldfts vis directly communicate the proper info to this vi.

Connector Pane

Front Panel

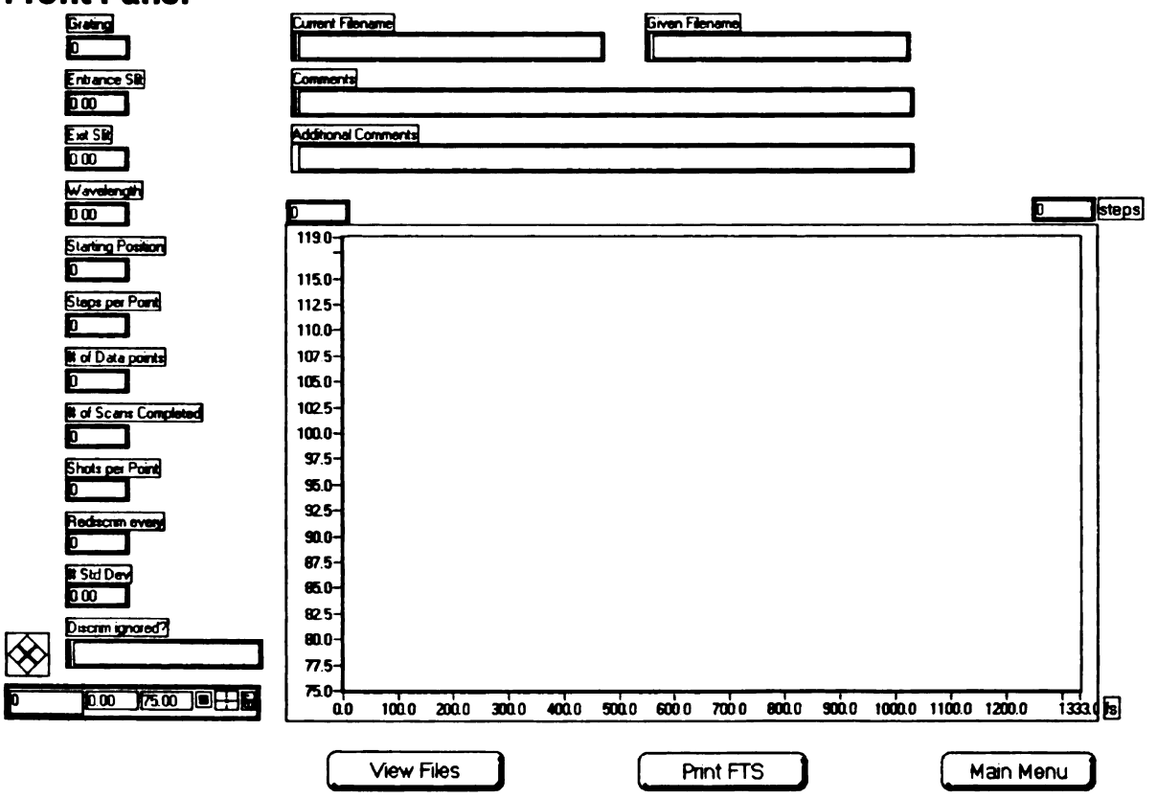

Block Diagram

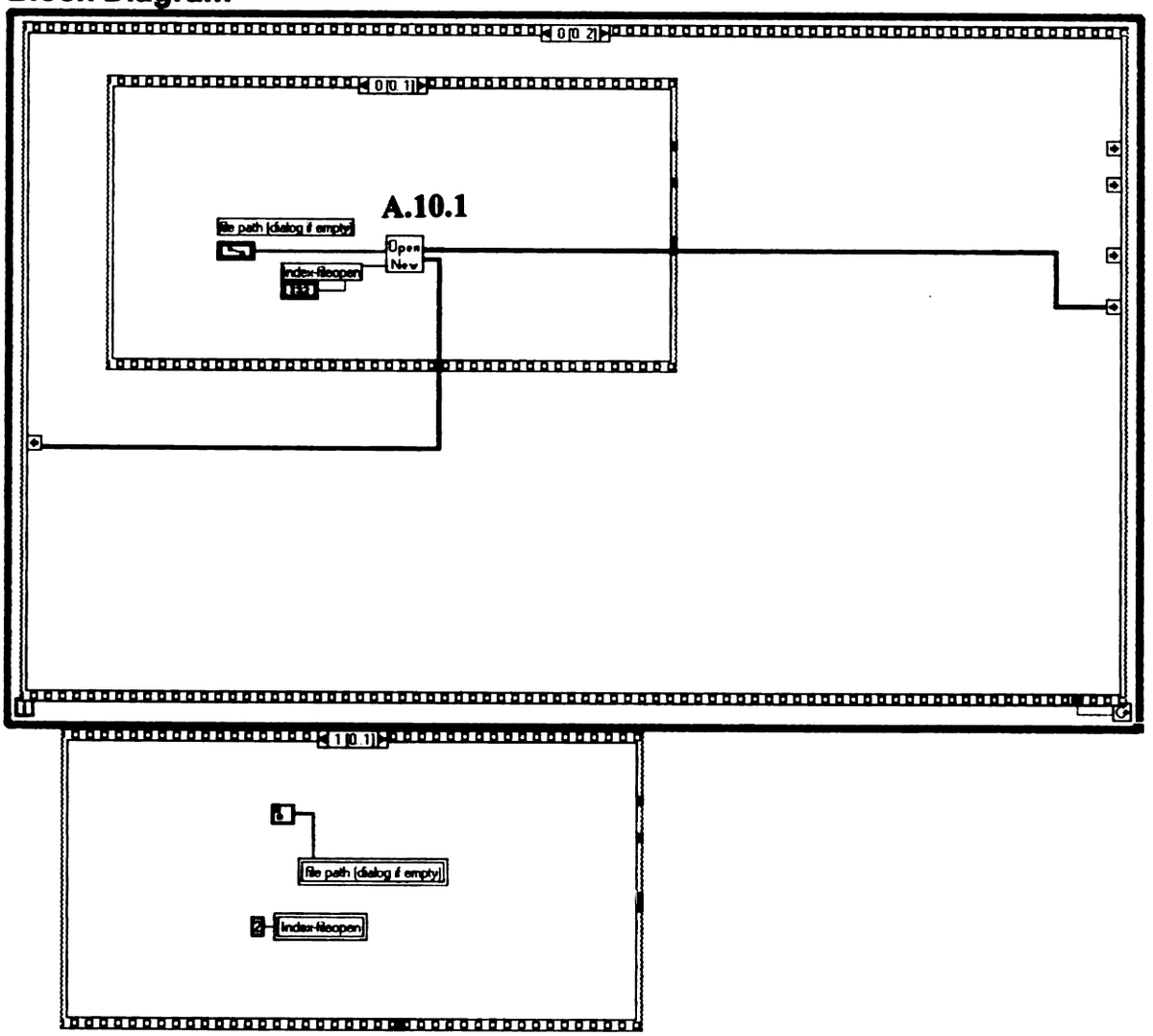

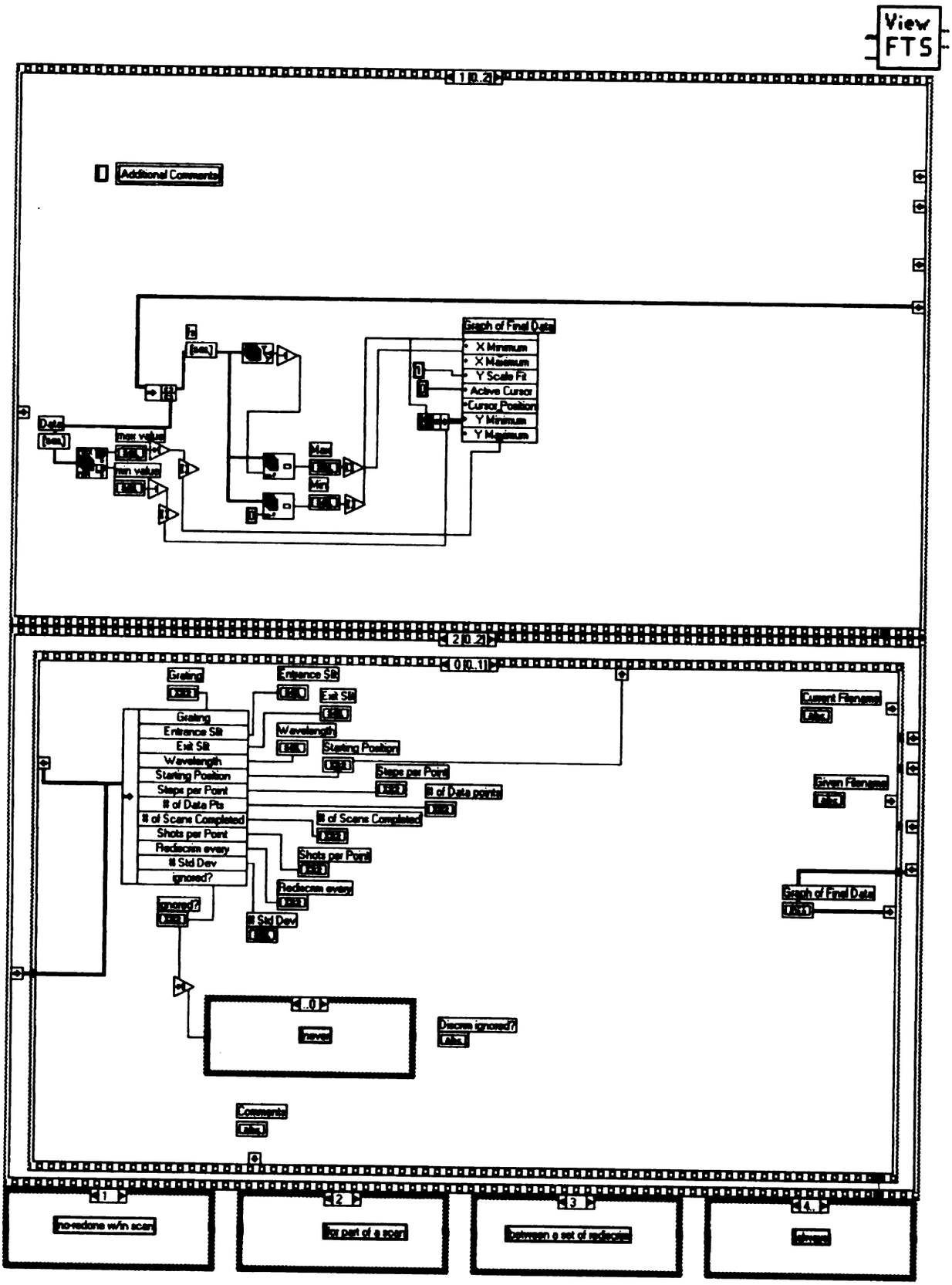
View FTS
Additional Comments
Graph of Final Data
X Minimum
X Maximum
Y Scale Fit
Active Cursor
Cursor Position
Y Minimum
Y Maximum
Data
max value
min value
Max
Min
Grating
Entrance Slit
Exit Slit
Wavelength
Starting Position
Steps per Point
# of Data Pts
# of Scans Completed
Shots per Point
Redscrns every
Std Dev
ignored?
Current Filename
Given Filename
Graph of Final Data
Comments
never
Discrns ignored?
no redone w/in scan
for part of a scan
between a set of redscrns
always

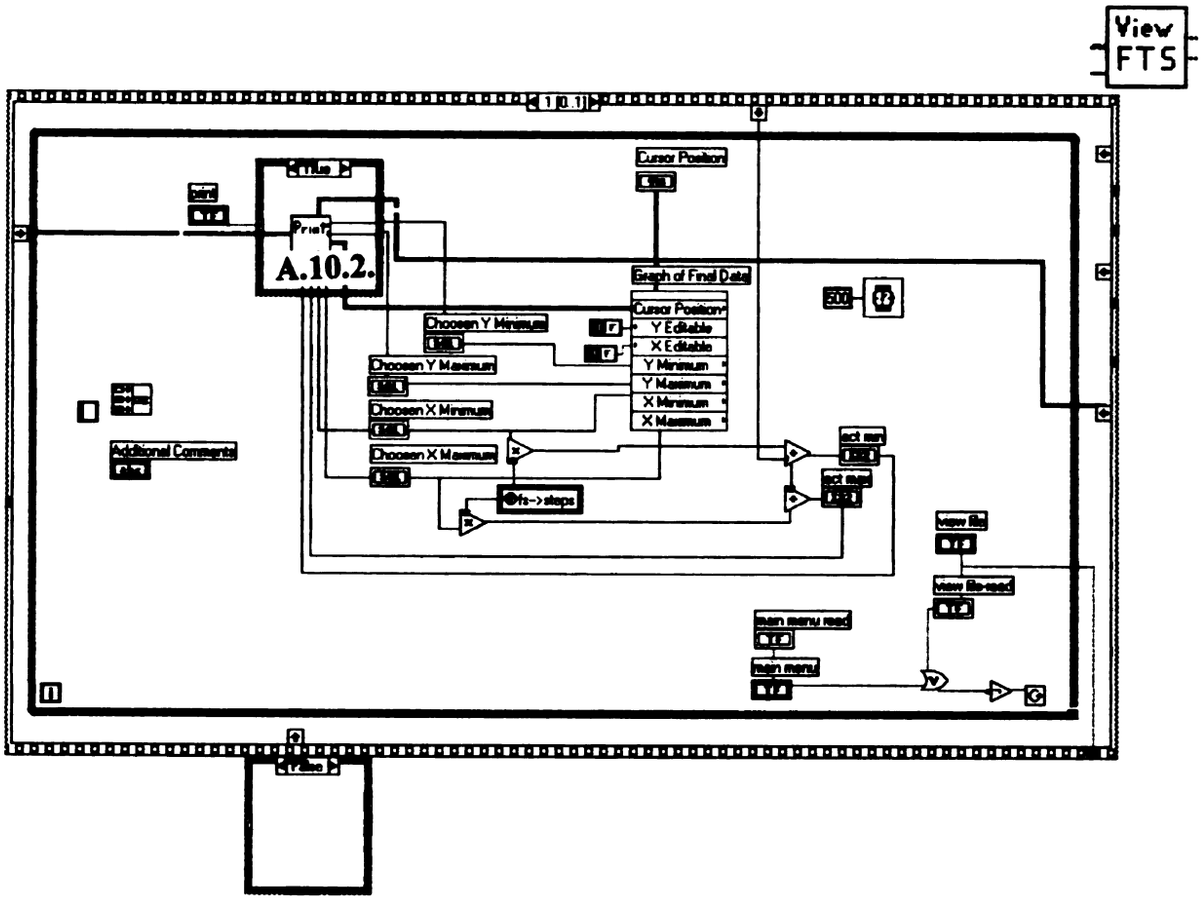
View FTS
A.10.2.
Cursor Position
Graph of Final Data
Cursor Position
Y Editable
X Editable
Y Minimum
Y Maximum
X Minimum
X Maximum
Choosen Y Minimum
Choosen Y Maximum
Choosen X Minimum
Choosen X Maximum
fts->steps
Additional Comments
act num
act num
view file
view file read
main menu read
main menu

A.10.1. opnnewfts2.vi (Open New)

This vi opens *.fts files (time data taken with this Labview program). Header info is transferred along with actuator position and data points to the viewing vi.

Connector Pane

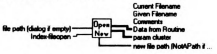

Front Panel

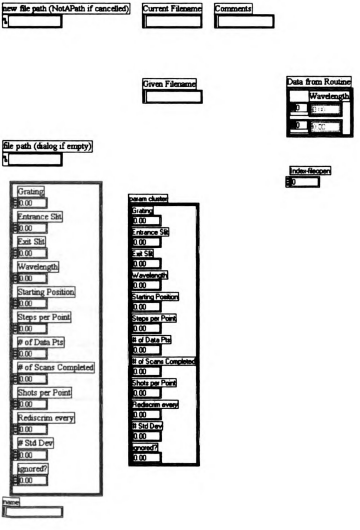

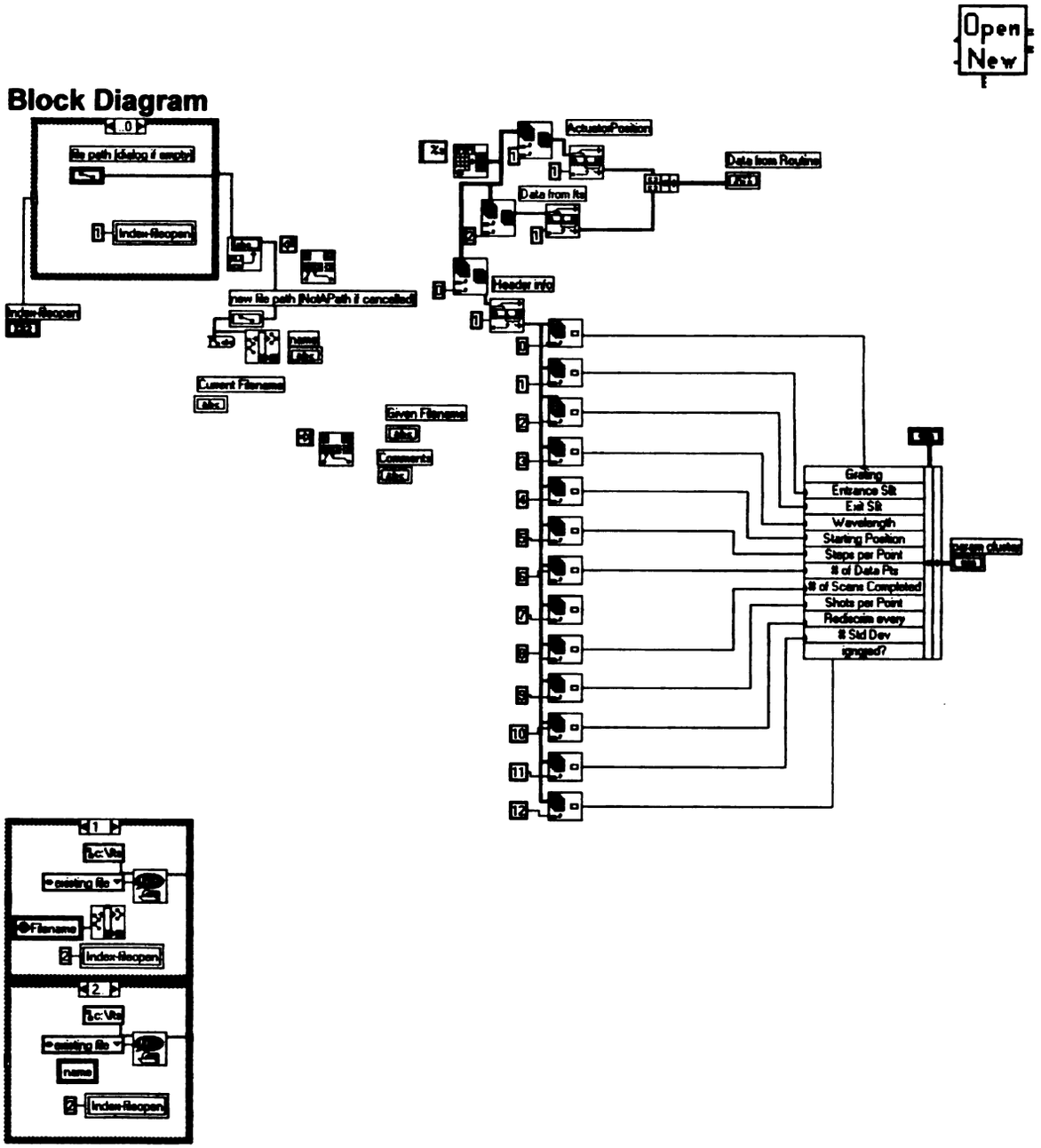
Block Diagram
Open
New
Index Reopen
Actuator Position
Data from Reg.vi
Data from file
Header info
new file path (NotAPath if cancelled)
Current Filename
Given Filename
Comments
Grating
Entrance Slit
Exit Slit
Wavelength
Starting Position
Steps per Point
# of Data Pts
# of Scans Completed
Shots per Point
Redicate every
Std Dev
ignored?
Filename
Index Reopen
Index Reopen

A.10.2. Printfts.vi (Print)

This vi prints the spectrum. Any user changes to range made in the view screen vi's (2 or 3) is kept for the final printing.

Connector Pane

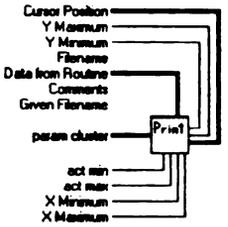

Front Panel

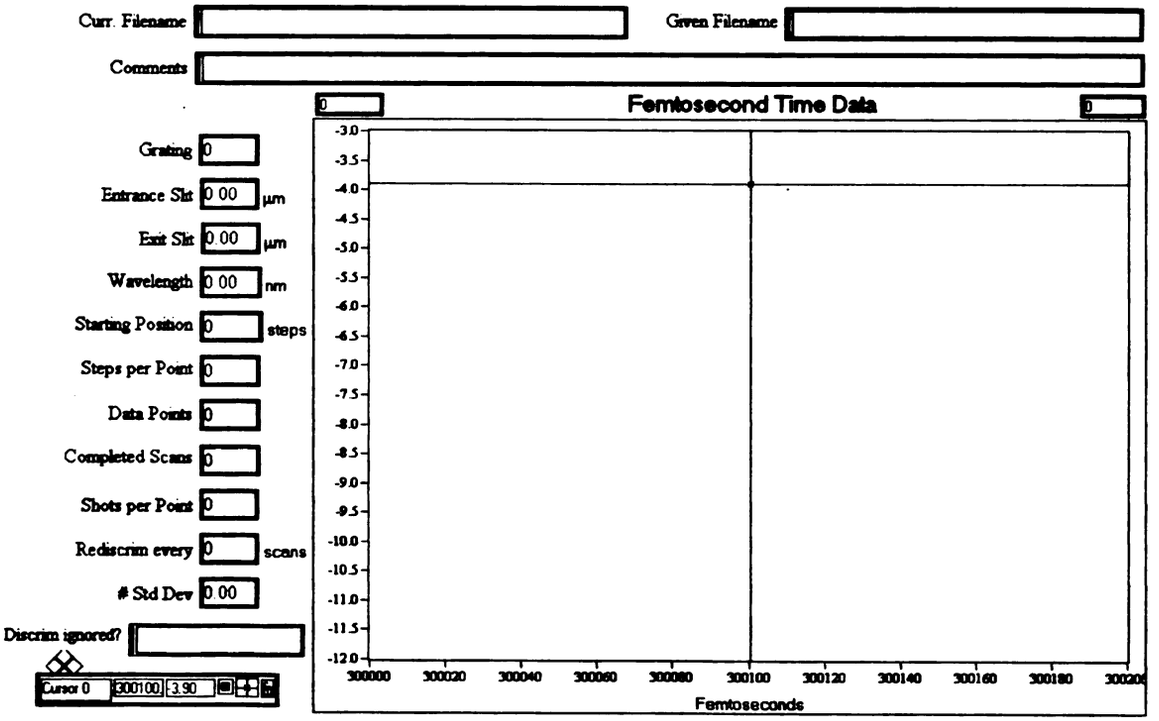

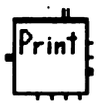

Block Diagram

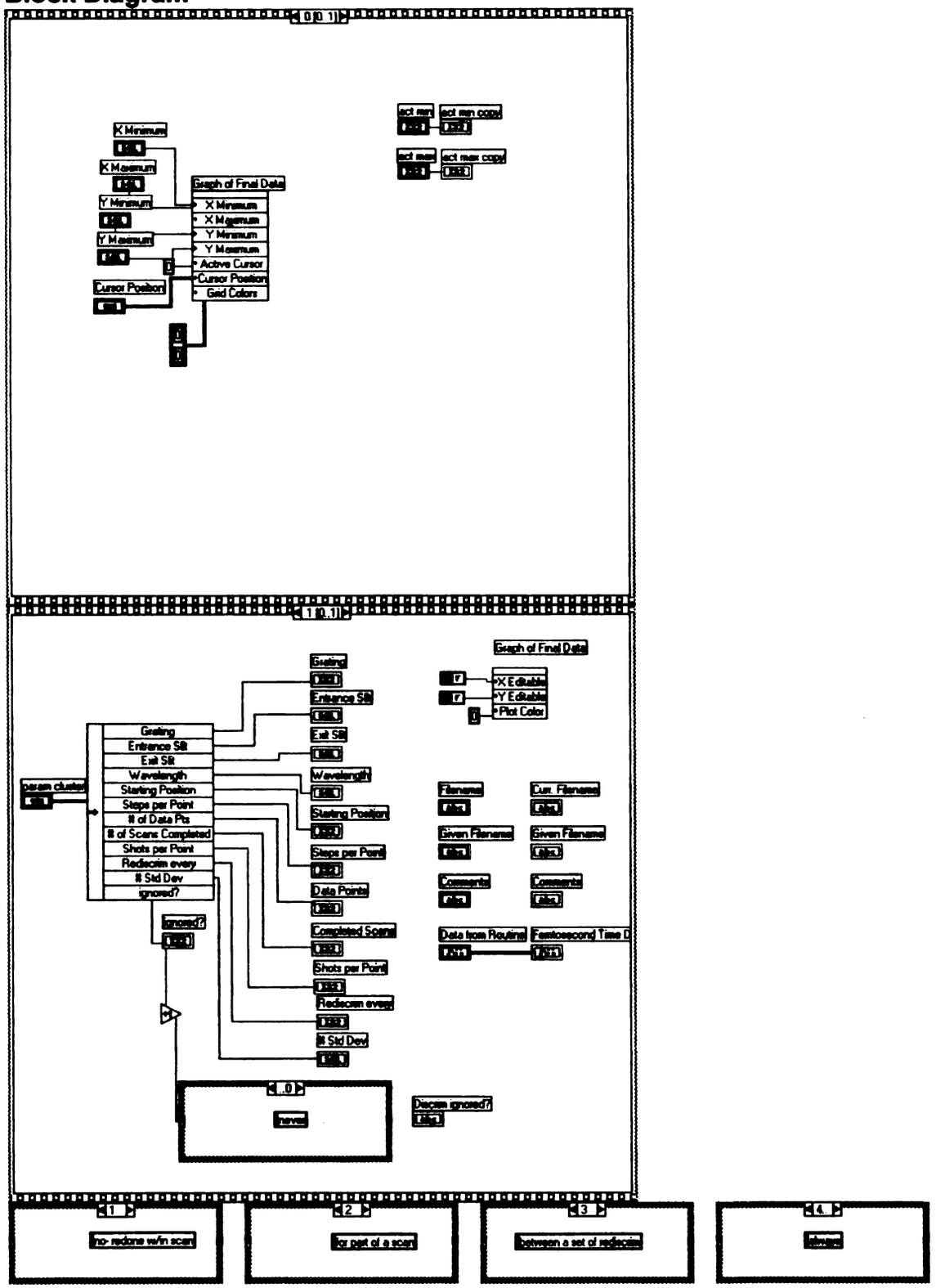

APPENDIX B

LABVIEW™ PROGRAM: WAVLENGTH SPECTRUM DATA ACQUISITION

B. LabVIEW™ Program: Wavelength Spectrum Data Acquisition – takespec2.vi (take data)

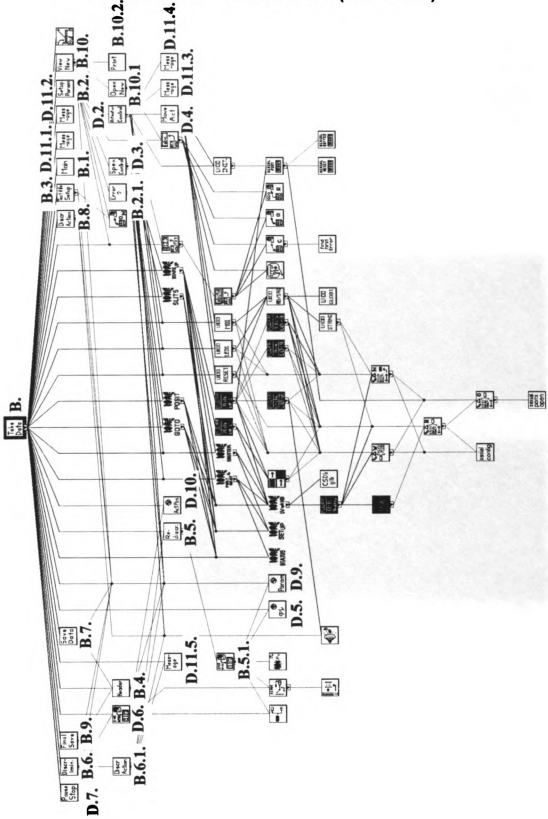

This vi is the part that controls the taking of the data. It presents other interactive vi's to the user which are described elsewhere. These vi's are used to setup files, hardware, etc. This vi uses this info to then start scan, show summed and unsummed scans to user as they are taken, allow the user to pause/stop scan, and saves scans of data as they are successfully completed. This vi then sends this data to the file management vi and forces it to show the recorded data without input from user needed. Then the user can choose to take more data or to look at other files.

Connector Pane

Front Panel

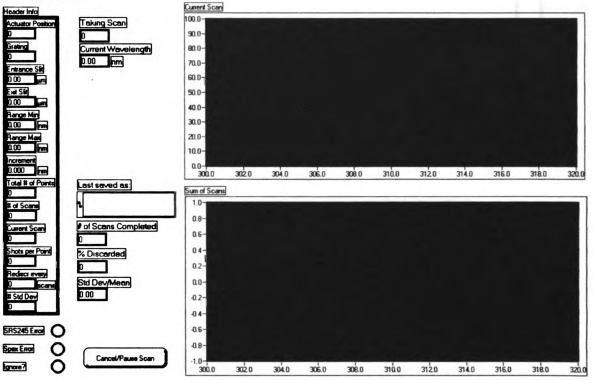

Take Data

Block Diagram

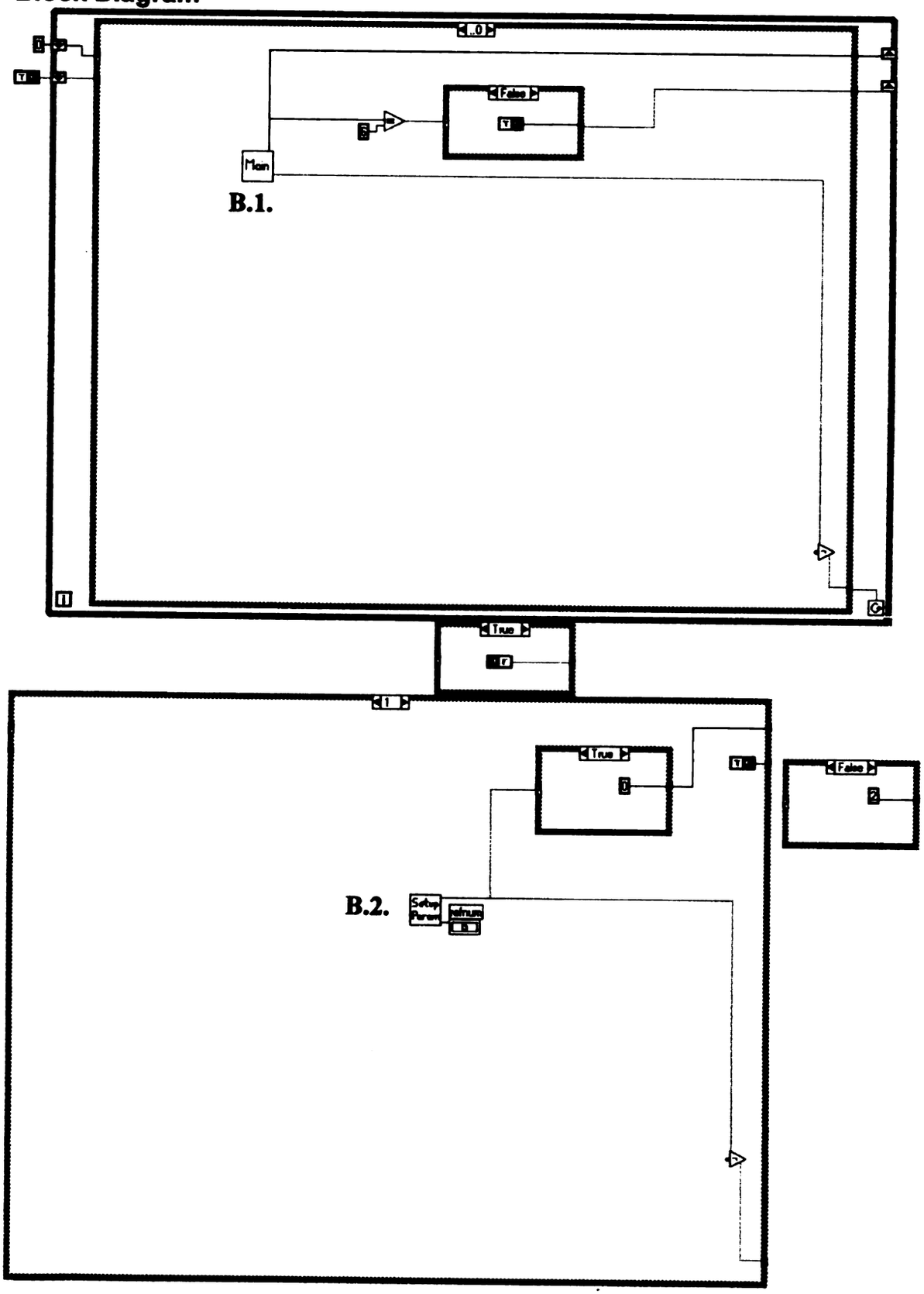

Take Data

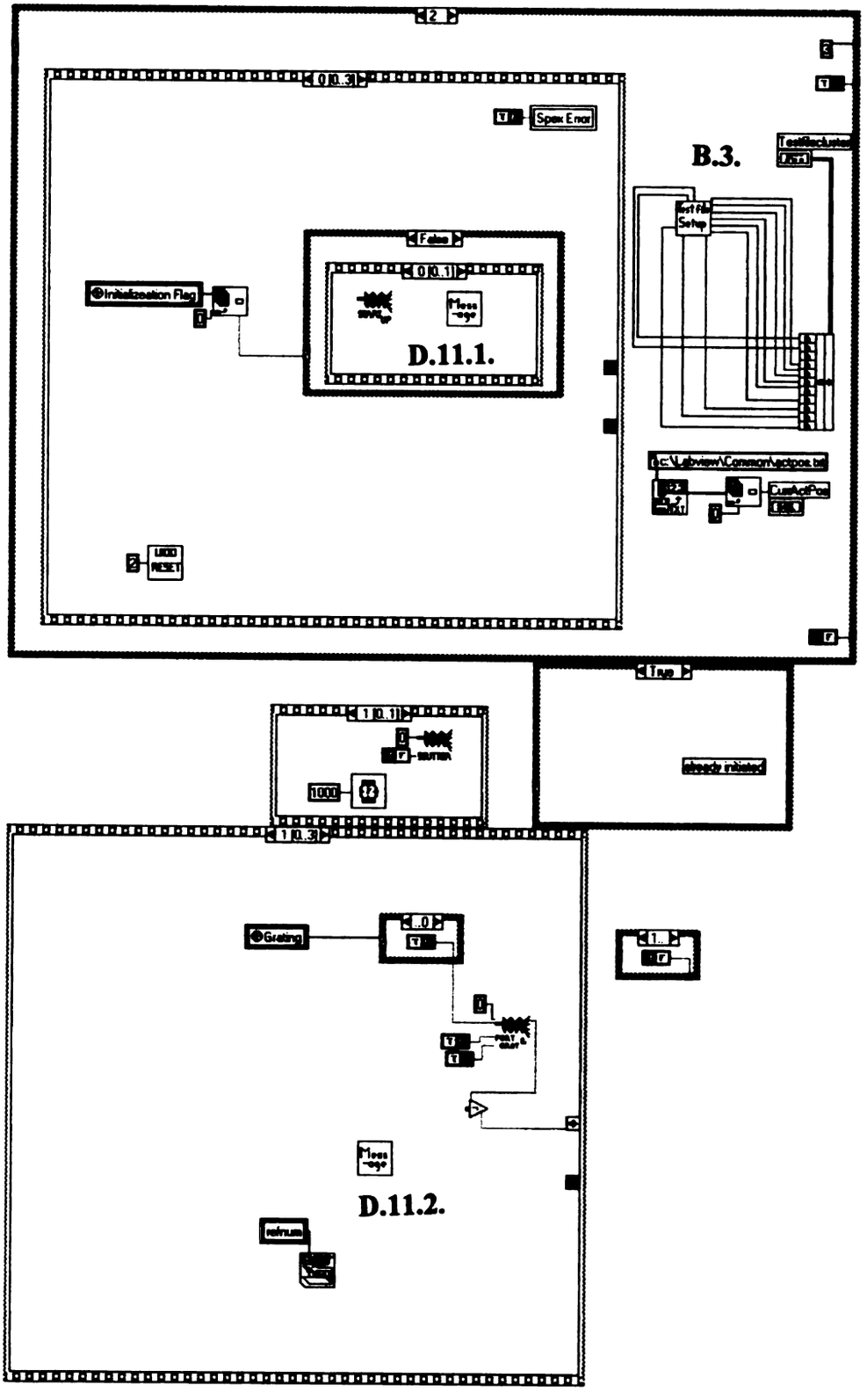

Take Data

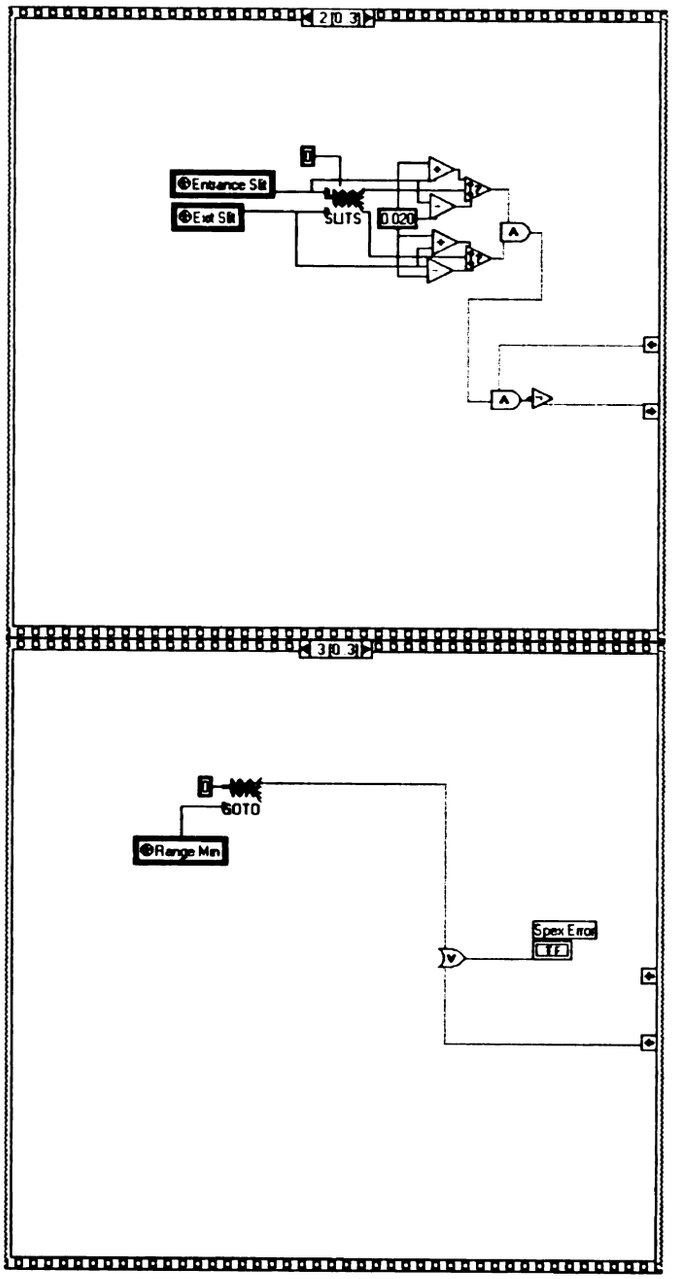
2 0 3
Entrance Slit
Exit Slit
SLITS
0.020
3 0 3
GOTO
Range Min
Spex Error
TF

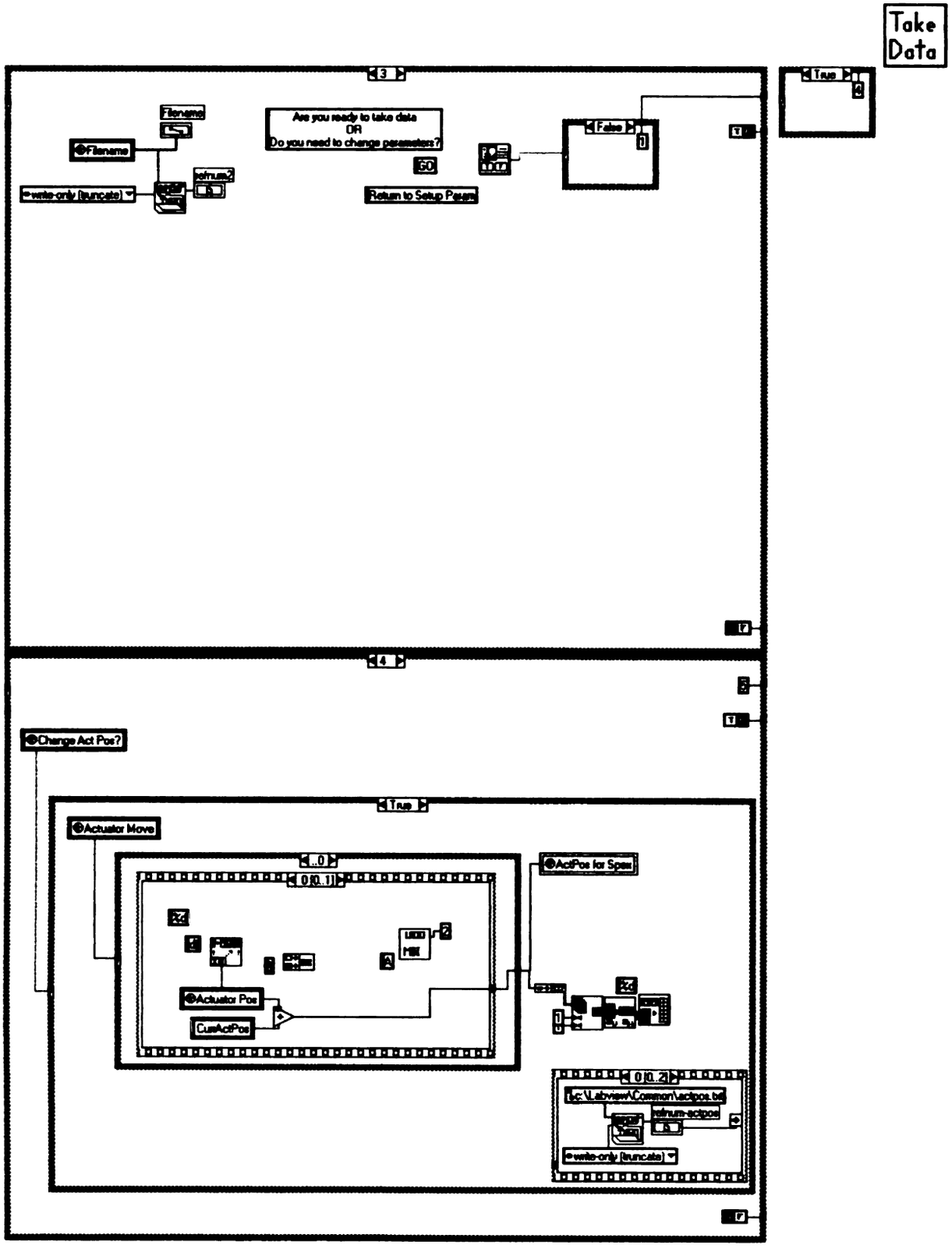
Take Data
3
Filename
Filename
write-only (truncate)
refnum2
Are you ready to take data
OR
Do you need to change parameters?
GO
Return to Setup Params
False
0
True
4
Change Act Pos?
True
Actuator Move
...0
0 [0..1]
Actuator Pos
CurActPos
ActPos for Spec
0 [0..2]
c:\Labview\Common\actpos.txt
refnum-actpos
write-only (truncate)

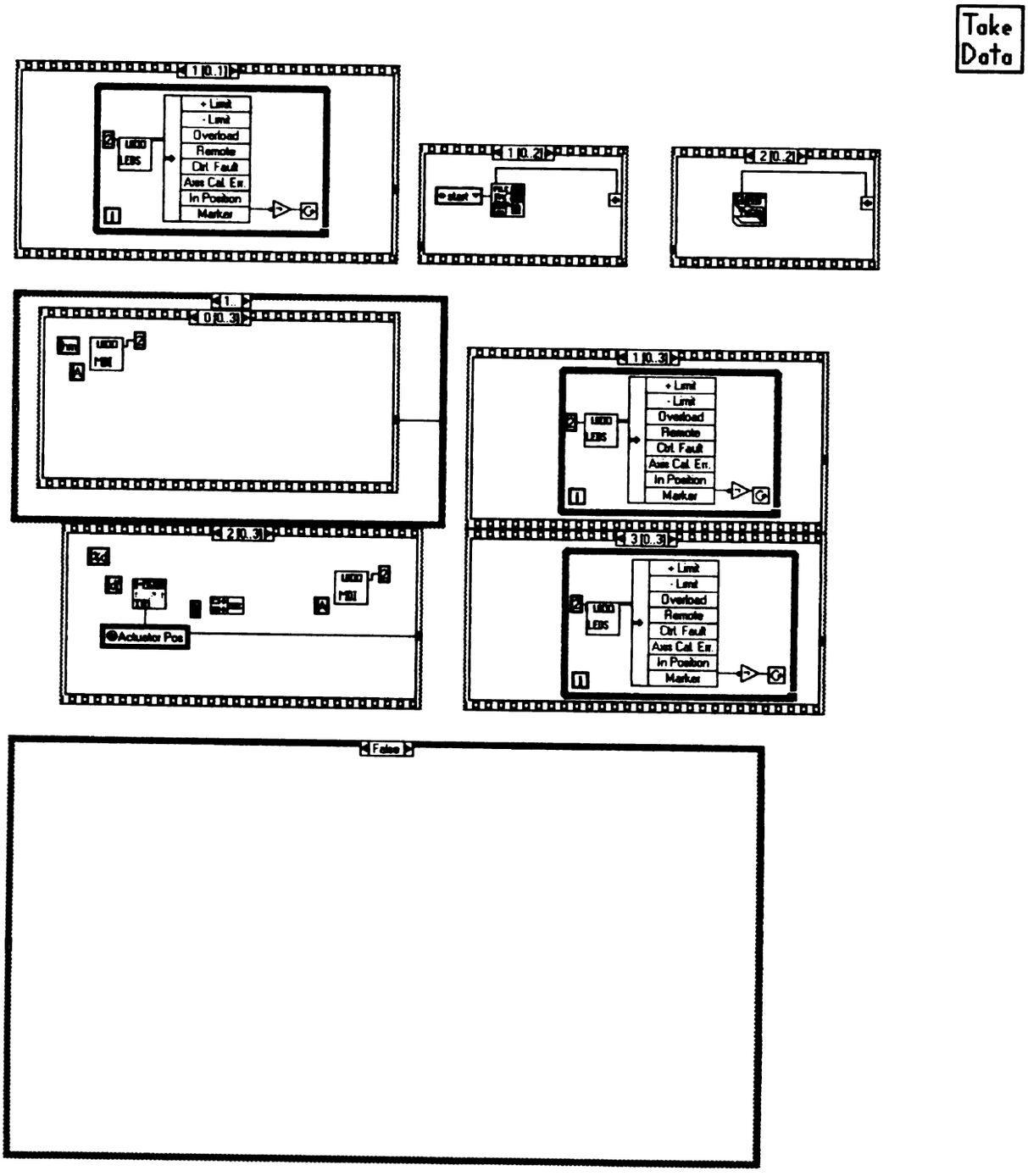
Take Data
1 [0..1]
+ Limit
- Limit
Overload
Remote
Ctrl. Fault
Axis Cal. Err.
In Position
Marker
1 [0..2]
start
2 [0..2]
1..
0 [0..3]
1 [0..3]
2 [0..3]
3 [0..3]
Actuator Pos
False

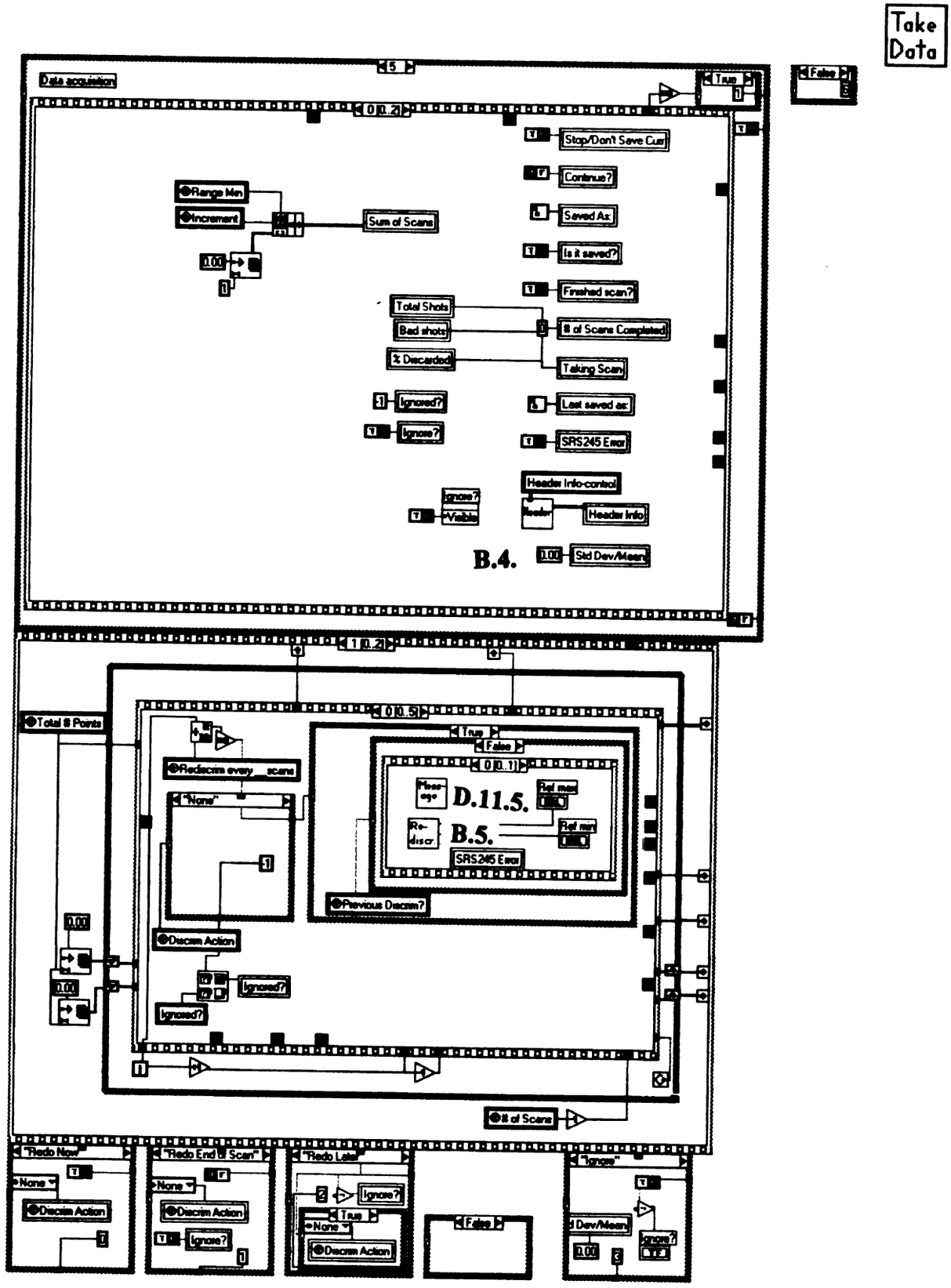
Take Data
Data acquisition
Stop/Don't Save Curr
Continue?
Saved As:
Is it saved?
Finished scan?
Range Min
Increment
Sum of Scans
Total Shots
Bad shots
% Discarded
# of Scans Completed
Taking Scan
Ignored?
Ignore?
Last saved as:
SRS245 Error
Header Info-control
Header Info
Std Dev/Mean
B.4.
Total # Points
Rediscrim every ... scans
"None"
D.11.5.
B.5.
SRS245 Error
Previous Discrim?
Discrim Action
Ignored?
# of Scans
"Redo Now"
"Redo End of Scan"
"Redo Last"
"Ignore"
None
Discrim Action
Ignore?
True
False

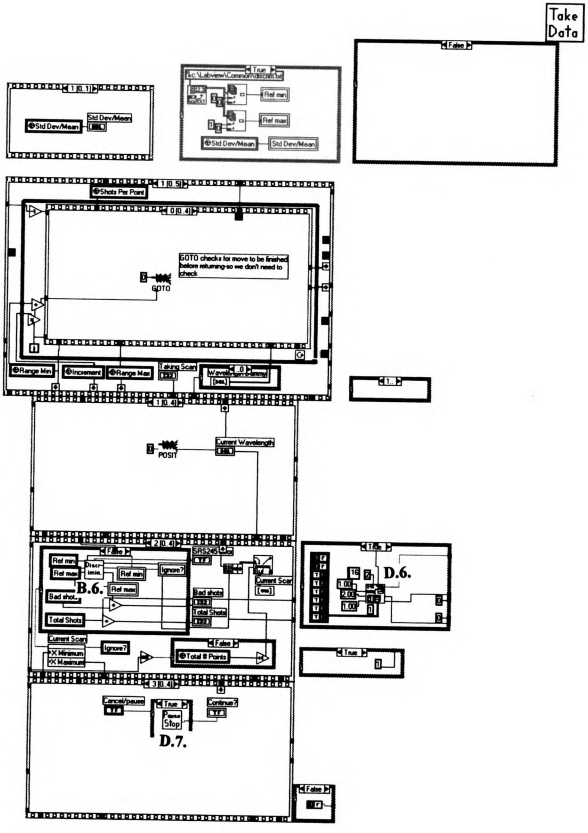
Take Data
False
True
Std Dev/Mean
Ref num
Shots Per Point
GOTO checks for move to be finished before returning so we don't need to check.
GOTO
Range Min
Increment
Range Max
Current Wavelength
POSIT
Ignore?
Bad shots
Total Shots
Current Scan
Minimum
Maximum
Total # Points
Cancel/pause
Continue?
Stop
B.6.
D.6.
D.7.

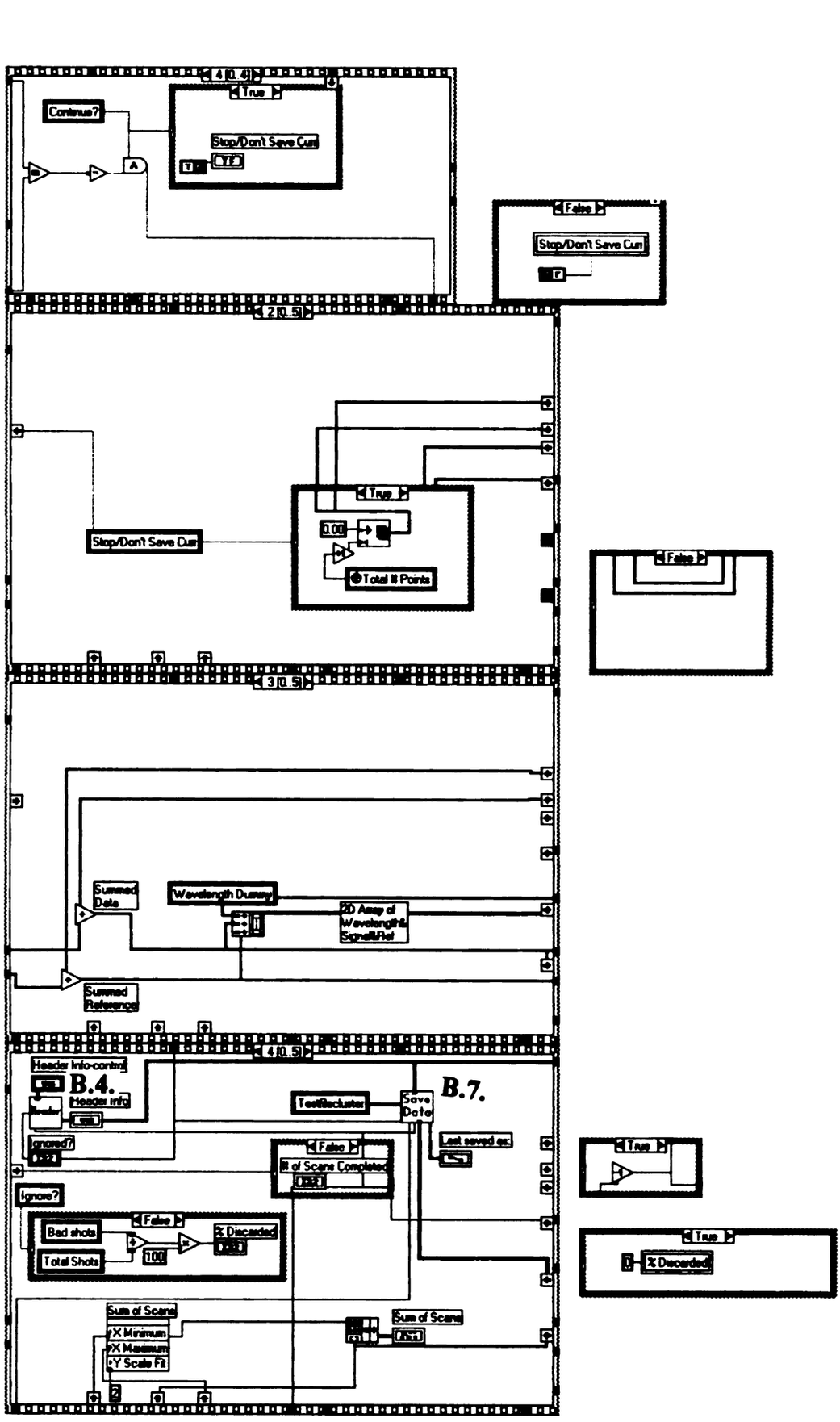
Take Data
4 [0..4]
True
Continue?
Stop/Don't Save Curr
TF
A
False
Stop/Don't Save Curr
2 [0..5]
True
0.00
Total # Points
Stop/Don't Save Curr
False
3 [0..5]
Summed Data
Wavelength Dummy
2D Array of Wavelength& Signal/Ref
Summed Reference
4 [0..5]
Header Info-control
B.4.
Header Info
Header
Ignored?
Ignore?
TestRecluster
Save Data
B.7.
Last saved as:
False
# of Scans Completed
Bad shots
Total Shots
100
% Discarded
True
% Discarded
Sum of Scans
X Minimum
X Maximum
Y Scale Fit
Sum of Scans

Take Data

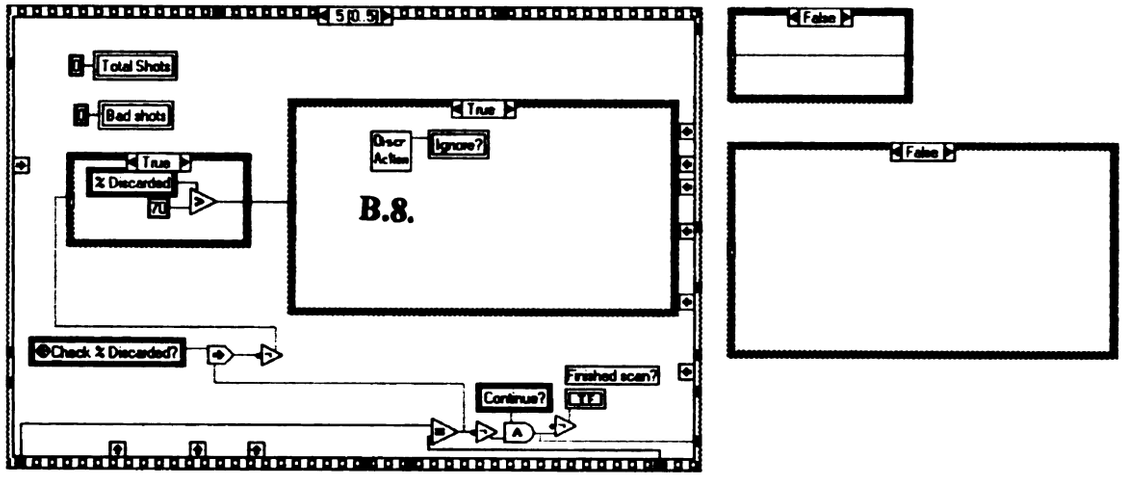
5 [0..5]
Total Shots
Bad shots
True
% Discarded
/0
True
Discr Action
Ignore?
B.8.
Check % Discarded?
Continue?
Finished scan?
False
False

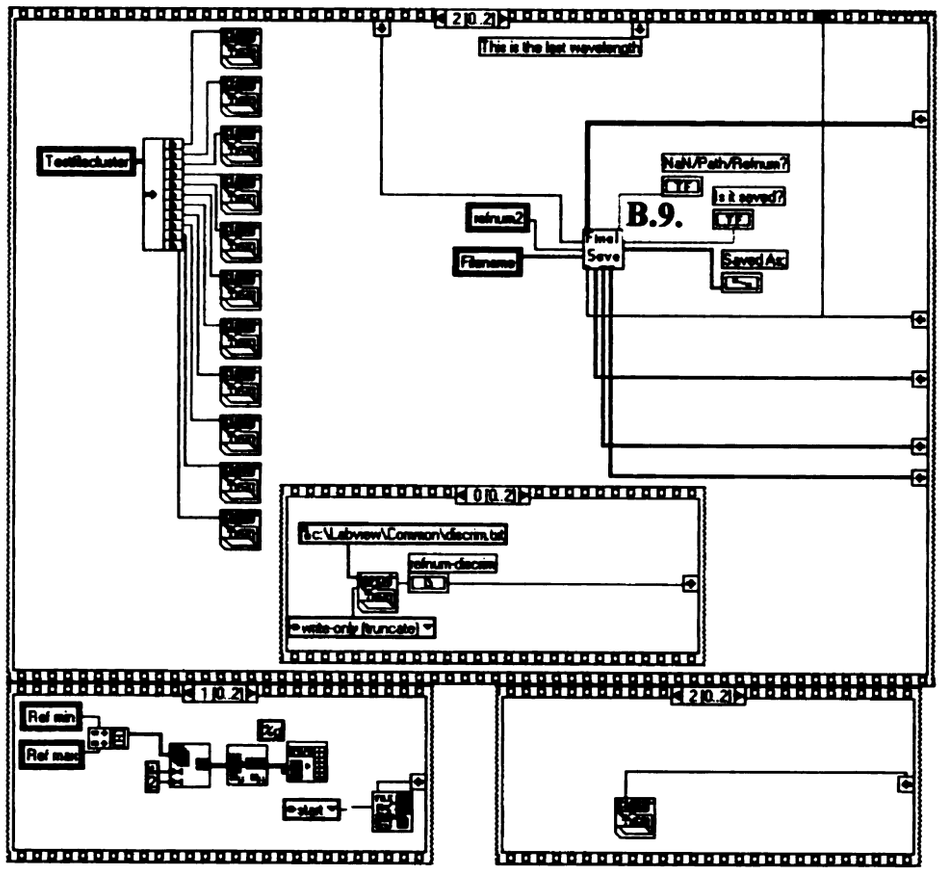
2 [0..2]
This is the last wavelength
TestBlockuter
NaN/Path/RefNum?
is it saved?
refnum2
Filename
Final Save
Saved Acc
B.9.
0 [0..2]
c:\Labview\Common\discrim.txt
refnum-discrim
write-only (truncate)
1 [0..2]
Ref min
Ref max
start
2 [0..2]

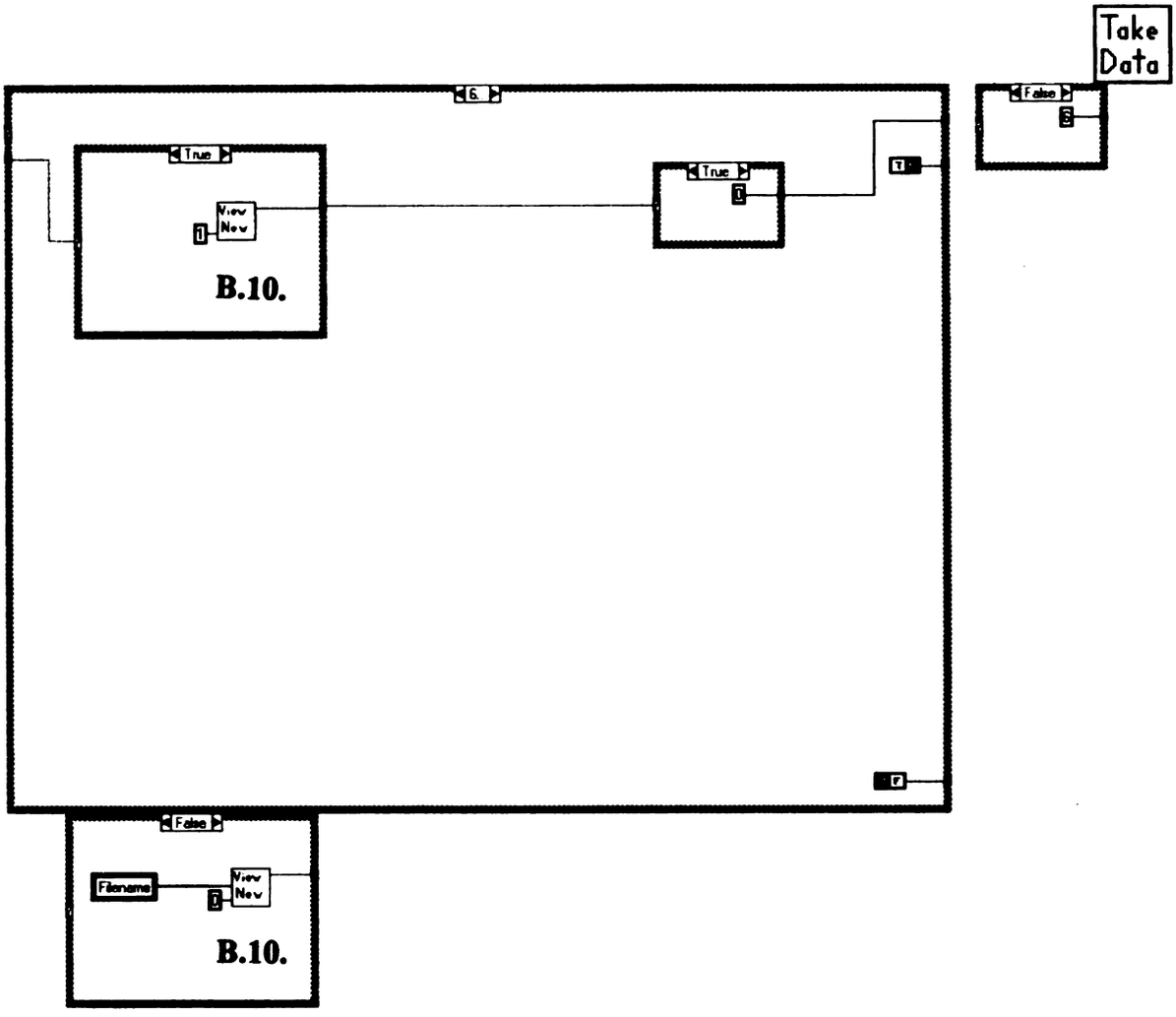
Take Data
False
S
6
True
View Nav
1
B.10.
True
1
T
F
False
Filename
View Nav
1
B.10.

B.1. Specpgm.vi (Main)

This vi is the starting point of the spectral scan program. The user decides between taking data and looking at previously taken spectra- either *.wnm or *.spc files. If the program is properly begun here, the user can go between both parts of the program easily. Ie. start with file management and then go to take data and back again, or start with take data and then go to file management and back again. (Or stay within one part of the program the whole time.)

Connector Pane

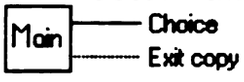

Front Panel

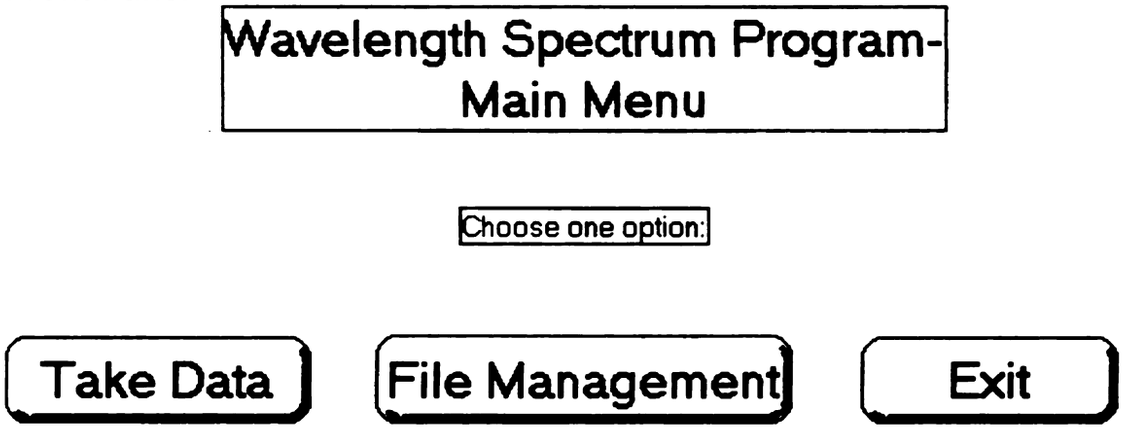

Main

Block Diagram

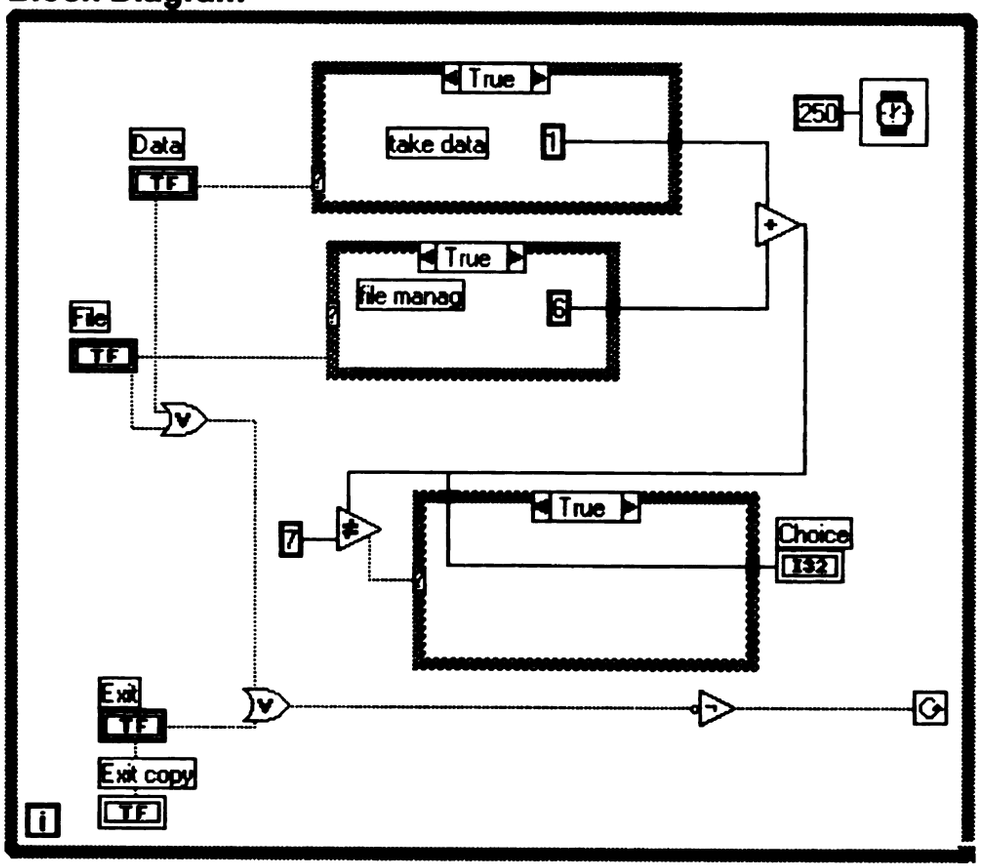

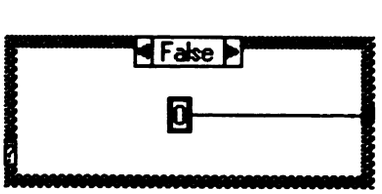

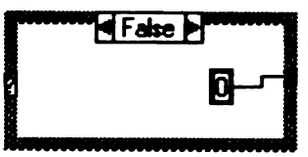

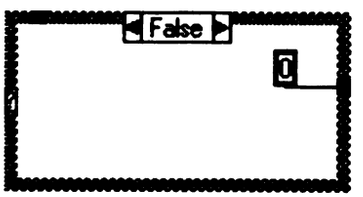

B.2. paramspec3.vi (Setup Param)

This vi writes the parameters to the global parameters vi so that all subsequent vi's have access to the initial conditions. If the program has been run earlier without Labview having been quit, the parameters from the previous run are shown on the screen (allowing the user to make only the necessary changes). The parameters are used to setup the resulting data file and data acquisition and setup the spectrometer and actuator. The user has the ability to control the spectrometer and the actuator during this screen in order to find the best locations. (OR use separate instrumental control vi to move/change settings).

Connector Pane

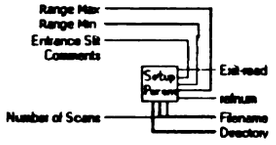

Front Panel

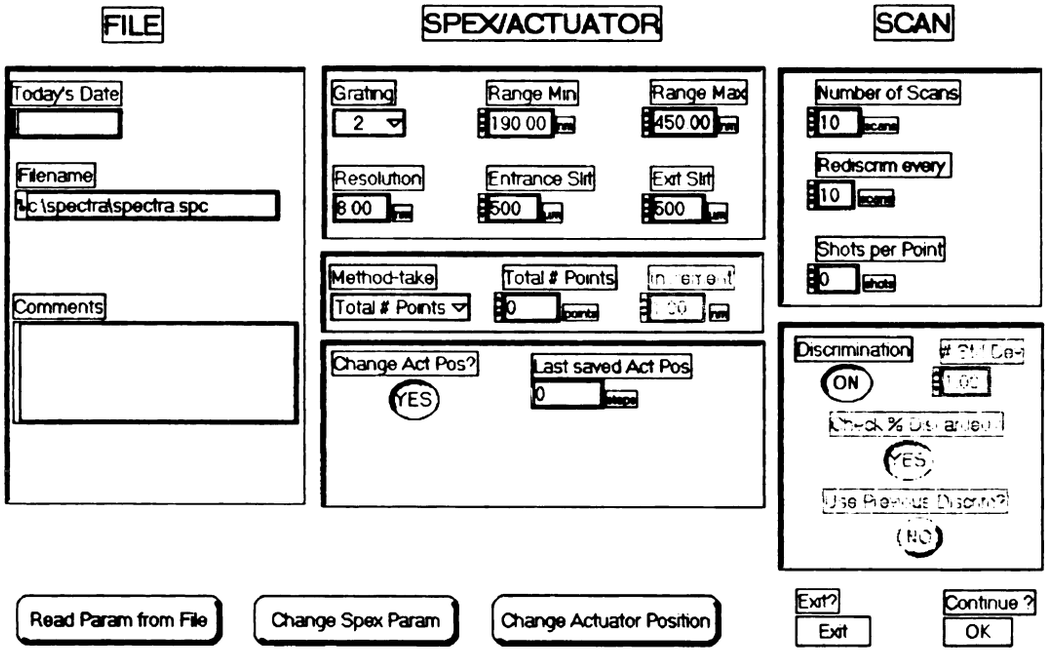

Setup Param

Block Diagram

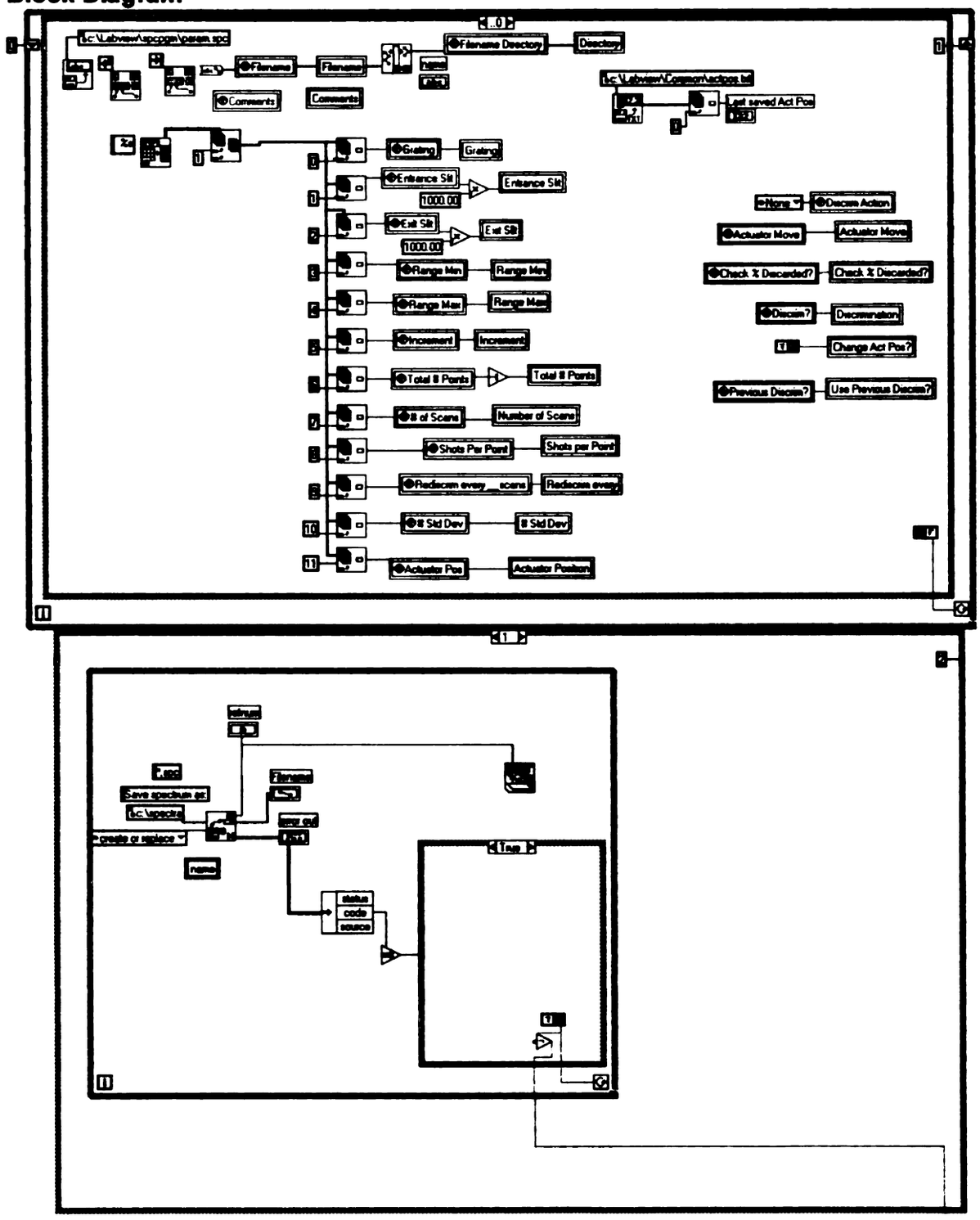

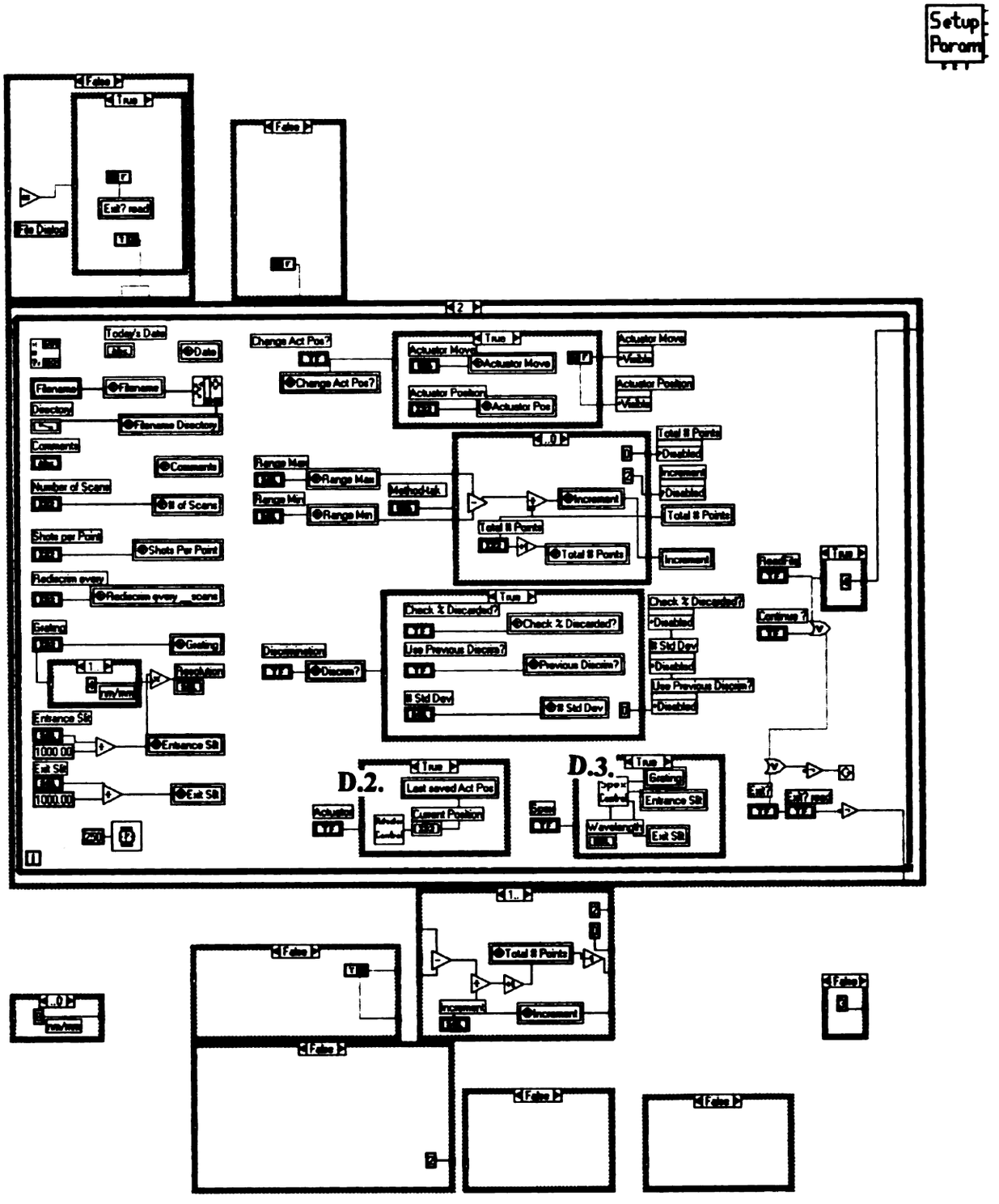
Setup Param
False
True
Exit? read
File Dialog
False
?
Today's Date
Date
Filename
Filename
Directory
Filename Directory
Comments
Comments
Number of Scans
# of Scans
Shots per Point
Shots Per Point
Rediscrim every
Rediscrim every ... scans
Gating
Gating
Resolution
Entrance Slit
1000.00
Entrance Slit
Exit Slit
1000.00
Exit Slit
Change Act Pos?
Change Act Pos?
Actuator Move
True
Actuator Move
Actuator Move
Visible
Actuator Position
Actuator Pos
Actuator Position
Visible
Range Max
Range Max
Range Min
Range Min
Method-tak
..0
Increment
Total # Points
Disabled
Increment
Disabled
Total # Points
Total # Points
Total # Points
Increment
Discrimination
Discrim?
Check % Discarded?
True
Check % Discarded?
Use Previous Discrim?
Previous Discrim?
Std Dev
Std Dev
Check % Discarded?
Disabled
Std Dev
Disabled
Use Previous Discrim?
Disabled
ReadFile
True
Continue ?
Exit?
Exit? read
D.2.
True
Last saved Act Pos
Current Position
Actuator
D.3.
True
Gating
Entrance Slit
Wavelength
Exit Slit
Save
1..
Total # Points
Increment
False
False
False
False
False
..0

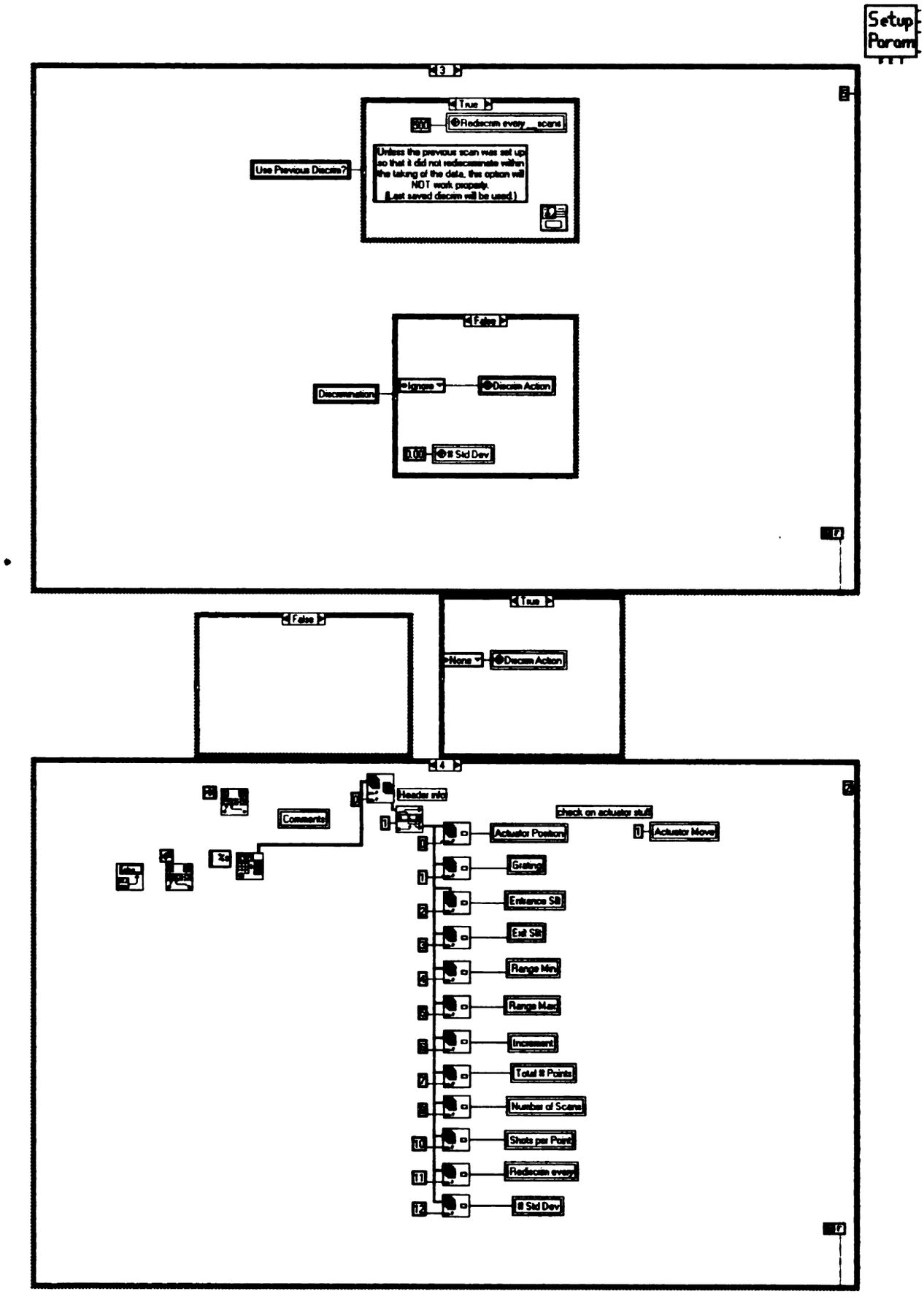
Setup Param
3
True
Redecim every __ scans
Use Previous Decim?
Unless the previous scan was set up so that it did not redecimate within the taking of the data, this option will NOT work properly.
(Last saved decim will be used.)
False
Decimation
Decim Action
Std Dev
False
True
None
Decim Action
4
Header info
Comments
Check on actuator stuff
Actuator Position
Actuator Move
Grating
Entrance Slit
Exit Slit
Range Min
Range Max
Increment
Total # Points
Number of Scans
Shots per Point
Redecim every
Std Dev

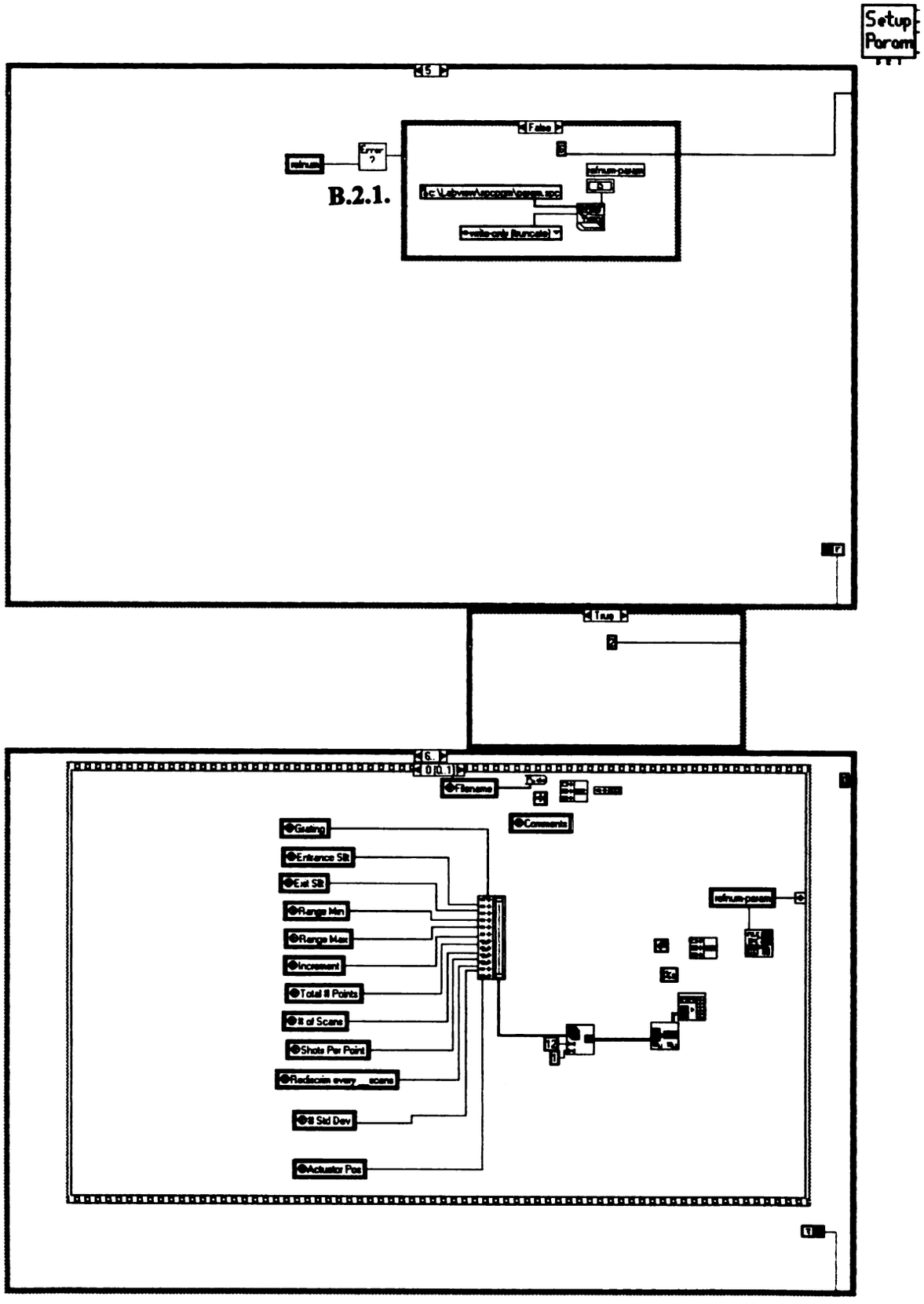
Setup Param
5
False
refnum
Error ?
refnum-param
c:\Labview\scope\wave.spc
write only (truncate)
B.2.1.
True
6
0 (0..1)
Filename
Comments
Gating
Entrance Slit
Exit Slit
Range Min
Range Max
Increment
Total # Points
# of Scans
Shots Per Point
Redscan every ___ scans
Std Dev
Actuator Pos
refnum-param

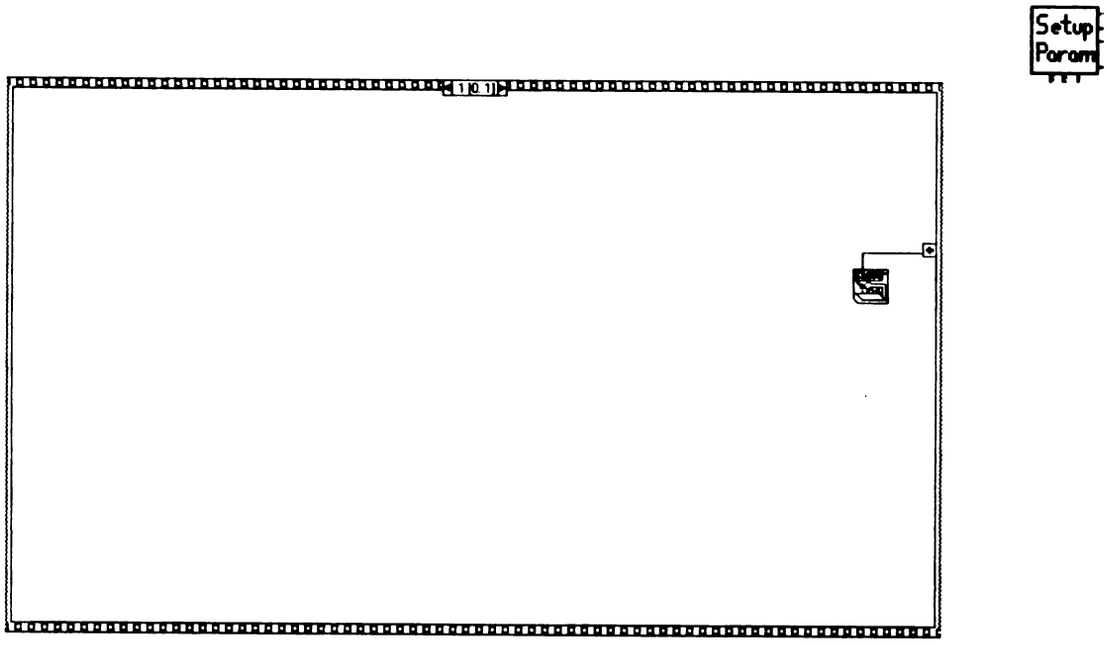
Setup
Param
1 0 1

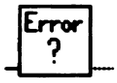

B.2.1. Errorspec.vi (Error ?)

This vi examines the setup parameters for any errors including too many scans, slit size out of usual range, wavelength range and/or grating error, max-min or increment problems. If there is a problem, this vi closes the opened file and the take data vi returns user to parameters setup screen to try again.

Connector Pane

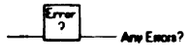

Front Panel

Block Diagram

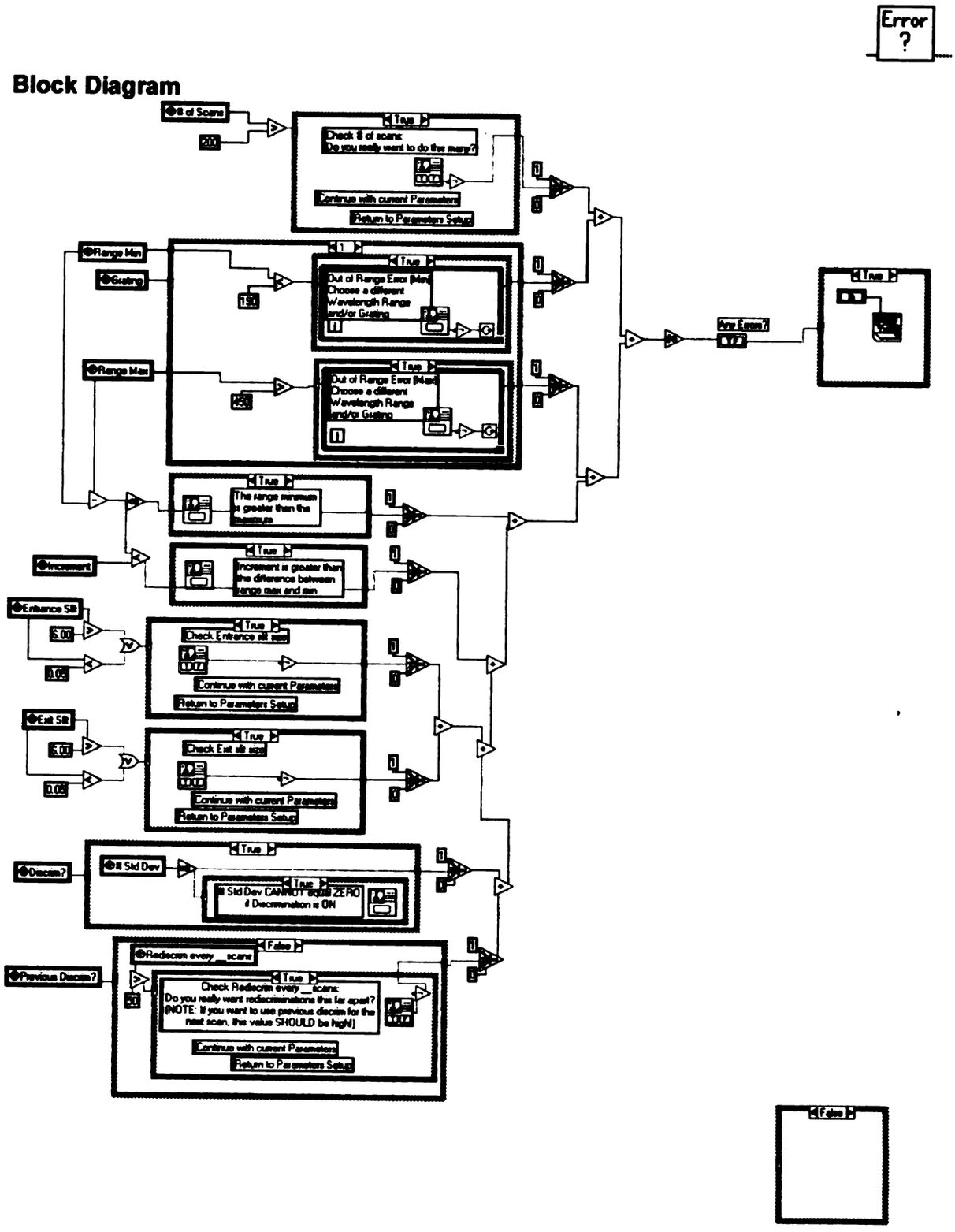

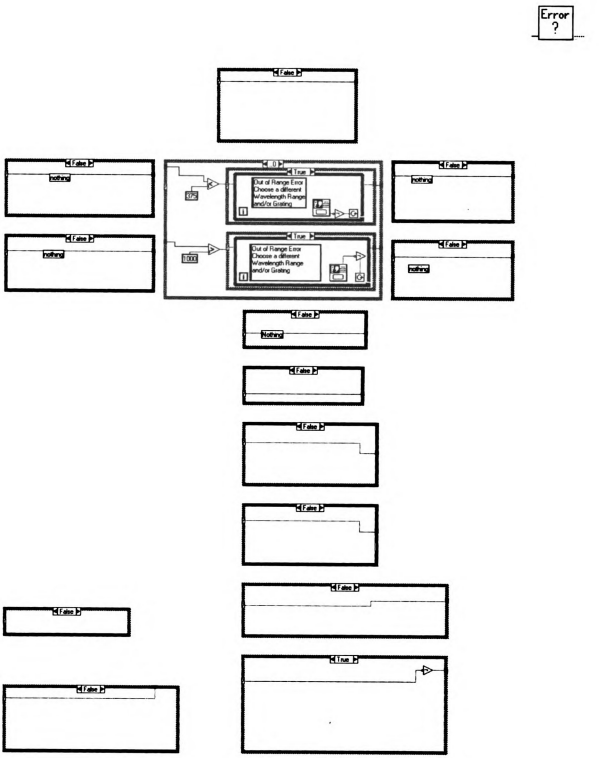
Error
?
False
nothing
True
Out of Range Error
Choose a different
Wavelength Range
and/or Grating
1.0E-9
1.00E-9

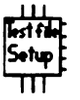

B.3. Testspec.vi (Test file Setup)

This vi opens the intermediate files (to save every 10 scans incrementally). It opens them, closes them and then opens them in the write-only truncate mode so that the file is overwritten each time a new scan completes successfully.

Connector Pane

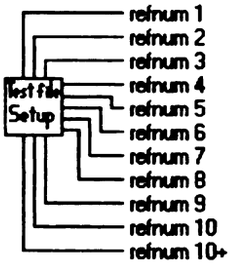

Front Panel

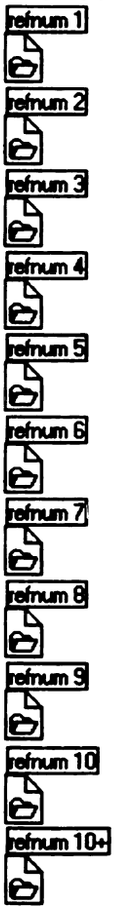

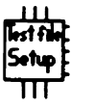

Block Diagram

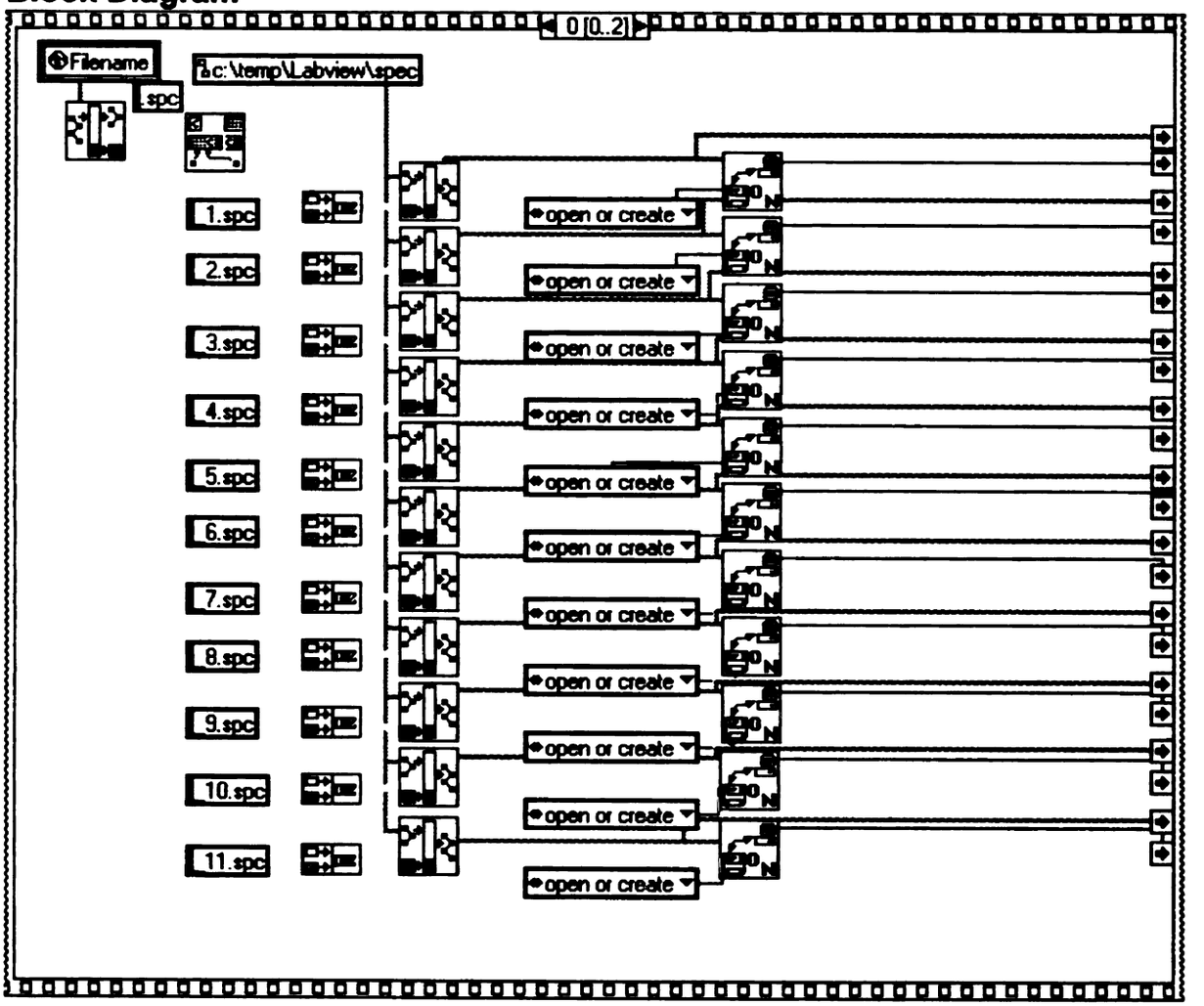

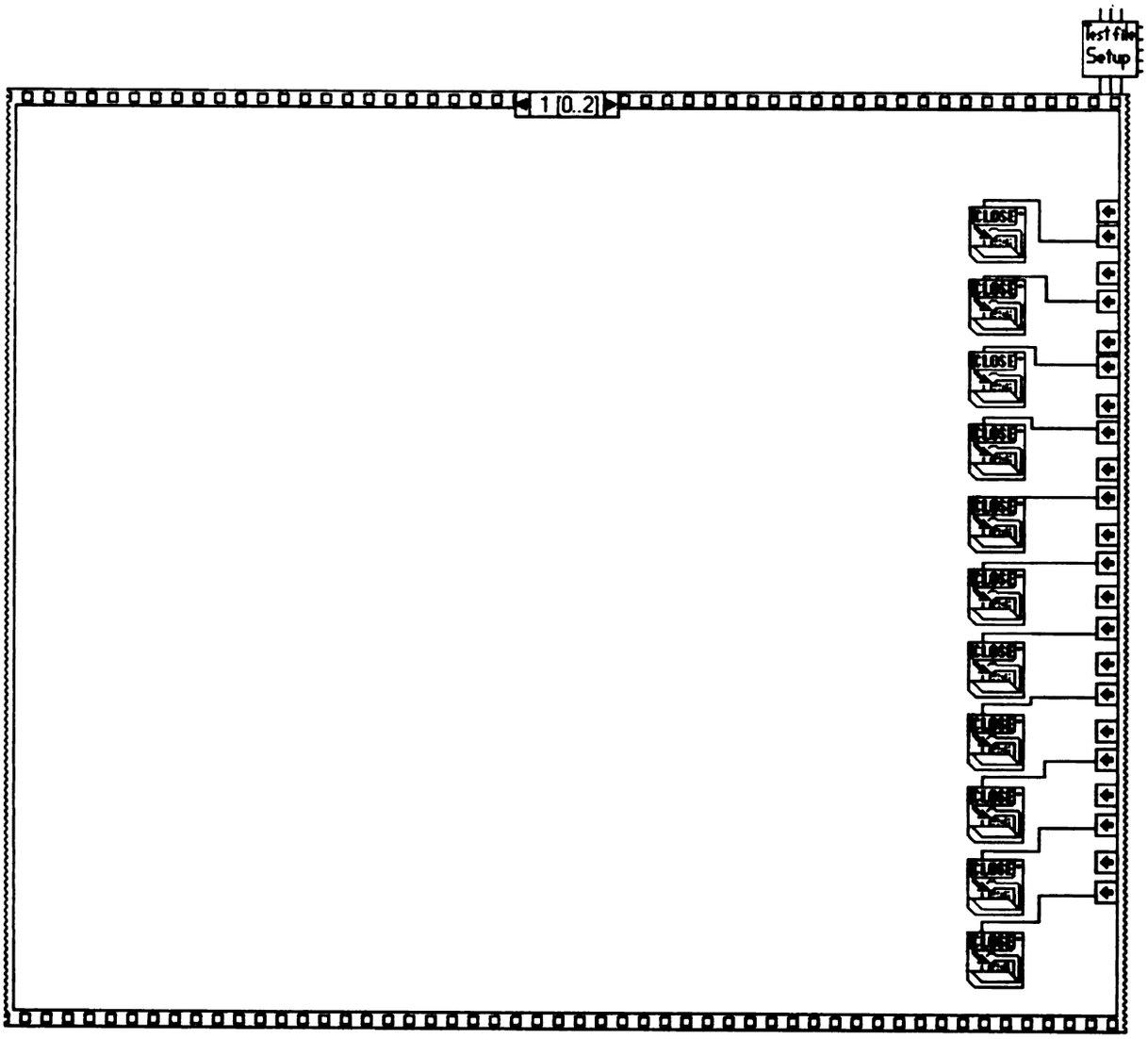
test file
Setup
1 [0..2]

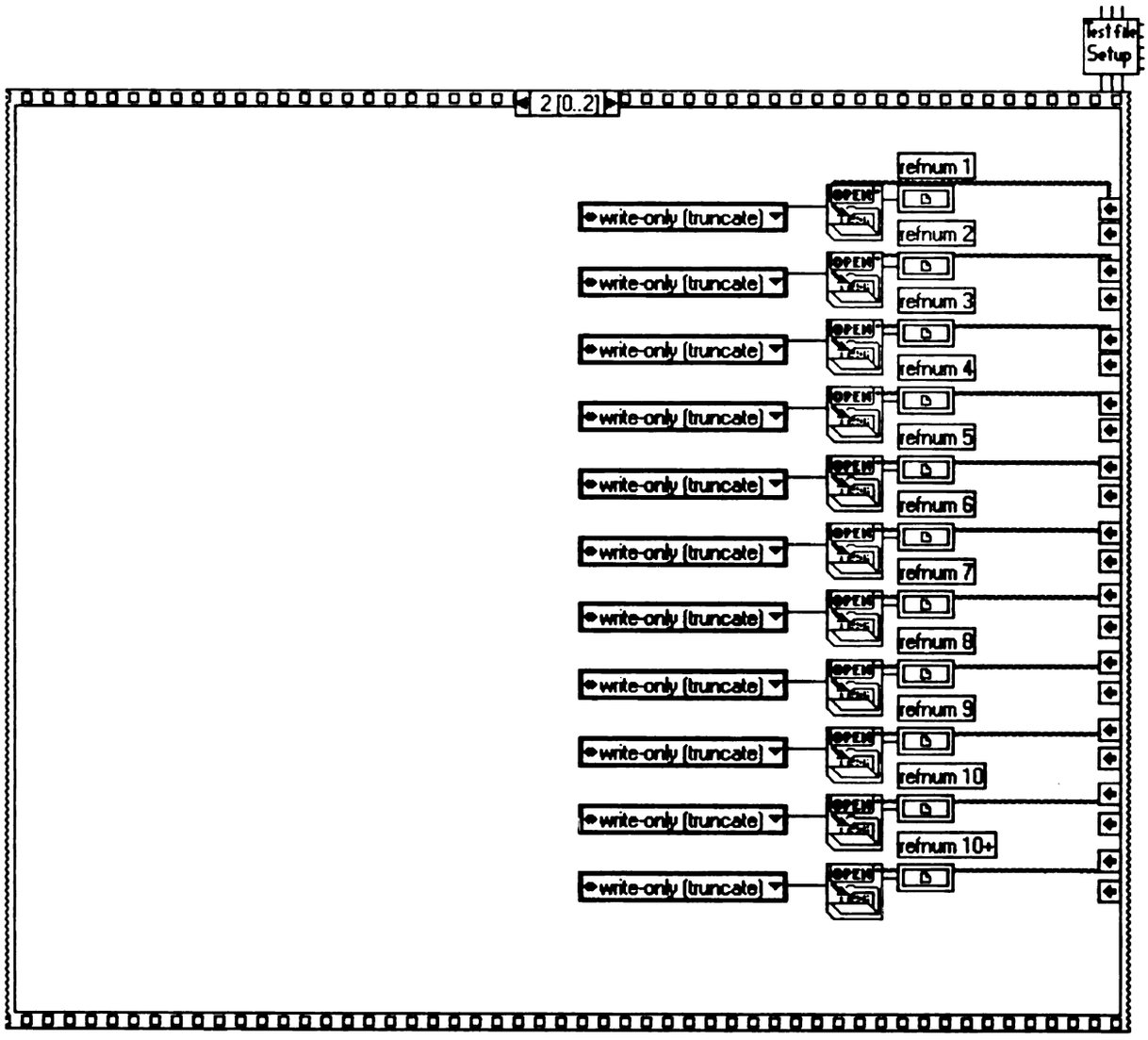
test file Setup
2 [0..2]
refnum 1
write-only (truncate)
refnum 2
write-only (truncate)
refnum 3
write-only (truncate)
refnum 4
write-only (truncate)
refnum 5
write-only (truncate)
refnum 6
write-only (truncate)
refnum 7
write-only (truncate)
refnum 8
write-only (truncate)
refnum 9
write-only (truncate)
refnum 10
write-only (truncate)
refnum 10+
write-only (truncate)

B.4. Headerspec.vi (Header)

This vi assimilates the setup parameters into a header cluster that is used by other vi's.

Connector Pane

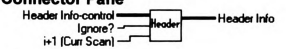

Front Panel

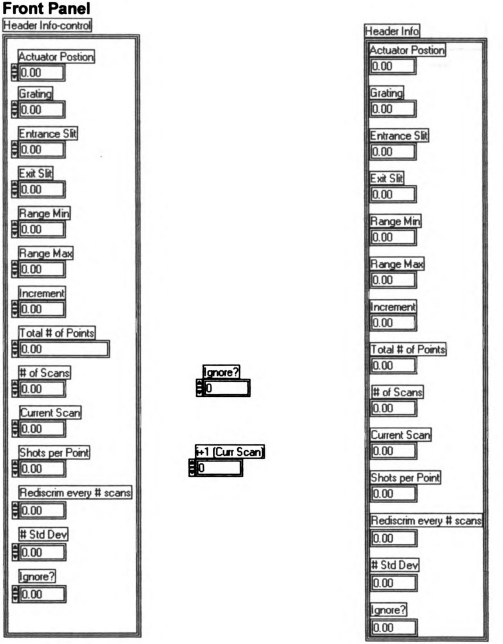

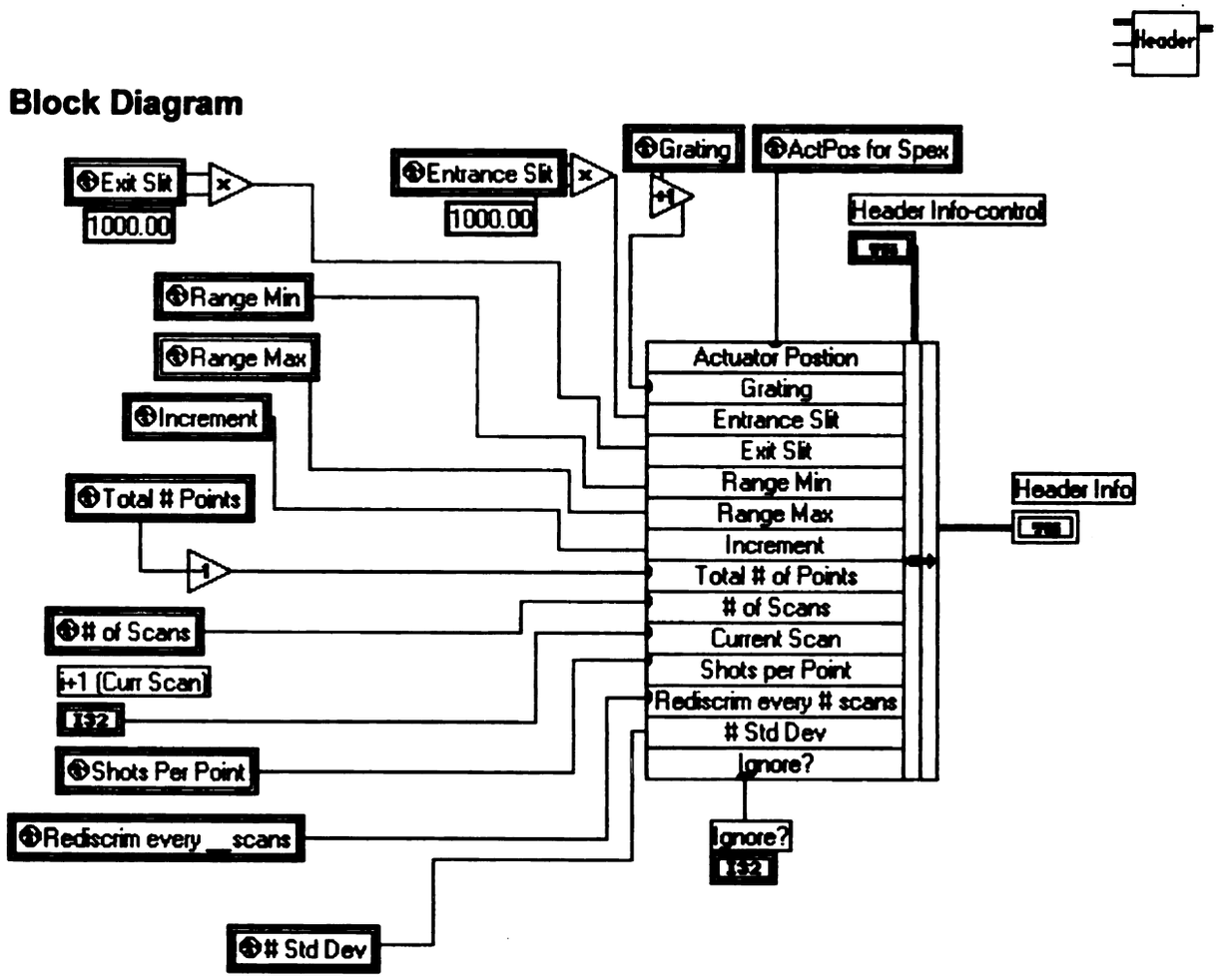
Header
Block Diagram
Exit Slit
1000.00
Entrance Slit
1000.00
Grating
ActPos for Spex
Header Info-control
Range Min
Range Max
Increment
Total # Points
# of Scans
i+1 (Curr Scan)
Shots Per Point
Rediscrim every __scans
Std Dev
Actuator Postion
Grating
Entrance Slit
Exit Slit
Range Min
Range Max
Increment
Total # of Points
# of Scans
Current Scan
Shots per Point
Rediscrim every # scans
Std Dev
Ignore?
Header Info
Ignore?

B.5. rediscrimspc.vi (Rediscr)

This vi takes 500 shots of data from the reference diode to determine the max and min values for the discrimination. The SRS 245 vi is written to compute max/min based on user preference for std dev. The max and min determined for discrimination is then passed back to take fts vi.

Connector Pane

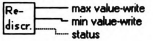

Front Panel

Block Diagram

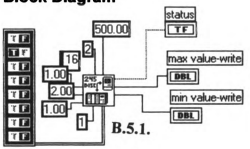

B.5.1.

B.5.1. SR 245_rediscr_spc.vi (245 DISC)

This vi is a variation on the SRS 245 vi from NI. This vi allows for input of GBIP, scan channels, # of scans, trigger setting and gives output of status and maximum and minimum values for discrimination. It determines these values from global variable defined by user for method of discrimination (standard deviation).

Connector Pane

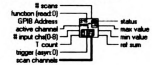

Front Panel

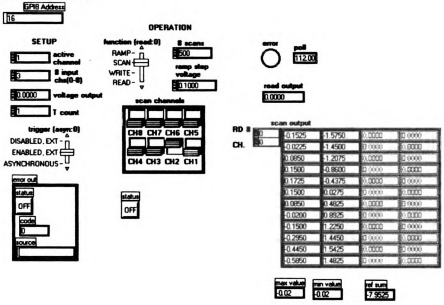

Block Diagram

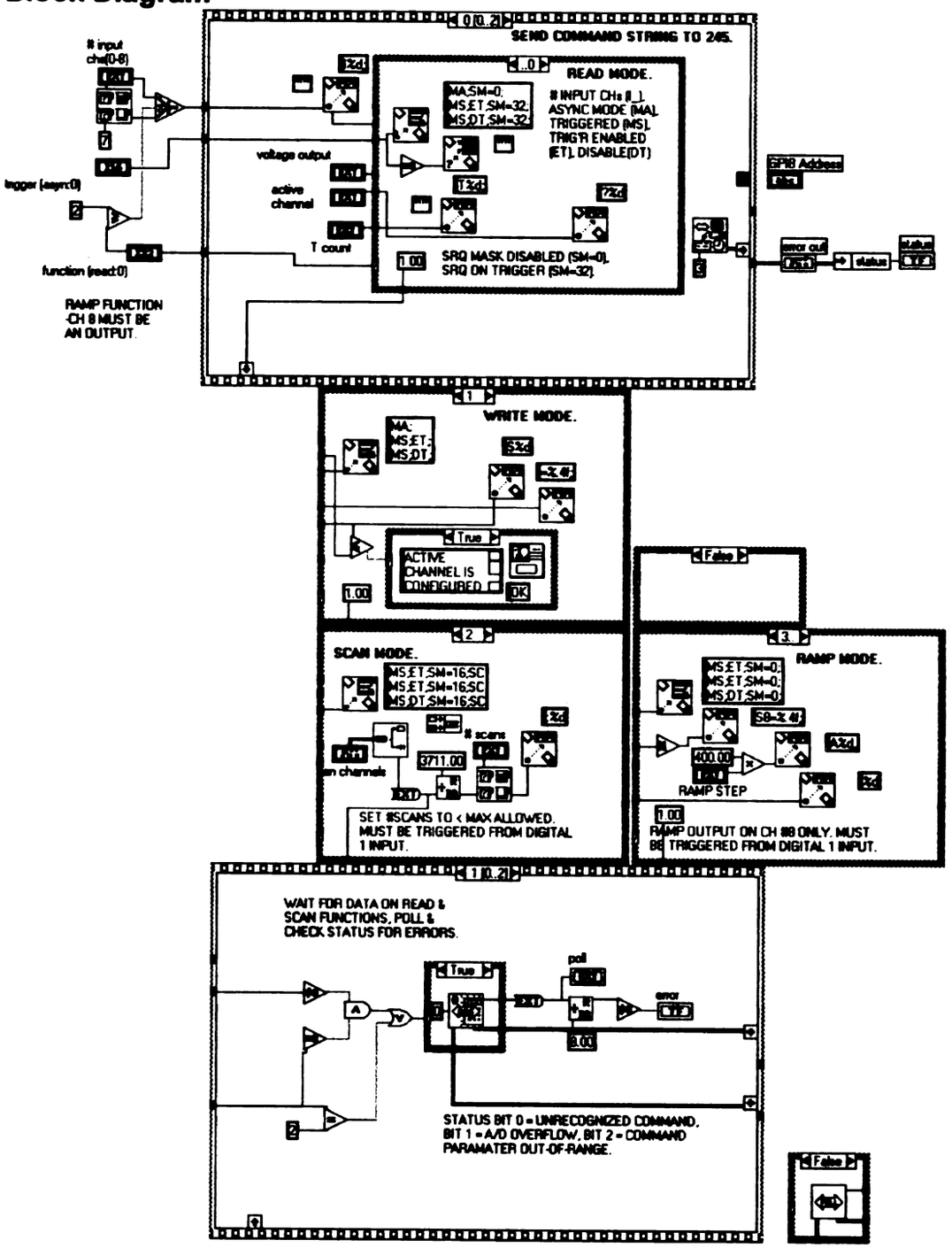

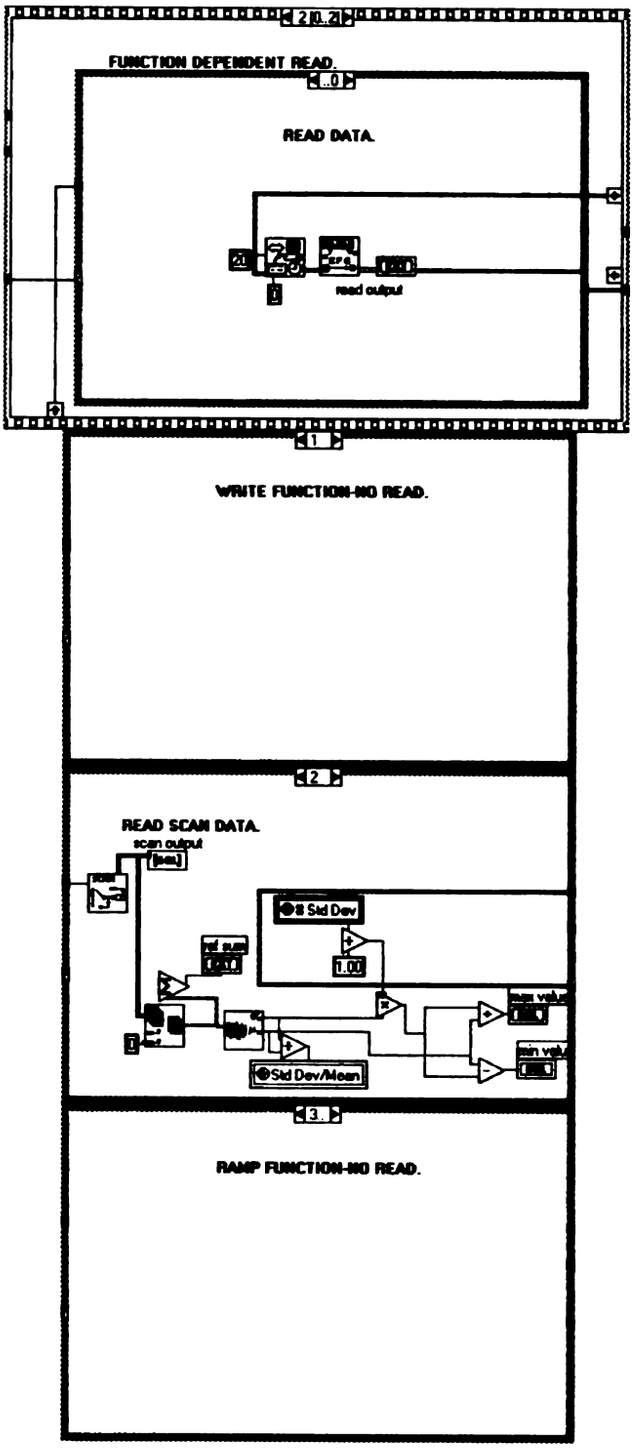
2 [0..2]
FUNCTION DEPENDENT READ.
..0
READ DATA.
read output
1
WRITE FUNCTION-NO READ.
2
READ SCAN DATA.
scan output
Std Dev
1.00
Std Dev/Mean
3
RAMP FUNCTION-NO READ.

B.6. discrimdataspc.vi (Discrimin)

This vi takes discriminated data (reference max/min determined by rediscrim vi). If a long wait occurs, vi asks user for action to take- ignore discrimination, ignore until next preset discrimination, ignore until end of scan then rediscriminate, or rediscriminate now. If the last option is chosen and a long wait occurs again, the computer alerts the user but will then take data by ignore discrimination until end of scan and then rediscriminate. If any ignore type options are chosen in the first screen, ignore becomes true within this vi and is transferred back to take data vi so that other data acquisition vi (non-discrimination) is used until proper time for rediscrimination (depends on option chosen).

Connector Pane

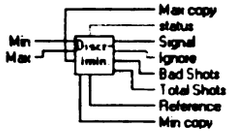

Front Panel

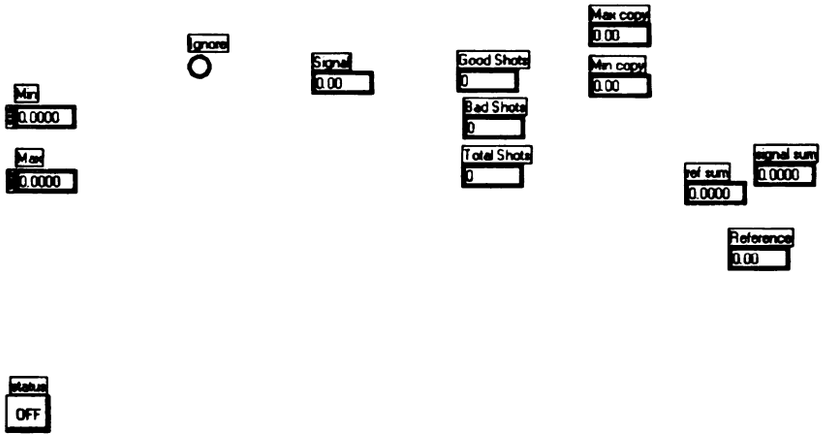

Block Diagram

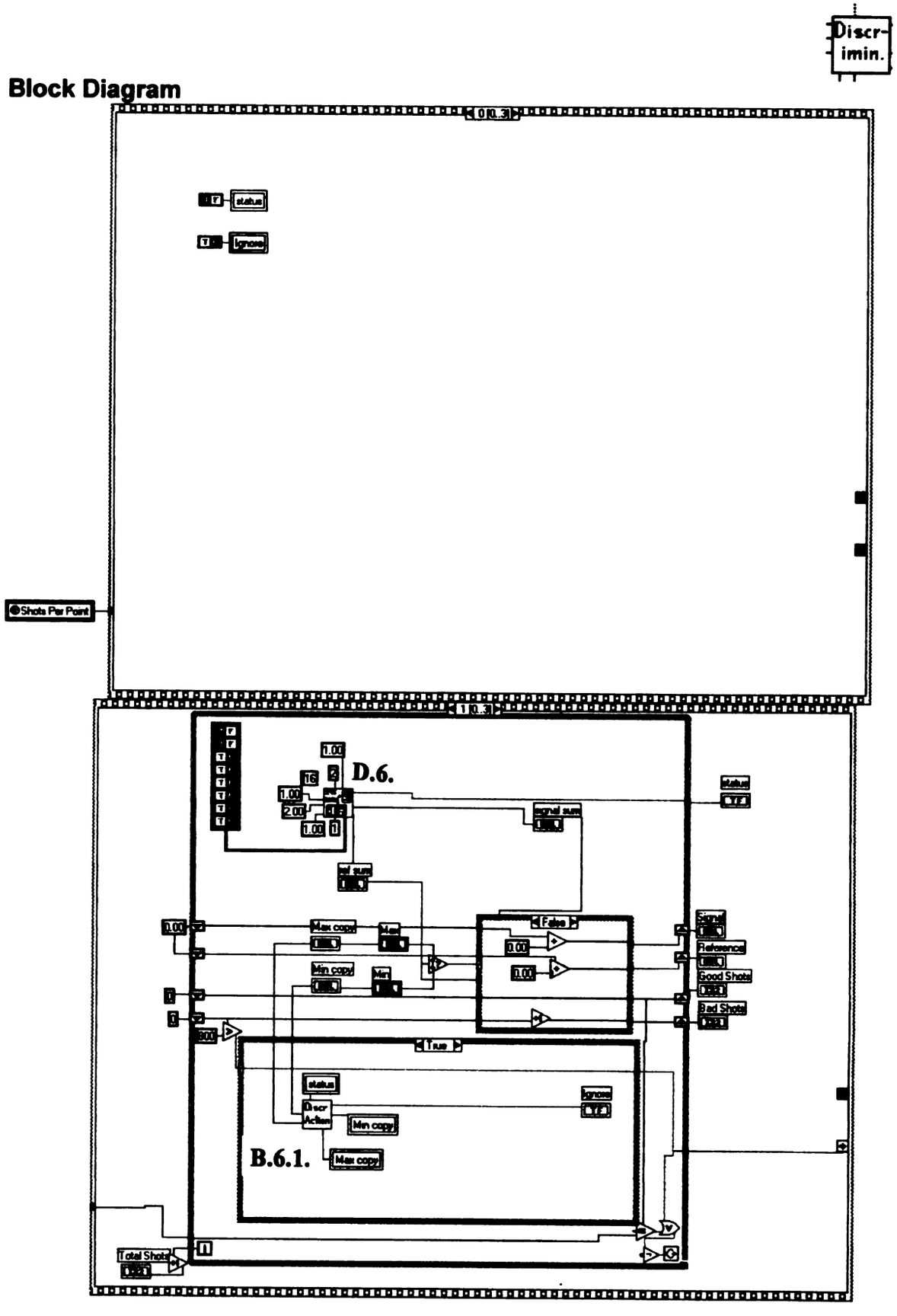

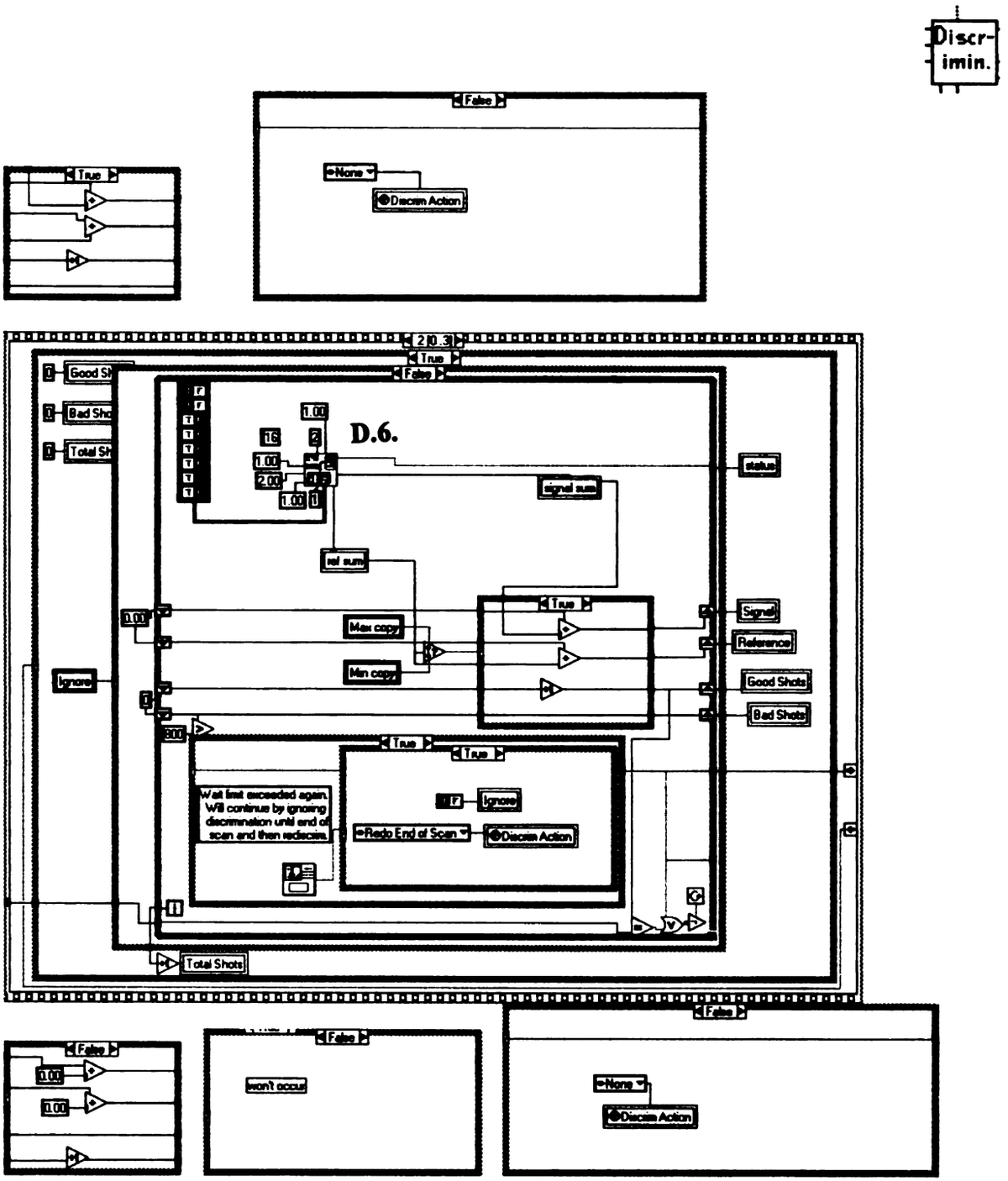
Discr-
imin.
False
None
Discrim Action
True
D.6.
Good Sh
Bad Sho
Total Sh
status
signal sum
Max copy
Min copy
Signal
Reference
Good Shots
Bad Shots
Ignore
Wait limit exceeded again.
Will continue by ignoring
discrimination until end of
scan and then rediscrim.
Redo End of Scan
Discrim Action
Total Shots
won't occur

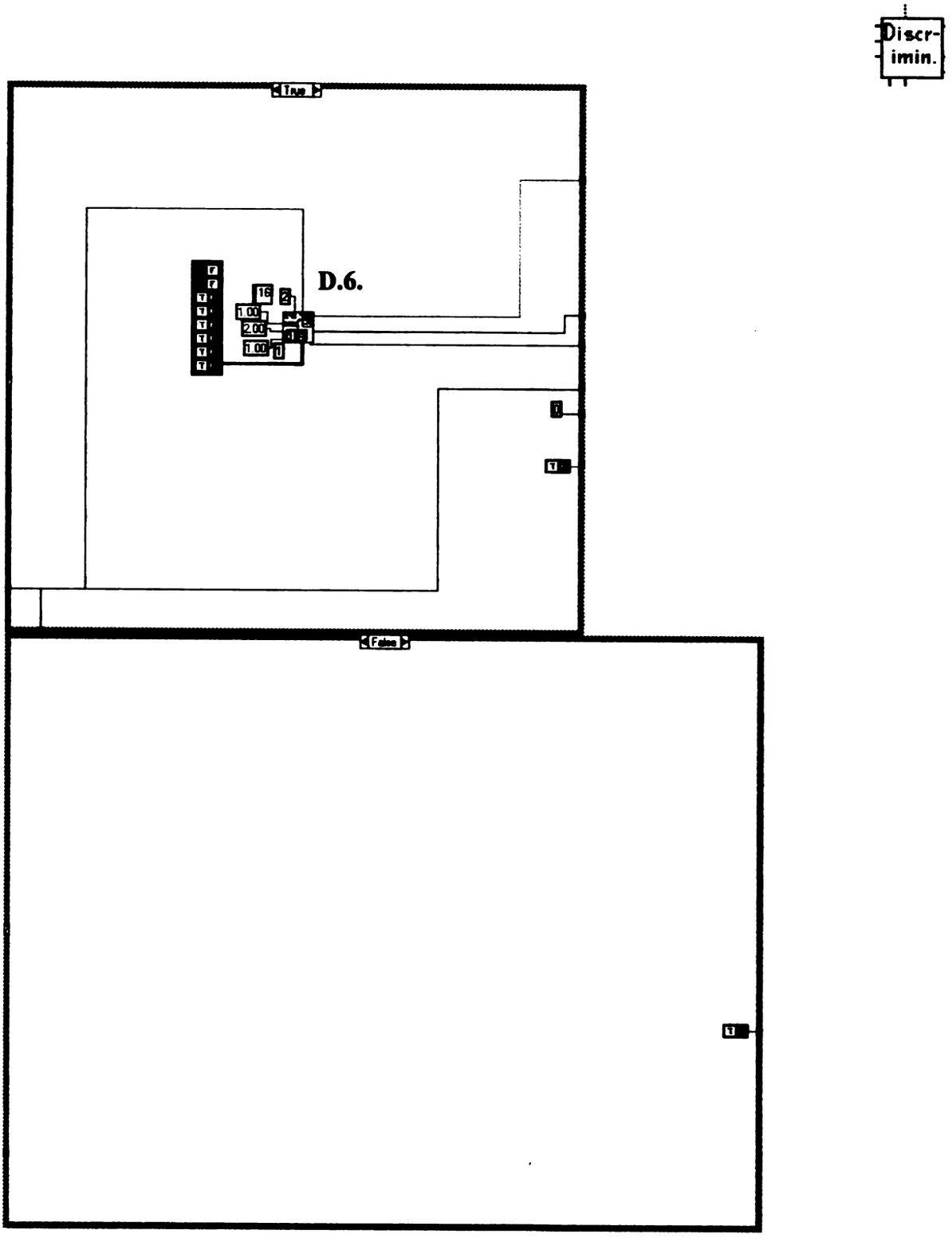
Discr-
imin.
True
D.6.
16
1.00
2.00
1.00
0
False

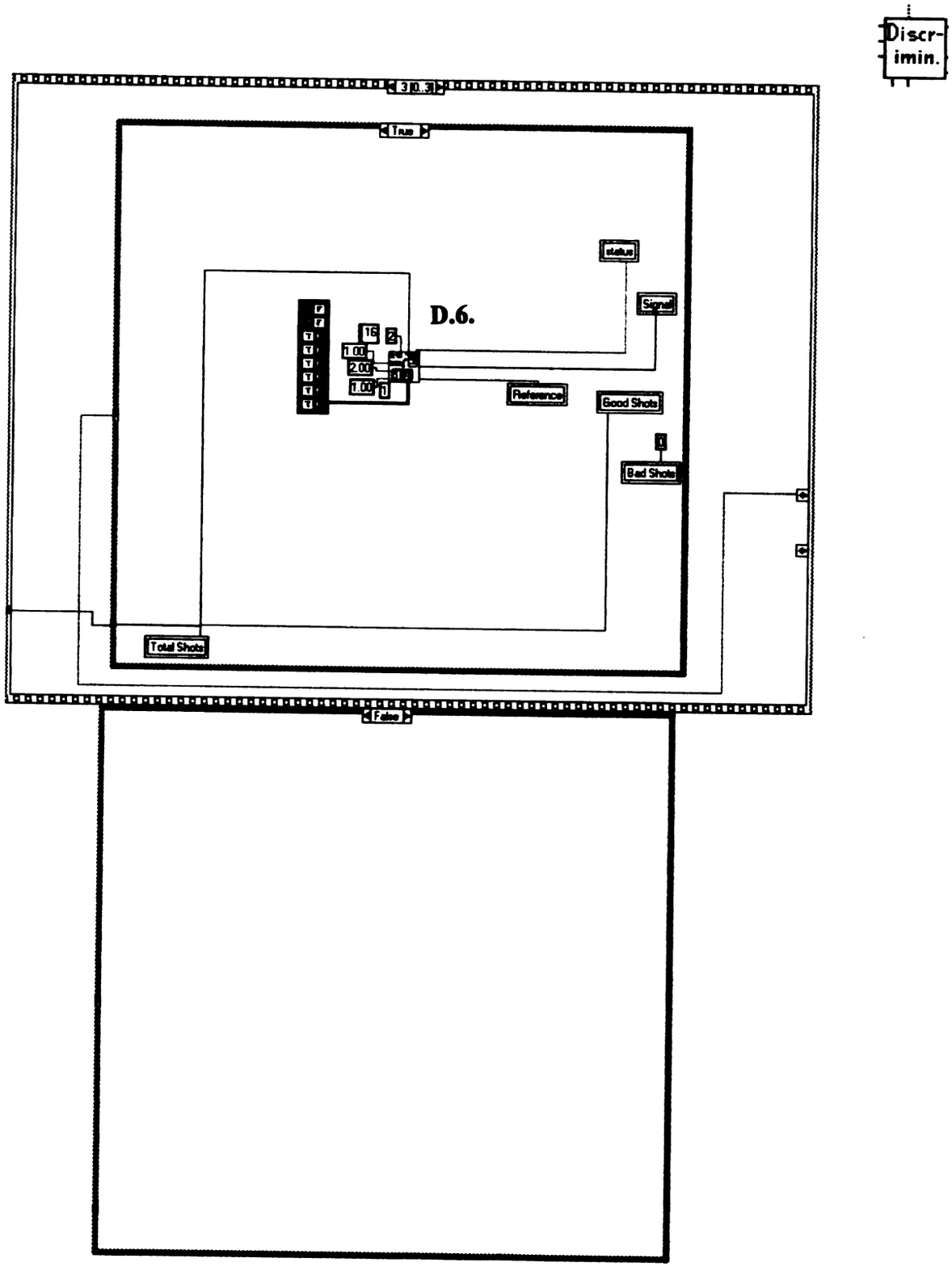
Discr-
imin.
3 [0..3]
True
status
Signal
D.6.
16
2
1.00
2.00
1.00
Reference
Good Shots
1
Bad Shots
Total Shots
False

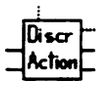

B.6.1. discrimactwaitspc.vi (Discr Action)

This is the vi that appears if there is too many bad shots in a row (called wait limit). This alerts user and waits for instruction on options. If redo now is called, this vi reruns rediscrim vi. For the other options, it sets the global variable to proper setting and returns to discrimdata vi.

Connector Pane

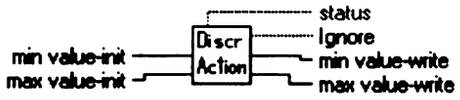

Front Panel

Wait limit exceeded- what would you like to do?

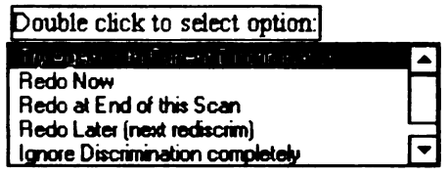

Block Diagram

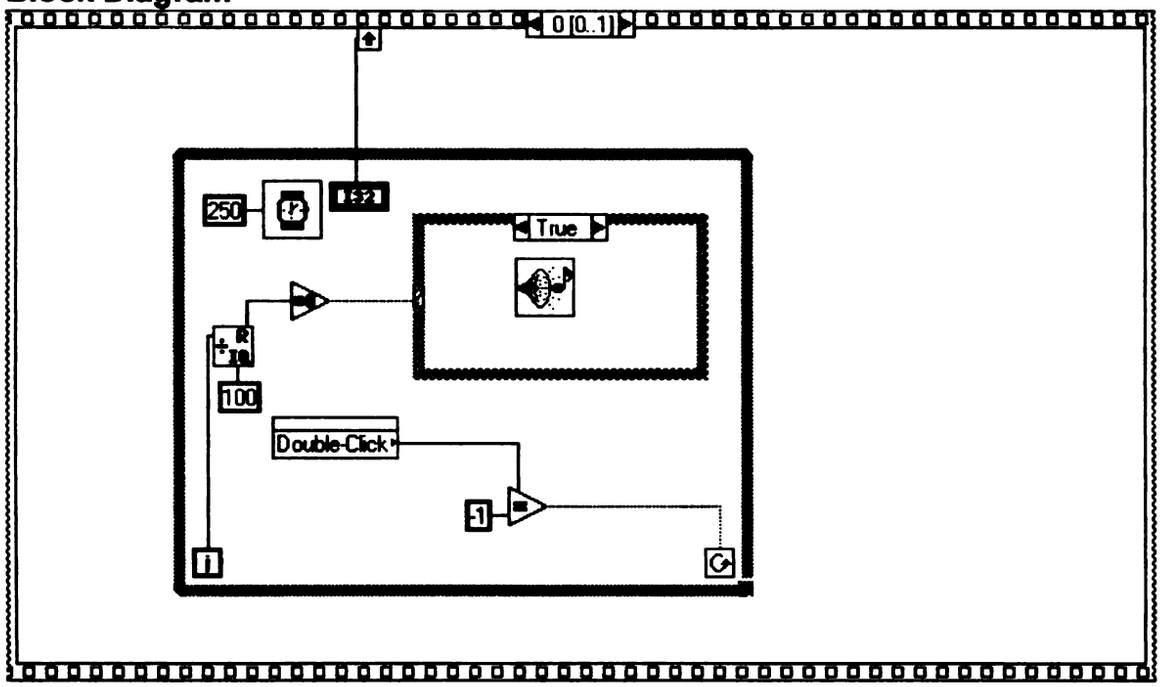

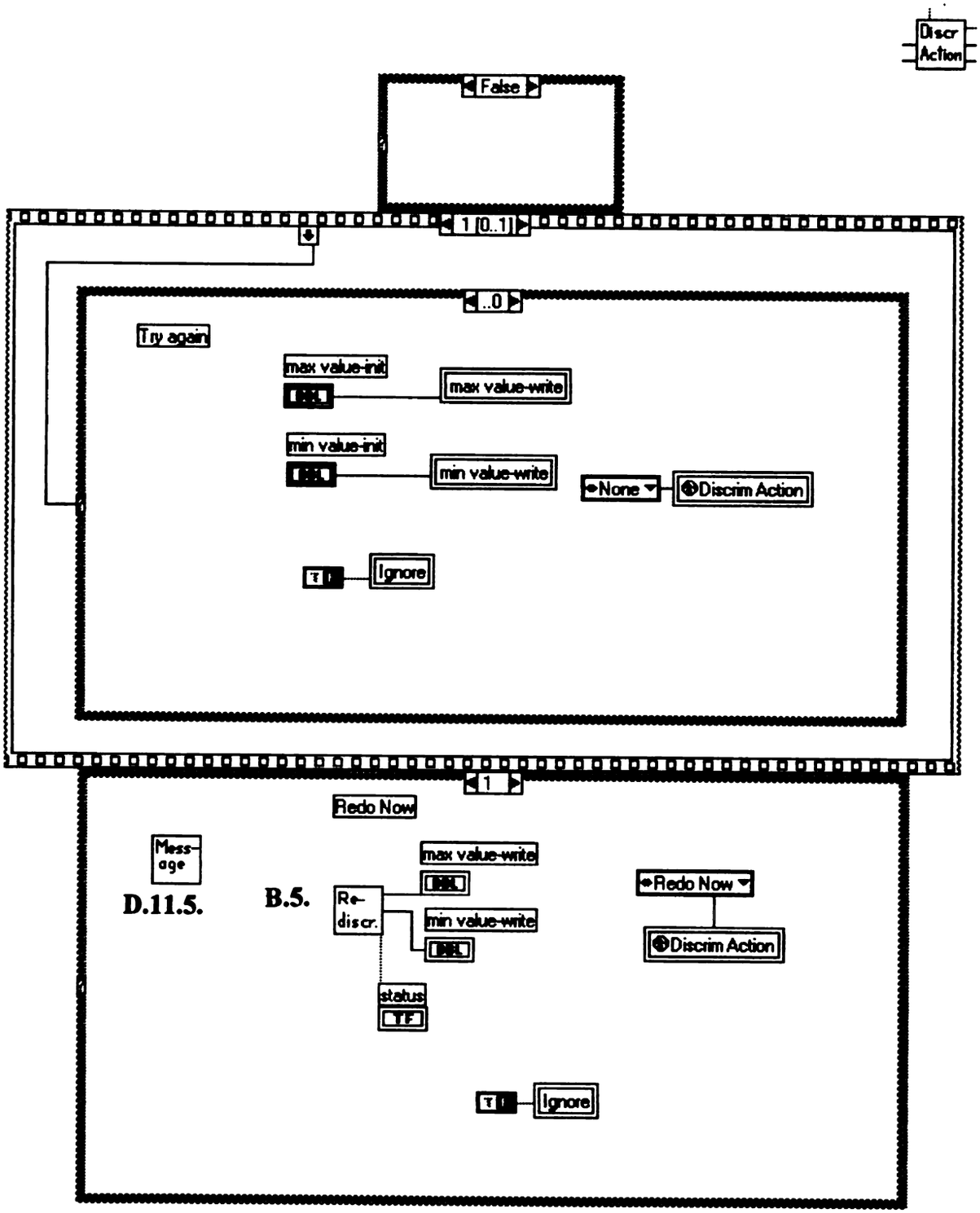
Discr Action
False
1 [0..1]
..0
Try again
max value-init
max value-write
min value-init
min value-write
None
Discrim Action
Ignore
1
Redo Now
Mess-age
D.11.5.
B.5.
max value-write
Re-discr.
min value-write
status
TF
Redo Now
Discrim Action
Ignore

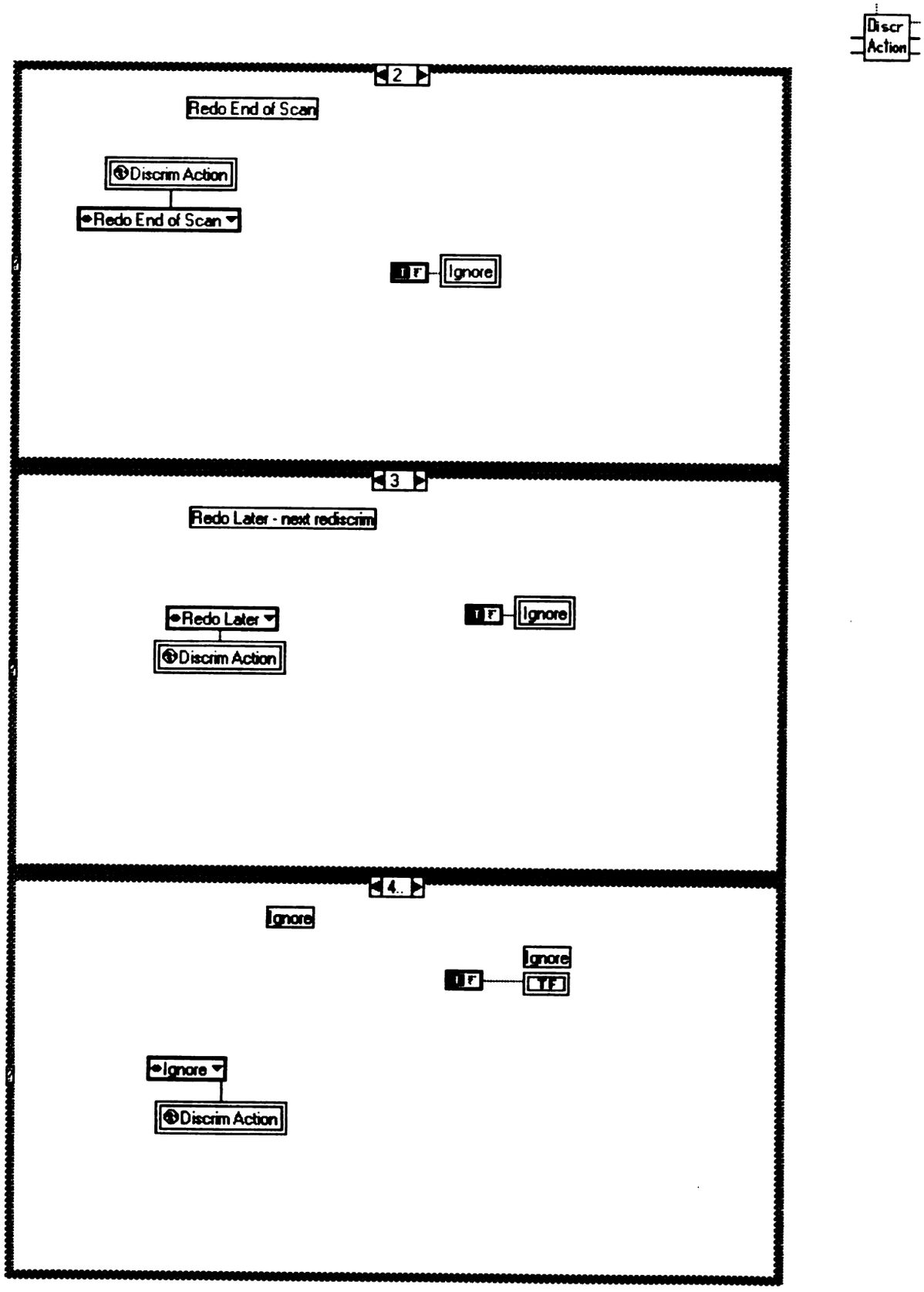
Discr Action
2
Redo End of Scan
Discrim Action
Redo End of Scan
TF
Ignore
3
Redo Later - next rediscrim
Redo Later
Discrim Action
TF
Ignore
4..
Ignore
Ignore
TF
TF
Ignore
Discrim Action

B.7. Savespec.vi (Save Data)

This vi saves the data after each scan completes successfully into one of the intermediate vi's. For example, if the user selects 50 scans total, test1.spc will contain the sum of scans 1-9, test2.spc witll contain the sum of scans 1-19, test3.spc is the sum of scans 1-29, etc.

Connector Pane

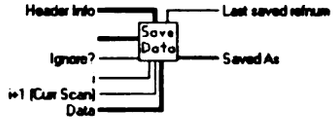

Front Panel

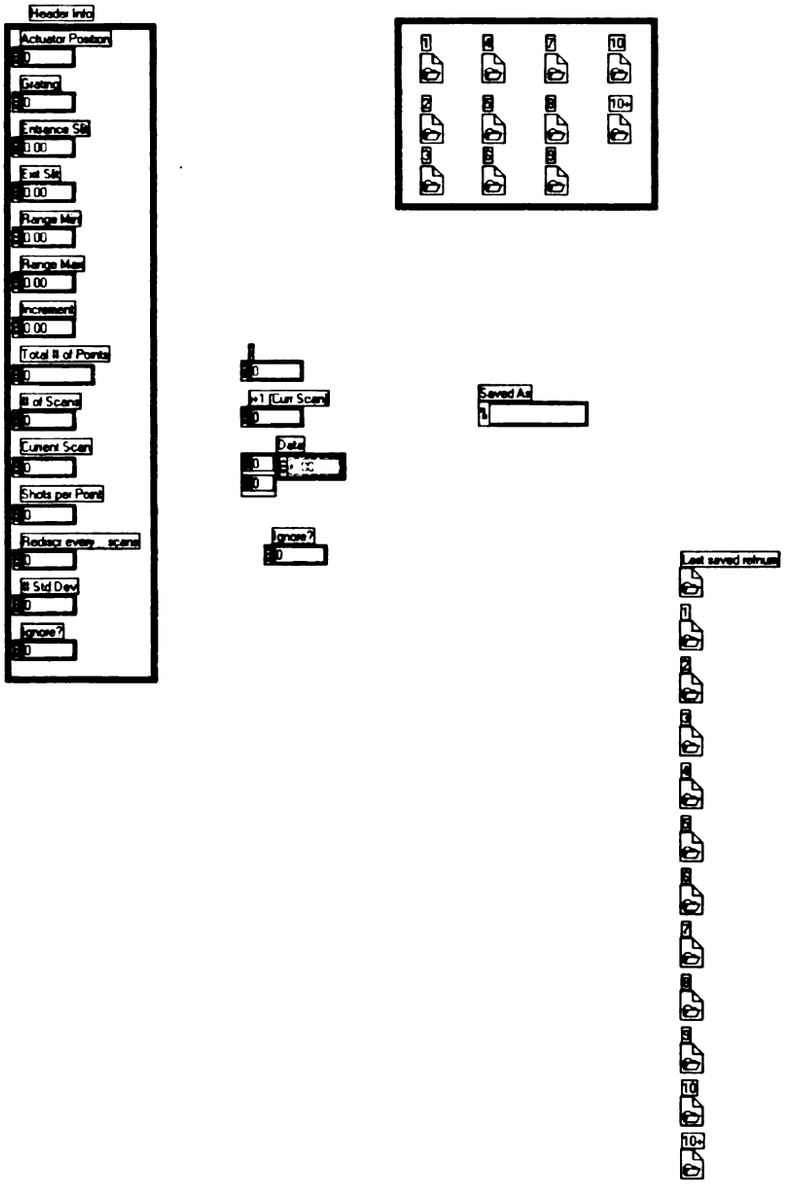

Block Diagram

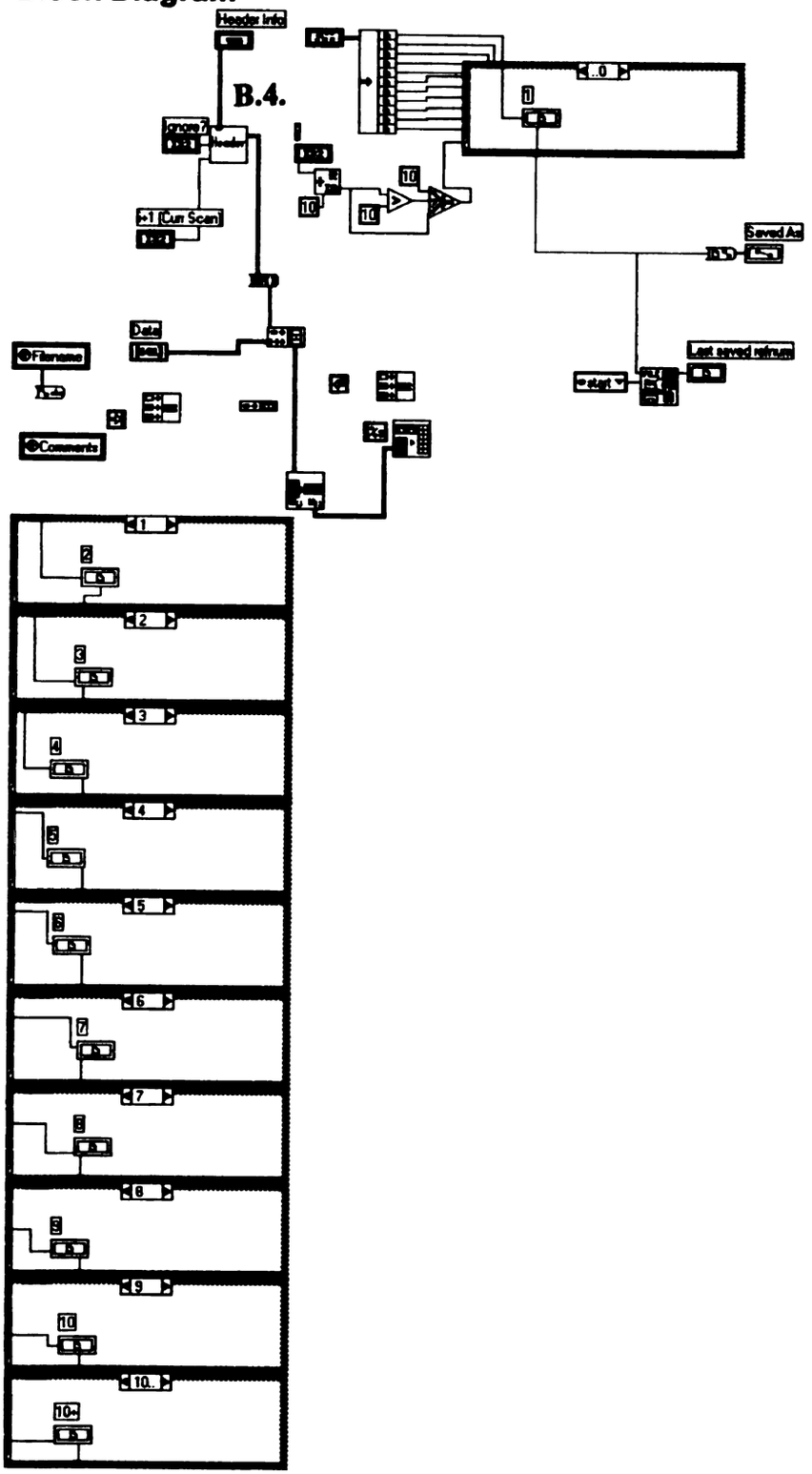

B.8. discrimactperspc.vi (Discr Action)

This is the vi that appears if the percentage discarded is too high. This alerts user and waits for instruction on options. For the options, it sets the global variable to proper setting and returns to discrimdata vi.

Connector Pane

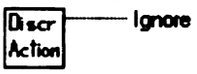

Front Panel

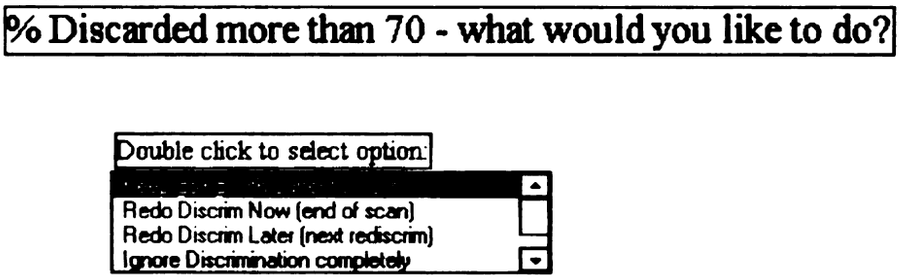

Block Diagram

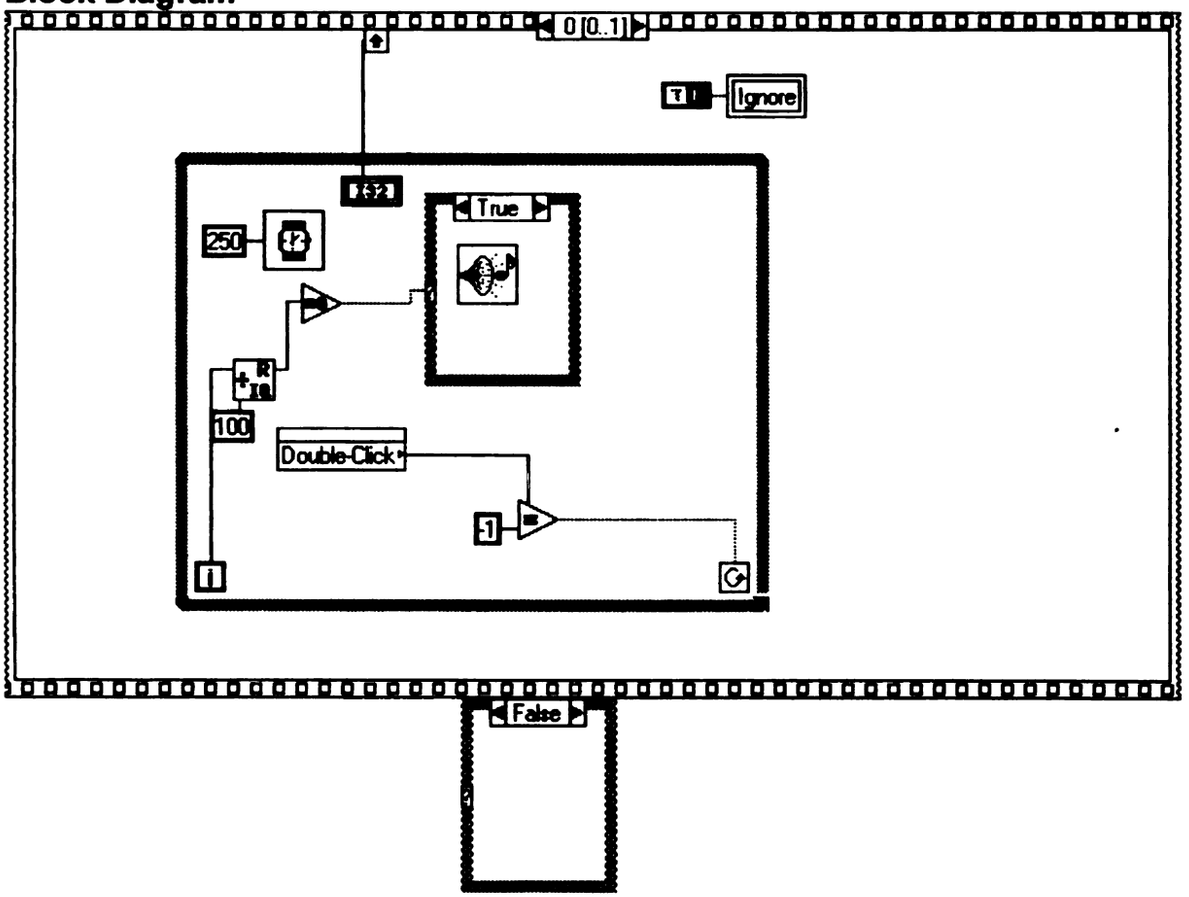

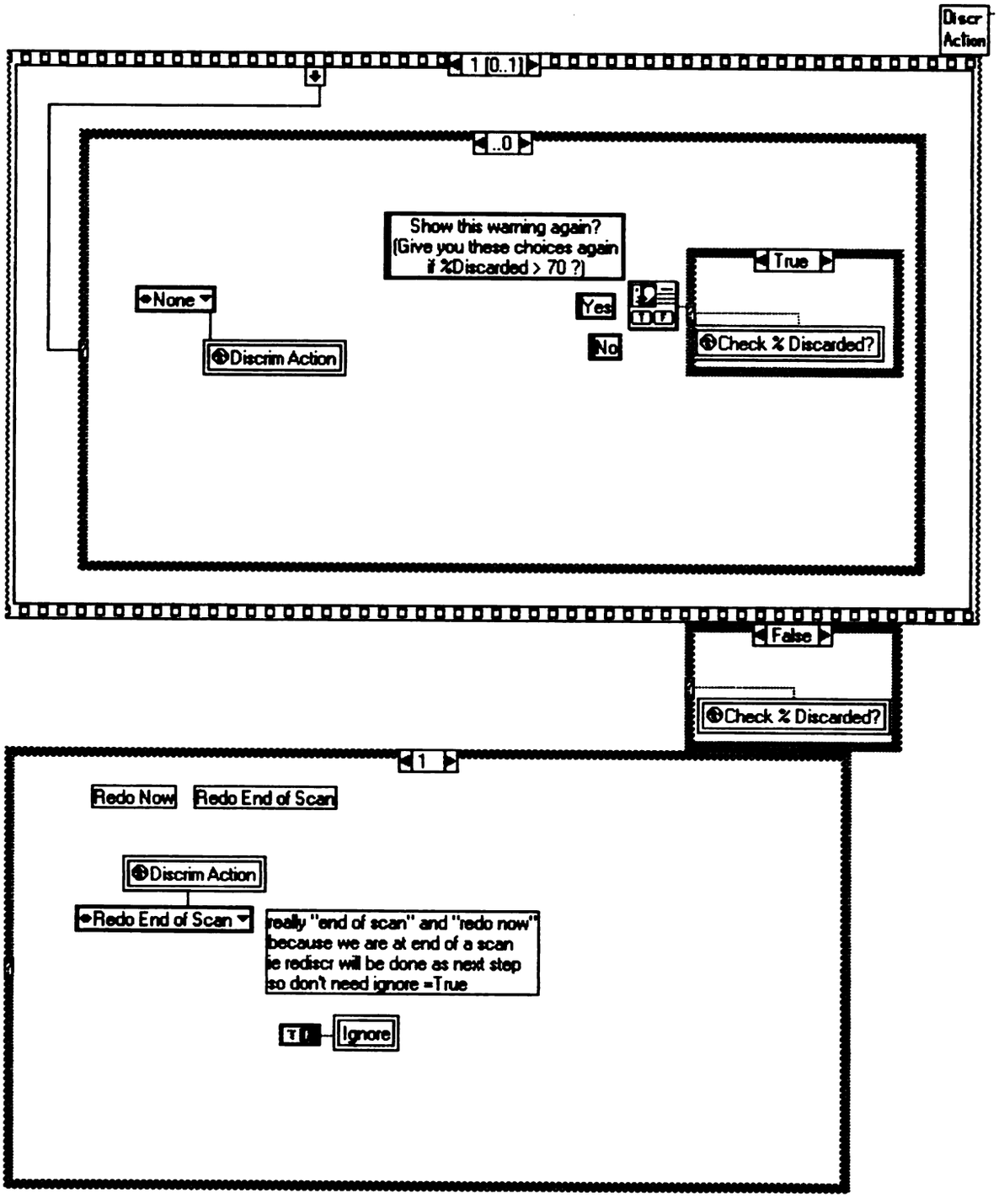
Discr Action
1 [0..1]
..0
Show this warning again?
(Give you these choices again
if %Discarded > 70 ?)
None
Discrim Action
Yes
No
True
Check % Discarded?
False
Check % Discarded?
1
Redo Now
Redo End of Scan
Discrim Action
Redo End of Scan
really "end of scan" and "redo now"
because we are at end of a scan
ie rediscr will be done as next step
so don't need ignore =True
Ignore

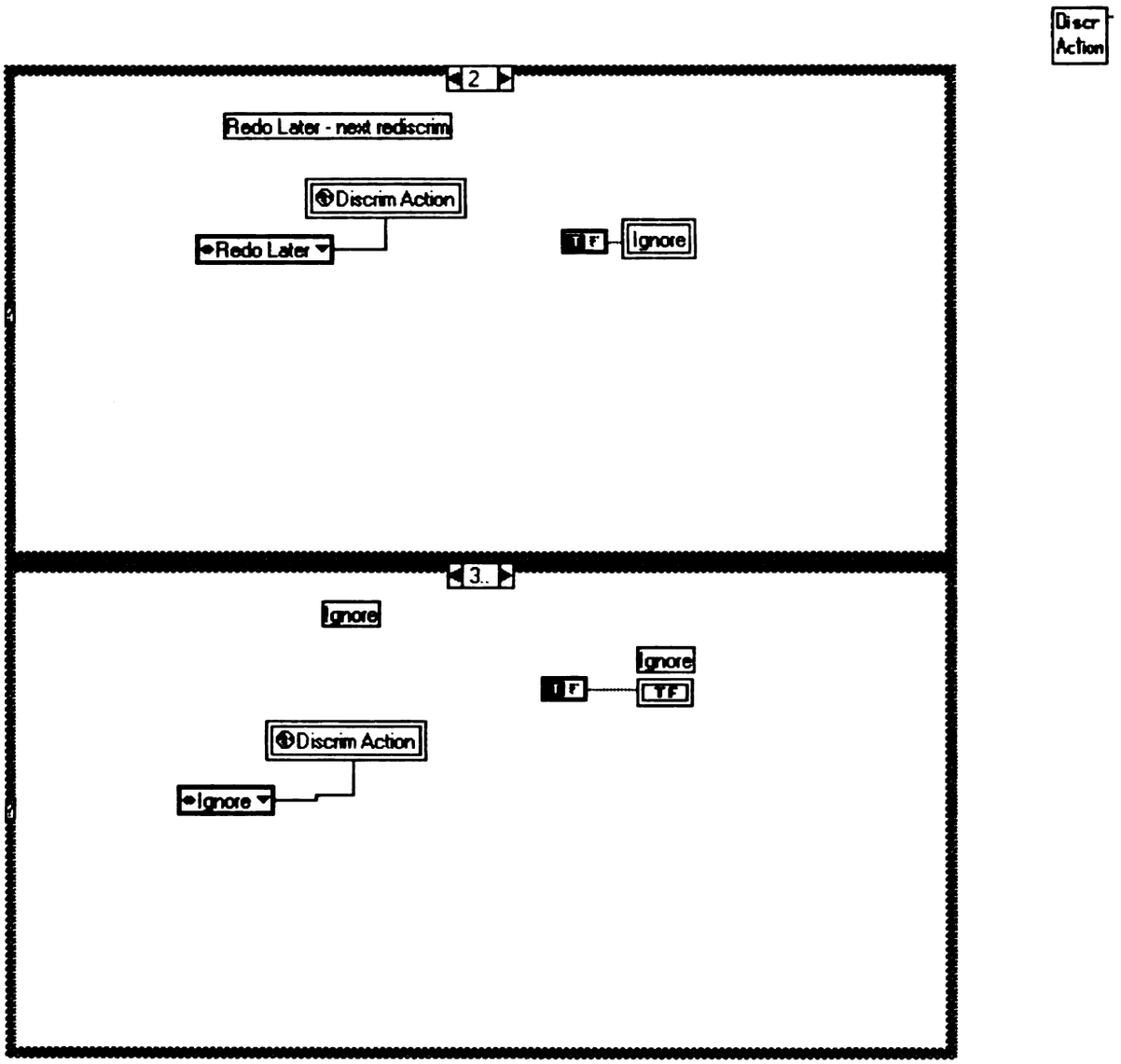
Discr Action
2
Redo Later - next rediscrim
Discrim Action
Redo Later
TF
Ignore
3..
Ignore
Ignore
TF
Discrim Action
Ignore

B.9. Finalspec.vi (Final Save)

This vi saves the data under the filename given in the setup parameters. This save occurs whether the set of scans completes normally or is stopped in the middle using the pause/stop button on the screen. (This save will not occur if the hard stop at the top of the screen is used.)

Connector Pane

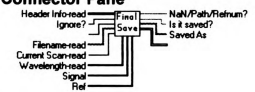

Front Panel

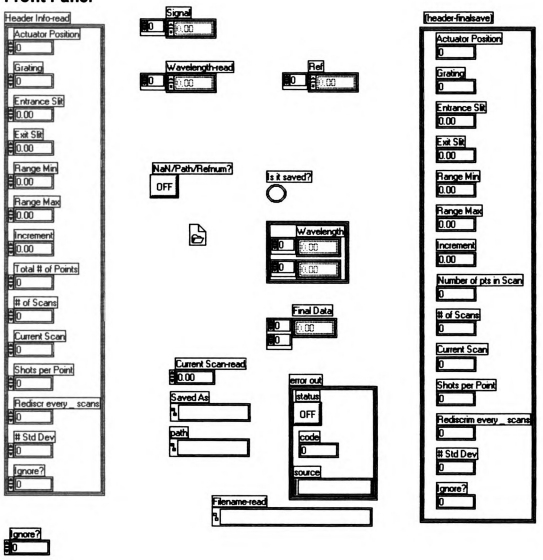

Block Diagram

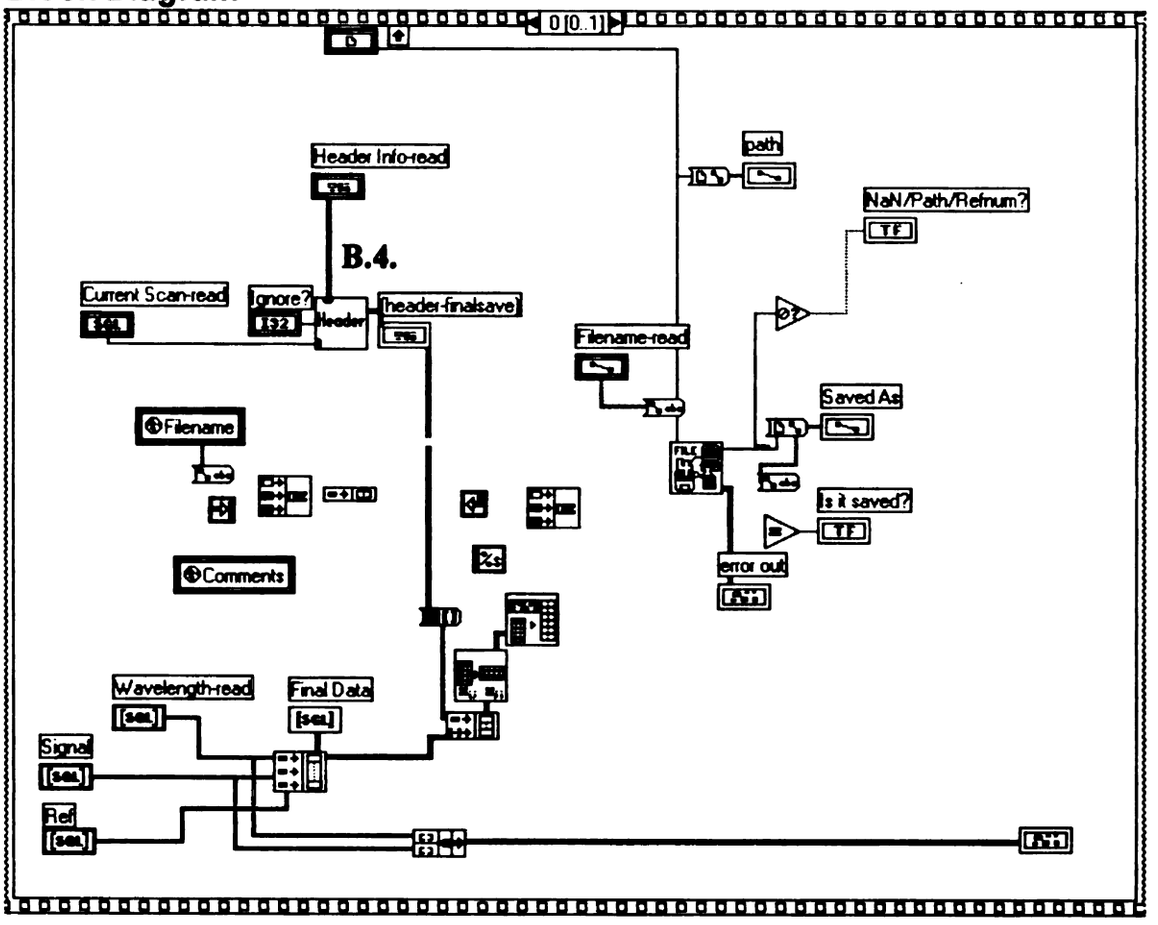

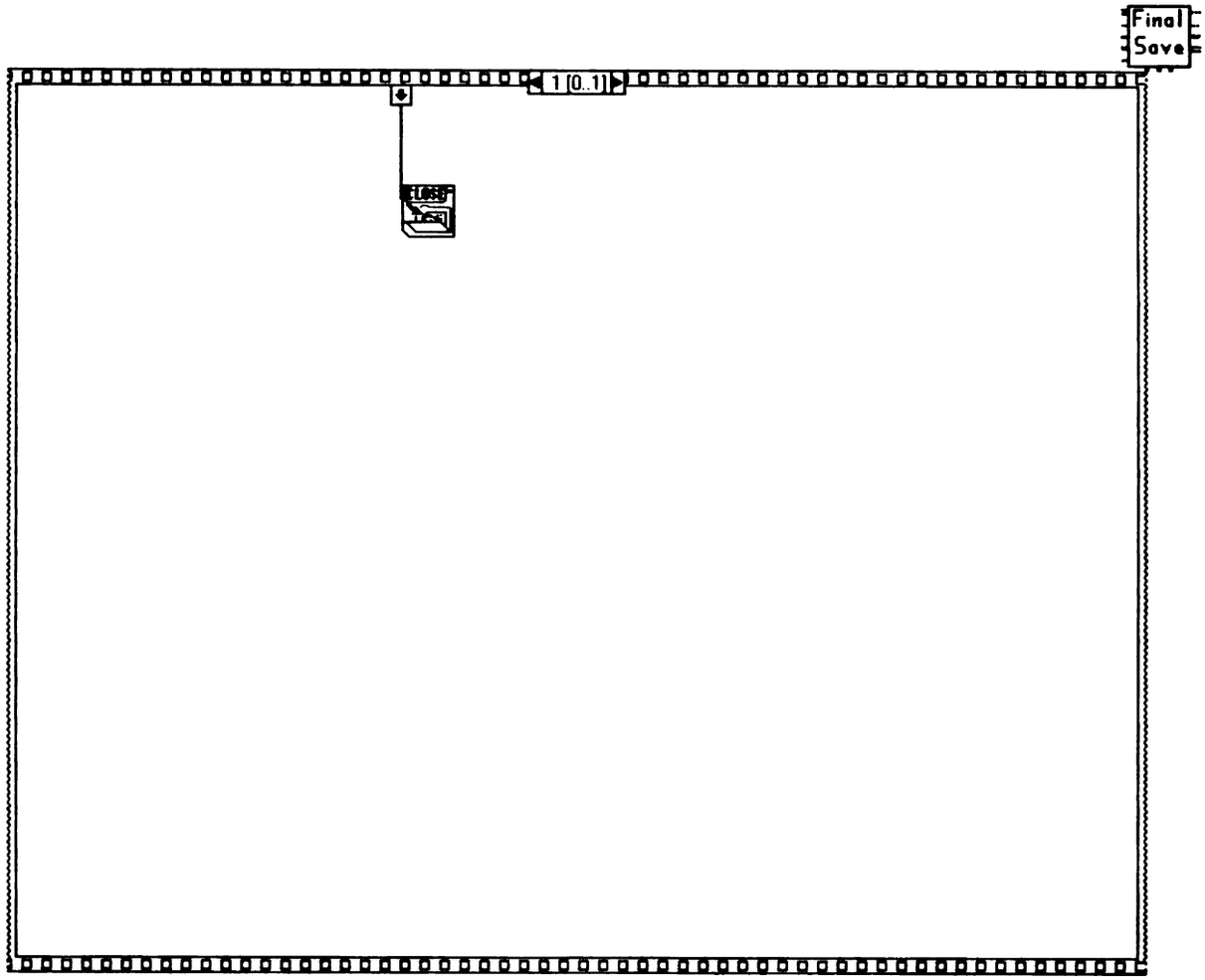
Final
Save
1 [0..1]

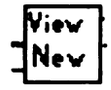

B.10. viewnewspec.vi (View New)

This vi will plot newer *.spc files and allow the user to print the spectrum, choose another file to view, or to return to taking data. The exit returns user to initial scan/spec program screen. The opennewspec vi directly communicates the proper info to this vi.

Note: the only difference between this vi and the viewoldspc vi is that older *.spc files had an error in the last wavelength recorded- and viewospc removes this incorrect 0 when finding max wavlength. These two vi's may be able to be combined if the 0 (and its corresponding data pt) can be deleted and then the range can be found using the Max/Min fcn vi.

Connector Pane

Front Panel

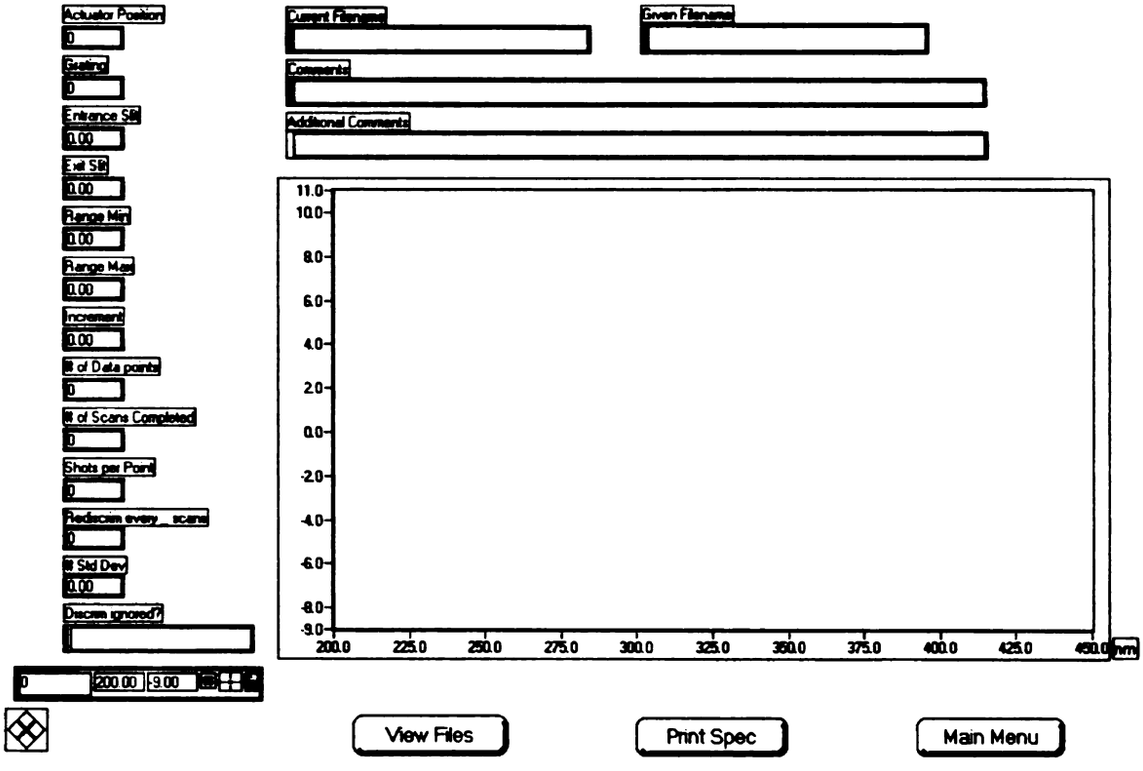

View
New

Block Diagram

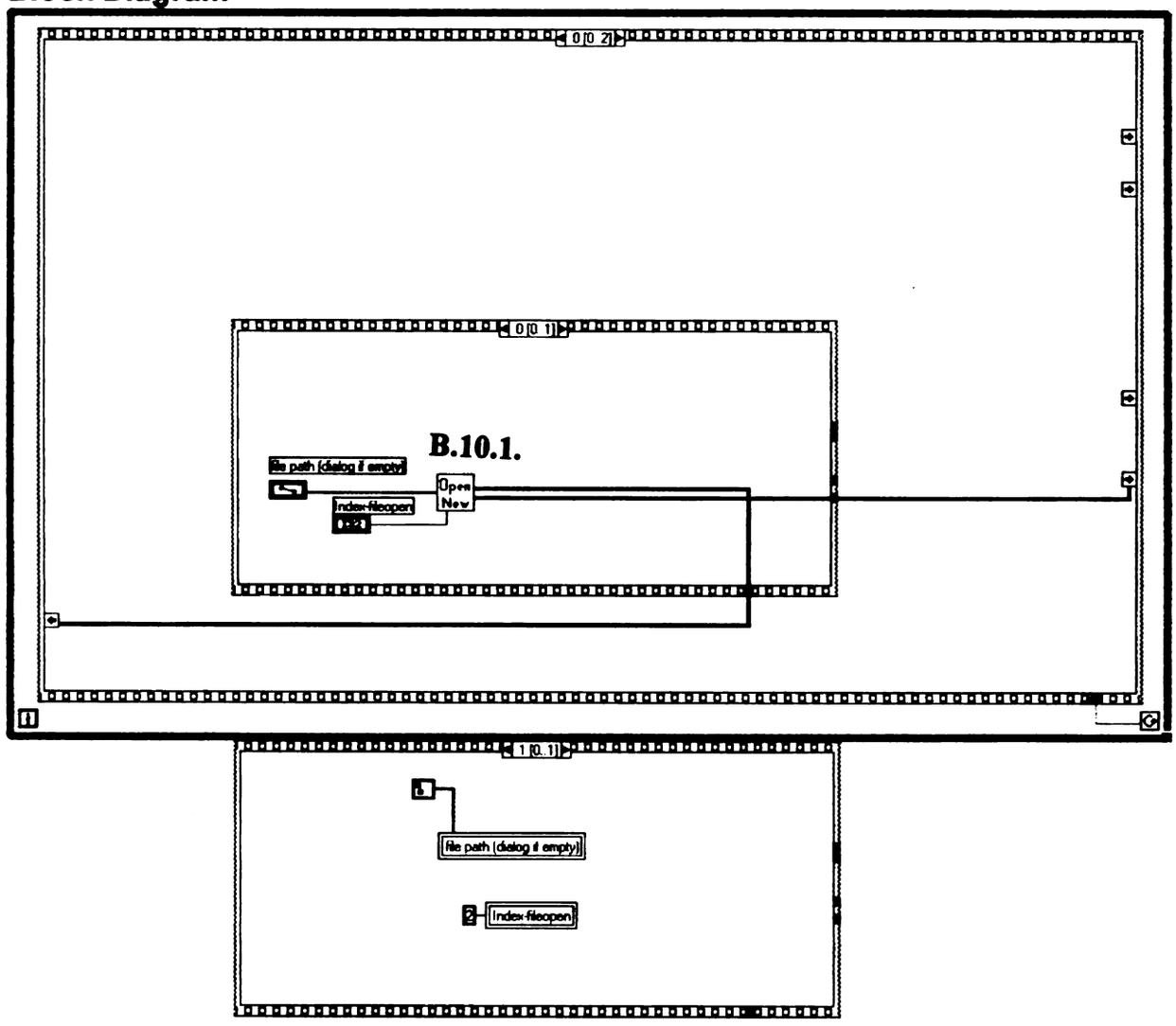

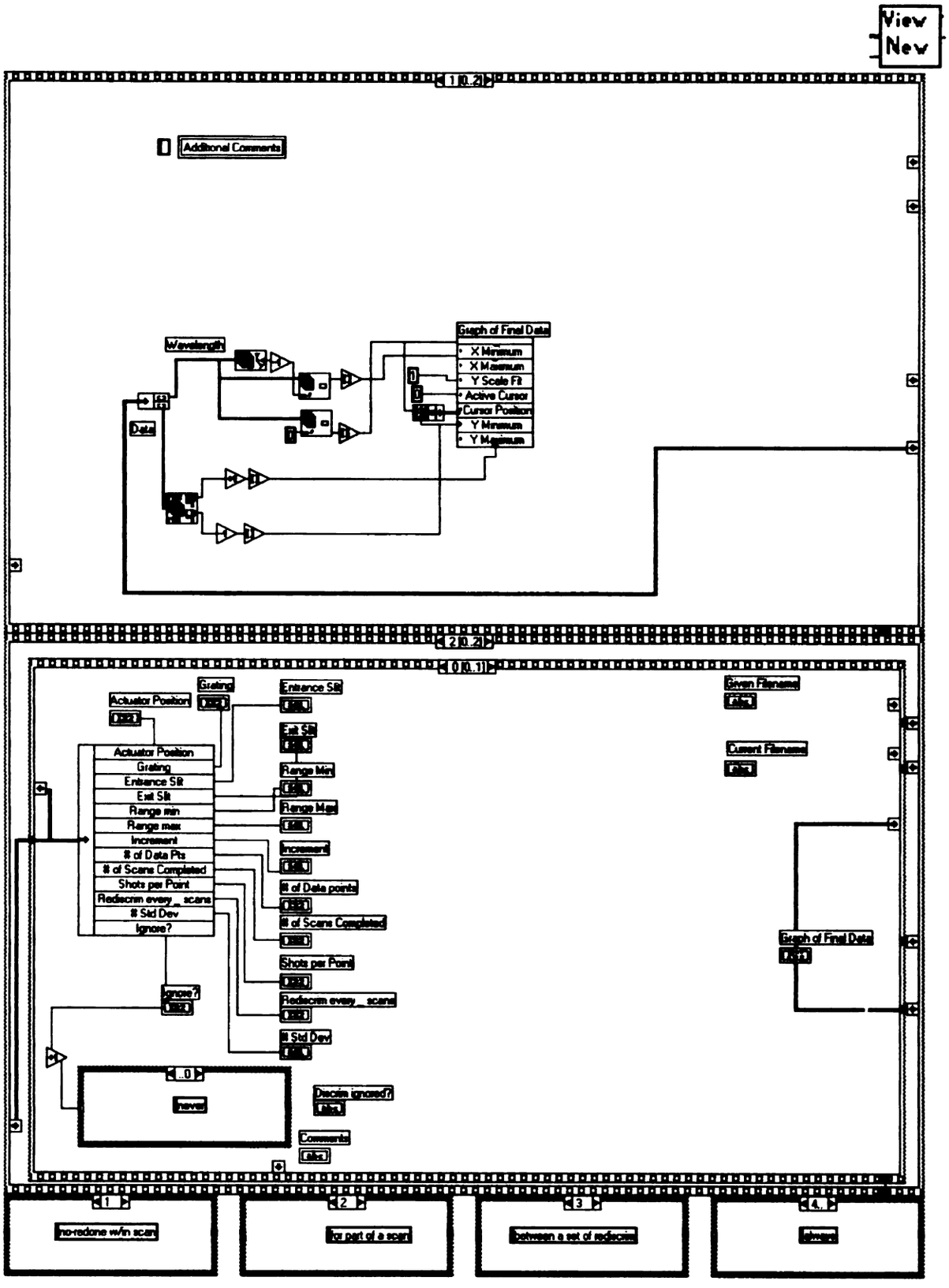
View
New
Additional Comments
Wavelength
Data
Graph of Final Data
X Minimum
X Maximum
Y Scale Fit
Active Cursor
Cursor Position
Y Minimum
Y Maximum
Actuator Position
Grating
Entrance Slit
Exit Slit
Range min
Range max
Increment
# of Data Pts
# of Scans Completed
Shots per Point
Rediscrm evesy_ scans
Std Dev
Ignore?
never
Decide ignored?
Comments
Given Filename
Current Filename
Graph of Final Data
no redone w/in scan
for part of a scan
between a set of rediscrims
always

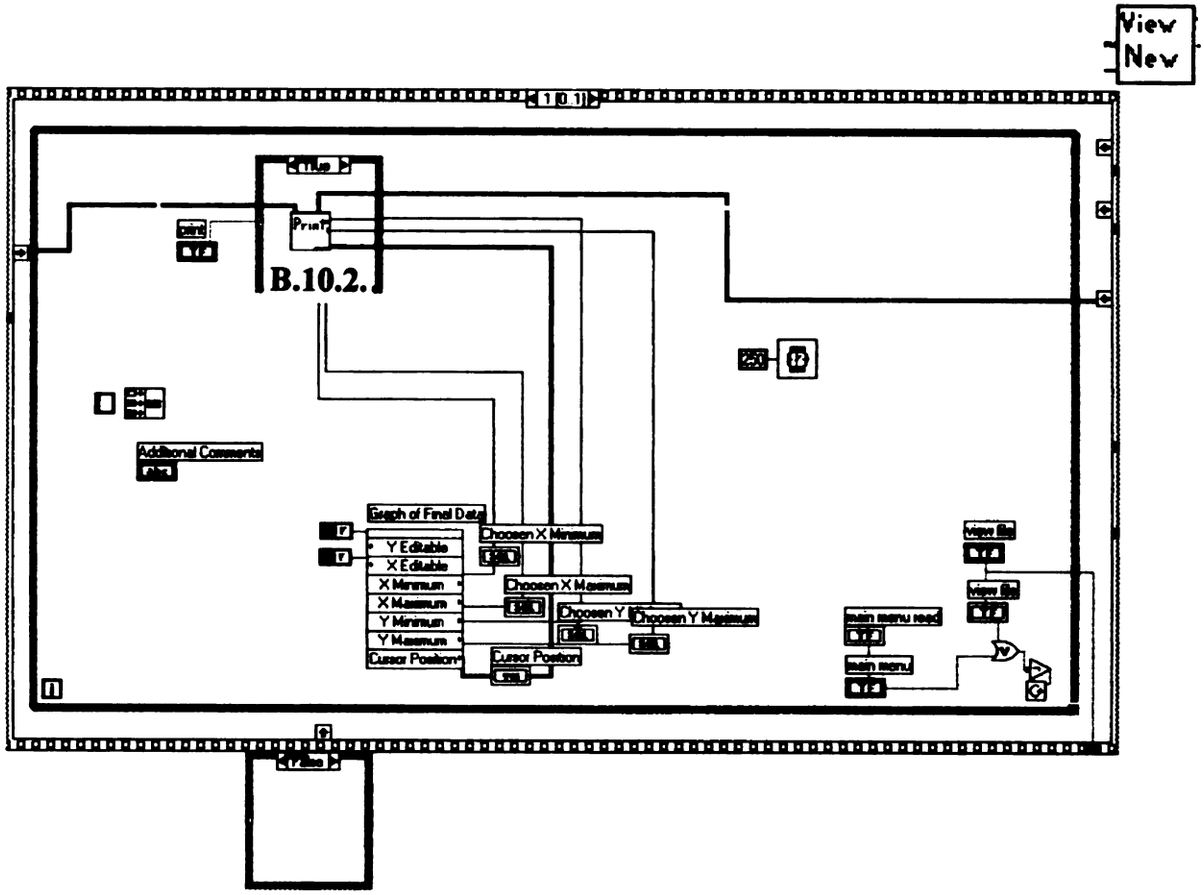
View
New
B.10.2.
Additional Comments
Graph of Final Data
Y Editable
X Editable
X Minimum
X Maximum
Y Minimum
Y Maximum
Cursor Position
Choosen X Minimum
Choosen X Maximum
Choosen Y Maximum
Cursor Position
main menu read
main menu

B.10.1. opnnewspec.vi (Open New)

This vi opens *.spc files (spectra taken with this Labview pgm). Header info is transferred along with wavelength and data pts to the viewing vi.

Connector Pane

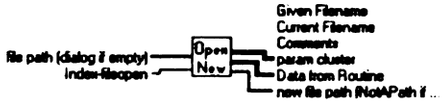

Front Panel

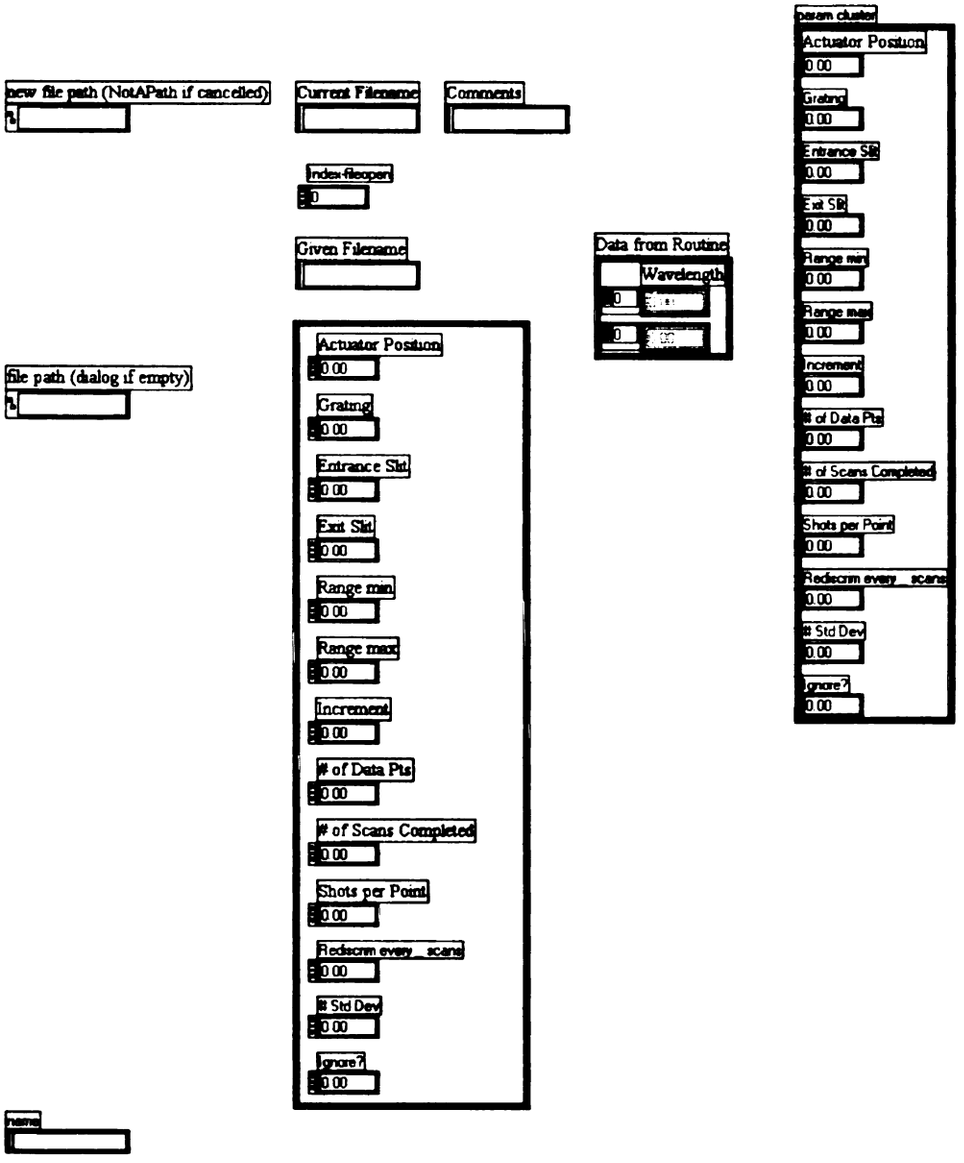

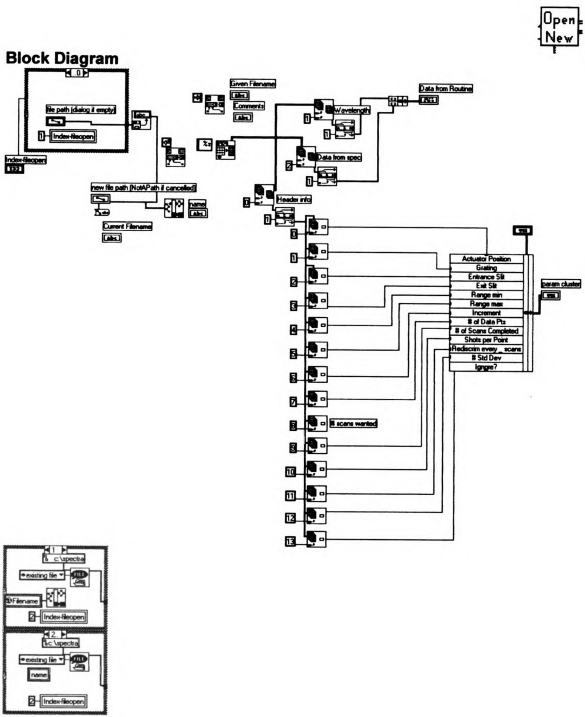
Open
New
Block Diagram
file path (dialog if empty)
Index filespec
Given Filename
Comments
Data from Routine
Wavelength
Data from spec
Header info
new file path (NotAPath if cancelled)
Current Filename
Actuator Position
Grating
Entrance Slit
Exit Slit
Range min
Range max
Increment
# of Data Pts
# of Scans Completed
Shots per Point
Redscrip every ... scans
Std Dev
Ignore?
beam cluster
scans wanted
existing file
name
Index filespec

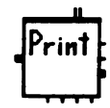

B.10.2. Printspec.vi (Print)

This vi prints the spectrum. Any user changes to range made in the view screen vi's is kept for the final printing as well as cursor position.

Connector Pane

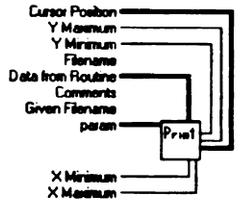

Front Panel

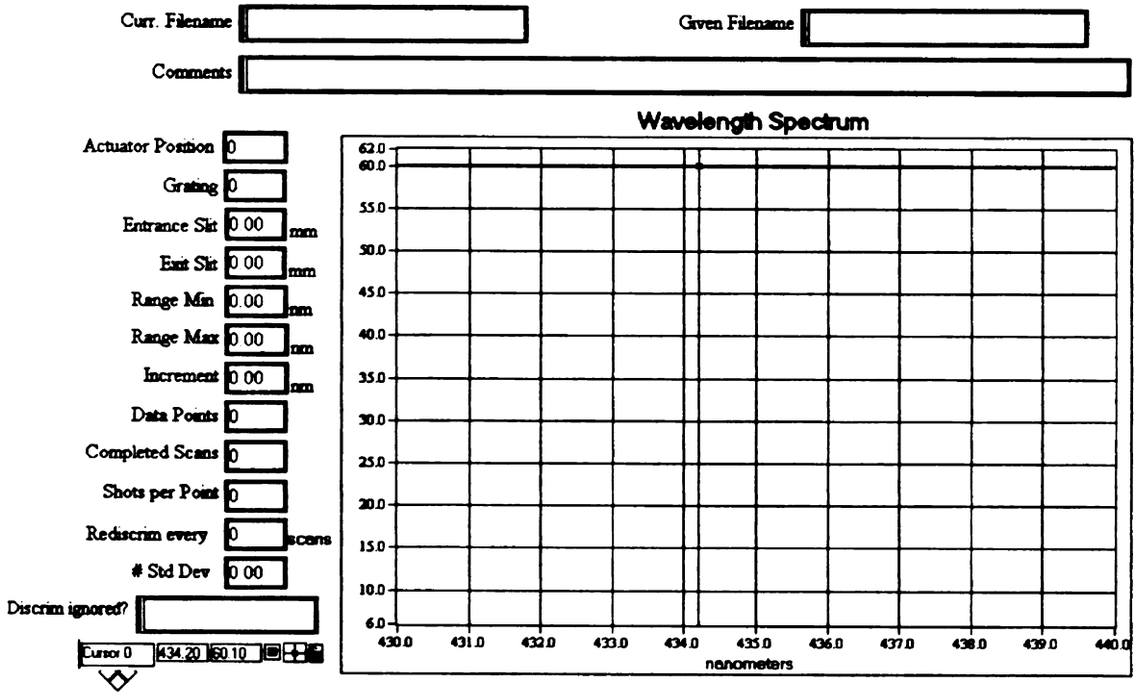

Block Diagram

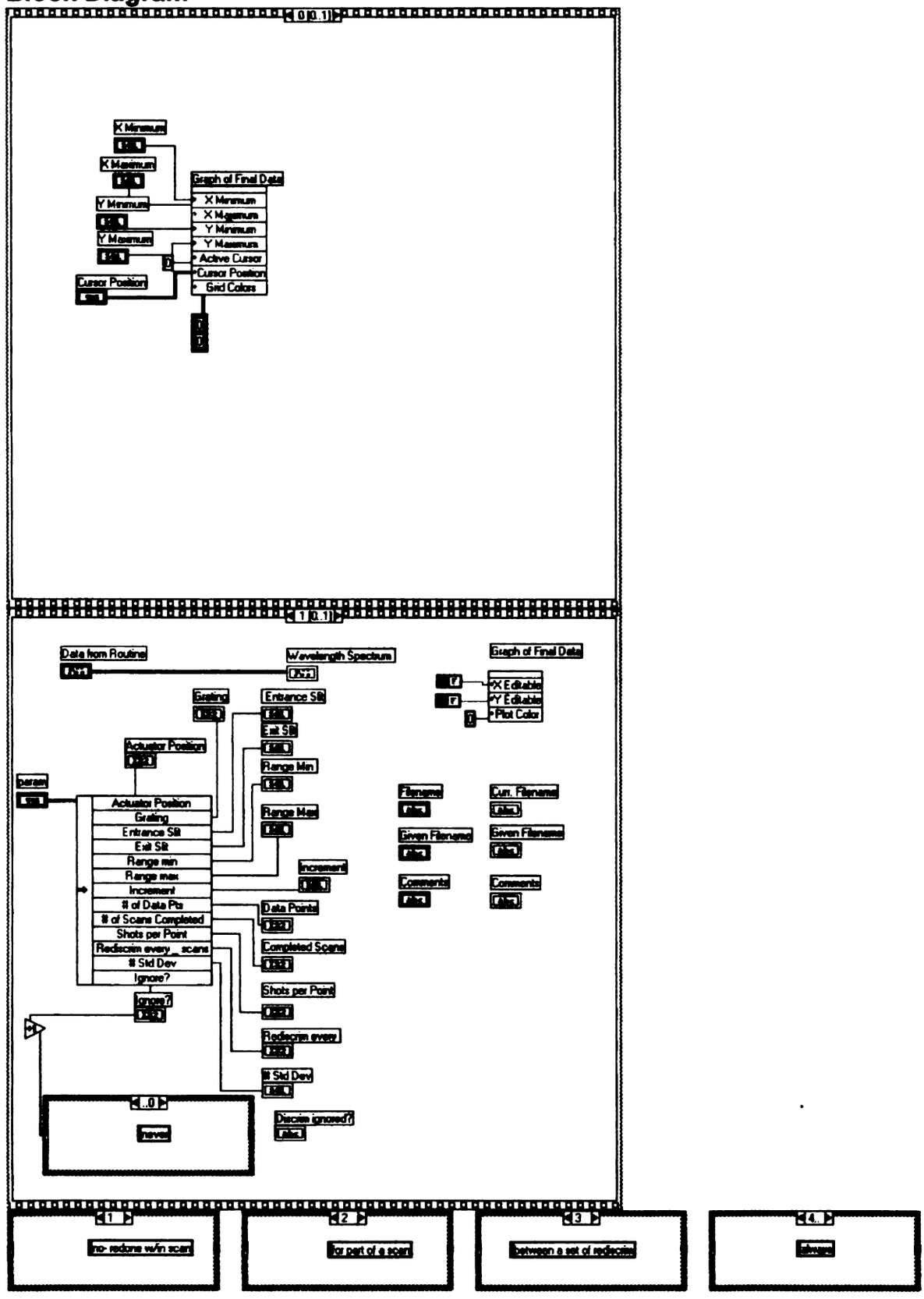

APPENDIX C

LABVIEW™ PROGRAM: INSTRUMENTAL CONTROL

C. LABVIEW™ PROGRAM: INSTRUMENTAL CONTROL – INSTRCONTROL.VI (INSTR CONTROL)

This vi allows the user to move actuator or change spectrometer settings without needing to start one of the data acquisition programs.

Connector Pane

Front Panel

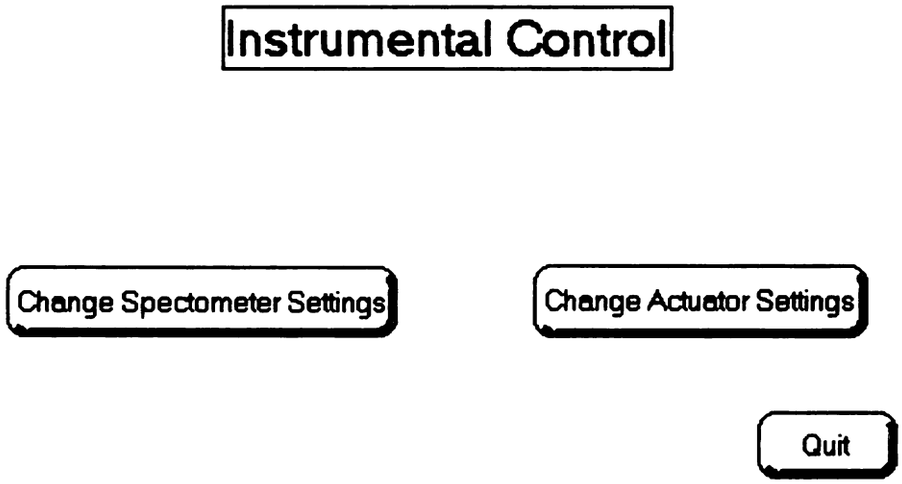

Block Diagram

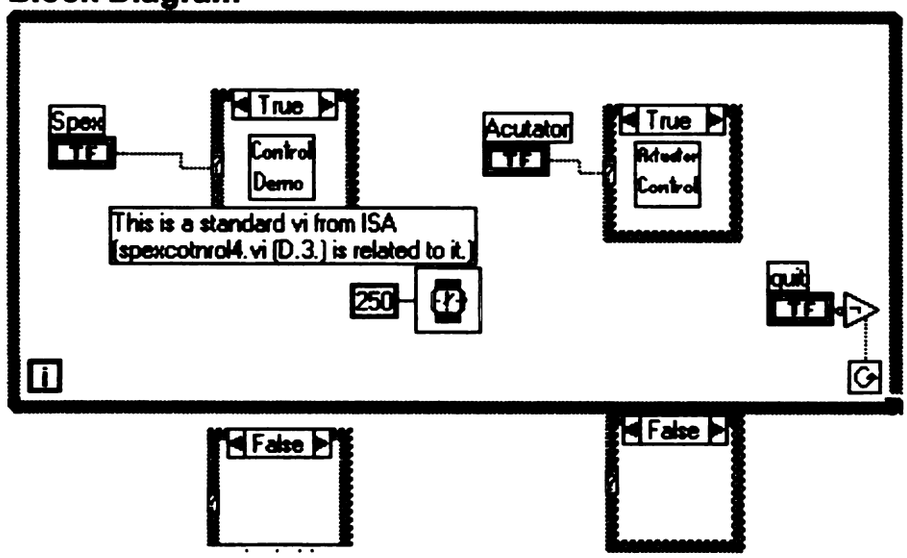

APPENDIX D

COMMON LABVIEW™ VIS

D. COMMON LABVIEW™ VIS

D.1. ftsglob.vi (Param)

This is the global vi for initial conditions. This vi allows these conditions to be read from or written to during any vi's of the scan pgm.

Connector Pane

Front Panel

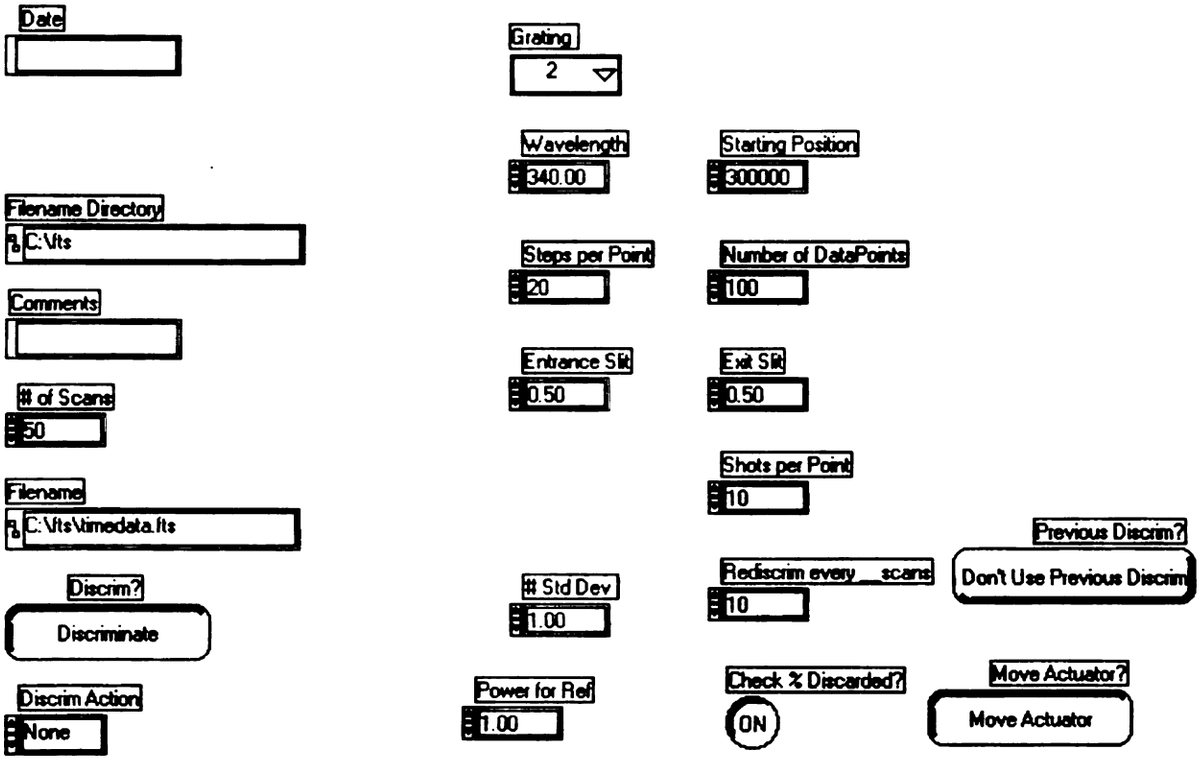

D.2. Actcontrol.vi (Actuator Control)

This vi is called when the actuator is to be moved. It first checks whether the Remote LED is lit (ie communication between UNIDEX 100 and computer serial port 2 has been established). If not it initializes the U100 and sets up communication. It sends actuator home twice and then goes to a user interface vi (Move Actuator) so the user can interactively move the actuator to desired setting. If the Remote LED is lit, the vi goes directly to the Move Actuator vi for interactive communication.

This vi checks In Position LED status before allowing another command to be completed avoiding lockups and crashes. Occasionally a separate RESET command may need to be sent if actuator is not responding (this may happen during a long period of being "on" but not used- communication seems to be forgotten in these cases.)

Connector Pane

Front Panel

Block Diagram

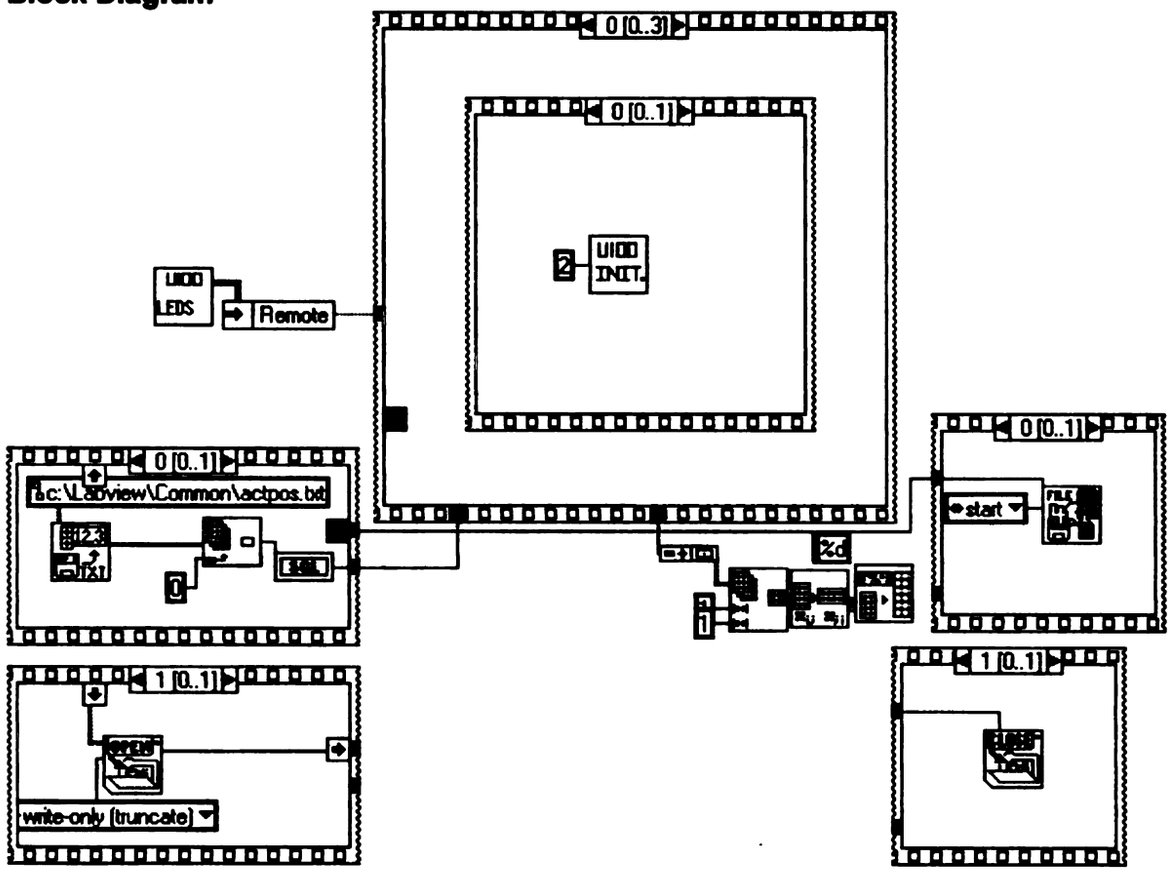

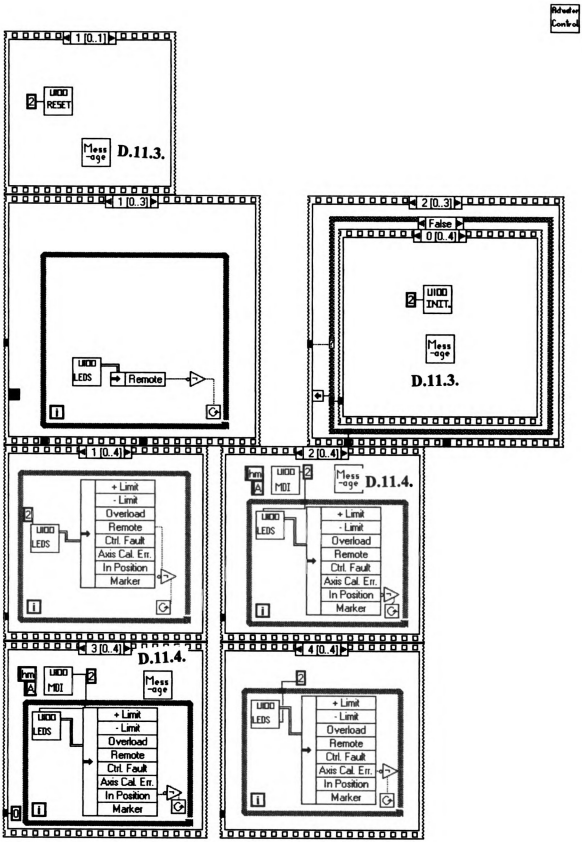
Advanced Control
1 [0..1]
2
U16
RESET
Mess -age
D.11.3.
1 [0..9]
U16
LEDS
Remote
2 [0..3]
False
0 [0..4]
2
U16
INIT.
Mess -age
D.11.3.
1 [0..4]
2
U16
LEDS
+ Limit
- Limit
Overload
Remote
Ctrl. Fault
Axis Cal. Err.
In Position
Marker
2 [0..4]
Prm A
U16
MDI
2
Mess -age
D.11.4.
U16
LEDS
+ Limit
- Limit
Overload
Remote
Ctrl. Fault
Axis Cal. Err.
In Position
Marker
3 [0..4]
Prm A
U16
MDI
2
Mess -age
D.11.4.
U16
LEDS
+ Limit
- Limit
Overload
Remote
Ctrl. Fault
Axis Cal. Err.
In Position
Marker
4 [0..4]
2
U16
LEDS
+ Limit
- Limit
Overload
Remote
Ctrl. Fault
Axis Cal. Err.
In Position
Marker

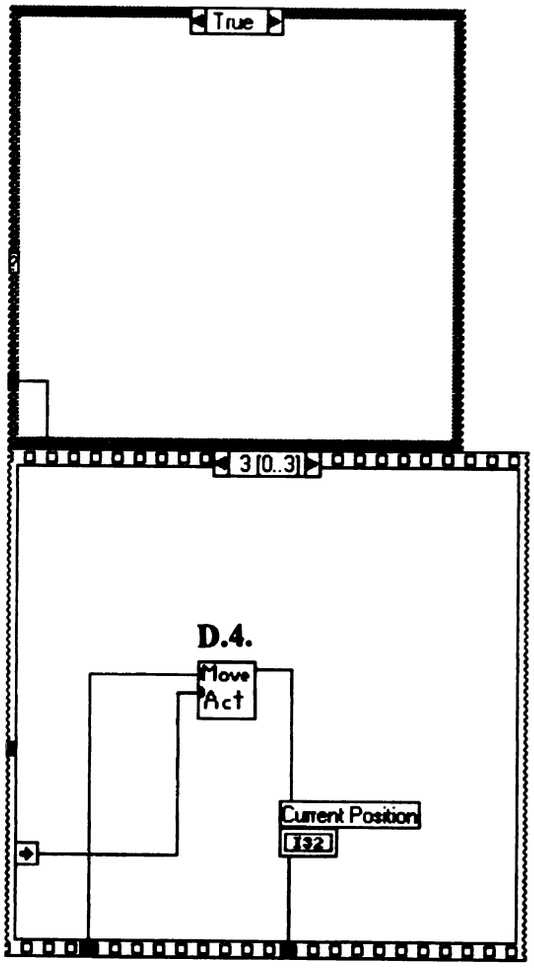

D.4.

D.3. spexcontrol4.vi (Spex Control)

This program is a modification of the ISA Labview program Control Demo.
If requested within the scanning programs, this window opens to allow user to input information to set up the spectrometer - grating, wavelength, slit widths. After the user findis the optimal settings for the current experiment, this program transfers the information back to the scanning programs. This program may also be run separately from the scanning programs.

Connector Pane

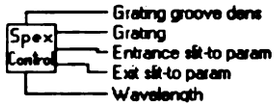

Front Panel

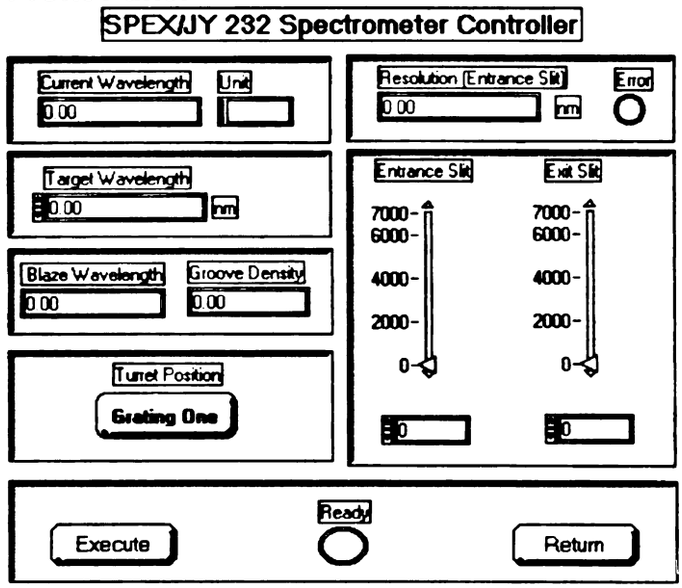

Spex Control

Block Diagram

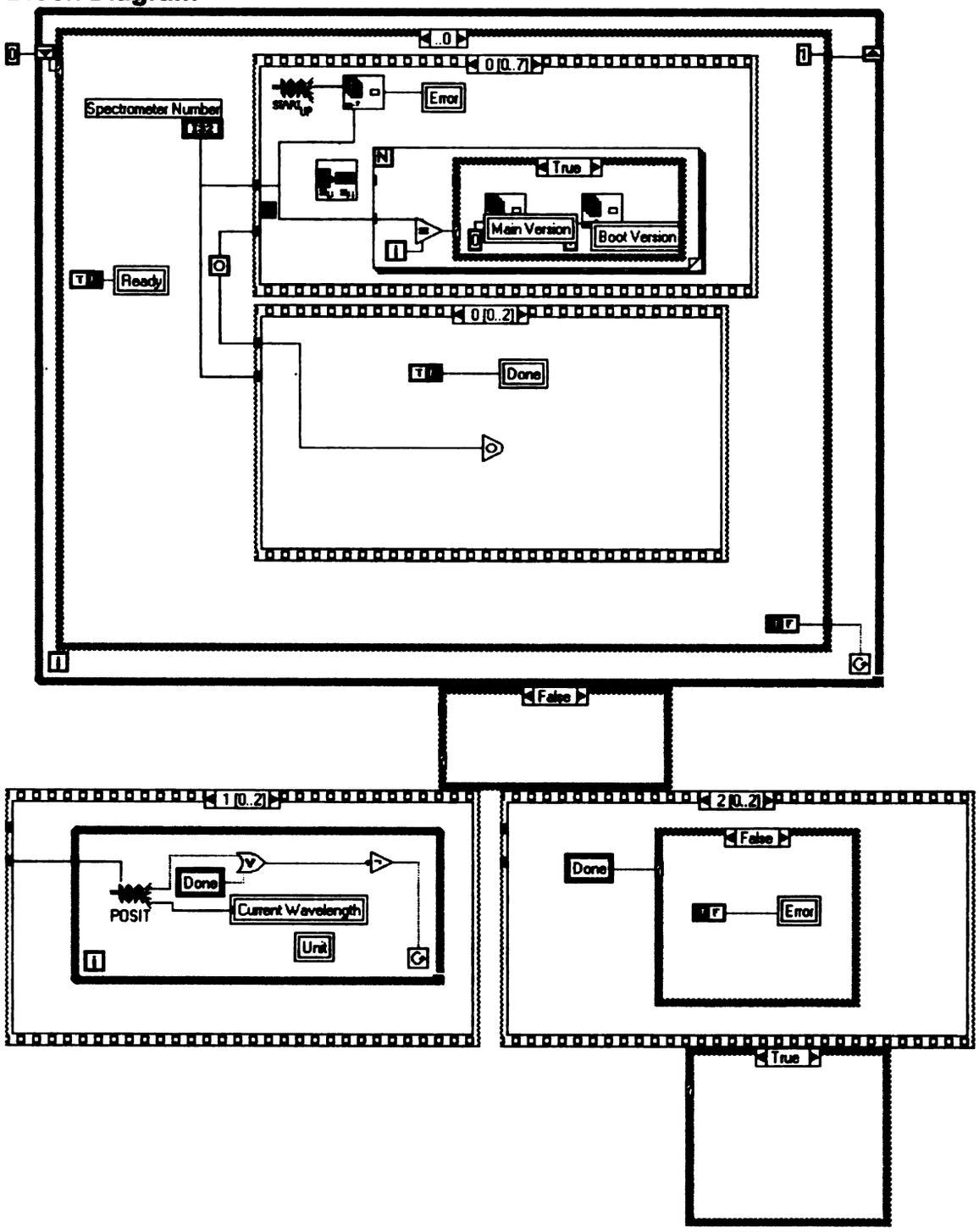

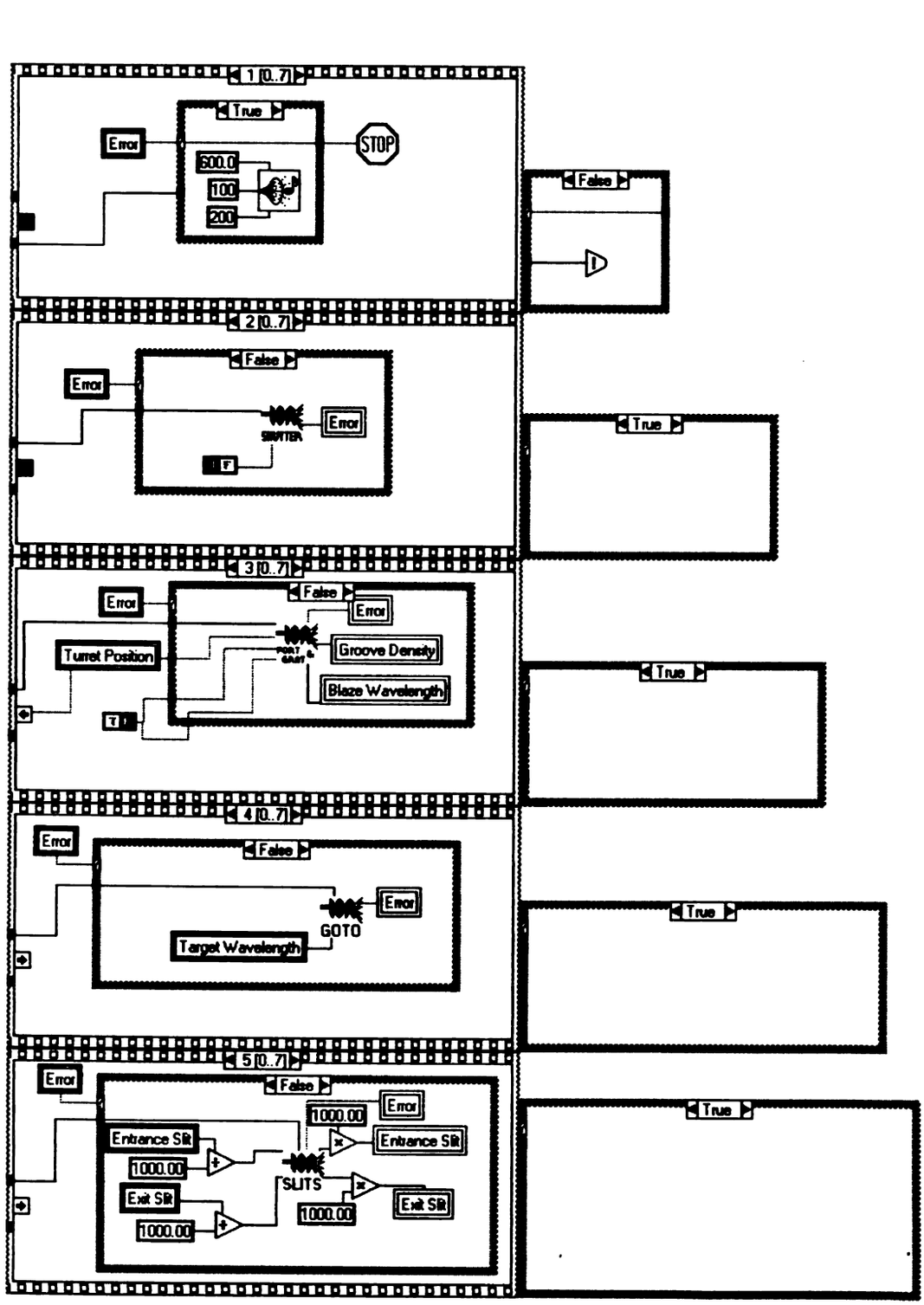
Spex Control
1 [0..7]
True
Error
STOP
600.0
100
200
False
2 [0..7]
False
Error
SHUTTER
Error
F
True
3 [0..7]
Error
False
Error
Turret Position
PORT GRAT #
Groove Density
Blaze Wavelength
T
True
4 [0..7]
Error
False
Error
GOTO
Target Wavelength
True
5 [0..7]
Error
False
1000.00
Error
Entrance Slit
Entrance Slit
1000.00
SLITS
Exit Slit
Exit Slit
1000.00
1000.00
True

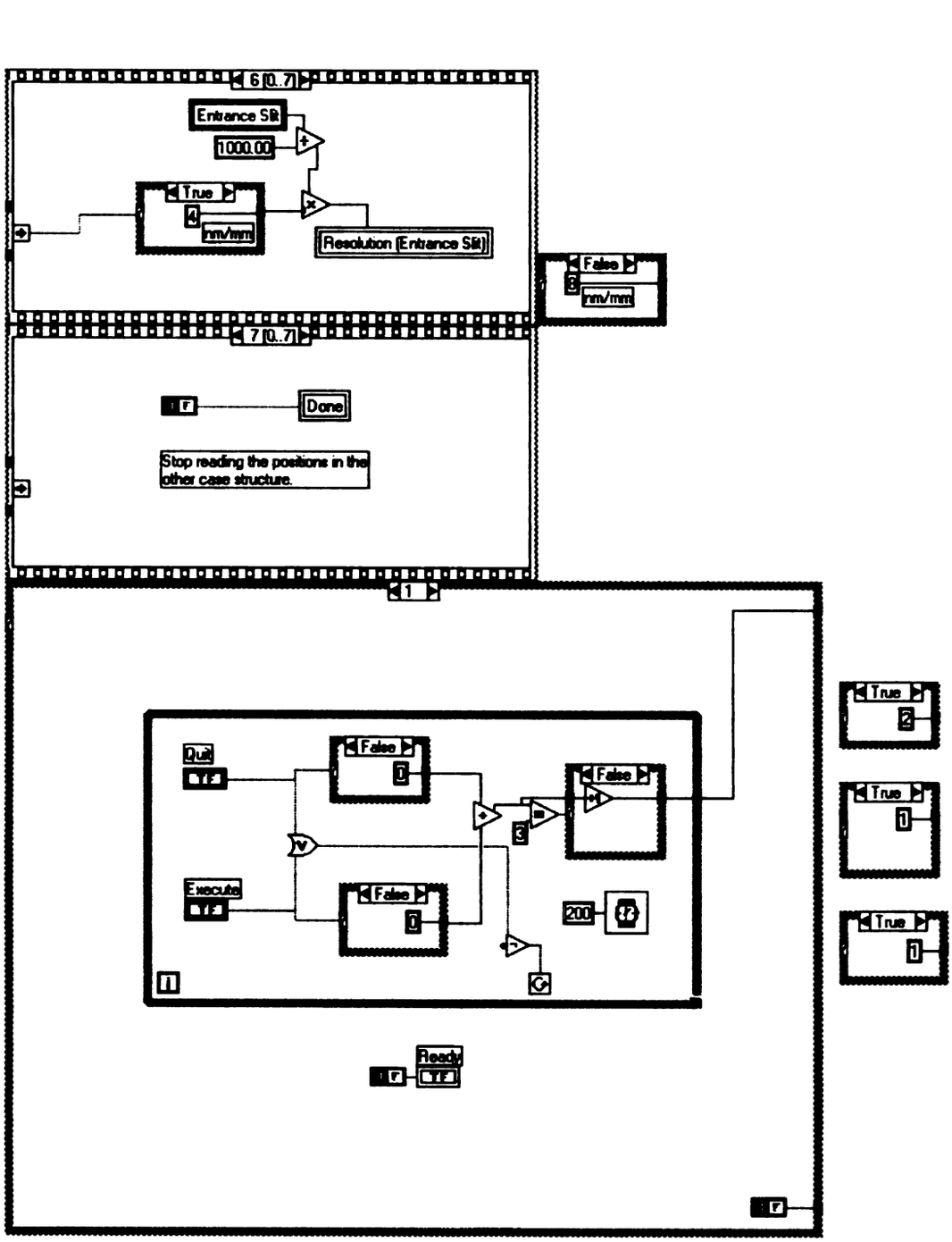
Spex Control
6 [0..7]
Entrance Slit
1000.00
True
4
nm/mm
Resolution (Entrance Slit)
False
3
nm/mm
7 [0..7]
Done
Stop reading the positions in the other case structure.
1
Quit
False
0
Execute
False
0
False
3
200
True
2
True
1
True
1
Ready

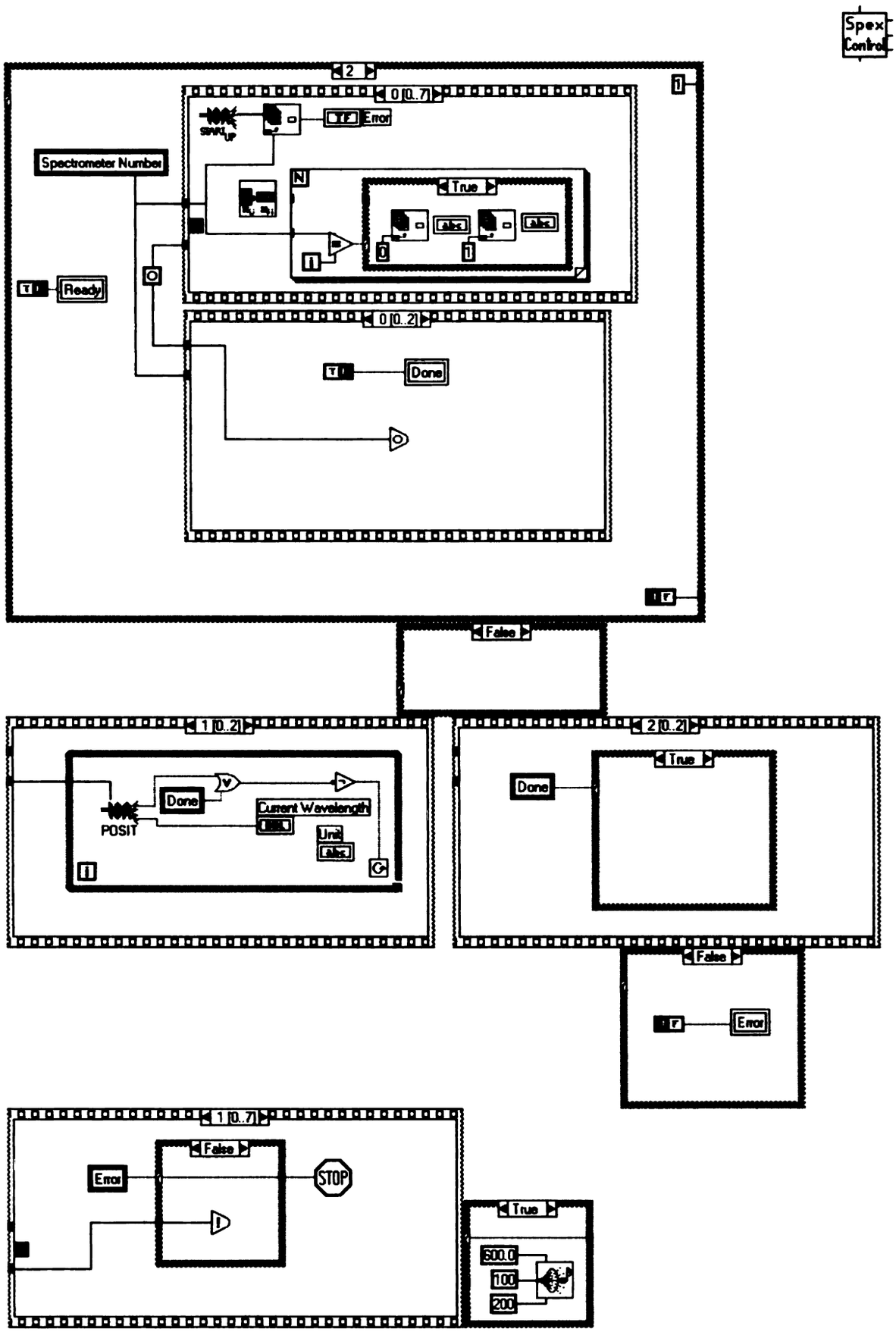
Spex Control
2
0 [0..7]
Error
Spectrometer Number
True
Ready
0 [0..2]
Done
False
1 [0..2]
Done
Current Wavelength
POSIT
Unit
2 [0..2]
Done
True
False
Error
1 [0..7]
False
Error
STOP
True
500.0
100
200

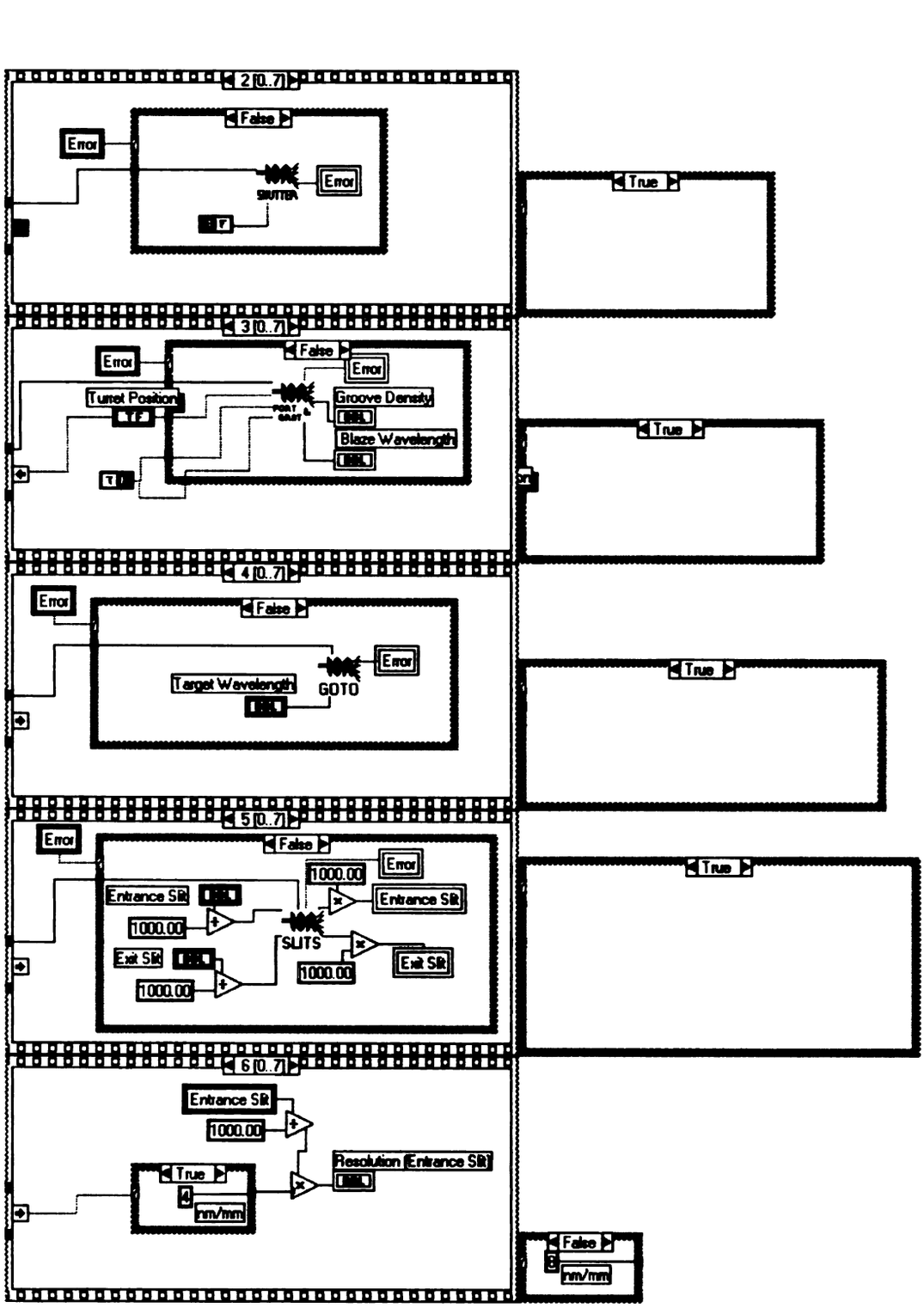
Spex Control
2 [0..7]
False
Error
SHUTTER
Error
True
3 [0..7]
False
Error
Turret Position
Groove Density
Blaze Wavelength
True
4 [0..7]
False
Error
Target Wavelength
GOTO
True
5 [0..7]
False
Error
1000.00
Entrance Slit
Exit Slit
SLITS
True
6 [0..7]
Entrance Slit
1000.00
Resolution Entrance Slit
True
nm/mm
False
nm/mm

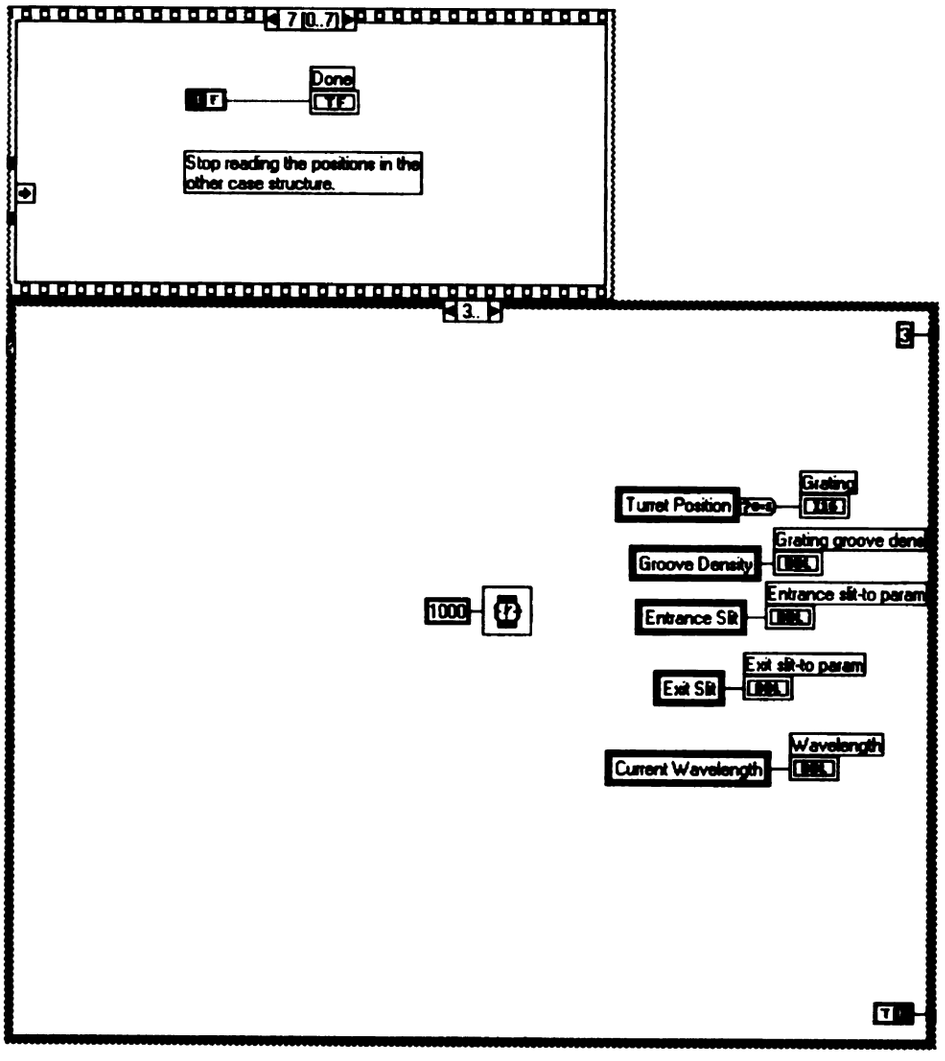
7 (0..7)
Done
TF
Stop reading the positions in the other case structure.
3..
3
Turret Position
Grating
Groove Density
Grating groove dens
1000
Entrance Slit
Entrance slit-to param
Exit Slit
Exit slit-to param
Current Wavelength
Wavelength

D.4. Moveact.vi (Move Act)

This vi allows the user to interactively move the actuator while it keeps track of where the actuator is (Counter global vi). This vi waits for In Position LED to be lit before allowing another move to avoid lockups and crashes.

Connector Pane

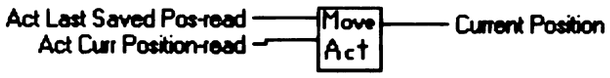

Front Panel

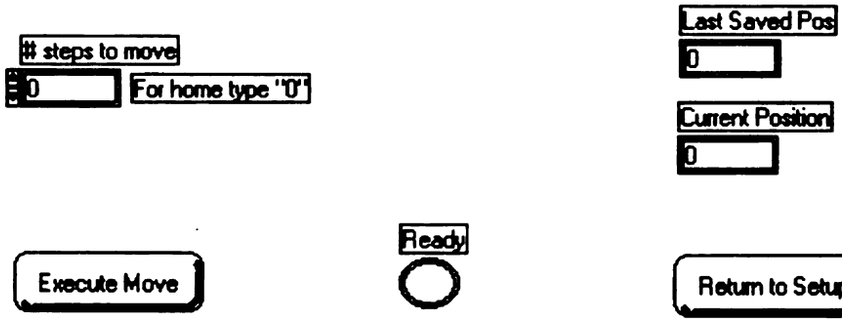

Block Diagram

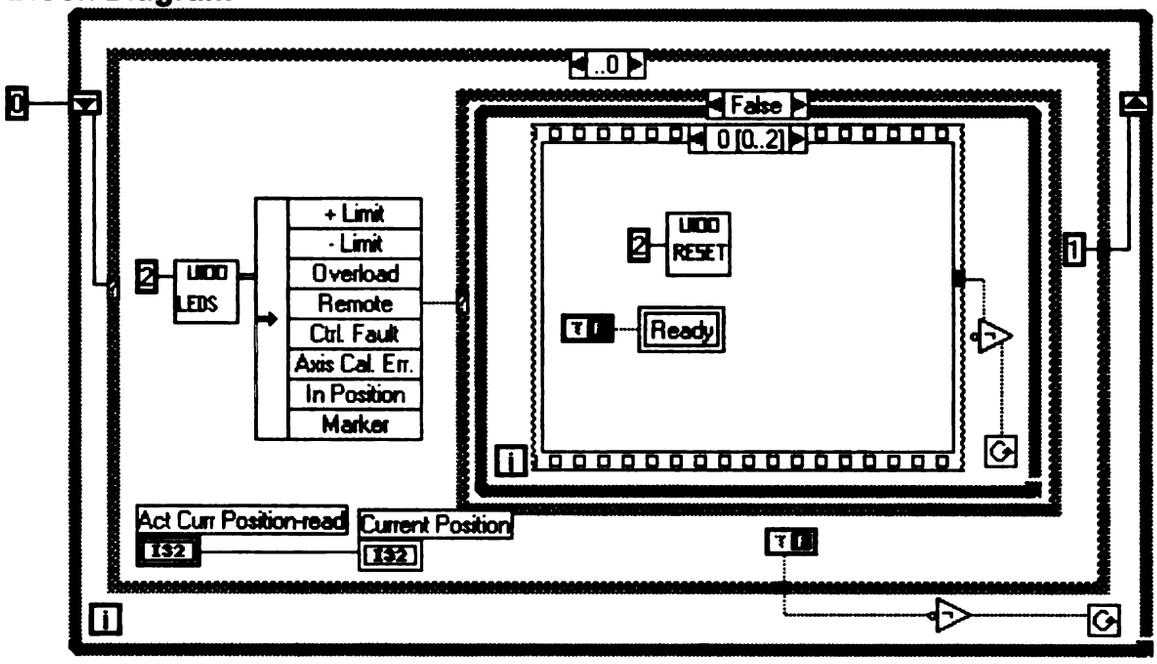

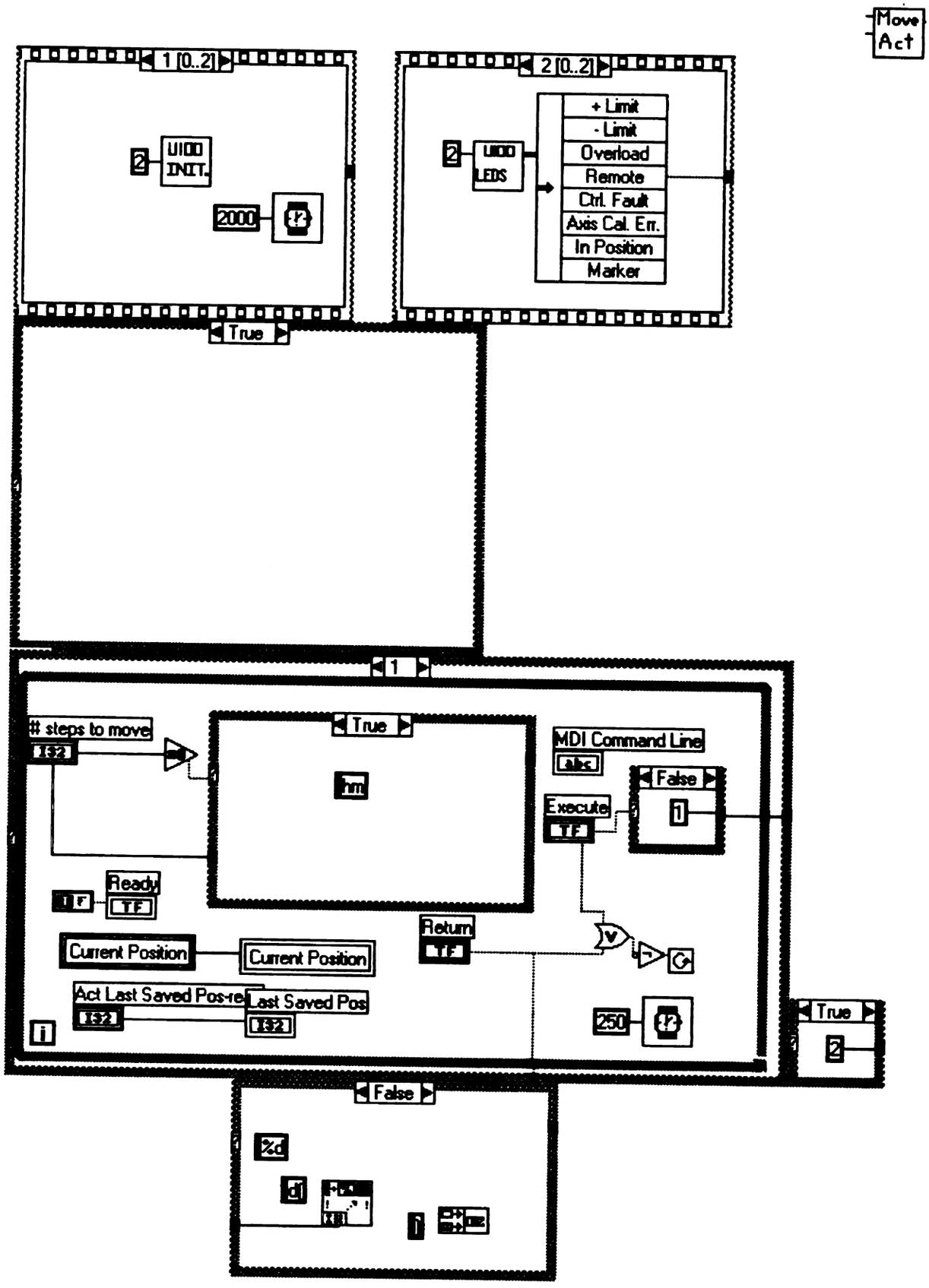
Move
Act
1 [0..2]
2
U16
INIT.
2000
2 [0..2]
2
U16
LEDS
+ Limit
- Limit
Overload
Remote
Ctrl. Fault
Axis Cal. Err.
In Position
Marker
True
1
steps to move
I32
True
hm
MDI Command Line
abc
False
Execute
TF
1
Ready
TF
Return
TF
Current Position
Current Position
Act Last Saved Pos-rel
I32
Last Saved Pos
I32
i
250
True
2
False
%d
d
i

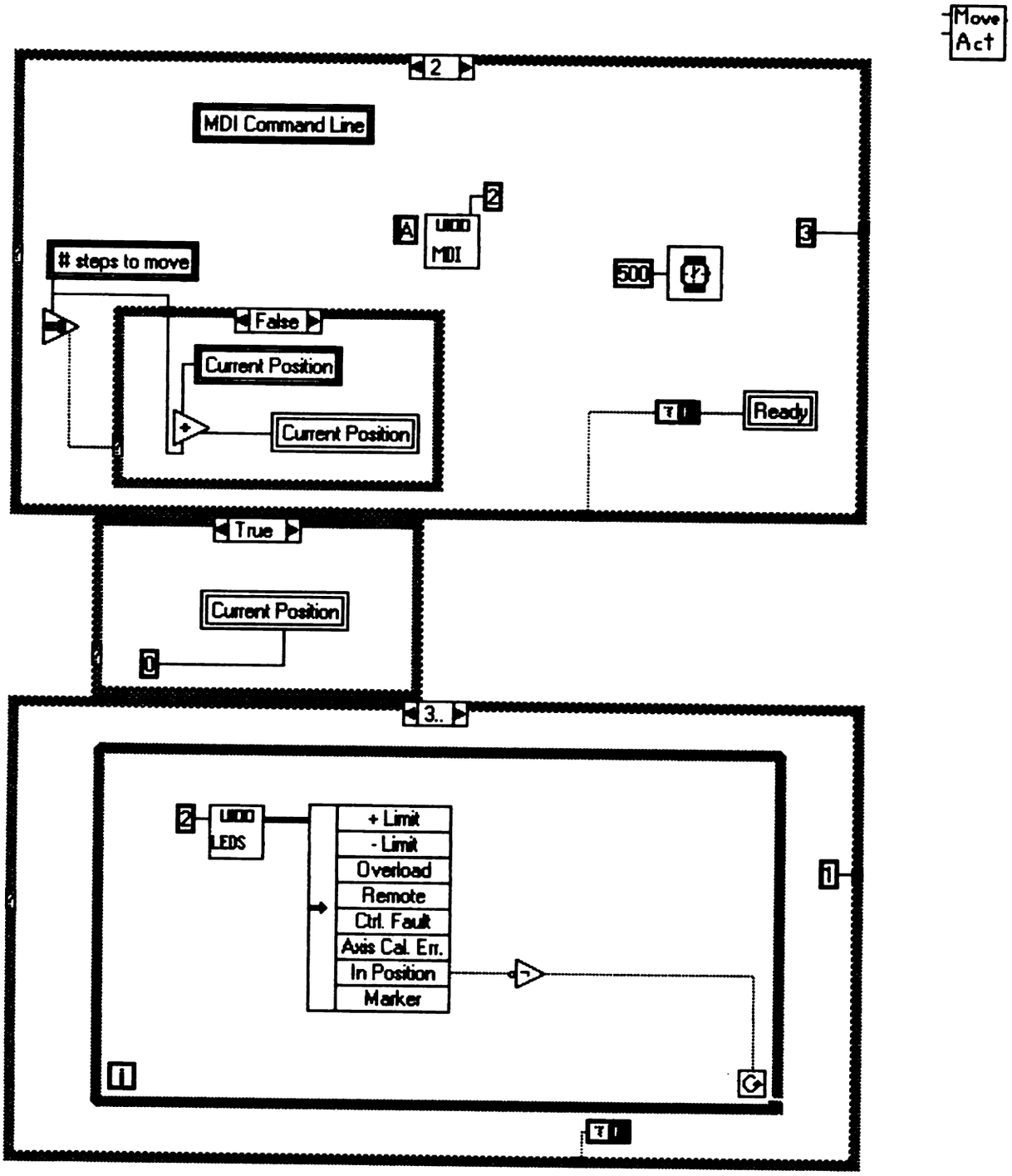
Move
Act
2
MDI Command Line
2
A
U8DD
MDI
3
steps to move
500
False
Current Position
Current Position
Ready
True
Current Position
0
3..
2
U8DD
LEDS
+ Limit
- Limit
Overload
Remote
Ctrl. Fault
Axis Cal. Err.
In Position
Marker
1
1

D.5. stddev_mean.vi (σ/μ)

This global vi keeps track of the ratio of the standard deviation to the mean of the reference data. (This gives the user an idea of how stable the laser is; this info is updated on the scan window for user to monitor.)

Connector Pane

Front Panel

D.6. SR245_takedata.vi (245 DATA)

This vi is a variation of the SRS 245 vi from NI. This vi takes non-discriminated data for fts scans. It allows for input of GPIB address, # scans, scan channels, triggered setting and gives output of error, sum ref, sum data.

Connector Pane

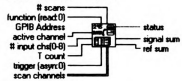

Front Panel

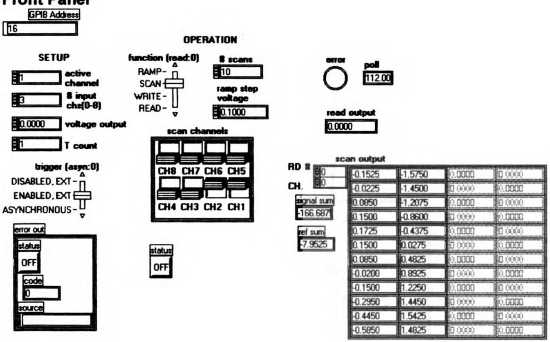

Block Diagram

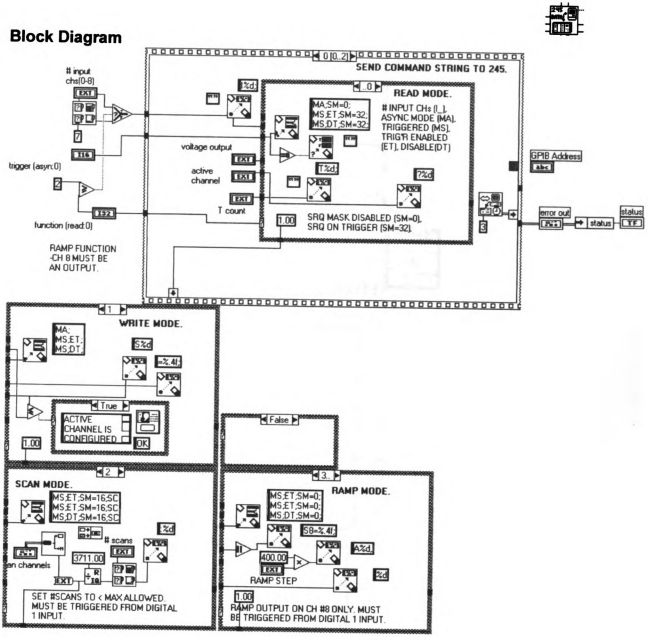

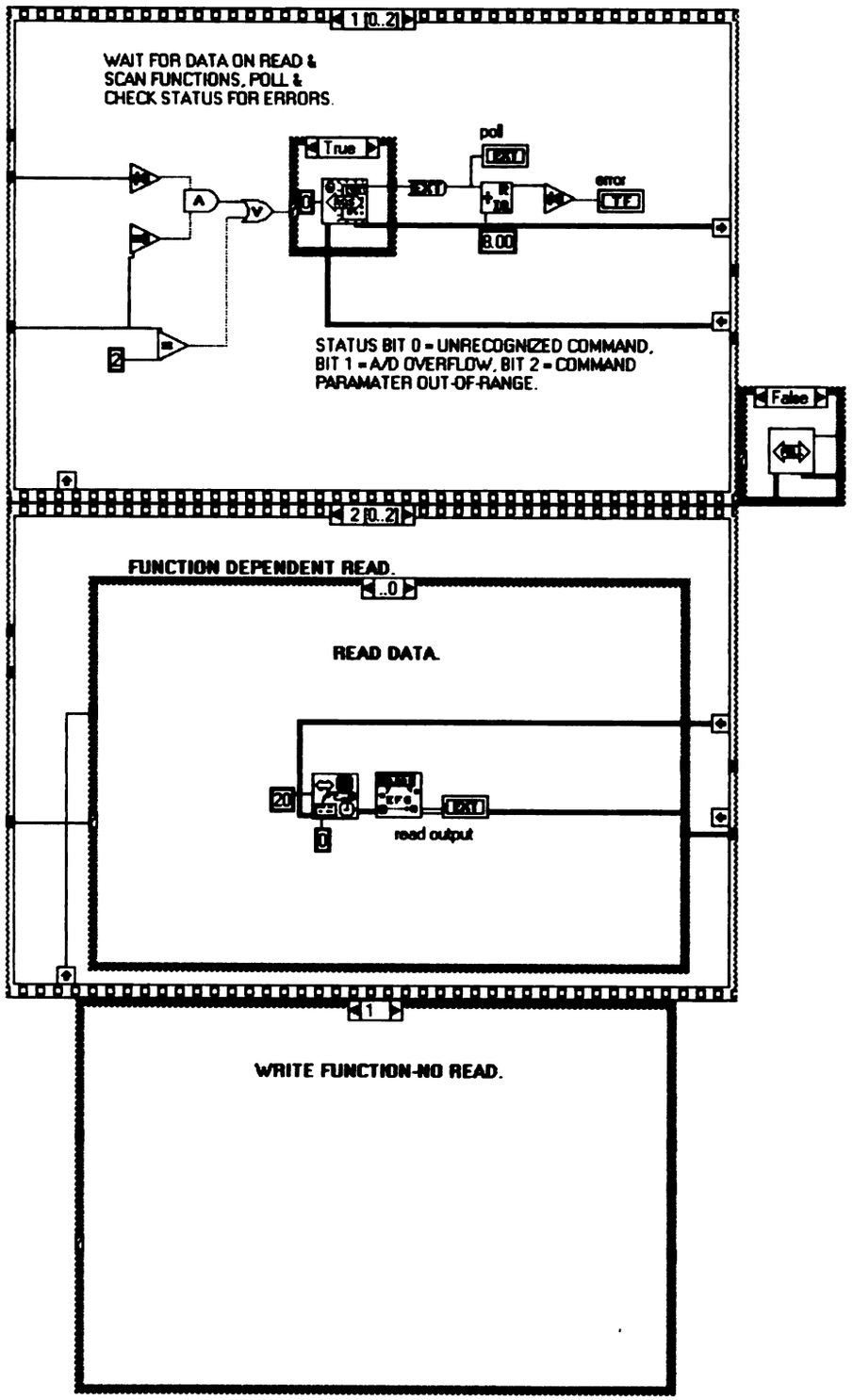
1 [0..2]
WAIT FOR DATA ON READ &
SCAN FUNCTIONS, POLL &
CHECK STATUS FOR ERRORS.
True
poll
error
3.00
STATUS BIT 0 = UNRECOGNIZED COMMAND,
BIT 1 = A/D OVERFLOW, BIT 2 = COMMAND
PARAMATER OUT-OF-RANGE.
False
2 [0..2]
FUNCTION DEPENDENT READ.
..0
READ DATA.
20
read output
1
WRITE FUNCTION-NO READ.

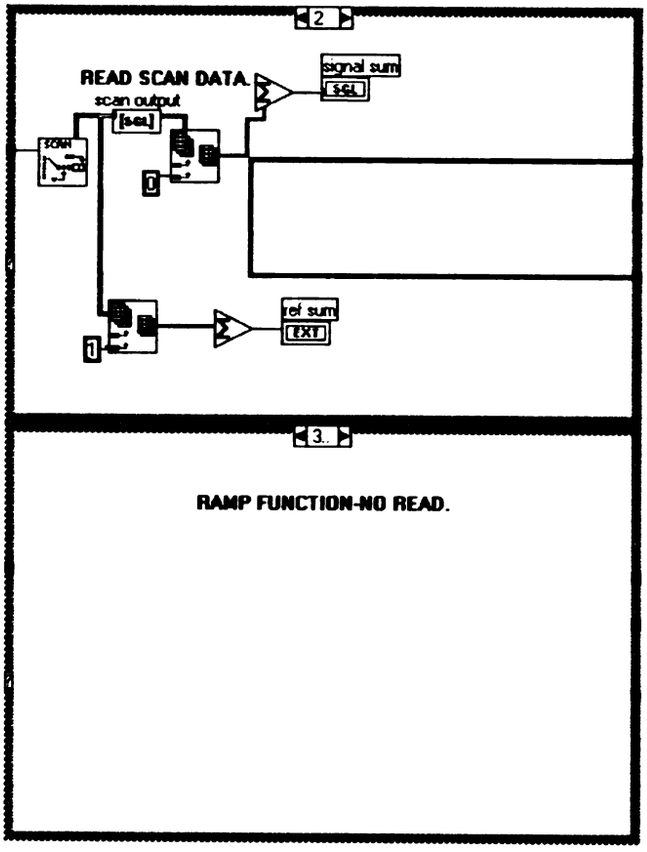
2
READ SCAN DATA.
scan output
signal sum
SIG
SCAN
0
ref sum
EXT
1
3..
RAMP FUNCTION-NO READ.

D.7. cnclpaus.vi (Pause Stop)

This vi allows the user to choose between stopping the scan or resuming the scan once the pause/stop button was pushed on the main take data vi screen. This info is passed to the take data vi and the appropriate action taken.

Connector Pane

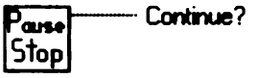

Front Panel

Block Diagram

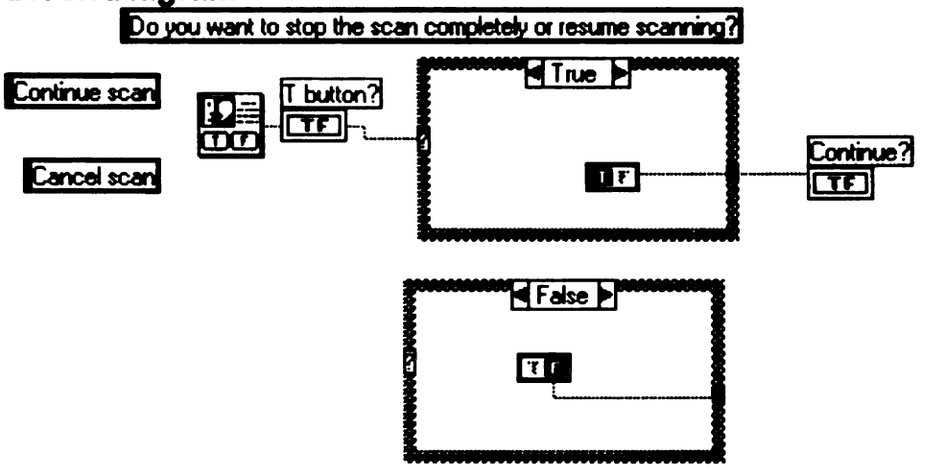

D.8. Actconversion.vi (Act Conv)

This global vi keeps track of actuator position whether in move act vi or within fts take data vi.

Connector Pane

Front Panel

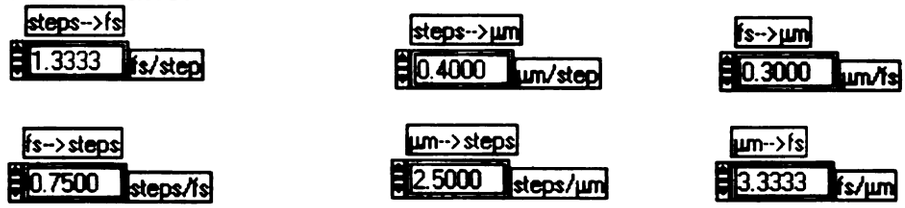

D.9. specglb.vi (Param)

This is the global vi for initial conditions. This vi allows these conditions to be read from or written to during any vi's of the scan pgm.

Connector Pane

Front Panel

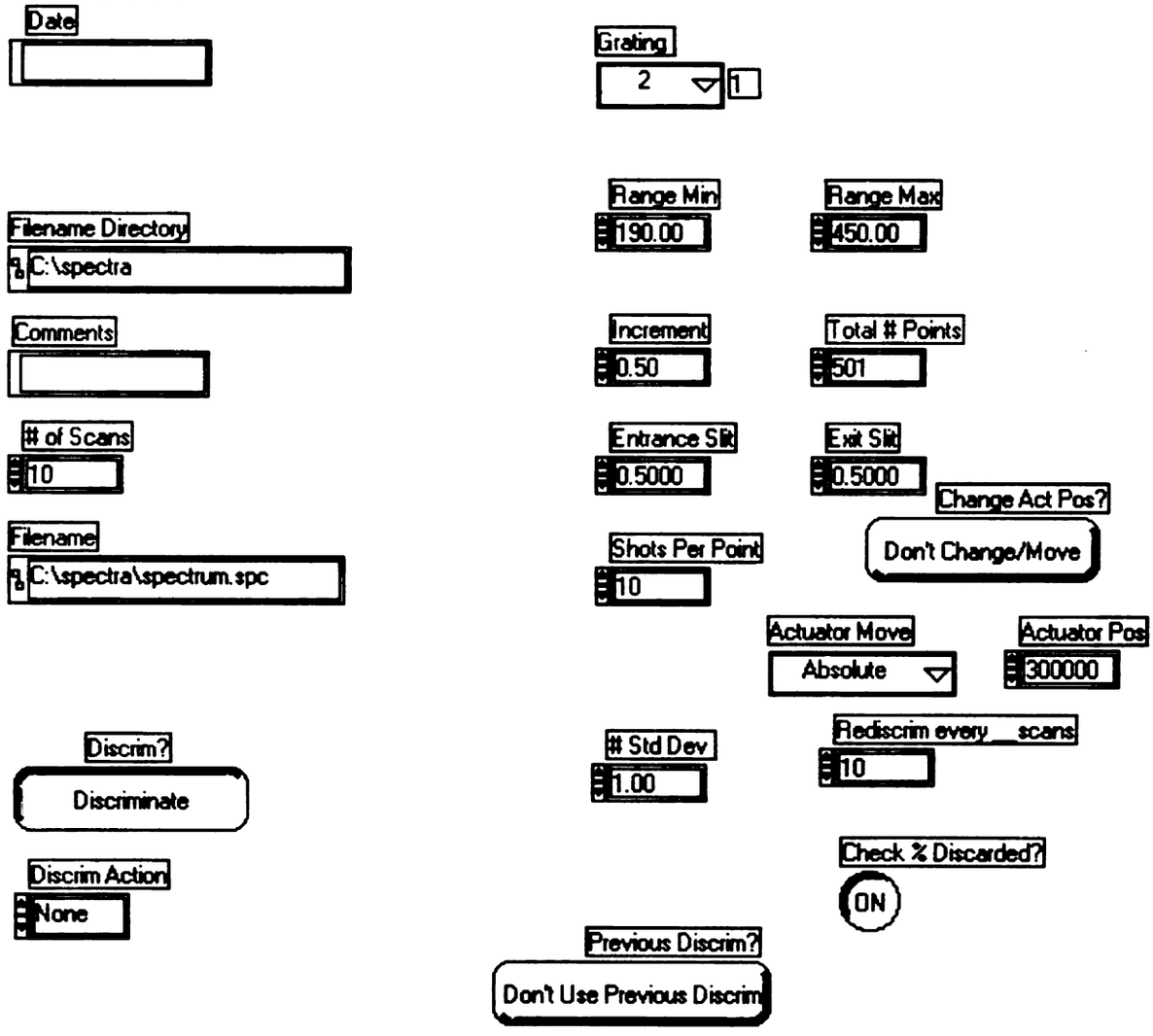

D.10. actposforspex.vi (Act Pos)

This global vi keeps track of actuator position whether in move act vi or within fts take data vi.

Connector Pane

Front Panel

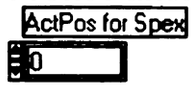

D.11. Messages

D.11.1. spexinitmess.vi (Message)

This vi just lets the user know that the spectrometer (Spex) is busy being initialized.

Connector Pane

Front Panel

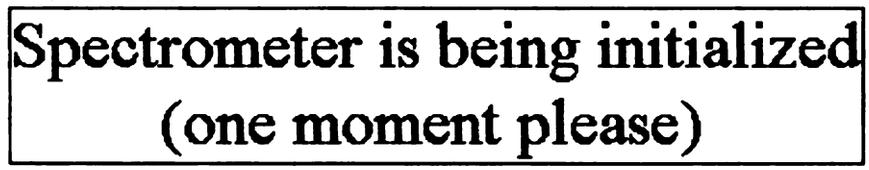

Block Diagram

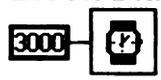

D.11.2. spexparamess.vi (Message)

This vi just lets the user know that the spectrometer (Spex) is busy configuring its settings (slits, grating, wavelength).

Connector Pane

Front Panel

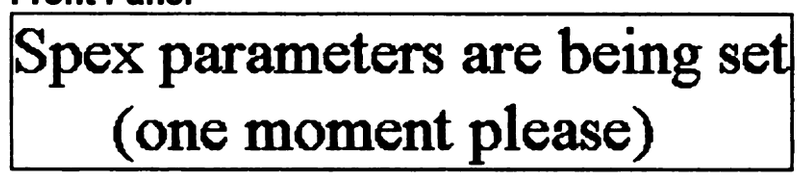

Block Diagram

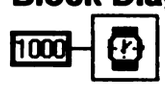

D.11.3. actmess.vi (Message)

This vi just lets the user know that the actuator is busy being initialized.

Connector Pane

Front Panel

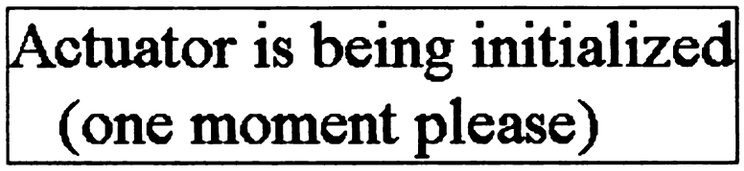

Block Diagram

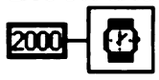

D.11.4. homemess.vi (Message)

This vi just lets the user know that the actuator is busy being sent home.

Connector Pane

Front Panel

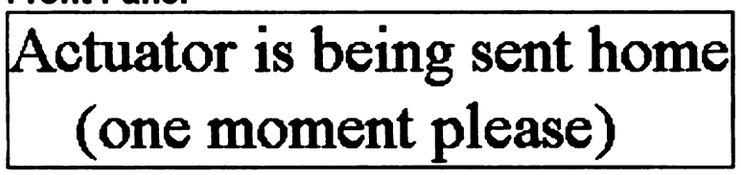

Block Diagram

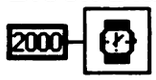

D.11.5. rediscrmess.vi (Message)

This vi lets user know that there will be a slight delay until reference data is read and calculated for max/min discrimination values.

Connector Pane

Front Panel

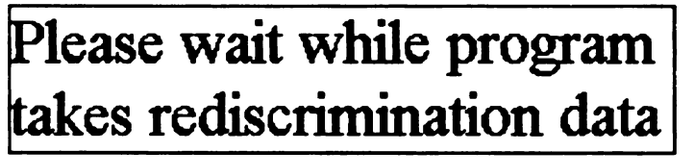

Block Diagram

APPENDIX E

FORTRAN PROGRAMS: ROTATIONAL ANISOTROPY FITTING

APPENDIX E. FORTRAN PROGRAMS: ROTATIONAL ANISOTROPY FITTING

E.1. Unidirectional Detection with A_S and $A_\perp$

```
      subroutine gencal (np,nd,cy,param,xdata,ydata)
      implicit real*8 (a-h, o-z)
      parameter (npt=100, ndt=2500)
      dimension cy(ndt), param(npt), xdata(ndt,2), ydata(ndt,2)
      parameter (pi=3.1415926d0)

      real*8 k, J, jmax

      dimension r(2000)

      B = param(1)
      BX = param(2)
      T = param(3)
      back = param(4)
      scale = param(5)
      As = param(6)
      Aperp = param(7)

      tmin = xdata(1,1)*1.0d-15
      tmax = xdata(nd,1)*1.0d-15
      dt = (tmax-tmin)*1.0d-15/dble(nd-1)

      w1 = 4.0d0*pi*B*2.99792458d10
      k = 0.69506d0
      tau1 = 180.0d0
      BkT = BX/(k*T)

      do i=1,nd

c       convert femtosecond to second
        t = xdata(i,1)*1.0d-15
        tau = tau1*1.0d-15

            amp = dexp(-(t/tau)**2)

        tmp = 0.0d0
        Q = 0.0d0
        do J=0.0d0,500.0d0, 1.0d0
          rjt = (0.13333d0+0.26667d0*dcos(2.0d0*w1*J*t)) -
            As*(0.13333d0+0.26667d0*dcos(2.0d0*w1*J*t)) - Aperp*amp
c         pj = dexp(-((J-jmax)/dj)**2)
          pj = dble(2*J+1)*dexp(-J*(J+1)*BkT)
          tmp = tmp + rjt*pj
          Q = Q + pj
        end do
        r(i) = tmp / Q
        cy(i) = back + scale * r(i)
      end do

      return
      end
```

E.2. Unidirectional Detection with A_S and $A_{A/B}$

```
      subroutine gencal (np,nd,cy,param,xdata,ydata)
      implicit real*8 (a-h, o-z)
      parameter (npt=100, ndt=2500)
      dimension cy(ndt), param(npt), xdata(ndt,2), ydata(ndt,2)
      parameter (pi=3.1415926d0)

      real*8 k, J, jmax

      dimension r(2000)

      B = param(1)
      BX = param(2)
      T = param(3)
      back = param(4)
      scale = param(5)
      As = param(6)
      AAB = param(7)

      tmin = xdata(1,1)*1.0d-15
      tmax = xdata(nd,1)*1.0d-15
      dt = (tmax-tmin)*1.0d-15/dble(nd-1)

      w1 = 4.0d0*pi*B*2.99792458d10
      k = 0.69506d0
      tau1 = 180.0d0
      BkT = BX/(k*T)

      do i=1,nd

c       convert femtosecond to second
        t = xdata(i,1)*1.0d-15
        tau = tau1*1.0d-15

            amp = dexp(-(t/tau)**2)

        tmp = 0.0d0
        Q = 0.0d0
        do J=0.0d0,500.0d0, 1.0d0
          rjt = (0.13333d0+0.26667d0*dcos(2.0d0*w1*J*t)) -
            As*((0.13333d0+0.26667d0*dcos(2.0d0*w1*J*t)) + AAB*amp)
c         pj = dexp(-((J-jmax)/dj)**2)
          pj = dble(2*J+1)*dexp(-J*(J+1)*BkT)
          tmp = tmp + rjt*pj
          Q = Q + pj
        end do
        r(i) = tmp / Q
        cy(i) = back + scale * r(i)
      end do

      return
      end
```

REFERENCES

6. REFERENCES

1 *Femtochemistry -Ultrafast Dynamics of the Chemical Bond*, Vol. I and II, edited by A. H. Zewail (World Scientific, Singapore, 1994).

2 A. H. Zewail, J. Phys. Chem. **100**, 12701 (1996).

3 M. Dantus, M. J. Rosker, and A. H. Zewail, J. Chem. Phys. **87**, 2395 (1987).

4 *Femtosecond Chemistry*, Vol. I and II, edited by J. Manz and L. Woste (Verlag Chemie GmbH, Heidelberg, 1995).

5 *Femtochemistry: Ultrafast Chemical and Physical Processes in Molecular Systems*, edited by M. Chergui (World Scientific, Singapore, 1996).

6 *Femtochemistry and Femtobiology*, edited by V. Sundstrom (World Scientific, Singapore, 1997).

7 U. Marvet and M. Dantus, Chem. Phys. Lett. **256**, 57 (1996).

8 Q. Zhang, U. Marvet, and M. Dantus, Faraday Discussion **108**, 63 (1997).

9 Q. Zhang, U. Marvet, and M. Dantus, J. Chem. Phys. **109**, 4428 (1998).

10 U. Marvet, Q. Zhang, E. J. Brown, and M. Dantus, J. Chem. Phys. **109**, 4415 (1998).

11 I. Pastirk, E. J. Brown, Q. Zhang, and M. Dantus, J. Chem. Phys. **108**, 4375 (1998).

12 U. Marvet, E. J. Brown, and M. Dantus, PCCP Phys. Chem. Chem. Phys. **2**, 885 (2000).

13 U. Marvet and M. Dantus, Chem. Phys. Lett. **245**, 393 (1996).

14 P. Gross and M. Dantus, J. Chem. Phys. **106**, 8013 (1997).

15 U. Marvet, Q. Zhang, and M. Dantus, J. Phys. Chem. Special Edition: Femtochemistry **102**, 4111 (1998).

16 M. Dantus and P. Gross, in *Encylcopedia of Applied Physics*, Vol. 22 (WILEY-VCH Verlag GmbH, 1998).

17 E. J. Heller, Acc. Chem. Res. **14**, 368 (1981).

18 Y.-X. Yan and K. A. Nelson, J. Chem. Phys. **87**, 6240 (1987).

19 R. Bersohn and A. H. Zewail, Ber. Bunsenges. Phys. Chem. **92**, 373 (1988).

20 D. Huber and E. J. Heller, J. Chem. Phys. **89**, 4752 (1988).

21 J. S. Baskin and A. H. Zewail, J. Phys. Chem. **98**, 3337 (1994).

22 J. S. Cao and K. R. Wilson, J. Chem. Phys. **106**, 5062 (1997).

23 J. Manz, in *Femtochemistry and Femtobiology*, edited by V. Sundstrom (World Scientific, Singapore, 1997).

24 L. Dhar, J. A. Rogers, and K. A. Nelson, Chem. Rev. **94**, 157 (1994).

25 L. Zehnder, Zeitschr. f. Instrkde. **11**, 275 (1891).

26 L. Mach, Zeitschr. f. Instrkde. **12**, 89 (1892).

27 G. Porter, Discuss. Faraday Soc. **9**, 60 (1950).

28 G. Porter and B. Ward, Proc. R. Soc. London **287**, 457 (1965).

29 R. L. Fork, C. H. Brito-Cruz, P. C. Becker, and C. V. Shank, Opt Lett. **12**, 483 (1987).

30 A. Baltuska, Z. Y. Wei, M. S. Pshenichnikov, and D. A. Wiersma, Opt. Lett. **22**, 102 (1997).

31 F. 97, J. Phys. Chem. Special Edition: Femtochemistry **102**, 4021 (1998).

32 A. H. Zewail, J. Chem. Soc. Faraday Trans. II **85**, 1221 (1989).

33 M. Dantus, R. M. Bowman, J. S. Baskin, and A. H. Zewail, Chem. Phys. Lett. **159**, 406 (1989).

34 M. Gruebele, G. Roberts, M. Dantus, R. M. Bowman, and A. H. Zewail, Chem. Phys. Lett. **166**, 459 (1990).

35 J. Spenser, J. S. Baskin, and A. H. Zewail, J. Phys. Chem. **98**, 3337 (1994).

36 P. M. Felker, J. Phys. Chem. **96**, 7844 (1992).

37 P. M. Felker and A. H. Zewail, in *Femtosecond Chemistry*, edited by J. Manz and L. Woste (Verlag Chemie GmbH, Weinheim, 1995).

38 R. M. Bowman, M. Dantus, and A. H. Zewail, Chem. Phys. Lett. **174**, 546 (1990).

39 T. Baumert, V. Engel, C. Meier, and G. Gerber, Chem. Phys. Lett. **200**, 488 (1992).

40 M. H. M. Jannsen, M. Dantus, H. Guo, and A. H. Zewail, Chem. Phys. Lett. **214**, 281 (1993).

41 *Femtosecond Laser Pulses: Principles and Experiments*, edited by C. Rulliere (Springer-Verlag, Berlin, 1998).

42 M. Gruebele and A. H. Zewail, J. Chem. Phys. **98**, 883 (1993).

43 A. H. Zewail, in *Femtochemistry*, Vol. I, edited by J. Manz and L. Woste (VHS, Heidelberg, 1995).

44 E. J. Brown, I. Pastirk, and M. Dantus, J. Phys. Chem. A **103**, 2912 (1999).

45 E. J. Brown, I. Pastirk, and M. Dantus, J. Phys. Chem. A., (accepted) (2001).

46 J. P. Heritage, T. K. Gustafson, and C. H. Lin, Phys. Rev. Lett. **34**, 1299 (1975).

47 M. D. Fayer, Ann. Rev. Phys. Chem. **33**, 63 (1982).

48 T. S. Rose and M. D. Fayer, Chem. Phys. Lett. **117**, 12 (1985).

49 T. S. Rose, W. L. Wilson, G. Wackerle, and M. D. Fayer, J. Chem. Phys. **86**, 5370 (1987).

50 W. H. Hesselink and D. A. Wiersma, Phys. Rev. Lett. **43**, 1991 (1979).

51 *Applications of Picosecond Spectroscopy to Chemistry*, edited by K. Eisenthal (D.Reidel, Dordrecht, 1984).

52 G. R. Fleming, *Chemical Applications of Ultrafast Spectroscopy* (Oxford, NY, 1986).

53 A. B. Myers and R. M. Hochstrasser, IEEE J. Quant. Elect. **QE-22**, 1482 (1986).

54 K. Duppen and D. A. Wiersma, J. Opt. Soc. Am. B **3**, 614 (1986).

55 D. A. Wiersma and K. Duppen, Science **237**, 1147 (1987).

56 Y.-X. Yan, L.-T. Cheng, and K. A. Nelson, in *Advances in Non-Linear Spectroscopy*, edited by R. J. H. Clark and R. E. Hester (Wiley, New York, 1987).

57 J. Chesnoy and A. Mokhtari, Phys. Rev. A **38**, 3566 (1988).

58 D. McMorrow, W. T. Lotshaw, and G. A. Kenney-Wallace, IEEE J. Quantum Electron. **QE-24**, 443 (1988).

59 L. Genberg, Q. Bao, S. Gracewski, and R. J. D. Miller, Chem. Phys. **131**, 81 (1989).

60 Nibbering, D. A. Wiersma, and K. Duppen, Phys. Rev. Lett. **66**, 2464 (1991).

61 U. Banin, A. Waldman, and S. Ruhman, J. Chem. Phys. **96**, 2416 (1992).

62 N. F. Scherer, L. D. Ziegler, and G. R. Fleming, J. Chem. Phys. **96**, 5544 (1992).

63 M. Cho, S. J. Rosenthal, N. F. Scherer, L. D. Ziegler, and G. R. Fleming, J. Chem. Phys. **96**, 5033 (1992).

64 S. A. Passino, Y. Nagasawa, and G. R. Fleming, J. Chem. Phys. **107**, 6094 (1997).

65 W. P. de Boeij, M. S. Pshenichnikov, and D. A. Wiersma, Annu. Rev. Phys. Chem. **49**, 99 (1998).

66 M. N. Yang and G. R. Fleming, J. Chem. Phys. **110**, 2983 (1999).

67 C. C. Hayden and D. W. Chandler, J. Chem. Phys. **103**, 10465 (1995).

68 M. Motzkus, S. Pedersen, and A. H. Zewail, J. Phys. Chem. **100**, 5620 (1996).

69 M. Schmitt, G. Knopp, A. Materny, and W. Kiefer, Chem. Phys. Lett. **270**, 9 (1997).

70 M. Schmitt, G. Knopp, A. Materny, and W. Kiefer, Chem. Phys. Lett. **280**, 339 (1997).

71 S. Meyer, M. Schmitt, A. Materny, W. Kiefer, and V. Engel, Chem. Phys. Lett. **281**, 332 (1997).

72 S. Meyer, M. Schmitt, A. Materny, W. Kiefer, and V. Engel, Chem. Phys. Lett. **287**, 753 (1998).

73 R. L. Abrams, J. F. Lam, R. C. Lind, D. G. Steel, and P. F. Liao, in *Optical Phase Conjugation*, edited by R. A. Fisher (Academic, New York, 1983).

74 H. J. Eichler, P. Gunter, and D. W. Pohl, *Laser-Induced Dynamic Gratings* (Springer, Berlin, 1986).

75 A. M. Weiner, S. D. Silvestri, and E. P. Ippen, J. Opt. Soc. Am. B **2**, 654 (1985).

76 C. J. Bardeen and C. V. Shank, Chem. Phys. Lett. **203**, 535 (1993).

77 D. T. Leeson, O. Berg, and D. A. Wiersma, J. Phys. Chem. **98**, 3913 (1994).

78 S. Mukamel, *Principles of Nonlinear Optical Spectroscopy* (Oxford, NY, 1995).

79 T. Joo, Y. W. Jia, and G. R. Fleming, J. Chem. Phys. **102**, 4063 (1995).

80 P. Vohringer, D. C. Arnett, T. S. Yang, and N. F. Scherer, Chem. Phys. Lett. **237**, 387 (1995).

81 I. Pastirk, V. V. Lozovoy, and M. Dantus, Chem. Phys. Lett. **333**, 76 (2001).

82 Y. Prior, Appl. Opt. **19**, 1741 (1980).

83 J. A. Shirley, R. J. Hall, and A. C. Eckbreth, Opt. Lett. **5**, 380 (1980).

84 S. Williams, R. N. Zare, and L. A. Rahn, J. Chem. Phys. **101**, 1072 (1994).

85 W. M. Zhang, V. Chernyak, and S. Mukamel, J. Chem. Phys. **110**, 5011 (1999).

86 E. J. Brown, Q. Zhang, and M. Dantus, J. Chem. Phys. **110**, 5772 (1999).

87 M. Dantus, Annu. Rev. Phys. Chem. **52**, 639 (2001).

88 R. J. Gordon and S. A. Rice, Ann. Rev. Phys. Chem. **48**, 601 (1997).

89 *Chemical Reactions and Their Control on the Femtosecond Timescale*, Vol. 101, edited by P. Gaspard and I. Burghardt (Wiley, New York, 1997).

90 R. S. Judson and H. Rabitz, Phys. Rev. Lett. **68**, 1500 (1992).

91 A. Assion, T. Baumert, M. Bergt, T. Brixner, B. Kiefer, V. Seyfried, M. Strehle, and G. Gerber, Science **282**, 919 (1998).

92 J. S. Cao, C. J. Bardeen, and K. R. Wilson, Phys. Rev. Lett. **80**, 1406 (1998).

93 C. W. Hillegas, J. X. Tull, D. Goswami, D. Strickland, and W. S. Warren, Opt. Lett. **19**, 737 (1994).

94 M. M. Wefers and K. A. Nelson, Opt. Lett. **20**, 1047 (1995).

95 A. M. Weiner, Prog. Quantum Electron. **19**, 161 (1995).

96 N. F. Scherer, A. J. Ruggiero, M. Du, and G. R. Fleming, J. Chem. Phys. **93**, 856 (1990).

97 P. Brumer and M. Shapiro, Acc. Chem. Res. **22**, 407 (1989).

98 C. Chen, Y.-Y. Yin, and D. S. Elliot, Phys. Rev. Lett. **64**, 507 (1990).

99 L. C. Zhu, V. Kleiman, X. N. Li, S. P. Lu, K. Trentelman, and R. J. Gordon, Science **270**, 77 (1995).

100 V. Yakovlev, C. J. Bardeen, J. Che, J. Cao, and K. R. Wilson, J. Chem. Phys. **108**, 2309 (1998).

101 C. J. Bardeen, J. Che, K. R. Wilson, V. Yakovlev, V. A. Apkarian, C. C. Martens, R. Zadoyan, B. Kohler, and M. Messin, J. Chem. Phys. **106**, 8486 (1997).

102 Y. J. Yan, L. E. Fried, and S. Mukamel, J. Phys. Chem. **93**, 8149 (1989).

103 I. Pastirk, E. J. Brown, B. I. Grimberg, V. V. Lozovoy, and M. Dantus, Faraday Discuss. **113**, 401 (1999).

104 E. J. Brown, I. Pastirk, B. I. Grimberg, V. V. Lozovoy, and M. Dantus, J. Chem. Phys. **111**, 3779 (1999).

105 I. Pastirk, V. V. Lozovoy, B. I. Grimberg, E. J. Brown, and M. Dantus, J. Phys. Chem. A **103**, 10226 (1999).

106 V. V. Lozovoy, B. I. Grimberg, E. J. Brown, I. Pastirk, and M. Dantus, J. Raman Spectrosc. **31**, 41 (2000).

107 V. V. Lozovoy, I. Pastirk, E. J. Brown, B. I. Grimberg, and M. Dantus, Int. Rev. Phys. Chem. **19**, 531 (2000).

108 V. V. Lozovoy, B. I. Grimberg, I. Pastirk, and M. Dantus, Chem. Phys. **267**, 99 (2001).

109 V. V. Lozovoy, I. Pastirk, M. G. Comstock, and M. Dantus, Chem. Phys. **266**, 205 (2001).

110 R. L. Fork, B. I. Greene, and C. V. Shank, Appl. Phys. Lett. **38**, 671 (1981).

111 J. A. Valdmanis, R. L. Fork, and J. P. Gordon, Opt. Lett. **10**, 131 (1985).

112 J. A. Valdmanis and R. L. Fork, IEEE J. Quantum Electron. **22**, 112 (1986).

113 G. R. Fowles, *Introduction to Modern Optics* (Dover Publications, Mineola, N.Y., 19198975).

114 M. Dantus, Ph.D., California Institute of Technology, (1991).

115 U. Marvet, Ph.D., Michigan State University, (1998).

116 R. L. Fork, C. V. Shank, and R. T. Yen, Appl. Phys. Lett. **41**, 223 (1982).

117 D. S. Bethune, Appl. Opt. **20**, 1897 (1981).

118 D. J. Kane and R. Trebino, Opt. Lett. **18**, 823 (1993).

119 R. Trebino and D. J. Kane, J. Opt. Soc. Am. A-Opt. Image Sci. Vis. **10**, 1101 (1993).

120 P. M. Felker, J. S. Baskin, and A. H. Zewail, J. Phys. Chem. **90**, 724 (1986).

121 P. M. Felker and A. H. Zewail, J. Chem. Phys. **86**, 2460 (1987).

122 R. Heather and H. Metiu, Chem. Phys. Lett. **157**, 505 (1989).

123 R. G. Gordon, J. Chem. Phys. **45**, 1643 (1966).

124 R. N. Zare, Mol. Photochem. **4**, 1 (1972).

125 R. M. Bowman, M. Dantus, and A. H. Zewail, Chem. Phys. Lett. **161**, 297 (1989).

126 M. Dantus, R. M. Bowman, and A. H. Zewail, Nature **343**, 737 (1990).

127 I. Fischer, M. J. J. Vrakking, D. M. Villeneuve, and A. Stolow, Chem. Phys. **207**, 331 (1996).

128 O. M. Sarkisov, F. E. Gostev, V. V. Lozovoy, E. A. Sviridenkov, A. A. Titov, D. G. Tovbin, and S. Y. Umanskii, Russ. Chem. Bull. **45**, 553 (1996).

129 V. V. Lozovoy, S. A. Antipin, F. E. Gostev, A. A. Titov, D. G. Tovbin, O. M. Sarkisov, A. S. Vetchinkin, and S. Y. Umanskii, Chem. Phys. Lett. **284**, 221 (1998).

130 R. J. LeRoy, J. Chem. Phys. **52**, 2683 (1970).

131 J. I. Steinfeld, R. N. Zare, L. Jones, M. Lesk, and W. Klemperer, J. Chem. Phys. **42**, 25 (1965).

132 J. C. D. Brand and A. R. Hoy, Can. J. Phys. **60**, 1209 (1982).

133 J. C. D. Brand, A. R. Hoy, A. K. Kalkar, and A. B. Yamashita, J. Molec. Spectrosc. **95**, 350 (1982).

134 U. Heemann, H. Knöckel, and E. Tiemann, Chem. Phys. Lett. **90**, 17 (1982).

135 A. J. Holmes, K. P. Lawley, T. Ridley, R. J. Donovan, and P. R. R. Langridge-Smith, J. Chem. Soc. Faraday Trans. **87**, 15 (1991).

136 E. J. Brown, R. Sloan, M. Mackert, and M. Dantus. Dantus Group/Simulations/Rotational Anisotropy. [Online] Available http://www.cem.msu.edu/~dantus/ra/ra.html, (July 2001), (Direct link to RA Simulation, http://www.cem.msu.edu/~dantus/ra/ra_sim.html).

137 J. S. Baskin, M. Gupta, M. Chachisvilis, and A. H. Zewail, Chem. Phys. Letters **275**, 437 (1997).

138 B. Friedrich and D. Herschbach, J. Phys. Chem. **99**, 15686 (1995).

139 B. Friedrich and D. Herschbach, Phys. Rev. Lett. **74**, 4623 (1995).

140 D. Normand, L. A. Lompré, and C. Cornaggia, J. Phys. B **25**, L497 (1992).

141 P. Dietrich, D. T. Strickland, M. Laberge, and P. B. Corkum, Phys. Rev. A **47**, 2305 (1993).

142 W. Kim and P. M. Felker, J. Chem. Phys. **104**, 1147 (1996).

143 W. S. Kim and P. M. Felker, J. Chem. Phys. **107**, 2193 (1997).

144 H. Sakai, C. P. Safvan, J. J. Larsen, K. M. Hilligsøe, K. Hald, and H. Stapelfeldt, J. Chem. Phys. **110**, 10235 (1999).

145 J. J. Larsen, I. Wendt-Larsen, and H. Stapelfeldt, Phys. Rev. Lett. **83**, 1123 (1999).

146 D. M. Villeneuve, S. A. Aseyev, P. Dietrich, M. Spanner, M. Y. Ivanov, and P. B. Corkum, Phys. Rev. Lett. **85**, 542 (2000).

147 H. Kono, S. Koseki, M. Shiota, and Y. Fujimura, J. Phys. Chem., (submitted).

148 M. Comstock, I. Pastirk, and M. Dantus, in *Ultrafast Phenomena XII*, edited by T. Elsaesser, S. Mukamel, M. M. Murnane, and N. F. Scherer (2000), pp. 17.

149 J. H. Posthumus, J. Plumridge, M. K. Thomas, K. Codling, L. J. Frasinski, A. J. Langley, and P. F. Taday, J. Phys. B-At. Mol. Opt. Phys. **31**, L553 (1998).

150 T. Seideman, J. Chem. Phys. **103**, 7887 (1995).

151 J. Ortigoso, M. Rodríguez, M. Gupta, and B. Friedrich, J. Chem. Phys. **110**, 3870 (1999).

152 J. Tellinghuisen, J. Chem. Phys. **58**, 2821 (1973).

153 J. Tellinghuisen, J. Chem. Phys. **76**, 4736 (1982).

154 J. P. Perrot, B. Femelat, J. L. Subtil, M. Broyer, and J. Chevaleyre, Molec. Phys. **61**, 85 (1987).

155 X. Zheng, S. Fei, M. C. Heaven, and J. Tellinghuisen, J. Mol. Spectrosc. **149**, 399 (1991).

156 K. Lawley, P. Jewsbury, T. Ridley, P. Langridge-Smith, and R. Donovan, Molec. Phys. **75**, 811 (1992).

157 Q. L. Liu, J.-K. Wang, and A. H. Zewail, Nature **364**, 427 (1993).

158 J.-K. Wang, Q. L. Liu, and A. H. Zewail, J. Phys. Chem. **99**, 11309 (1995).

159 T.-S. Yang, R. Zhang, and A. Myers, J. Chem. Phys. **100**, 8573 (1994).

160 I. Pastirk, B. I. Grimberg, V. V. Lozovoy, and M. Dantus, Abstr. Pap. Am. Chem. Soc. **220**, 439 (2000).

161 Y. R. Shen, *The Principle of Nonlinear Optics* (Wiley, NY, 1984).

162 S. Mukamel, M. Cho, and G. R. Fleming, J. Chem. Phys. **98**, 5314 (1993).

163 B. I. Grimberg, V. V. Lozovoy, M. Dantus, and S. Mukamel, J. Phys. Chem., (submitted).

164 P. H. Vaccaro, in *Nonlinear Spectroscopy for Molecular Structure Determination*, edited by E. Hirota, R. W. Field, J. P. Maier, and S. Tsuchiya (Blackwell Scientific Publications Ltd., London, 1997).

165 J. J. Sakurai, *Modern Quantum Mechanics*, Revised ed. (Addison-Wesley, Reading, MA, 1994).

166 G. C. Schatz and M. A. Ratner, *Quantum Mechanics in Chemistry* (Prentice-Hall, Englewood Cliffs, NJ, 1993).

167 T. Joo, Y. Jia, J.-Y. Yu, M. J. Lang, and G. R. Fleming, J. Chem. Phys. **104**, 6089 (1996).

168 P. H. Vaccaro, in *Molecular Dynamics and Spectroscopy by Stimulated Emission Pumping*, edited by H.-L. Dai and R. W. Field (World Scientific, Singapore, 1995).

169 Except for the phase-conjugate arrangement which is similar to a backward box configuration that has been limited to one plane. See Reference 73 also.

170 J. A. Leegwater and S. Mukamel, J. Chem. Phys. **101**, 7388 (1994).

171 T. Meier, V. Chernyak, and S. Mukamel, J. Chem. Phys. **107**, 8759 (1997).

172 G. R. Fleming and M. H. Cho, Ann. Rev. Phys. Chem. **47**, 109 (1996).

173 Y. J. Yan and S. Mukamel, J. Chem. Phys. **94**, 179 (1991).

174 M. Cho, M. Du, N. F. Scherer, G. R. Fleming, and S. Mukamel, J. Chem. Phys. **99**, 2410 (1993).

175 M. Cho, G. R. Fleming, and S. Mukamel, J. Chem. Phys. **98**, 5314 (1993).

176 M. Morgen, W. Price, P. Ludowise, and Y. Chen, J. Chem. Phys. **102**, 8780 (1995).

177 A. B. Myers and R. M. Hochstrasser, J. Chem. Phys. **85**, 6301 (1986).

178 T. Joo and A. C. Albrecht, Chem. Phys. **173**, 17 (1993).

179 S. A. Schaertel, D. Lee, and A. C. Albrecht, J. Raman Spectrosc. **26**, 889 (1995).

180 H. Li and W. Kong, J. Chem. Phys. **107**, 3777 (1997).

181 T. A. W. Wasserman, P. H. Vaccaro, and B. R. Johnson, J. Chem. Phys. **106**, 6314 (1997).

182 T. Muller, T. A. W. Wasserman, P. H. Vaccaro, and B. R. Johnson, J. Chem. Phys. **108**, 4 (1998).

183 T. A. Wasserman, P. H. Vaccaro, and B. R. Johnson, J. Chem. Phys. **108**, 7713 (1998).

184 D. A. Long, *Raman Spectroscopy* (McGraw-Hill, NY, 1977).

185 D. A. Long, in *Non-Linear Raman Spectroscopy and Its Chemical Applications*, edited by W. Kiefer and D. A. Long (D. Reidel, Dordrecht, 1982).

186 G. Herzberg, *Molecular Spectra and Molecular Structure: II. Infrared and Raman Spectra of Polyatomic Molecules*, 11th ed. (D. Van Nostrand Company, Inc., NY, 1945).

187 E. B. Wilson, J. C. Decius, and P. C. Cross, *Molecular Vibrations* (Dover, NY, 1955).

188 F. A. Cotton, *Chemical Applications of Group Theory*, 2nd ed. (Wiley, NY, 1963).

189 M. Nisoli, S. DeSilvestri, O. Svelto, R. Szipocs, K. Ferencz, C. Spielmann, S. Sartania, and F. Krausz, Opt. Lett. **22**, 522 (1997).

190 H. E. Lessing and A. von Jena, in *Laser Handbook*, Vol. 3, edited by M. L. Stich (Amsterdam, 1979).

191 B. S. Wherrett, A. L. Smirl, and T. F. Boggess, IEEE J. Quantum Electron. **QE-19**, 680 (1983).

192 T. F. Heinz, S. L. Palfrey, and K. B. Eisenthal, Opt. Lett. **9**, 359 (1984).

193 R. A. Engh, J. W. Petrich, and G. R. Fleming, J. Phys. Chem. **89**, 618 (1985).

194 Although this derivation for the FWM signal is correct, we have found that the factor of two in the anisotropic portion of the signal (sin $2\omega_1\tau$) yields incorrect rotational periods. Simply removing the factor of two in this sine expression produces correct rotational periods. Reference 87 gives a related derivation that does not contain this factor of two in the anisotropic component of the FWM signal.

195 J. S. Baskin, P. M. Felker, and A. H. Zewail, J. Chem. Phys. **84**, 4708 (1986).

196 Y. Liang, S. Augst, S. L. Chin, Y. Beaudoin, and M. Chaker, J. Phys. B: At. Mol. Opt. Phys. **27**, 5119 (1994).

197 F. London, Trans. Faraday Soc. **33**, 8 (1937).

198 C. Hattig and B. A. Hess, J. Phys. Chem. **100**, 6243 (1996).

199 M. Morgen, W. Price, L. Hunziker, P. Ludowise, M. Blackwell, and Y. Chen, Chem. Phys. Lett. **209**, 1 (1993).

200 E. P. Ippen and C. V. Shank, Appl. Phys. Lett. **26**, 92 (1975).

201 B. I. Greene and R. C. Farrow, J. Chem. Phys. **77**, 4779 (1982).

202 B. I. Greene and R. C. Farrow, Chem. Phys. Lett. **98**, 273 (1983).

203 M. Golombok, Kenney-Wallace, and S. C. Wallace, J. Phys. Chem. **89**, 5160 (1985).

204 C. Kalpouzos, W. T. Lotshaw, D. McMorrow, and G. A. Kenney-Wallace, J. Phys. Chem. **91**, 2028 (1987).

205 C. Kalpouzos, D. McMorrow, W. T. Lotshaw, and G. A. Kenney-Wallace, Chem. Phys. Lett. **150**, 138 (1988).

206 Y. J. Chang, P. Cong, and J. D. Simon, J. Phys. Chem. **99**, 7857 (1995).

207 T. Lian, Y. Kholodenko, B. Locke, and R. M. Hochstrasser, J. Phys. Chem. **99**, 7272 (1995).

208 G. R. Meredith, B. Buchalter, and C. Hanzlik, J. Chem. Phys. **78**, 1533 (1983).

209 C. H. Lin, J. P. Heritage, T. K. Gustafson, R. Y. Chiao, and J. P. McTague, Phys. Rev. A **13**, 813 (1976).

210 G. Herzberg, *Molecular Spectra and Molecular Structure: III. Electronic Spectra and Electronic Structure of Polyatomic Molecules* (D. Van Nostrand Company, Inc., NY, 1966).

211 L. S. Vasilenko, N. N. Rubtsova, and E. B. Khvorostov, Zh. Éksp. Teor. Fiz. **113**, 826 (1998).

212 R. J. H. Clark and D. M. Rippon, J. Chem. Soc. Faraday Trans. II **69**, 1496 (1973).

213 V. P. Spiridonov, A. G. Gershikov, and B. S. Butayev, J. Mol. Struct. **52**, 53 (1979).

214 C. J. Reid and M. W. Evans, J. Chem. Soc. Faraday Trans. II **75**, 1218 (1979).

215 *DMS Raman/IR Atlas*, edited by B. Schrader and W. Meier (Verlag Chemie GmbH, Wienheim, 1974).

216 S. Ruhman, A. G. Joly, and K. A. Nelson, J. Chem. Phys. **86**, 6563 (1987).

217 S. N. Thakur and L. Goodman, J. Chem. Phys. **78**, 4356 (1983).

218 R. Vasudev and J. C. D. Brand, Chem. Phys. **37**, 211 (1979).

219 S. Ruhman, L. R. Williams, A. G. Joly, B. Kohler, and K. A. Nelson, J. Phys. Chem. **91**, 2237 (1987).

220 W. T. Lotshaw, D. McMorrow, N. Thantu, J. S. Melinger, and R. Kitchenham, J. Raman Spectrosc. **26**, 571 (1995).

221 D. McMorrow, N. Thantu, J. S. Melinger, S. K. Kim, and W. T. Lotshaw, J. Phys. Chem. **100**, 10389 (1996).

222 R. N. Zare, J. Chem. Phys. **40**, 1934 (1964).

223 J. Tellinghuisen, J. Quant. Spectrosc. Radiat. Transfer **19**, 149 (1978).

224 G. Herzberg, *Molecular Spectra and Molecular Structure: I. Spectra of Diatomic Molecules* (D. Van Nostrand Company, Inc., NY, 1950).

225 N. F. Scherer, R. J. Carlson, A. Matro, M. Du, A. J. Ruggiero, V. Romero-Rochin, J. A. Cina, G. R. Fleming, and S. A. Rice, J. Chem. Phys. **95**, 1487 (1991).

226 D. M. Jonas, S. E. Bradforth, S. A. Passino, and G. R. Fleming, J. Phys. Chem. **99**, 2594 (1995).

227 T. Smith, L. W. Ungar, and J. A. Cina, J. Lumin. **58**, 66 (1994).

228 R. K. Sander and K. R. Wilson, J. Chem. Phys. **63**, 4242 (1975).

229 N. F. Scherer, D. M. Jonas, and G. R. Fleming, J. Chem. Phys. **99**, 153 (1993).

230 S. Meyer, M. Schmitt, A. Materny, W. Kiefer, and V. Engel, Chem. Phys. Lett. **301**, 248 (1999).

231 D. J. Tannor, R. Kosloff, and S. A. Rice, J. Chem. Phys. **85**, 5805 (1986).

232 D. J. Tannor and S. A. Rice, Adv. Chem. Phys. **70**, 441 (1988).

233 J. J. Gerdy, M. Dantus, R. M. Bowman, and A. H. Zewail, Chem. Phys. Lett. **171**, 1 (1990).

234 J. L. Herek, A. Materny, and A. H. Zewail, Chem. Phys. Lett. **228**, 15 (1994).

235 W. S. Warren and A. H. Zewail, J. Chem. Phys. **75**, 5956 (1981).

236 M. S. Pshenichnikov, W. P. d. Boeij, and D. A. Wiersma, Phys. Rev. Lett. **76**, 4701 (1996).

237 J. S. Melinger, A. Hariharan, S. R. Gandhi, and W. S. Warren, J. Chem. Phys. **95**, 2210 (1991).

238 B. W. Shore, J. Martin, M. P. Fewell, and K. Bergmann, Phys. Rev. A **52**, 566 (1995).

239 National Instruments - Computer-Based Measurement and Automation. [Online] Available http://www.ni.com, (July 2001), (Instrument Driver Network, http://zone.ni.com/idnet/).

240 Stanford Research Systems Home Page. [Online] Available http://www.srsys.com, (July 2001), .

241 JY Horiba formerly Instruments S. A., Inc. SPEX, JY, Dilor, Raman, spectrometers,fluorescence,ICP, gratings for spectroscopy. [Online] Available http://www.jyinc.com, (July 2001), .

242 Aerotech Motion Control Positioning Systems. [Online] Available http://www.aerotech.com, (July 2001), .